LCH Laboratoire de Constructions Hydrauliques
Laboratory of Hydraulic Constructions

ÉCOLE POLYTECHNIQUE
FÉDÉRALE DE LAUSANNE

Communication 49

Monitoring of steel-lined pressure shafts considering water-hammer wave signals and fluid-structure interaction

Fadi Hachem

Editeur : Prof. Dr A. Schleiss

Lausanne, 2011

Communications du Laboratoire de Constructions Hydrauliques ISSN 1661-1179
Ecole Polytechnique Fédérale de Lausanne
Editeur: Prof. Dr A. Schleiss

N° 22 2005 INTERREG IIIB - Projet ALPRESERV. Conférence sur la problématique de la sédimentation dans les réservoirs - Gestion durable des sédiments dans les réservoirs alpins

N° 23 2005 Master of Advanced Studies (MAS) in hydraulic schemes
Collection des articles des travaux de diplôme

N° 24 2006 S. Sayah
Efficiency of brushwood fences in shore protection against wind-wave induced erosion

N° 25 2006 P. Manso
The influence of pool geometry and induced flow patterns in rock scour by high-velocity plunging jets

N° 26 2006 M. Andaroodi
Standardization of civil engineering works of small high-head hydropower plants and development of an optimization tool

N° 27 2006 Symposium érosion et protection des rives lacustres
Bases de dimensionnement des mesures de protection des rives lacustres

N° 28 2007 A. Vela Giró
Bank protection at the outer side of curved channels by an undulated concrete wall

N° 29 2007 F. Jordan
Modèle de prévision et de gestion des crues - Optimisation des opérations des aménagements hydroélectriques à accumulation pour la réduction des débits de crue

N° 30 2007 P. Heller
Méthodologie pour la conception et la gestion des aménagements hydrauliques à buts multiples

N° 31 2007 P. Heller
Analyse qualitative des systèmes complexes à l'aide de la méthode de Gomez & Probst

N° 32 2007 J. García Hernández, F. Jordan, J. Dubois, J.-L. Boillat
Routing System II - Modélisation d'écoulements dans des systèmes hydrauliques

N° 33 2007 Symposium - Flussbauliche Massnahmen im Dienste des Hochwasserschutzes, der Umwelt, Gesellschaft und Wirtschaft / Mesures d'aménagement des cours d'eau pour la protection contre les crues, l'environnement, la société et l'économie

N° 34 2007 B. Rosier
Interaction of side weir overflow with bed-load transport and bed morphology in a channel

N° 35 2007 A. Amini
Contractile floating barriers for confinement and recuperation of oil slicks

Preface

High head pressure tunnels and shafts of hydropower plants with low rock overburden have to be steel-lined. Since the water can reach in an uncontrolled way the rock surface in case of failure of these water-conveying systems, high damages due to landslides and debris flow can occur. Furthermore high strength steel is used nowadays for such steel liners, which have an increased risk brittle and fatigue failure. Storage hydropower plants and especially pumped-storage power plants are operating today more and more under rough conditions in order to satisfy the highly volatile peak energy demand. Therefore, an enhancement of the existing theoretical design model for steel-lined pressure shafts and tunnels is necessary. Finally due to the considerable risk of these hydraulic structures also new, non-intrusive monitoring methods have to be developed. Dr. Fadi Hachem addressed these issues during his thesis research. Regarding the question of appropriate design methods he applied for the first time the fluid-structure interaction which results in different wave speeds during transient operation and water-hammer formation compared to the normally used quasi-static approach. Furthermore he developed successfully a new monitoring approach, which allows to detect, to locate and to quantify the formation of week zones along steel lined pressure shafts and tunnels. The method is based on the analysis of water hammer signals produced by transient operation of the hydropower plant. Thus the monitoring method is non-intrusive and continuously. Dr. Fadi Hachem validated the new proposed monitoring method with systematic tests at a sophisticated experimental set-up in the laboratory. Dr. Fadi Hachem tested for the first time the performance of geophones for the assessment of water hammer signals. For the analysis of the highly dynamic and high frequency data he used advanced statistical and mathematical methods. He showed the application and implementation with in-situ measurements at the Grimsel II pumped-storage power plant in Switzerland. We would like to thank Prof. Didia Cameira Covas from Instituto Superior Tecnico de Lisboa, Portugal for his support and guidance during the project as invited academic guest and for his valuable comments also as member of the jury. We thank also the other members of the jury Prof. François Avellan, LMH-EPFL and Dr. Christophe Nicolet, Power Vision Engineering for their helpful comments and suggestions. The study was part of the research project HydroNet for the design, manufacture and operation of pumped storage plants funded by the Swiss Competence Center Energy and Mobility (CCEM), the Swiss

Electrical Research and the Swiss Office for Energy. The authors wish also to acknowledge the financial support of Lombardi Foundation for the experimental installation and Kraftwerke Oberhasli KWO for their support during the prototype measurements at the Grimsel 2 pumped-storage power plant.

Prof. Dr. ANTON J. SCHLEISS

To my beloved wife, KARIMA
and
my beautiful daughter, CATHERINA

Abstract

Monitoring of steel-lined pressure shafts considering water-hammer wave signals and fluid-structure interaction

In the past, the safety margin for dynamic water pressure loads in steel-lined pressure tunnels and shafts was considered as acceptable by using conventional design safety factors. Due to high peak energy demands, existing plants are operating nowadays under rough conditions to regulate the discharge and power with relatively fast and repeated opening and closing of turbines and pumps. The economic and social costs due to production losses, when these water conveying structures are emptied for investigations and repairs, are considerable. Furthermore, the failure of pressure tunnels and shafts may produce catastrophic landslides and debris flows.

An extensive literature review showed that the existing design methods have been based on the idea of keeping the allowable stress in steel liner below yielding threshold. These methods use also some rules for construction details and tolerances which minimize the risk of formation of high local concentrated stresses. Since the beginning of use of very high-strength steel liners in new hydro plants, the actual design methods and safety assessment have become inappropriate. This type of steel has a high risk of brittle failure and fatigue. Therefore, an enhancement of the existing theoretical design model for steel-lined pressure tunnels and shafts is necessary.

Generally applicable approaches for estimating the quasi-static, which means without Fluid–Structure Interaction (FSI) and frequency-dependent water-hammer, wave speed in steel-lined pressure tunnels have been analyzed.

The external constraints and assumptions of these approaches are discussed in detail and the reformulated formulas are then compared to commonly used expressions. For thin steel liners and weak rock mass modulus, Jaeger's and Parmakian's relationships overestimate the water-hammer velocity by approximately $3 - 4.5\,\%$, while in Halliwell's formula this overestimation reaches $7.5\,\%$. The quasi-static wave speed is significantly influenced by the state of the backfill concrete and the near-field rock zone (cracked or uncracked). In the case when these two layers are cracked, the quasi-static wave speed is overestimated in between $1\,\%$ and $8\,\%$ compared to uncracked concrete and near-field rock layers.

Depending on the stiffness of steel liner and penstock, the FSI leads to significant difference in wave speeds values.

As a first step, a fluid-structure interaction model is proposed as a basis for the development of new design criteria which consider fracture mechanics to access the response of high-strength steel liners. The effect of the backfill concrete and the surrounding rock mass has been mechanically modeled by a spring, a dashpot, and a lumped additional mass. The quadratic dispersion equation which results from FSI model, has been solved in the frequency domain through a numerical example. In this example and compared to the quasi-static case, the FSI approach results up to 13 % higher wave speed values in the high-frequency range (higher than 600 Hz) and up to 150 % lower values for frequencies between 150 and 300 Hz. In the intermediate frequency range (between 80 and 800 Hz), the precursor mode has a cut-off frequency which depends on the longitudinal distribution of the stiffness of the liner. The first acoustic mode begins to propagate at a frequency near 525 Hz. This cut-off frequency depends on the radial stiffness of the steel liner. For practical applications, the aforementioned wave speed differences in the quasi-static and FSI cases can be tolerated because of the uncertainty in the estimation of the rock mass characteristics and the presence of air in the water. The dynamic pressures obtained from classical water-hammer theory are not overly affected by such differences in wave speed while the FSI may lead to higher extreme dynamic pressures with higher frequencies.

The influence of local drop of wall stiffness of pressurized waterways on the pressure wave speed and wave dissipation during transients was investigated experimentally. The weak reaches are resulting from local deterioration of the backfill concrete and the rock mass surrounding the steel liner. The change of wave speed generated by the weakening of the radial liner supports creates reflection boundaries for the incident pressure waves. A new signal processing procedure to identify the presence of these weak reaches has been proposed and validated by physical experiment tests. During water-hammer events, pressure and vibration records have been acquired at the both ends of a multi-reach steel test pipe. The weak reaches are simulated by replacing the steel reaches with Aluminum and PVC materials. The acquired data have been assessed using, amongst others, the Fourier Transform, wavelet decomposition, and cross-correlation techniques. The developed new monitoring method shows that wave speed and wave dissipation ratio are good indicators of the presence of local and large changes in stiffness. This method is also able to locate the weakness of stiffness along the test pipe when one PVC reach is used. When steep front wave have been generated inside the test pipe, it was possible to locate the position of the weak reach boundaries with a maximum relative mean error of 5.9 %. The severity of the local stiffness change has been also estimated with a maximum relative mean error of 20.6 %.

In-situ measurements from a pressure shaft have been carried out to validate the new signal processing procedure. The prototype measurements use dynamic

pressure and geophone sensors placed at both ends of the pressure shaft of the Grimsel II pumped-storage plant, in the Canton of Bern, in Switzerland. The data are acquired continuously and accessed on-line via internet. Different approaches to estimate the wave speed and wave dissipation generated inside the pressure shaft during start-up and shut-down of pumps and turbines have been applied. The relatively small water-hammer pressure fluctuations combined with the homogeneous quality of the rock mass surrounding the pressure shaft made it difficult to apply the entire localization procedure. Nevertheless, monitoring charts have been established based on the statistical quality control of the two indicators namely the water-hammer wave speed and the wave dissipation coefficient. The wave speed was assessed from the Fourier transformation spectrums ($\mathcal{F}$) while the dissipation coefficient was determined by computing the root mean square (RMS) of the signal followed by an exponential regression fitting. Three control limits representing the actual state of the shaft wall have been set on these charts from the acquired and processed pressure data. These limits and the overall behaviour of the pattern of future measured points will be used for on-line monitoring of the shaft. The control limits of the monitoring charts for the water-hammer wave speed should be revised after acquiring a longer series of in-situ measurements. The control limits of the exponential dissipation coefficient computed during the pump and turbine start-up modes can be used for on-line monitoring. During the pump and turbine shut-down modes, the dissipation coefficient has encountered a shift of about 55 %. Additional measurements are needed to understand its global pattern behaviour.

Keywords: Acoustic, drop of wall stiffness, geophones, monitoring, pipes, signal processing, steel-lined pressure tunnels, time and frequency domains, transient pressure signals, water-hammer, wave dissipation, wave reflections, wave speed, wavelet decomposition.

Résumé

Surveillance des puits blindés en considérant les coups de bélier et l'interaction fluide-structure

Dans le passé, la marge de sécurité liée aux sollicitations dynamiques générées par l'eau dans les puits et tunnels blindés était considérée comme acceptable à condition d'utiliser les facteurs de sécurité conventionnels. En raison de la forte demande de l'énergie de pointe, les centrales hydro-électriques doivent opérer à des vitesses variables pour assurer avec efficacité, flexibilité et sécurité l'équilibre entre la production et la demande. Le réglage de la puissance des turbines ou des pompes s'effectue ainsi à travers des changements de débit de plus en plus rapides et multiples. Les pertes économiques et sociales générées par un arrêt de production pour vider, ausculter et éventuellement réparer ces ouvrages sont considérables. D'autre part, la rupture de blindage sous l'effet des pressions intérieures dynamiques a des conséquences catastrophiques. La quantité importante de l'eau de fuite peut enclencher des glissements de terrain et la formation des laves torrentielles dévastatrices.

La recherche bibliographique a montré que les méthodes de dimensionnement utilisées actuellement sont basées sur l'idée de maintenir la contrainte de traction dans l'acier du blindage au-dessous de la limite d'élasticité de l'acier utilisé. D'autres critères liés à des détails de construction et à des limites de tolérance sont également respectés pour diminuer le risque de formation des contraintes locales excessives dans le blindage. Ces méthodes de dimensionnement ainsi que l'analyse de la sécurité des puits et tunnels blindés sont devenues insuffisantes pour dimensionner les blindages fabriqués à partir des aciers à haute résistance dans les nouvelles centrales hydro-électriques. Les problèmes engendrés par l'utilisation de ce type d'acier, notamment la rupture fragile et la fatigue, obligent les chercheurs à améliorer et/ou modifier le modèle théorique actuel de calcul.

Des approches générales pour estimer la vitesse de propagation des coups de bélier à l'inérieur des puits et tunnels blindés ont été analysées dans le cas quasi-statique, c'est-à-dire, sans considérer l'interaction fluide-structure (FSI) et la dépendance entre la vitesse et la fréquence. Les conditions aux bords ainsi que les hypothèses prises en considération dans l'établissement de ces approches

sont présentées et discutées en détail. Les expressions reformulées sont également comparées à d'autres formules qui sont actuellement utilisées. Dans le cas des blindages en acier de faible épaisseur entourés de rocher à faible module d'élasticité, les relations proposées par Jaeger et Parmakian surestiment la vitesse des ondes de l'ordre de $3 - 4.5\,\%$ alors que dans la formule de Halliwell, la surestimation atteint $7.5\,\%$. La vitesse quasi-statique des ondes est significativement influencée par l'état du béton de remplissage et du rocher entourant le blindage (fissuré ou pas). Dans le cas où ces deux matériaux sont considérés comme fissurés, la vitesse quasi-statique est surestimée entre $1\,\%$ et $8\,\%$ relativement au cas du béton et rocher non fissurés. En fonction du degré de rigidité de blindage, le FSI engendre des différences significatives dans la vitesse des coups de bélier.

Dans une première étape, un modèle basé sur le phénomène d'interaction fluide-structure (FSI) a été proposé pour le développement des nouveaux critères de dimensionnement qui considèrent la mécanique de rupture fragile pour analyser la réponse des blindages en acier à haute résistance. Dans ce modèle, le béton de remplissage et la roche entourant le blindage sont modélisés par un ressort, un amortisseur, et une masse additionnelle. L'équation de dispersion quadratique résultante de ce modèle FSI a été résolue dans le domaine fréquentiel à travers un exemple numérique. Dans cet exemple et dans l'intervalle des hautes fréquences (supérieure à $600\,\mathrm{Hz}$), l'approche FSI génère des vitesses d'onde $13\,\%$ au-dessus de celles obtenues dans le cas quasi-statique. Cette différence de vitesse peut atteindre les $150\,\%$ au-dessous du cas quasi-statique pour les fréquences entre $150\,\mathrm{Hz}$ et $300\,\mathrm{Hz}$. Dans l'intervalle de fréquence [$80\,\mathrm{Hz}$; $800\,\mathrm{Hz}$], le mode de propagation lié aux ondes précurseurs présente une basse fréquence de coupure qui dépend de la distribution longitudinale de la rigidité du blindage. Le premier mode d'onde acoustique commence à propager à partir d'une fréquence proche de $525\,\mathrm{Hz}$. La fréquence de coupure relative à ce mode est fonction de la rigidité radiale du blindage. Dans la pratique, la différence de vitesse des coups de bélier entre le cas FSI et le cas quasi-statique est considérée comme tolérable en raison de l'incertitude dans l'estimation des propriétés mécaniques du rocher et de la présence de l'air dans l'eau. Les pressions dynamiques obtenues par l'approche théorique classique des coups de bélier sont peut influencées par cette différence de vitesse de l'onde alors que le FSI peut engendrer des pressions dynamiques extrêmes à hautes fréquences.

L'influence de la détérioration locale de la rigidité de la paroi des puits et tunnels blindés sur la célérité et la dissipation de l'onde de pression durant les phénomènes transitoires a été étudiée expérimentalement. La formation des régions de puits de faible rigidité est une conséquence de la détérioration de la résistance du béton de remplissage et du massif rocheux qui entourent le blindage. Le changement de la célérité de l'onde associé à cet affaiblissement de la rigidité du support de blindage crée des frontières acoustiques réfléchissantes pour les ondes incidentes. Une méthode innovatrice pour détecter la présence de ces portions de faible rigidité est proposée et validée par des séries d'essais sur mo-

dèle physique à échelle réduite. Les signaux des pressions dynamiques et des vibrations radiales de la paroi d'une conduite d'essai ont été mesurés à ses deux extrémités durant les évènements des coups de bélier. La conduite d'essai est construite à partir de plusieurs bouts liés ensemble par des flasques. Les bouts de faible rigidité ont été modélisés en remplaçant les parties en acier par d'autres fabriquées en aluminium ou PVC. Les signaux mesurés ont été traités et analysés en utilisant, entre autres, la Transformation de Fourier, les ondelettes, et la technique de cross-corrélation. La nouvelle méthode de surveillance montre que la vitesse de propagation et le facteur de dissipation des ondes sont des bons indicateurs de la présence d'un affaiblissement local important de la rigidité radiale de la conduite. Cette méthode est également capable de localiser l'endroit de cet affaiblissement lorsqu'un seul bout de PVC est utilisé. Quand des ondes à front raide ont été générées dans la conduite d'essai, il a été possible de localiser les deux extrémités de la partie en PVC avec une erreur moyenne maximale de 5.9 %. La sévérité du changement de la rigidité de la conduite a pu être estimée avec une erreur moyenne maximale de 20.6 %.

Des mesures in-situ ont été effectuées pour valider la méthode de détection et de localisation des bouts de puits de faible rigidité. Ces mesures utilisent des capteurs de pressions dynamiques et des géophones placés sur les deux extrémités du puits blindés de l'aménagement pompage-turbinage de Grimsel II, situé dans le Canton de Berne, en Suisse. Les données ont été acquises d'une manière continue avec une accessibilité en ligne via l'internet. Différentes approches ont été appliquées dans le but d'estimer la célérité et la dissipation d'énergie de l'onde de pression durant l'enclenchement et l'arrêt des pompes et des turbines. Les faibles variations de la pression dynamique de service combinées avec l'existence d'une masse rocheuse homogène entourant le blindage ont rendu difficile l'application de la totalité de la procédure de surveillance proposée. Néanmoins, des graphes de surveillance basés sur le principe de contrôle de qualité ont pu être établis pour les deux indicateurs, à savoir, la célérité et le coefficient exponentiel de dissipation de l'onde. La vitesse de l'onde a été estimée à partir de la Transformation de Fourier ($\mathcal{F}$). Quant au coefficient de dissipation, il a été déterminé par un calcul de RMS du signal acquis suivi d'une régression exponentielle. Trois limites de contrôle qui représentent l'état actuel de la rigidité de la paroi du puits blindés ont été définies sur les graphiques de surveillance. Ces limites ainsi que les tendances globales des nuages des points actuels et futures seront utilisés pour surveiller la paroi du puits blindés. Les limites de contrôle relatives à la vitesse de l'onde doivent être révisées après l'acquisition d'une plus longue série de mesures. Les limites qui correspondent au coefficient exponentiel de dissipation de l'onde durant l'enclenchement des pompes et turbines peuvent être utilisées pour la surveillance du puits blindé. Durant les modes de fermeture des machines hydrauliques, les valeurs de coefficient de dissipation ont subi un changement de 55 %. Pour expliquer ce décalage, des longues séries de mesure de pression sont nécessaires.

Keywords: Acoustique, célérité des ondes, conduites, coups de bélier, décomposition par ondelettes, détérioration de la rigidité de la paroi, dissipation des ondes, domaine temps et domaine fréquence, géophones, puits et tunnels blindés, réflexions des ondes, signaux de pression transitoires, surveillance, traitement du signal.

Zusammenfassung

Überwachung von gepanzerten Druckschächten durch Analyse der Druckstosssignale sowie der Fluid-Struktur Interaktion

In der Vergangenheit wurde die Anwendung von konventionellen Sicherheitskoeffizienten für die Dimensionierung von gepanzerten Druckstollen und -schächten für dynamische Wasserdrücke als ausreichend betrachtet. Durch die steigende Nachfrage an Spitzenenergie sind bestehende Kraftwerke heutzutage jedoch anspruchsvolleren Betriebsbedingungen unterworfen, welche durch zahlreiche und schnelle Betriebsänderungen von Pumpen und Turbinen gekennzeichnet sind. Die Produktionsverluste bei einer Entleerung der Triebwasserwege zur Überprüfung oder zur Ausführung von Reparaturarbeiten sind beträchtlich. Zudem kann das Versagen oder der Bruch eines Druckstollens oder -schachtes katastrophale Auswirkungen haben.

Eine ausführliche Literaturstudie hat gezeigt, dass die vorhandenen Bemessungsgrundlagen darauf basieren, die Spannungen in den Panzerungen auf den elastischen Bereich zu begrenzen. Bestehende Bemessungsmethoden berücksichtigen Ausführungsregeln für konstruktive Details sowie Toleranzen, um das Risiko von Spannungskonzentrationen zu minimieren. Seit der vermehrten Verwendung von hochfesten Panzerungen in Hochdruckkraftwerken sind die Bemessungsgrundlagen und die Sicherheitskriterien nicht mehr ausreichend. Hochfeste Stähle bergen ein vergrössertes Risiko von Spröd- oder Ermüdungsbrüchen, weshalb eine Erweiterung des vorhandenen Berechnungsmodells für Druckschächte und Druckstollen erforderlich ist.

Generell gültige Ansätze zur Abschätzung der "quasi-statischen" Wellengeschwindigkeit in gepanzerten Druckstollen wurden untersucht, d.h. ohne Fluid-Struktur Interaktion (FSI) und frequenzabhängigen Druckstössen. Die äusseren Randbedingungen und Hypothesen dieser Ansätze wurden detailliert diskutiert und die hergeleiteten Formeln mit bestehenden, häufig benutzten Ausdrücken verglichen. Für dünne Panzerungen und einen schwachen Felsmodul überschätzen die Jaeger- und die Parmakian-Gleichungen die Druckstossgeschwindigkeit um rund $3 - 4.5\,\%$, die Formel nach Halliwell gar um $7.5\,\%$. Die quasi-statische Wellengeschwindigkeit wird erheblich vom Zustand des Hinterfüllbetons und des nahen Felsmassivs (gerissen oder intakt)

beeinflusst. Falls beide die Panzerung umgebenden Schichten gerissen sind, wird die quasi-statische Druckwellengeschwindigkeit im Vergleich zu ungerissenem Beton und Fels um 1 % bis 8 % überschätzt. In Abhängigkeit der Festigkeit der Panzerung führt die FSI zu signifikanten Abweichungen der Werte der Druckwellengeschwindigkeit.

In einem ersten Schritt wurde ein Fluid-Struktur Interaktionsmodell erarbeitet, das als Grundlage für neue Bemessungskriterien dient, welche die Bruchmechanik zur Beurteilung des Verhaltens von hochfesten, gepanzerten Triebwasserwegen miteinbeziehen. Der Hinterfüllbeton und das umschliessende Felsmassiv wurden mechanisch als Feder, Dämpfer und eine zusätzliche Masse modelliert. Die aus dem FSI-Modell hervorgehende quadratische Dispersionsrelation wurde im relevanten Frequenzbereich anhand eines numerischen Beispiels gelöst. Für diesen Fall und verglichen mit dem quasi-statischen Verhalten, resultieren aus dem FSI-Ansatz bis zu 13 % höhere Werte der Wellengeschwindigkeit im Hochfrequenzbereich (höher als 600 Hz) und bis zu 150 % tiefere Werte für Frequenzen zwischen 150 und 300 Hz. Im mittleren Frequenzbereich (zwischen 80 und 800 Hz) hat der Vorläufermodus (Poisson's effect) eine Grenzfrequenz, die von der Längsverteilung der Panzerungsfestigkeit abhängt. Die erste akustische Mode beginnt sich bei einer Frequenz nahe 525 Hz fortzupflanzen. Diese Grenzfrequenz hängt von der radialen Festigkeit der Panzerung ab. In der Praxis können obengenannte Geschwindigkeitsunterschiede zwischen quasi-statischem und FSI-Modell aufgrund der Unsicherheit bezüglich Felsbeschaffenheit und Lufteinschlüssen im Wasser toleriert werden. Die mit der klassischen Druckstosstheorie berechneten dynamischen Drücke werden nicht übermässig beeinträchtigt von solchen Unterschieden in der Wellengeschwindigkeit. Die FSI hingegen kann zu höheren dynamischen Drücken mit höheren Frequenzen führen.

Im physikalischen Modell wurde der Einfluss eines lokalen Abfalls der Stollen- oder Schachtfestigkeit auf die Geschwindigkeit und die Dämpfung der Druckwelle experimentell untersucht. Solche Schwachstellen sind die Folge von zerbrochenem Füllbeton oder Felsmassiv, welche die Panzerung umschliessen, allenfalls auch von Feinrissen in derselben. Die durch eine Schwachstelle hervorgerufene Geschwindigkeitsänderung der Druckwelle erzeugt eine fiktive Reflexionsgrenze für die einfallende Druckwelle. Die vorgeschlagene, neuartige Methode der Signalverarbeitung zur Identifizierung und Lokalisierung der Schwachstellen wurde im physikalischen Modell überprüft. An beiden Enden einer modularen, stahlgefertigten Versuchsleitung wurden während Druckstossereignissen, die durch das rasche Schliessen eines Schiebers am Modellende simuliert wurden, Druck- und Vibrationssignale aufgezeichnet. Die Schwachstellen mit verminderter Festigkeit wurden erzeugt, indem einzelne Abschnitte der Stahlleitung durch Rohrstücke aus Aluminium oder PVC ersetzt wurden. Die aufgezeichneten Signale wurden unter anderem durch Fourier-Transformation, Wavelet-Dekomposition und Kreuzkorrelation untersucht und beschrieben. Die

neu entwickelte Überwachungsmethode zeigt, dass Geschwindigkeit und Dämpfungsgrad der Druckwelle gute Indikatoren für lokale und signifikante Änderungen der Festigkeit sind. Im Falle eines eingebauten PVC-Rohrstücks erlaubt sie sogar die genaue Lokalisierung des Festigkeitsverlusts in der Versuchsleitung. Bei steil ansteigenden oder abfallenden Wellen in der Versuchsleitung ist eine Lokalisierung der Grenzen der Schwachstelle mit einem maximalen relativen Fehler von 5.9 % möglich. Der Schweregrad des Festigkeitsverlustes konnte mit einem maximalen relativen mittleren Fehler von 20.6 % abgeschätzt werden.

Zur Validierung der neu entwickelten Methode der Signalverarbeitung wurden Prototypmessungen durchgeführt. Dabei wurde der Druckschacht des Pumpspeicherkraftwerks Grimsel II im Kanton Bern (Schweiz) an beiden Enden mit dynamischen Drucksonden und Geophonen ausgerüstet. Auf die kontinuierlich aufgezeichneten Daten kann online direkt zugegriffen werden. Zur Abschätzung der Geschwindigkeit und Dämpfung der beim Anfahren oder Abschalten der Maschinen entstehenden Druckwellen im Druckschacht, wurden verschiedene Ansätze angewandt. Die relativ kleinen Druckschwankungen kombiniert mit der homogenen Felsqualität vor Ort erschwerten jedoch die direkte Anwendung der gesamten Lokalisierungsmethode. Trotzdem konnten Überwachungsdiagramme erstellt werden, die basierend auf den beiden Indikatoren Geschwindigkeit und Dämpfung der Druckwellen eine statistische Qualitätskontrolle der Druckschachtpanzerung erlauben. Die Druckwellengeschwindigkeit wurde durch Fourier-Transformationsspektren beschrieben, während der Dämpfungskoeffizient mittels Effektivwert des Signals, ergänzt mit einer exponentiellen Regression berechnet wurde. In den Überwachungsdiagrammen konnten durch die aufgezeichneten und ausgewerteten Druckmessungen drei charakteristische Kontrollwerte für den aktuellen Zustand des Druckschachts definiert werden. Diese Werte sowie das Verhalten zukünftiger Druckaufzeichnungen können zur Online-Überwachung des Schachts benutzt werden. Die drei Kontrollwerte in den Überwachungsdiagrammen sollten nach einer längeren Messperiode überprüft und allenfalls angepasst werden. Der Grenzwert des exponentiellen Dämpfungskoeffizienten, der für den Anfahrbetrieb von Pumpen und Turbinen berechnet wurde, kann ebenfalls zur Online-Überwachung benutzt werden. Im Verlauf der Messperiode wurde für das Abschalten der Pumpen und Turbinen beim Dämpfungskoeffizient eine zeitliche Verschiebung von 55 % festgestellt. Zum Verständnis dieses Verhaltens sind zusätzliche Messungen nötig.

Kennworte: Akustik, Druckstoss, Festigkeitsverlust der Panzerung, Geophone, gepanzerte Triebwasserwege, Geschwindigkeit von Druckwellen, instationäre Drucksignale, Leitungen, Reflektion von Druckwellen, Signalverarbeitung, Überwachung, Wavelet-Dekomposition, Wellendissipation, Zeit- und Frequenzanalyse.

Contents

Chapter 1

Introduction

This chapter presents the context and formulates the main objectives of this research project. It also describes the structure of the present report and provides the methodology that has been used.

1.1 Context

The current electricity market offers an excellent opportunity for hydropower producers to increase their daily peak energy production. In addition to its attractive market price, this energy is essential to avoid blackouts which could cover large areas and cause major economical losses.

Modern power plants are expected to operate at variable speed in a wide range of output power with improved efficiency, flexibility and safety. Therefore, the pumped-storage power generation has gained in importance since it allows storing and generating high peak energy by moving water back and forth between two reservoirs located at different elevations.

Since 1980s, very few fundamental research has been performed on pressure shafts and tunnels of hydropower plants. Nevertheless, there is still a need to enhance monitoring and design methods by integrating more precisely the interaction between water, steel lining and rock mass. The results of such further investigations stand for a crucial target since the collapse of the shallow buried pressure shaft of Cleuson-Dixence hydropower plant in Switzerland in December 2000 (Starnberger and Chène, 2011).

The present research work is one of the civil engineering task in the framework of the multidisciplinary project HydroNet I. It concerns the design and monitoring of steel-lined pressure shafts and tunnels under internal loads.

The research consortium HydroNet I (http://hydronet.epfl.ch) has been established in 2007. It is co-financed by CCEM and Swisselectric research and aims to converge towards a consistent, standardized methodology for design, manufacturing, operation, monitoring and control of pumped-storage plants. The different partners and main objectives of this consortium are shown in Fig. 1.1.

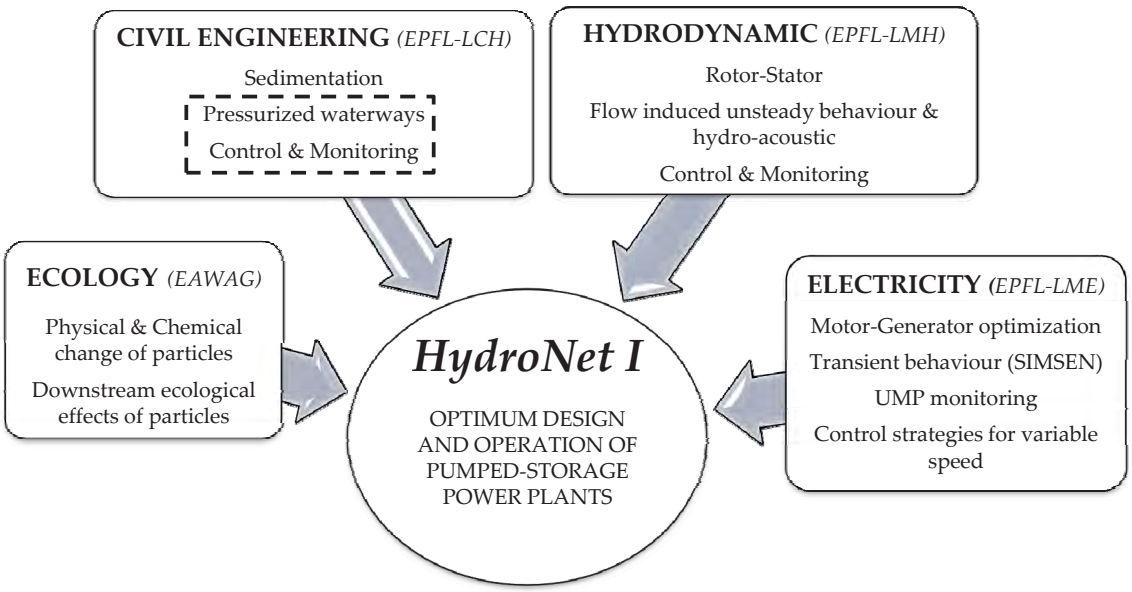

Figure 1.1: The stakeholders and main objectives of HydroNet I research project consortium (2007-2011).

1.2 Practical relevance and main objectives of this research work

The actual design rules for pressure steel-lined tunnels and shafts are the result of research that has been conducted mainly during the period of construction of hydropower plant in Europe between the 40s and the 80s. The true behaviour of combined steel-concrete-rock linings is not yet fully understood, especially the influence of severe transient flow phenomena, such as water-hammer effects, on the short and long term structural behaviour, fatigue, and safety of the lining. The existing design methods have been based on the idea of keeping the allowable stress in steel liner below yielding point and respecting some construction details and tolerances to minimize stress raiser points. These design methods and safety assessment have become inappropriate since the beginning of use of very high strength steel liners which have a significant risk of brittle failure and fatigue.

The monitoring of existing steel-lined shafts and tunnels is normally done using pressure sensors, water level measurements, and downstream and upstream flowmeters. The water pressure records are usually used to check the amplitude of the transient pressures relative to a critical operation value defined during the design phase. No further advanced analyses and pressure signal processing is done. When a liner failure occurs, the water flow discharge increases and exceeds a predefined threshold. The security butterfly valve at the upstream end of the shaft closes automatically to limit the quantity of water leaking from the shaft towards the rock surface. Nevertheless, catastrophic consequences can occur because of the considerable leakage volume combined with hydraulic jacking

of the rock mass. Any further and additional investigation of the steel-liner regarding excessive local deformations and steel yielding requires the interruption of operation and the dewatering of the shaft for visual checking. Furthermore, no information can be easily obtained regarding the stiffness of the backfill concrete and the rock mass surrounding the steel-liner.

The objectives of this research project and its main practical applications can be summarized as follows:

- Enhancement of the basis of the existing theoretical model to open the door for future development, including the application of fracture mechanics, to assess the response of high-strength steel which is used as the lining for shafts of new hydro plants.
- Development of new and non-intrusive monitoring method for steel-lined pressure shafts and tunnels, based on the Fluid-Structure Interaction and on the processing of the wave reflections during water-hammer. It is a real time procedure, which can detect the occurrence, severity and location of a change in the wall stiffness of shafts and tunnels, based on recorded dynamic pressure signals at both accessible ends.

1.3 Structure and methodology of the study

The structure of the present report is presented in Fig. 1.2. The main objectives of each chapter can be summarized as follows:

Chapter 2 gives an overview of existing methods for load sharing calculations and design guidelines. A discussion is provided between calculations for axisymetrical isotropic and anisotropic rock masses surrounding the steel liner. Also, non-destructive assessment methods based on hydraulic and non-hydraulic technologies, which have already been adapted from the oil and gas industries, are reviewed. Finally, gaps in knowledge are identified and some new research fields are suggested.

Chapter 3 provides the basic theoretical tools needed to investigate the design and monitoring of steel-lined pressure tunnels and shafts. These tools include fluid transient models and some signal processing techniques.

Chapter 4 focuses on the analysis of the wave speed propagation in rock-bored steel-lined tunnels and shafts. It reviews the most relevant contributions in deriving the wave speed formulae and extends the use of the FSI model, derived by Kuiken (1984), to the field of steel-lined tunnels and shafts. Some examples with a sensitivity analysis of the main parameters are also provided in this chapter.

Chapter 5 presents and describes the design of the test facility for the validation of the monitoring procedures. The shaft is modeled by a single-layer system of the test pipe. The water-hammer events are generated inside the test pipe by

closing a shut-off valve at its downstream end. For the detection of longitudinal stiffness heterogeneity, different geometric configurations of the steel test pipe were examined by changing systematically the position of an aluminum and PVC pipe reach.

Chapter 6 presents and analyzes the experimental results. New monitoring approaches for detecting, locating and quantifying structurally weak reaches of steel-lined pressure tunnels and shafts are provided.

Chapter 7 describes the Grimsel II pumped-storage plant and presents the in-situ monitoring system which was designed and is used to acquire the pressure and vibration measurements from the shaft at the high pressure side of the plant.

In **Chapter 8** the in-situ measurement data are presented and analyzed. The new monitoring approaches proposed in Chapter 6 are applied at the Grimsel II pressure shaft. The difficulties encountered by the application of these approaches on a prototype are also presented.

Finally, **Chapter 9** gives the general conclusions, recommendations and outlook for further research.

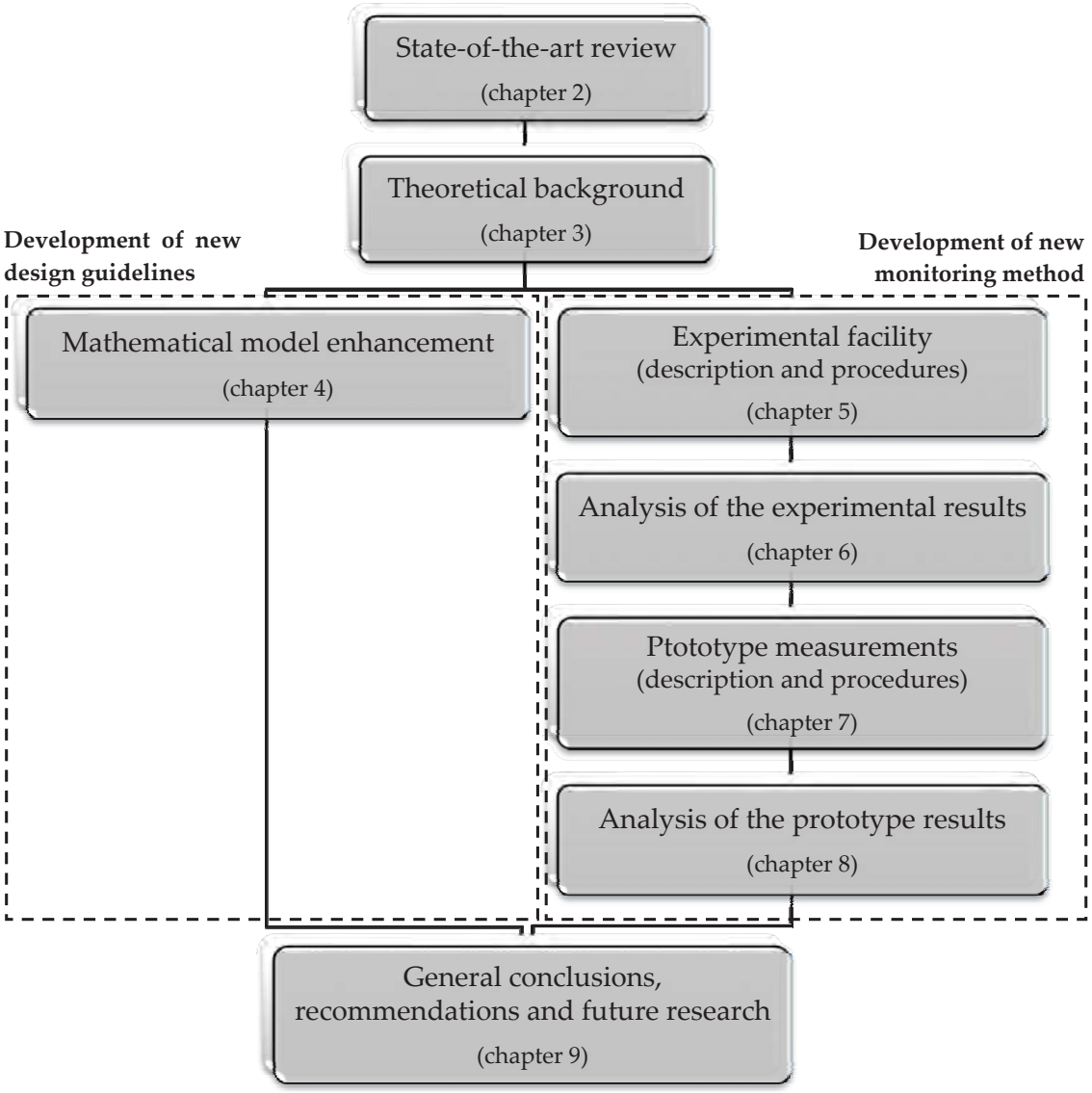

Figure 1.2: The main structure of the research report.

Chapter 2

State-of-the-art

This chapter gives an overview of existing methods for load sharing calculations and design guidelines for steel-lined pressure tunnels and shafts under internal water pressure. A discussion is provided between calculations for axisymetrical isotropic and anisotropic rock masses surrounding the liner. Furthermore, high strength steel is more and more often used for steel liners. For such steel, design methods based on yielding strength can be questioned. Also, non-destructive assessment methods based on hydraulic and non-hydraulic technologies, which have already been adapted from the oil and gas industries, are reviewed. Finally, gaps in knowledge are identified and some new research niches are suggested. A part of this chapter has been published in Hachem and Schleiss (2009).

2.1 Design methodologies

2.1.1 Current design criteria for steel liners

Basic criteria for the design of steel-lined sections of tunnels and shafts as recommended by Schleiss (1985; 1986 and 1988) are:

A. working stress and deformation of the steel liner; and,
B. load-bearing capacity of the rock mass

Condition A

This refers to the behaviour of the steel liner, and includes:

A1. stability of the steel liner under external water pressure;
A2. limiting working stresses in the steel liner; and,
A3. limiting local deformation of steel liner (crack bridging).

Condition A1 In accordance with normal practice, a factor of safety of 1.5 against buckling should be adopted. If the acting external water pressure is based, because of a lack of field data, on very conservative assumptions, a safety factor of

between 1.15 and 1.30 is sufficient. In the case of a sandwich lining, the compressive stresses in inner concrete ring should be well below the ultimate strength of concrete (the safety factors applied in the different codes are varying from 1.8 to 2.5).

Condition A2 The stresses in the steel liner are derived based on the compatibility of the radial displacements of the steel and rock at their boundary, as transmitted by the backfill concrete. Load sharing between steel liner and rock should be determined by taking into account a cracked backfill concrete (no tangential stresses can be transmitted) and the effect of a crack stress-relieved rock zone.

Condition A3 The steel liner must be able to bridge any cracks in the backfill concrete which develop under internal pressure. Since, for reasons of symmetry, a minimum of two cracks will occur, the maximum expected width of the cracks will be equal to the half of the total circumferential deformation of the rock mass under internal pressure. This condition comes only into play for very thin steel liners as in case of sandwich linings with steel membranes where thickness are not governed by buckling.

Condition B

The purpose of this condition is, on one hand, to check the load sharing assumed for Condition A2 and, on the other hand, to guarantee sufficient security against rock mass failure. The maximum rock mass participation is equal to the mechanical pressure developed at the boundary between the steel liner (or backfill concrete) and the rock at which the rock can no longer share the load. In principle, this limited load sharing is reached as soon as the maximum tensile stresses in the rock mass caused by that boundary pressure exceed the natural stresses in the rock mass (in a plan perpendicular to tunnel axis).

The current design procedure has been described in detail by Schleiss (1988) through a general design diagram including conditions A and B (Fig. 2.1) at the example of the Lower Pressure Tunnel of the North Fork Stanislaus River Hydroelectric Project in California.

In the following, the design criteria for internal water pressure are discussed more in detail.

2.1.2 Load sharing between the steel liner and surrounding rock mass

2.1.2.1 Radial symmetric calculation model

The determination of the load sharing between the steel lining, the backfill concrete and the surrounding rock mass is normally based on elastic theory. The radial deformation of the steel liner is put equal to the radial deformation of the

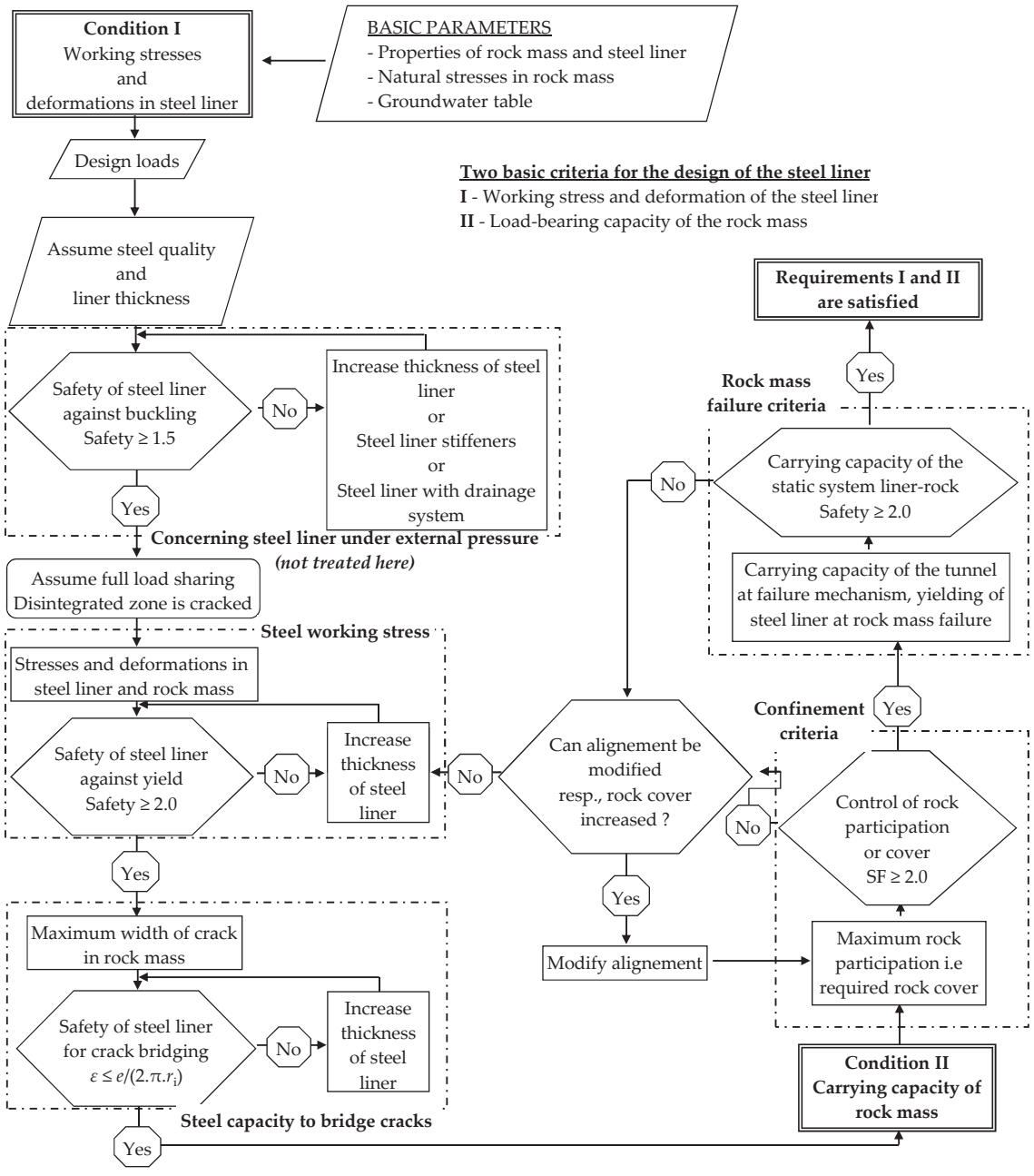

Figure 2.1: Design diagram for steel-lined pressure tunnels and shafts (after Schleiss, 1988).

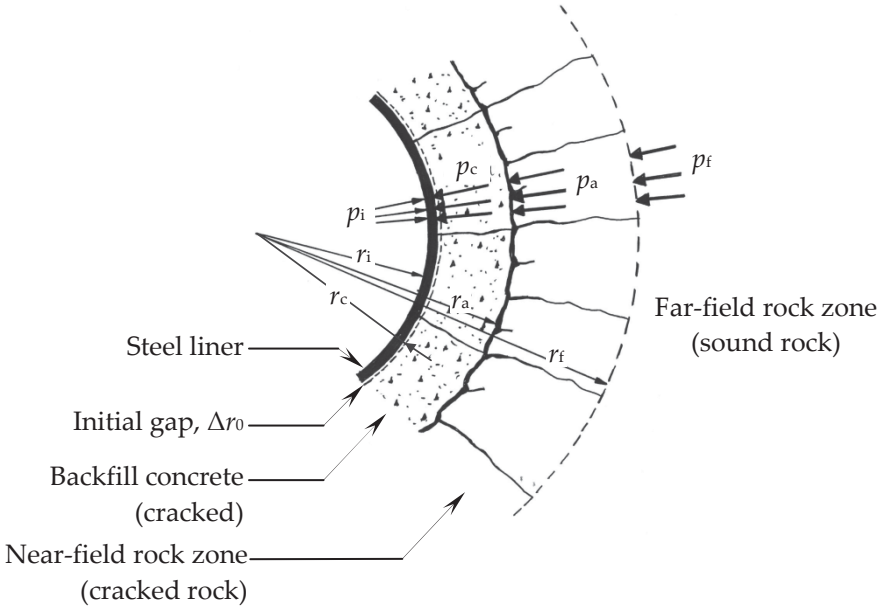

Figure 2.2: Calculation model for steel liners with axisymetrical behaviour (after Schleiss, 2007).

backfill concrete and the rock mass in the so called "compatibility condition of deformations".

For the calculation of the load sharing, five different zones are considered (Fig. 2.2):

1. *Steel lining*, which is in direct contact with the pressurized water. It provides an impervious membrane and carries a certain part of the internal pressure p_i

2. *Initial gap*, between steel and backfill concrete. The steel liner will shrink as a result of the contact with cold water, leaving a small gap Δr_0 between the two materials. A typical value of Δr_0 equal to 0.25 ‰ of r_i is often used in design corresponding to a temperature decrease of 20 °C. The gap caused by the shrinkage of the backfill concrete is normally filled by grouting before the pressure shaft or tunnel is put into operation.

3. *Concrete*, as a backfill between the steel liner and the excavated rock. Having a tensile strength of about 1 to 2 MPa, the backfill concrete is normally fissured under internal pressure and cannot transmit tangential stresses.

4. *Near-field rock zone*, which corresponds to the disturbed part of the rock mass as a result of excavation methods and of the change in the stress field around tunnel. Being cracked, this part of the rock mass cannot transfer tensile stresses. The external radius r_f and the modulus of elasticity E_{crm} for this disturbed zone are the two most important parameters to be determined for

the design. The external radius r_f of the disturbed rock is normally estimated at between one to five times the excavated tunnel radius r_a (Brekke and Ripley, 1987). Nishida et al. (1982) have shown that for mechanical excavation by "Tunnel Boring Machine" (TBM), r_f was roughly 0.3 m, and for excavation by "drill and blast", r_f was roughly 0.5 to 1.3 m, both measured in 5 m diameter tunnel in crystalline rock. Therefore, for good rock conditions, values of r_f higher than 1.0 to 1.5 times r_a are considered as very conservative. Schleiss (1988) suggested 0.5 to 1.0 m for tunnels excavated by (TBM) and 1.0 to 2.0 m for drill and blast.

5. *Far-field rock zone*. This non-disturbed zone is assumed as a homogeneous, isotropic and elastic material having a mean elastic deformation modulus E_{rm} that can be measured in-situ by using standard tests such as plate loading, radial or plate jacking, dilatometer, geophysical exploration (Grant and West, 1965) and so on, or estimated for example by the Hoek-Brown method (Hoek, 2006) or by *RMR* or *Q* indexes (Bieniawski, 1973; Gurocak et al., 2007).

2.1.2.2 Solving the compatibility condition

Analytical methods On the basis of the compatibility of deformations, Table 2.1 illustrates approaches for the calculation of the load transfer suggested by various authors. The main differences between these approaches arise from assumptions regarding the backfill concrete (cracked or uncracked), the extension of the disturbed rock zone as well as the annular gap.

The effect on the rock mass participation and the presence of an annular gap can change the results significantly. For example, increasing the outer radius of the disturbed rock zone from $2\,r_a$ to $5\,r_a$ decreases the percentage of the load transferred to rock from 45 to 20 %. Decreasing the modulus of elasticity of the disturbed rock mass, having an outer radius of $3\,r_a$, from 75 to 50 % of E_{rm} decreases the load transferred percentage from 40 to 35 %.

Graphical methods Several authors have developed graphs for the design of steel liners (Nicolopoulos, 1983; Seeber, 1975).

Seeber (1975) suggested a graphical solution of the compatibility condition of deformations at the steel-rock interface. Its application is illustrated in the Lower Pressure Tunnel of the North Fork Stanislaus River Hydroelectric Project. In this project, Schleiss (1988) enhanced Seeber-diagram in order to take into account the rock confinement (bearing capacity of rock mass) and the crack bridging criteria in isotropic rock mass. Once the internal water pressure has been fitted between the working line of the rock mass (upper right quadrant of Fig. 2.3) and the working line of the steel liner (lower right quadrant), the strain and hoop stress

Table 2.1: Load transfer calculation techniques for steel liners of tunnels and shafts under internal pressures.

Reference	Compatibility of the steel-concrete-rock system: ***Steel*** =	***Backfill concrete*** +	***Near-field rock zone (cracked)*** +	***Far-field rock zone (sound)*** +	***Initial gap,*** Δr_0	Remarks
Tâche, J. (1949)	$[(p_s \cdot r_i^2)/(E_s \cdot e)] \cdot (1-\nu_s^2)$	$[(p_c \cdot r_c)/E_c] \cdot (1-\nu_c^2) \cdot \ln(r_a/r_c)$	$[(p_c \cdot r_c)/E_{rm}] \cdot (1-\nu_r^2) \cdot \ln(r_f/r_a)$	$[(p_c \cdot r_c)/E_{rm}] \cdot (1-\nu_r^2) \cdot (1+\nu_r)$	not considered	-
Brekke, T.L. (1987) after Gumensky and Chu	$(p_s \cdot r_i^2)/(E_s \cdot e)$	treated as sound rock	treated as sound rock	$[(p_c \cdot r_c)/E_{rm}] \cdot (1+\nu_r)$	not considered	-
Vaughan, E.W. (1956)	$(p_s \cdot r_i^2)/(E_s \cdot e)$	$[(p_c \cdot r_c)/E_c] \cdot (1-\nu_c^2) \cdot \ln(r_a/r_c)$	$[(p_c \cdot r_c)/E_{rm}] \cdot (1-\nu_r^2) \cdot \ln(r_f/r_a)$	$[(p_c \cdot r_c)/E_{rm}] \cdot [(z^2+r_f^2)/(z^2-r_f^2)+\nu_r] \cdot k_p$	$r_i \cdot \alpha_1 \cdot \Delta T$	k_p is the ratio of plastic to elastic deformation of rock
Brekke, T.L. (1987) after Patterson	$(p_s \cdot r_i^2)/(E_s \cdot e)$	$(p_c/E_c) \cdot [(r_a^2-r_c^2)/(2 \cdot r_a)]$	$(p_c \cdot r_c/E_{rm}) \cdot [(r_f^2-r_a^2)/(2 \cdot r_a \cdot r_f)]$	$[(p_c \cdot r_c)/E_{rm}] \cdot (1+\nu_r)$	$0.0003 \cdot r_i$	-
Brekke, T.L. (1987) after Moody	$(p_s \cdot r_i^2)/(E_s \cdot e)$	$(p_c+p_a) \cdot (r_a-r_c)/(2 \cdot E_c)$	treated as sound rock	$[(p_c \cdot r_c)/E_{rm}] \cdot (1+\nu_r)$	Considered but not formulated	
Brekke, T.L. (1987) after Laufer and Seeber	$[(p_s \cdot r_i^2)/(E_s \cdot e)] \cdot (1-\nu_s^2)$	treated as sound rock	treated as sound rock	$[(p_c \cdot r_c)/E_{rm}] \cdot (1+\nu_r)$	$0.0003 \cdot r_i$	-
Brekke, T.L. (1987) after Ramos and Abrams	$(p_s \cdot r_i^2)/(E_s \cdot e)$	treated as cracked rock	$[(p_c \cdot r_c)/E_{rm}] \cdot \ln(r_f/r_a)$	$[(p_c \cdot r_c)/E_{rm}] \cdot (1+\nu_r)$	$0.0002 \cdot r_i$	-
Brekke, T.L. (1987) after Kruse	$[(p_s \cdot r_i^2)/(E_s \cdot e)] \cdot (1-\nu_s^2)$	$[(p_c \cdot r_c)/E_c] \cdot \ln(r_a/r_c)$	$[(p_c \cdot r_c)/E_{rm}] \cdot \ln(r_f/r_a)$	$[(p_c \cdot r_c)/E_{rm}] \cdot (1+\nu_r)$	$0.0001 \cdot r_i$	-
Brekke, T.L. (1987) after Jacobsen	$[(p_s \cdot r_i^2)/(E_s \cdot e)] \cdot (1-\nu_s^2)$	treated as sound rock	$[(p_c \cdot r_c)/E_{rm}] \cdot \ln(r_f/r_a)$	$[(p_c \cdot r_c)/E_{rm}] \cdot (1+\nu_r)$	$0.0005 \cdot r_i$	-
Schleiss, A.J. (1988)	$(p_s \cdot r_i^2)/(E_s \cdot e)$	$[(p_c \cdot r_c)/E_c] \cdot (1-\nu_c^2) \cdot \ln(r_a/r_c)$	$[(p_c \cdot r_c)/E_{rm}] \cdot (1-\nu_r^2) \cdot \ln(r_f/r_a)$	$[(p_c \cdot r_c)/E_{rm}] \cdot (1+\nu_r)$	$0.00025 \cdot r_i$	-
Moore, E.T. (1989)	$[(p_s \cdot r_i^2)/(E_s \cdot e)] \cdot (1-\nu_s^2)$	$[(p_c \cdot r_c)/E_c] \cdot \ln(r_a/r_c)$	$[(p_c \cdot r_c)/E_{crm}] \cdot \ln(r_f/r_a)$	$[(p_c \cdot r_c)/E_{rm}] \cdot (1+\nu_r)$	$r_i \cdot \alpha_1 \cdot \Delta T$; and it's nil in tropical and semi-tropical zones	E_{crm} = 50 to 75% of E_{rm} (Eskilsson, 1999)
USACE, EM 1110-2-2901 (1997)	$[(p_s \cdot r_i^2)/(E_s \cdot e)] \cdot (1-\nu_s^2)$	$[(p_c \cdot r_c)/E_c] \cdot \ln(r_a/r_c)$	$[(p_c \cdot r_c)/E_{crm}] \cdot \ln(r_f/r_a)$	$[(p_c \cdot r_c)/E_{rm}] \cdot (1+\nu_r)$	$r_i \cdot \alpha_1 \cdot \Delta T$	-

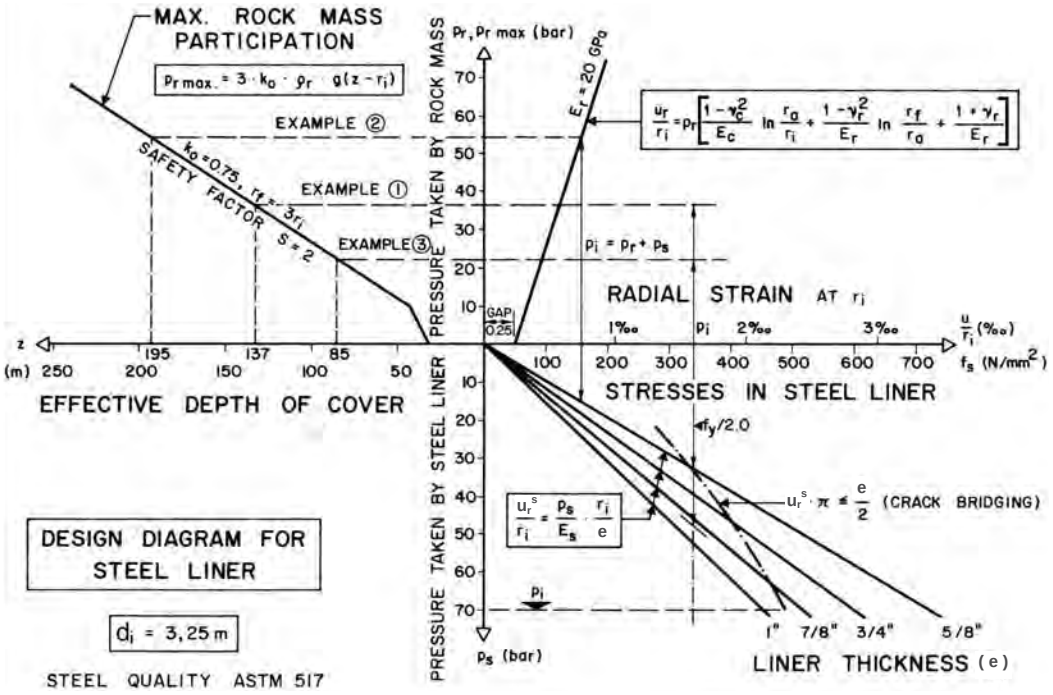

Figure 2.3: Seeber design diagram including maximum rock mass participation criterion (after Schleiss, 1988).

in the steel liner can be obtained directly as well as the load sharing between the steel liner and the concrete-rock system.

The required effective depth of cover (upper left quadrant) and the crack bridging criteria (lower right quadrant) will be discussed later.

Numerical methods If the rock behavior is anisotropic and inhomogeneous around the tunnel, analytical solutions are not available anymore and numerical methods as finite element approaches have to be used.

2.1.2.3 Anisotropic rock mass behaviour

If the behavior of rock mass is anisotropic (for example, bedding, foliation, jointing, and so on) the circumferential stresses in the steel liners can vary considerably. A rough estimation is often used for axisymetrical rock mass behavior by using an overall rock mass stiffness equal to the minimum value that the rock can have (Brekke and Ripley, 1987). Nevertheless, with such approach, the non-axisymetrical deformation of the steel liner is not taken into account.

Eristov (1967) and (1968) has studied the behavior of pressure tunnel linings in anisotropic, orthotropic elastic media by dividing the lining into n_b beam elements. He established an analytical system that gives the total radial deformation at θ angle, $\Delta r\,(\theta)$, along the liner perimeter as a function of the internal pressure,

the steel liner characteristics and the elastic reaction coefficients of the rock mass k_x and k_y ($k_x < k_y$) measured in two perpendicular directions x and y. A relation has been also given to estimate the reaction coefficients of the rock mass in the θ direction.

These relationships can be written, according to Fig. 2.4, as follows:

$$\Delta r(\theta) = \frac{p_i\, r_i^2}{E_s\, e} - \frac{k_x\, \Delta r_x\, r_i^2}{E_s\, e} + p_\theta\, \frac{3\, r_i^2}{E_s\, e^2} \left(\frac{4}{\pi} - \theta\, \sin(\theta) - \cos(\theta) \right) \tag{2.1}$$

where;

$$p_\theta = \left(k_\theta\, \Delta r\,(\theta) - k_x\, \Delta r_x \right)\, \Delta S \tag{2.2}$$

$$k_\theta = \frac{k_x\, k_y}{k_x\, \sin^2(\theta) + k_y\, \cos^2(\theta)} \tag{2.3}$$

$$\Delta S = \frac{2\, \pi\, r_i}{n_b} \tag{2.4}$$

and n_b is the number of beam elements of the steel liner having the length of ΔS.

By solving Eq. (2.1), the radial deformation $\Delta r\,(\theta)$, the bending moment, the normal forces, and the tangential stress in liner can be found. Figs. 2.5 (a) and (b) illustrate an example plot of results for $n_b = 12$.

It should be mentioned that Eristov's method is similar to the Finite Element Analysis described in US Army Manual (USACE, 1997). In this Manual, the radial and tangential spring stiffnesses (elastic reaction coefficients) are estimated, for a 2-D calculation model, from equations (2.5) and (2.6).

$$k_\theta = \frac{E_{\mathrm{rm}}\,(\theta)\ \alpha}{1 + \nu_r} \tag{2.5}$$

$$k_{t\theta} = k_\theta\, \frac{G_{\mathrm{rm}}\,(\theta)}{E_{\mathrm{rm}}\,(\theta)} = 0.5\, \frac{k_\theta}{1 + \nu_r} \tag{2.6}$$

where α is the arc defining the beam elements, in radians.

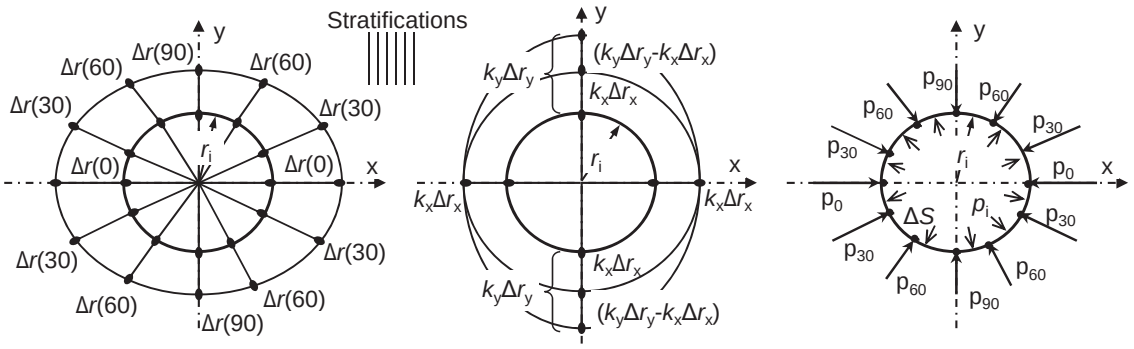

Figure 2.4: Calculation model according to Eristov (1967, 1968) for steel liners in anisotropic rock mass. At left: non-axisymetric deformation of steel liner, in the middle: elastic reactions of the steel liner and at right: elastic reaction forces between steel liner and rock.

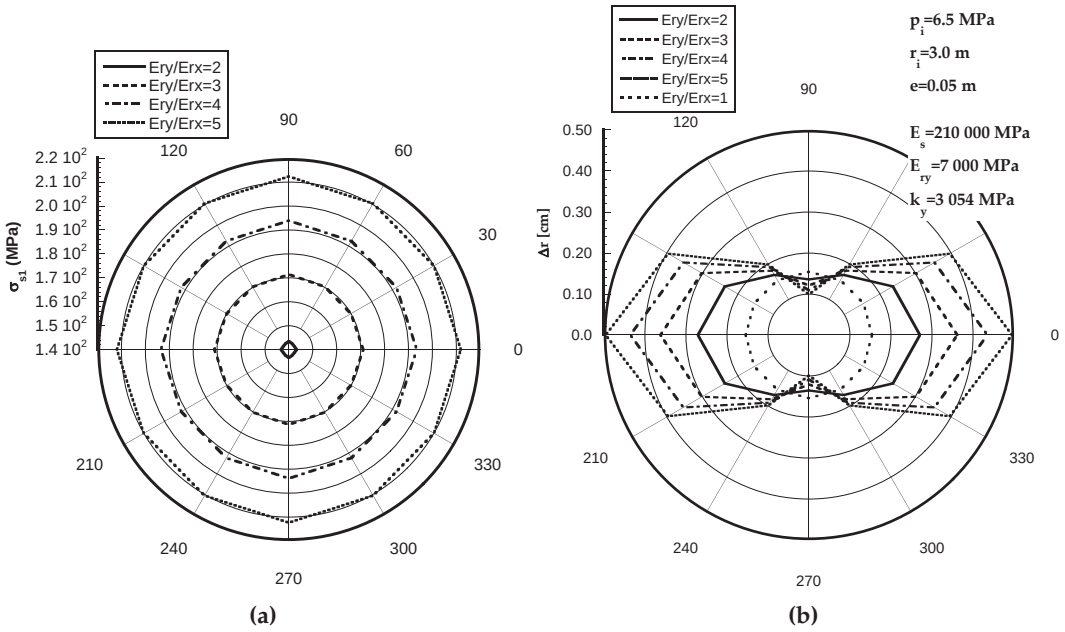

Figure 2.5: Results of a calculation example from Eristov (1967, 1968) model, (a) tangential stresses in liner, (b) radial deformation of liner.

2.1.3 Assessment of the maximum rock mass participation

The calculation techniques solving the compatibility condition for load transfer assume directly a full load sharing with the rock. Therefore, the question is for which minimum rock cover, full load sharing can be admitted.

It is clear that for a tunnel or shaft situated very close to the ground surface

or to the underground caverns and chambers, the steel lining has to be designed for full internal pressures without taking into account load transfer to the rock. For regions with low rock cover, the capacity of the rock mass to withstand the pressures transmitted from the steel lining is usually determined by in-situ stress measurements like hydraulic jacking or fracturing, overcoring, borehole slotting, and flat jack. Among all these methods, it has experienced that hydraulic fracturing is the easiest, quickest and most convenient technique giving reliable results (Kumar et al., 2004). It is very well described in Haimson and Cornet (2003).

Often, when the rock cover is below 20 r_i (Schleiss 1988 and 1992) no load sharing is considered. In the Indian Standards (1996), no load sharing is taken into account if the overburden weight is less than 40 % vertically and 120 % horizontally compared with the internal water pressure under normal loading conditions.

The left hand side of Fig. 2.3 shows the maximum rock mass participation curve calculated by Schleiss (1988) as a function of overburden rock. This curve has been implemented in the design diagram for the Lower Pressure Tunnel of the North Fork Stanislaus River Hydroelectric Project. A safety factor of 2.0 was used.

In assessing adequate confinement, most of the designers use static head considering only the upsurge water levels in the surge tank. The best way to assess the maximum rock mass participation is to measure in-situ rock stresses in boreholes near the future tunnel or shaft. Since such measurements are not always available, the rock mass participation can be estimated from overburden as the Fig. 2.3. Nevertheless, an assumption of the ratio between the minimum horizontal stress and the overburden has to be made (k_0 value). Sheory (1994) developed an elasto-static thermal stress model of the earth and provide a simplified formula to estimate k_0.

It has to be noted that the minimum primary stress can be lower than the one caused by the overburden measured perpendicular to the rock surface for steep slopes (Seeber, 1985a). When measuring the perpendicular distance to the rock surface, protruding ridges and noses do not affect the stress in the rock masses in a valley side, and should therefore be neglected. Simplified topographic maps with smooth contour lines, drawn inside such protruding features, should be drawn (Broch, 1984).

2.1.4 Crack bridging

Seeber (1975) proposed a crack bridging criteria since the liner must be able to bridge the cracks in the backfill concrete. In the most critical case, only two cracks can occur in the backfill concrete. To bridge these cracks safely, Seeber stated that the steel wall thickness must be at least equal or higher than the crack width in a stratified rock mass having distinct elasticity modulus in both directions, parallel and perpendicular to stratifications. So, the crack bridging criteria without considering a safety factor, was defined by:

$$e \geq 2\,u_r^s \Rightarrow \frac{u_r^s}{r_i} \leq \frac{e}{2\,r_i} \tag{2.7}$$

where u_r^s is the radial deformation and r_i the internal radius of the liner.

According to Schleiss (1988), for a radial-symmetrical and isotropic behavior of rock mass the deformation u_r^s leads to a uniform increase of the steel liner perimeter. For a safety factor equal to 2.0 and assuming that in minimum two cracks occur, the crack bridging criteria becomes:

$$e \geq 2\,\pi\,u_r^s \Rightarrow \frac{u_r^s}{r_i} \leq \frac{e}{2\,\pi\,r_i} \tag{2.8}$$

In the lower right quadrant of Fig. 2.3, this crack bridging criteria is implemented in the design diagram.

For a detailed assessment of the crack bridging criteria, Seeber and Danzl (1988) defined a critical ratio $\left(d_{f\,\max}/e\right)_{\text{crit}}$, where $d_{f\,\max}$ is the width of the largest crack in backfill concrete, taking into consideration the properties of steel, the friction coefficient between steel liner and concrete, μ_{sc} as well as, the internal pressure and the internal radius to steel thickness ratio (r_i/e). They proposed a relation for $\left(d_{f\,\max}/e\right)_{\text{crit}}$ in anisotropic stratified rocks as follows:

$$\left(d_{f\,\max}/e\right)_{\text{crit}} = 2\,\frac{u_r^s}{e} \tag{2.9}$$

where

$$\frac{u_r^s}{r_i} = 0.5\,\frac{\varepsilon_m}{1-\varepsilon_m}\,\frac{1}{\mu_{sc}}\,\ln\left(\frac{f_y - p_i\,\dfrac{r_i}{e}}{f_m - p_i\,\dfrac{r_i}{e}}\right) \tag{2.10}$$

and f_m and ε_m are respectively the maximum strength and the corresponding strain of steel used.

2.1.5 Comparison of recommendations and codes for the design of steel liners

2.1.5.1 Loads and load combinations

In Europe, the C.E.C.T. (1980) recommendations have been developed for the design and construction of steel-lined tunnels and shafts. The US Army Manuals (USACE, 1995 and 1997) give recommendations for design of permanent steel linings. The Indian Standards (1996) treats the subject of the structure design of steel lining.

For the design of penstocks and steel-lined tunnels, the allowable stress method is used in which all loads (both dead and live loads) have a load factor equal to 1.0. These loads include:

- *Construction loads* (handling, erecting, and so on)

- *Live loads* (earthquake)
- *Dead loads* (weight of the structure and rock loads)
- *Intermittent loads* (filling and drainage of tunnel)
- *Service loads* that are divided to:

    1. Maximum static head minus the head losses plus the water-hammer and surge during load rejection when all units are operating with normal governor closure time
    2. Minimum static head minus the water-hammer and down surge occurring when all units operate from speed no load to full load acceptance
    3. The head at transient maximum surge.

- *Emergency loads* which include:

    1. Maximum static head plus water-hammer and surge during partial gate closure in critical time of $(2\,L/a)$ s at maximum rate with the cushioning stroke being inoperative in one unit
    2. Same as No. 1 but with the cushioning stroke being inoperative in all units.

- *Exceptional loads* including:

    1. Unforeseen operation that produce instantaneous changes in the flow rate
    2. Rapid closure of turbine gates in less than $(2\,L/a)$ s for maximum flow rate
    3. Rhythmic opening and closing of the turbine gates when complete cycle of gate operation is performed in $(4\,L/a)$ s.

The combinations of loads adopted by different recommendations are given in Table 2.2.

The water-hammer or overpressure calculated by the elastic water column theory (Parmakian, 1963) and (Jaeger, 1977), is in general assumed to increase linearly along the developed length of the shaft, between the connection point of the shaft with the surge tank or with the water intake and the nearest downstream closing valve.

Table 2.2: Loads and load combinations (normal, intermittent, emergency and exceptional) for steel lining design, according to the three recommendations: C.E.C.T (1980), USCA Manual (1995) and Indian standards (1996).

Loads	Loading Combinations															
	Normal					Intermittent				Emergency		Exceptional				
Construction	X											X				
Live								X	X				X			
Dead	X	X	X	X	X	X	X	X	X	X	X	X	X	X	X	X
Intermittent							X									
Service No. 1			X			X		X								
Service No. 2				X					X							
Service No. 3					X	X										
Emergency No. 1										X						
Emergency No. 2											X					
Exceptional No. 1														X		
Exceptional No. 2															X	
Exceptional No. 3																X
Considered in the recommandation																
C.E.C.T		O	O	O			O					O	O	O		
EM 1110-2-3001	O		O	O			O	O	O		O					
Indian Standards			O		O	O	O			O				O	O	

2.1.5.2 Equivalent and allowable stresses in steel liners

According to C.E.C.T. (1980) and as general rule, steel stresses are divided into primary and secondary stresses. The primary stresses induced deformations increase with the loads even after the yield strength is exceeded. Secondary stresses are local stresses where deformation stop to increases with forces when the elastic limit of the material used is reached. For circumferential or tangential stresses in steel liner, primary stresses are those caused by the internal pressure taking into consideration the initial gap and the resistance of the hosted rock, if it is considered. In longitudinal direction, primary stresses occur as a result of Poisson's effect of the circumferential stresses and caused by friction.

According to C.E.C.T. (1980), at least for primary stresses, all calculations have to be made in the elastic range. The equivalent stress in the steel, σ_{eq} is evaluated after combining longitudinal and circumferential stresses with the Hencky-Von Mises theory in triaxial state of stresses according to the relation:

$$\sigma_{\text{eq}} = \sqrt{0.5\ (\sigma_{s1} - \sigma_{s2})^2 + 0.5\ (\sigma_{s2} - \sigma_{s3})^2 + 0.5\ (\sigma_{s3} - \sigma_{s1})^2} \tag{2.11}$$

In plane stress condition ($\sigma_{s3} = 0$), Eq. (2.11) becomes:

$$\sigma_{\text{eq}} = \sqrt{\sigma_{s1}^2 - \sigma_{s1}\,\sigma_{s2} + \sigma_{s2}^2} \tag{2.12}$$

where σ_{s1}, σ_{s2} and σ_{s3} are respectively the tangential, radial and longitudinal stresses in the steel liner wall.

The equivalent stress should not be higher than the allowable stress at any point of the steel liner. In Table 2.3, ratios of the allowable steel stresses to yield or

Table 2.3: Allowable stresses in terms of what is used by some organization and codes.

Organization and Standard	Reference	Loading Combinations															
		Normal				Intermittent				Emergency				Exceptional			
		Without rock mass participation		With participation		Without rock mass participation		With participation		Without rock mass participation		With participation		Without rock mass participation		With participation	
		$\%f_y$	$\%f_u$	$\%f_y$	$\%f_u$	$\%f_y$	$\%f_u$	$\%f_y$	$\%f_u$	$\%f_y$	$\%f_u$	$\%f_y$	$\%f_u$	$\%f_y$	$\%f_u$	$\%f_y$	$\%f_u$
American Iron and Steel Institute (AISI)	Brekke,T.L. (1987) after AISI	100	67														
C.E.C.T.	C.E.C.T. (1980)	91		50		100								68-100		56	
Pacific Gas and Electric Company (PG&E)	Brekke,T.L. (1987) after PG&E	100	54	61	33												
Southern California Edison Company (SCE)	Brekke,T.L. (1987) after SCE	100	67	67	33												
US Army Corps of Engineers (USACE)	EM 1110-2-3001	50	25			67	33			100	50						
US Bureau of Reclamation (USBR)	Brekke,T.L. (1987) after USACE	100	67														
Indian Standards	IS (1995)	60	33	90	67	67	40	100		90	60	100		100			

tensile strengths as recommended in different sources are given. It can be noticed that for each load combination, these ratios are different if the internal pressure is shared or not with the rock mass.

2.1.6 Problematic nature of high strength steel

2.1.6.1 Historical development of the steel strength

The development of new steel grades was always driven by the demand of having optimal mechanical characteristics for different uses. To increase the yield strength of steel, alloying carbon and manganese has some adverse effects on the weldability of the steel. A second possibility is the heat treatment where fine-grained structure is obtained with a better toughness.

An updated version of the historical context of rolled steel products taken from Samuelsson and Schröter (2005) is shown in Figure 2.6.

Until 1950, steel which is today known as S355 J2 according to EN 10025, was considered as a high strength steel. From the 1960s, the application of the "Quenching and Tempering (QT)" process for steel grades began. Today, this process gives steel grades with yielding strength up to 1 100 MPa and more, although only grades up to 960 MPa yield stress are standardized. In the 1970s, the "Thermo-Mechanical Rolling" process was developed. This process produces grades up to 960 MPa with better welding performance than steels produced by (QT).

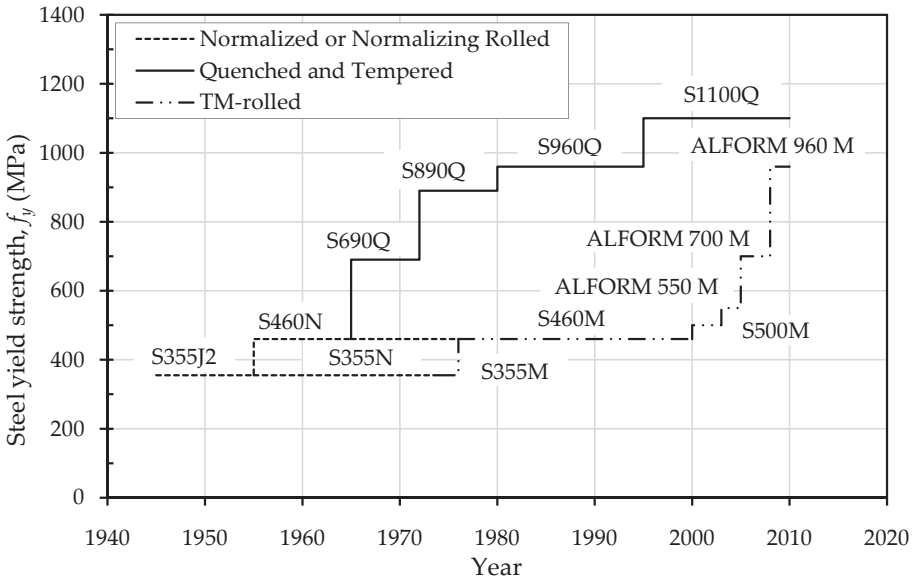

Figure 2.6: Historical development of yield strength for rolled steel products.

2.1.6.2 Requirement for yield to tensile strength ratio

Most of the design codes define an upper limit of the yield to tensile strength ratio. Normally, the yield strength considered in the design should not be higher than 80 % (for steel plates thicker than 50 mm) and than 90 % (for thinner steel plates) of the tensile strength. This limitation penalizes the use of high strength steels in structural applications. It has been shown that this limitation is not relevant because the toughness is independent of the yield to tensile strength ratio (Langenberg et al., 2000).

2.1.6.3 Ductility and toughness

The toughness is the ability of a material to absorb energy prior to fracture. The larger the area under the stress-strain curve, the tougher the material is. In general, the toughness decreases with increasing yield strength of steels.

High toughness and low carbon equivalent values in ductile steel allow for lower welding preheat temperatures, which in turn, result in less hardening and reduced tendency of cold cracking.

2.1.6.4 Hydrogen induced cracking

The cold cracking or delayed cracking is one of the most common and serious problems encountered in weldings of high strength steel. It can occur in the heat affected zone (HAZ) and in fusion zone (FZ) of the weldings. Tests have shown that hydrogen absorption can reach 7 ml/100 g under welding without using shielding materials (for example inert and semi-inert gases, blanket of granu-

lar fusible flux of limes, silica and so on). It can be reduced to 2 ml/100 g by using suitable shielding materials.

2.1.6.5 Corrosion and stress corrosion cracking

In the presence of oxygen and water, or under certain soil and electrical conditions, refined iron tends to return to its more stable form, ion oxide (rust). This reversion is an electrochemical natural process inherent to steel (AWWA, 2004).

Tensile stresses, cyclic stresses or high frequency vibrations acting combined with a corrosive environment can enhance or accelerate the deterioration of steel known as the phenomenon of "stress corrosion cracking". For high strength steel, the stress corrosion cracking is a sort of weakening due to hydrogen penetrating into cracks and diffusing from the cracks tips toward the material. The origin of this hydrogen can be H_2 gas molecules, water or dissociated H_2S molecules. The hydrogen interacts with the micro-fracture facilitating there initiation and propagation. High strength steels and their weldings are sensitive to such phenomenon in presence of water and humidity.

2.1.6.6 Fatigue loading and fatigue process

Fluctuations of internal pressures and potential structural vibrations of the steel liner are considered as fatigue loading. The consequence is time variation of the working stresses in the structure. Fatigue failures are avoided by ensuring that all critical features, such as longitudinal weldings of the steel liner, have an adequate fatigue strength. The most widely method used at the design stage, is based on the plot of stress (S) against the number of cycles to failure (N), which is known as an S-N curve for the relevant detail class of the weldings (Maddox, 1991).

Tagwerker (1980) has studied pressure oscillations in the power conduits of three hydropower stations producing peak-load. Based on a number of load cycles up to 1 000 cycles per year, and for ductile steel liners with a yield strength equal to 520 MPa, it was concluded that such oscillating loads are of no concern regarding fatigue strength of the linings. Nevertheless, Seeber (1985a) and (1985b) pointed out that not the somewhat higher static internal water pressures due to surge tank oscillation was the problem in some peak-load hydro plants but rather the high frequency of the dynamic water pressures due to water-hammer with smaller amplitudes.

It is also known that the fatigue strengths of welded details are independent of the tensile properties of the steel. As a consequence, the S-N design curves are also common to high strength steels welded satisfactory.

In fact, the validity of S-N curves for high strength steel was explained in Maddox (1991) and in Barsom and Rolfe (1999) in referring to the initiation and propagation of fatigue cracks. It was observed that the tensile strength of steel has little effect on the rate of propagation of a crack. Unwelded specimens show a benefit from increases of tensile strength as a result of the existence of crack

initiation, or incubation periods in addition to that required for propagation. On the contrary, welded specimens have a constant fatigue strength determined essentially by the propagation phenomenon alone. Such behavior is related to the presence of pre-existing crack like flaws, such as hydrogen inherent intrusions, for which in fact, crack initiation has been achieved.

Welded high strength steel, therefore, offers no intrinsic advantage in term of fatigue strength. On the contrary, there may be a higher number of potential cracks and flaws in the welds. The risk of having cracks that propagate beyond the critical size is therefore higher.

2.1.6.7 Corrosion fatigue

The fatigue design rules are normally based on the test data obtained in dry air at ambient temperature. Therefore, they do not consider corrosion which may have a significant influence on allowable fatigue stresses.

In fact, cracks accelerate corrosive attack. If the fluctuating stresses are high enough to propagate fatigue cracks from stress concentrations, corrosive reactions may accelerate their growth. Thus, the corrosion fatigue strength of a welded joint can be smaller than that under dry conditions. Furthermore, localized corrosive attack at stress concentrations and surface defects can increase the severity of the stress concentration and produce fatigue cracks.

2.1.7 Application of fracture mechanics theory to the steel liner design

2.1.7.1 The deterministic approach

In an unflawed member, the traditional design of a steel structure under tensile stresses is based on the criteria of preventing yielding by keeping the driving stress σ_{eq} below the resistance stress f_y. Accordingly, for structures containing initial cracks, the stress intensity factor, K_I is a calculated driving factor that must be kept below the resistance factor K_{IC} to prevent brittle fracture.

For steel liners, often crack-like defects are often present but designers normally assumed that, if a steel of sufficient ductility is used, local yielding occurs and redistributes stresses in the vicinity of stress raisers. This local yielding may not occur in high strength steel and therefore, the risk of a brittle failure will increase. Crack-like defects are normally considered in modern design when high strength steel is used in the structure of nuclear power plant, long span steel bridges and in aeronautical industry. The selection of materials and allowable stress levels is based on the fact that discontinuities may be present or may initiate and propagate under cyclic loads or stress corrosion cracking. Therefore, cracks size can reach a critical value where K_I becomes larger than K_{IC} producing the brittle failure of the steel.

The use of high strength steel liner using thick welded plates in hydropower plants together with the increase of the dynamic pressures, lead to a higher risk

of potential cracks in the steel liner weldings and thus, an increasing of the risk of brittle failure.

To illustrate the use of the fracture mechanics theory for selecting an appropriate material for the steel liner, the calculation results of an example (Barsom and Rolfe, 1999) are given in Figure 2.7. An internal pressure of 180 bars and a liner radius of 1.9 m are assumed. No load sharing with the surrounding rock is considered. The safety factor against yielding and brittle fracture of 2.0 is considered. An external surface flaw with a depth a_c equal to 25.4 mm and a depth to length ratio of 0.2 is assumed as the maximum crack size that could not be detected and repaired during steel liner inspections. The minimum steel liner thickness for handling purposes is considered equal to 25.4 mm.

The results show that the required steel liner thickness using the fracture mechanics theory increases with the increase of the yielding strength of the steel. For the same theory, the allowable tensile stress, f_s decreases when the yielding strength increases. Figure 2.7 shows that for steel yield strength higher than 900 MPa and for steels with relatively low values of K_{IC}, the fracture mechanics theory becomes critical when fracture is a possible mode of failure.

2.1.7.2 The probabilistic approach

The residual dispersion with random distributions of lattice defects in steel plates and weldings confirm the random nature of such material damages. Thus, a probabilistic rather than a deterministic approach should be used in modern design of steel liners.

Probabilistic Fracture Mechanics (PFM) is well developed in nuclear and aeronautical industries (Besuner and Tetelman, 1977; Nicholson and Ni, 1997; Provan, 1987). It should be also applied to steel liners of pressure tunnels built with welded high strength steel and loaded by high dynamic pressure fluctuations with high number of stress cycles.

The keystone of the PFM approach is a deterministic engineering model of one or more system failure modes combined with assumed or proposed statistical variations of controlling parameters expressed as cumulative Probability Distribution Functions (PDF). The basis of PFM is the simple axiom that a given mode of failure event (E) will occur when the stress σ_w associated with the failure mode exceeds the mode governing strength σ_f. The probability of failure according to mode (E) is given by:

$$\mathrm{P}\left(\mathrm{E}\right) = \mathrm{P}\left(Y < 0\right) = \mathrm{PDF}\left(y = 0\right) \tag{2.13}$$

where the strength margin Y is:

$$Y = \sigma_f - \sigma_w = G\left(x_i\right) \tag{2.14}$$

with $i = 1, \ldots, n_x$, depends on input variables (of number n_x) that affect component stress or strength or both, and G is a concise deterministic summary of all

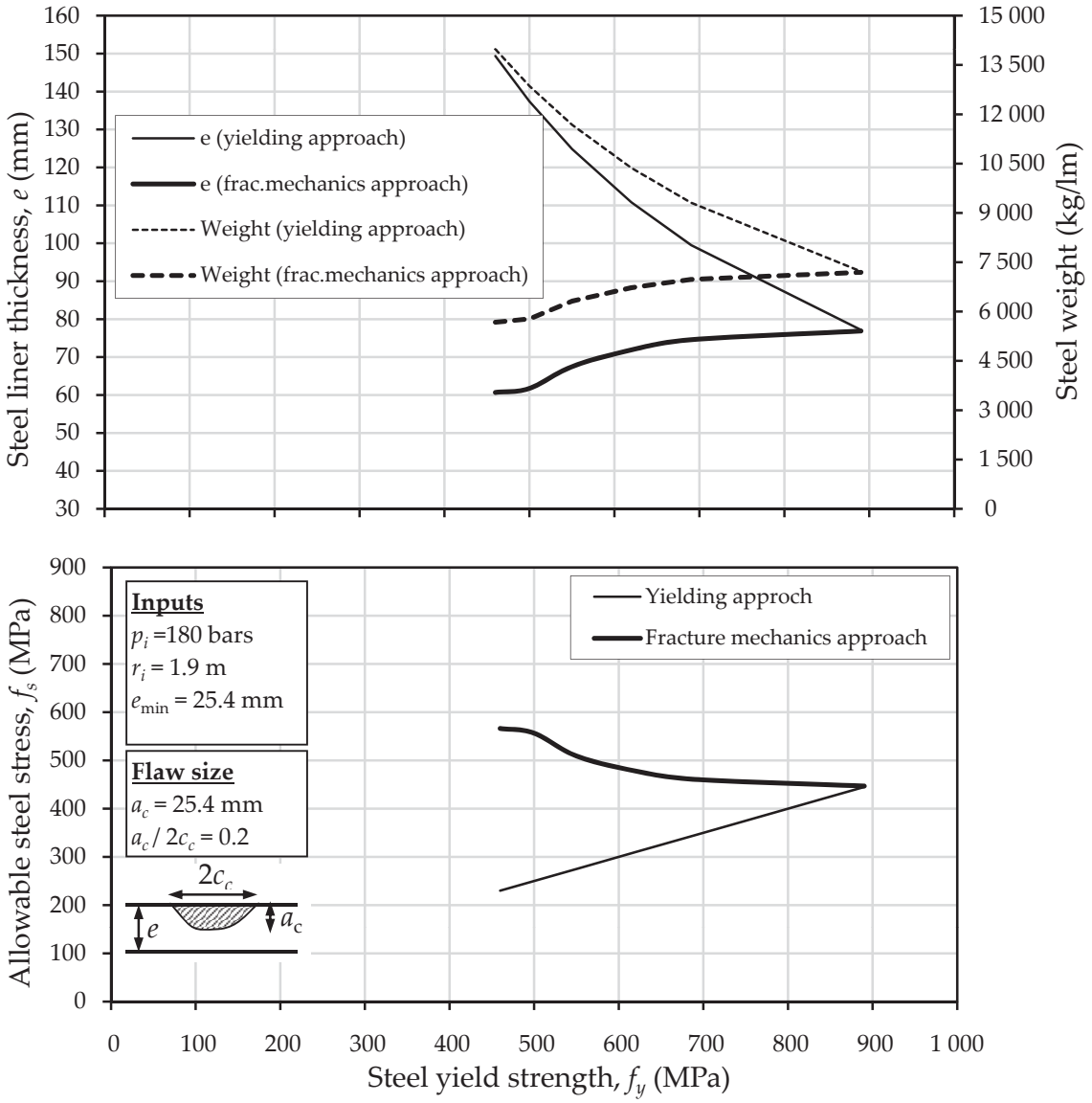

Figure 2.7: Calculation results of an example using the traditional and the fracture mechanics design approach. The upper figure shows the variation of the required steel liner thickness and the weight of steel liner as a function of the yield strength of the steel. The lower figure depicts the variation of the allowable tensile steel against the yield strength. Example's inputs are: $p_i = 18\,\text{MPa}$, $r_i = 1.9\,\text{m}$, Safety Factors against yielding and against brittle fracture $SF = 2.0$, $a_c = 25.4\,\text{mm}$ and $a_c/2\,c_c = 0.2$.

prior engineering experience, models and assumptions. The x_i are the values of the controlling parameters described as a random variables X_i with cumulative distribution functions assumed to be known and represented by:

$$\mathrm{PDF}\left(x_i\right) = \mathrm{P}\left(X_i \leq x_i\right) \tag{2.15}$$

The solution of Eqs. (2.14) and (2.15) to obtain $\mathrm{PDF}\left(Y\right)$ in Eq. (2.13) may be done in closed-form for simple cases or by using numerical solution, such as the Monte-Carlo (MC) simulation, if the $\mathrm{PDF}\left(x_i\right)$ and $G\left(x_i\right)$ distributions are complicated.

If it is assumed that the equivalent stress σ_{eq}, the yielding strength f_y and the brittle fracture strength f_f of a steel liner can be represented by normal distribution curves (Besuner and Tetelman, 1977), failure occurs by the yielding mode $\left(\mathrm{E}_y\right)$ $\left(Y_y = f_y - \sigma_{\mathrm{eq}} < 0\right)$ or by the fracture mode $\left(\mathrm{E}_f\right)$ $\left(Y_f = f_f - \sigma_{\mathrm{eq}} < 0\right)$ when the distribution curves overlap. This approach considers, for a given crack, that variations in f_f occur from variations in the steel fracture toughness, K_{IC} and in the depth of the critical crack, a_c according to equation:

$$f_f = \frac{K_{IC}}{\sqrt{\pi\, a_c}} \tag{2.16}$$

Another approach given by Nicholson and Ni (1997) considers statistically varying crack length, orientation and number. The crack length is described by two-parameter probability density function (Gamma distribution), the crack orientation is described by a uniform distribution and the crack number by a binomial distribution. Fracture mechanics is combined with extreme value probability theory (for example order statistics) to produce extreme value distribution for strength depending on the expected number of cracks in the steel liner, the parameters of the mode of the fracture model and the parameters of the crack length distribution.

2.2 Erection, control and testing

Fabrication of steel liners

Fabrication of penstocks and steel liners must be conform to the provisions of the C.E.C.T. (1980) (Annexes III, IV and V) and the ASME (2007) (Section VIII, Division 1). Steel cans are straight-seam product that can be fabricated in shop or in field. They are manufactured from plates that are edge-broken (crimped) and then rolled or formed using a plate-bending roll to have a continuous uniform curvature. Several types of bending rolls are available including: “Pyramid bending rolls”, “Pinch bending rolls” and “Initial pinch bending rolls”. The “Pyramid bending rolls” fabrication scheme is shown on Fig. 2.8. The photo presented in Fig. 2.9a shows the steel plates used in the preparation of the liner cans of the Siah Bishe pumped-storage power plant in Iran. Figs. 2.9b and 2.9c depict two

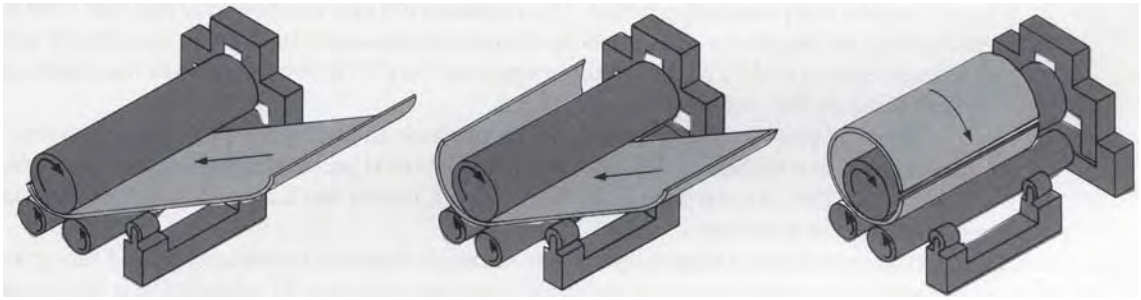

Figure 2.8: Pyramid bending rolls fabrication scheme of steel liners.

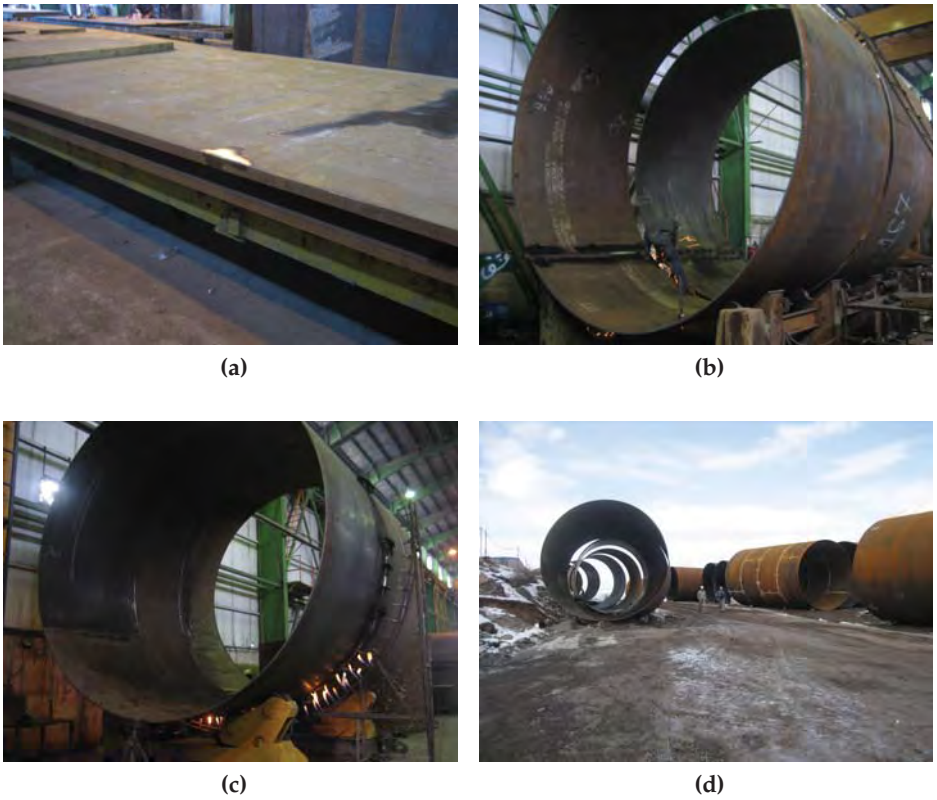

(a) (b)

(c) (d)

Figure 2.9: Photos showing the fabrication of steel liner cans for the pressure shaft of Siah Bishe pumped-storage power plant in Iran (photos: F. Hachem), (a) steel plates, (b) and (c) welding, and (d) steel liner reaches ready for erection.

photos of the welding process in factory. The photo given in Fig. 2.9d shows the steel liner reaches ready to be inserted inside the excavated shaft of the power plant.

Welds and more especially the longitudinal and circular welds require great care because they undergo the same forces as the basic element. With respect to ductility and resistance to brittle fracture under the action of a multi-axial stress

condition, the properties of the filler metal have to be adapted to those of the basic material. For the circular joints, in which the principal stress is exerted in the axis of the weld fillet, a filler metal can be selected having an elongation greater than of the basic material with a somewhat smaller breaking strength and yield point. The arc-welding and gas-welding processes used are generally restricted to shielded metal arc (SMAW), flux cored arc (FCAW), submerged arc (SAW), gas metal arc (GMAW) and gas tungsten arc (GTAW).

Extra stress concentration caused by a sudden change of cross section, deep grooves, lack of fusion and cracks must be avoided. The C.E.C.T. recommendations gives the tolerance on shape of the different configuration of welded edges. When different steel liner wall thicknesses are used, the transition is done at a rate of roughly 3 to 5 mm per can length. It should be mentioned that the difficulties of performing welds are increased when high-strength steels are used. In particular, the presence of water during the field welding of this type of material can cause brittleness and cracking.

The homogeneity of the welds and the quality of the welders' work and welding machines are inspected by using non-destructive testing (NDT). From the armada of existing NDT tests (Lüthi, 2010; McStraw, 1996; Zerjeski, 2006), methods such as radiographic, ultrasonic, magnetic particle, liquid penetration and X-ray are generally used for inspection. They can detect the location and size of defects (pores, slag inclusions, lack of fusion, cracks, and so on) to help inspectors to decide the necessity to undergoes reparation works.

Backfill concrete and grouting

Backfill concrete is a normal mixture of portland cement, sand, gravels and water and has the essential role to transmit internal loads from the liner to the surrounding rock mass. Its elasticity modulus, E_c, tensile strength, f_c, and compressive strength, $f_c^{'}$, are properties that influence the distribution of loads between the structure wall components.

In Section 2.1.2, the deformation of the concrete layer induced by the transferred pressure from steel liner, is determined elastically as in thick-walled cylinder which can or cannot take tension stresses. The later assumption is more realistic as the concrete is not reinforced and has a low tensile strength of about 1 to 2 MPa. The elasticity modulus, E_c, is related to $f_c^{'}$ by the well known relation $E_c = 5000\sqrt{f_c^{'}}$. For typical values of $f_c^{'}$ between 15 and 25 MPa, E_c varies between 19 400 MPa and 25 000 MPa, respectively.

After concreting, grouting materials are normally injected to fill the void spaces between the backfill concrete and the surrounding rock (contact grouting) and between the liner and the backfill concrete (skin or embedment grouting). The basic grouting is a portland cement mixed with bentonite as an additive to improve workability. Several other types of materials have been also used to facilitate penetration into small fissures, to decrease porosity, and so on.

The contact grouting is the first grouting process to be done after concreting. In tunnels and shafts less than 6 m in diameter, a single line spaced by 3 to 4 m is normally adequate. Thick mixes 1/1 (cement/water) by volume or thicker, with 2 % bentonite is usually appropriate. According to Benson (1986), modest pressure of 0.2 to 0.3 MPa are adequate.

The skin grouting is normally the second step. Grout mixes must be thinner, at least 1/3 (cement/water) by volume, with 2 % bentonite to improve fluidity and penetration. This type of grouting is done usually by rings (six to eight holes per ring) moving up-slope, with forward holes to allow drainage. While the allowable grout is dictated by steel liner dimensions, it is well known that skin grouting has led to buckling. So, pressures up to 50 % of the buckling are considered as appropriate.

If the rock quality is poor and the near-field zone is too much fractured, consolidation grouting are generally carried out by using the ring method and by grouting through the same holes as the skin grouting. Pressures of 50 % to 75 % of buckling pressure have been proposed (Benson, 1986). It is clear that, if the design for internal pressure is based on an allowable working stress disregarding load transfer to concrete and rock, consolidation grouting is not cost effective. In Indian-Standards (1996), the depth of the consolidation grouting to at least the diameter of the tunnel is recommended and a pressure up to 1.5 times the internal water pressure is proposed at the condition that safety against uplift of the overburden is ensured.

In-situ physical model tests for steel-lined pressure tunnels

In many important projects, in-situ tests have been carried out on model constructed inside the exploration galleries of the construction site (Cordelle and Doucerain, 1985; Müller, 1968; Surber, 1958). An example of such tests is presented and discused in detail in Appendix A. It concerns the “Super-Bissorte” power plant in France.

2.3 Assessment of the steel liner

2.3.1 Non-hydraulic assessment methods

Non-hydraulic assessment methods of wall condition of steel-lined pressure tunnels and shafts are mainly carried out during construction. These methods are applied separately to each component of the wall (steel liner, backfill concrete and rock mass) to assess its quality and verify its conformity with the applied codes.

During operation, the investigation of the steel liner regarding excessive local deformations, steel yielding, excessive corrosion and cracks requires a dewatering of the conveying system for visual checking or non-destructive testing. Such

inspection is costly (indirect economic loses) and often awkward due to the hostile conditions. Furthermore, no information can be easily obtained about the stiffness of the backfill concrete and rock mass surrounding the liner.

In water distribution, oil, and gas pipelines, acoustic based techniques have been used in leak detection monitoring of shallow underground pipelines. They allow users to scan the entire length of the inspected pipelines and to hear the noise coming up from the leak (Mays, 2000). Hunaidi (2006a) developed an acoustic method based on cross-correlating two accelerometer signals acquired from the pipe wall to determine the wave speed in a water distribution pipe reach. He used the standard theoretical wave speed formulae to extract the mean wall thickness of the pipe. Other assessment methods of the pipe wall condition including the CCTV camera and some non-intrusive techniques have been presented and discussed in Stephens (2008).

2.3.2 Hydraulic assessment methods

Traditionally, well equipped steel-lined shafts and tunnels are monitored by a set of pressure sensors, water level measurements and downstream–upstream flow meters. Pressure sensing devices are normally used to check the magnitude of the dynamic pressures relative to a predefined serviceability value. No further pressure signal processing is done since the sensors and the acquiring system are normally not fast enough to accurately collect high-frequency dynamic signals. If the water flow velocity exceeds a certain threshold, indicating a possible failure, a security shut-off valve closes automatically. This limits the volume of water leaking out from the failure by avoiding the emptying of the tunnel and reservoir upstream of the security valve. Even in this case, catastrophic failure consequences can occur since the volume of leaking water between the valve and the failure location may still be very high.

Besides these rather rudimentary hydraulic based monitoring systems, a number of more sophisticated techniques for pipeline failure and leak detection involving transient pressure waves have been applied in water, gas and oil networks. This began with a development of a sensitivity analysis for leak location processes by Liggett and Pudar (1992). Ferrante and Brunone (2003) used the wavelet transform and its local maxima lines to retain pressure information coming from a time domain analysis. Al-Shidhani et al. (2003) introduced the identification of pressure wave reflections using the wavelet decomposition. Covas et al. (2005a) focused on leakage detection in pipe systems by means of the standing wave difference method. Beck et al. (2005) described a method to detect pipeline features and leaks using the cross-correlation techniques of pressure wave measurements. Misiunas et al. (2005) proposed a continuous monitoring approach based on the timing of the initial and reflected pressure transient waves induced by the break. Fuentes et al. (2006) used the inverse transient analysis approach with genetic algorithms to find the optimal location of the leak. The same approach was adopted by Shamloo and Haghighi (2009) to determine numeri-

cally the leak parameters including their number, location, and size. Taghvaei et al. (2010) analyzed experimentally the pressure reflections from the leak using wavelet filtering followed by Cepstrum analysis. Stephens et al. (2008) presented an interesting approach to estimate the location of internal damage wall of a composite concrete-steel pipeline based on transient model combined with a Genetic Algorithm and field measurements. The altering of the wave speed in pipelines for feature identification application has been also mentioned in Taghvaei et al. (2008).

2.4 Remaining gaps in knowledge

2.4.1 Gaps in knowledge for design

The existing design methods for steel liner are based on the concept of keeping stresses below yielding strength. Using steel with high ductility combined with some construction details and tolerances have been considered as a safe design which minimizes the stress raiser points. Nevertheless, this design concept is not appropriate if very high strength steel with high risk of brittle failure is used. Schleiss (2002) pointed out that the design criteria, which have been outlined in Section 2.1.1, have to be adapted in the case of high risk of failure with catastrophic consequences.

For ductile steel liners, experience has shown that in view of water-hammer pressures, the issue of fatigue strength is not critical. Nevertheless, this will not be the case if high strength steel is used to resist severe dynamic pressure with high frequencies and high number of load cycles. This could occur in pumped-storage power plants.

2.4.2 Gaps in knowledge for monitoring

The non-hydraulic assessment review given in Section 2.3.1 reveals that intrusive but non-destructive monitoring methods are applied nowadays in steel-lined pressure tunnels and shafts. Besides their intrusive nature, the cost of such methods is high and the information derived from them cover small and local liner areas.

Acoustic methods used in pipelines monitoring have been carried out on relatively short pipe reaches of about 100 to 200 m long. Their application for monitoring long steel-lined pressure tunnels has to be checked.

For the assessment methods, it can be concluded that the existing monitoring systems for steel-lined tunnels and shafts cannot prevent catastrophic liner failure. It was shown in Section 2.3.2 that large number of sophisticated techniques that can deal with leak detection in pipelines exists. They all assume that the pressure wave speed is a constant value throughout the pipeline length. The work of Stephens et al. (2008) is, to the best knowledge of the author, the only ref-

erence found which investigate the wave reflections coming from weak reaches with different hydro-acoustic parameters such as wave speed. Nevertheless, this work needs the association of field and numerical model results. Therefore, new transient based methods for performing non-destructive and non-intrusive assessment of the wall of steel-lined pressure tunnels and shafts is still required. The main advantage of these methods is their ability to provide physical information regarding the structural condition of the tunnel wall over broader scale than the existing intrusive methods.

2.5 Conclusions

The literature review shows the existence of some gaps in knowledge for design and monitoring of steel-lined pressure shafts and tunnels. This research work suggests some interesting niches to explore and proposes some new and innovative methods and approaches. They can be summarized as follows:

- For design, a Fluid-Structure Interaction (FSI) theoretical model with axisymmetrical behavior and longitudinal motion is suggested. This new model can detect the compressional water mode and the radial and axial propagation modes in the steel liner and in the far field rock zone. The importance of such model consists in the resulting time-dependent stress diagrams for steel liner which can be used as input for the deterministic and probabilistic Fracture Mechanics models.
- For monitoring, a novel method based on processing the records of transient pressure waves is proposed. It is validated through laboratory experiments and tested, in prototype scale, on the pressure shaft of a pumped-storage power plant in Switzerland.

Chapter 3

Theoretical background

In this chapter, the basic theoretical tools needed to investigate efficiently the design and monitoring of steel-lined pressure tunnels and shafts are presented. These tools include the fluid transient models and some signal processing methods. The theoretical background given herein is concise and does not present all reflections and developments which have been carried out in this research work.

3.1 Fluid transients

3.1.1 Mass and Momentum equations for one-dimensional water-hammer flows

The water-hammer phenomenon in pressurized waterways has been studied long time ago. Allievi (1913) developed a general theory of water-hammer and showed that the connective term in the momentum equation was negligible. Further refinements to the governing equations were done by Jaeger (1933), Parmakian (1963), Chaudhry (1987), Wylie et al. (1993) and many others. Ghidaoui et al. (2005) gave an excellent overview of both theory and practice of water-hammer. The combined efforts of researchers have resulted in the following classical and quasi-static mass and momentum equations for one-dimensional water-hammer flows:

$$\frac{\partial q}{\partial x} + \frac{g\,\pi\,d_i^2}{4\,a^2}\,\frac{\partial h}{\partial t} = 0 \tag{3.1}$$

$$g\,\frac{\partial h}{\partial x} + \frac{4}{\pi\,d_i^2}\,\frac{\partial q}{\partial t} + \frac{4}{\rho_w\,d_i}\,\tau_w = 0 \tag{3.2}$$

in which, $q\,(x,t)$ is the flow discharge, $h\,(x,t)$ is the piezometric head, g is the gravitational acceleration, d_i is the internal diameter of the pipe or tunnel, a is the water-hammer wave speed, ρ_w is the water density, x is the spatial coordinate

along the longitudinal axis, t is the time, and τ_w is the shear stress at the water-wall interface.

According to Eqs. (3.1) and (3.2), when water flow in pressurized waterways is disturbed, spatial and temporal changes in the flow discharge and piezometric head will be generated. These transient flows are essentially unidirectional since the axial fluxes of mass and momentum are much higher than the other flow components. The equations governing the 1D water-hammer can seldom be solved analytically. Therefore, numerical techniques are used to approximate the solution like the method of characteristic (MOC) (Lister, 1960), the wave plan finite difference (FD) (Wood et al., 1966), the finite volume (FV), and the electrical analogy (Jaeger, 1977; Nicolet, 2007) methods.

Depending on the system stiffness of steel-lined pressure tunnels and penstocks, deviation from the quasi-static case may occur. Pressure waves in water produce dynamic forces on the steel liner and trigger vibrations. Such liner vibrations cause additional water pressure waves in return. This phenomenon is called "Fluid-Structure Interaction or FSI". In this case, other mathematical model than Eqs. (3.1) and (3.2) should be used. Some of these models can be found in Rubinov and Keller (1971 and 1978), Lavooij and Tijsseling (1991), Tijsseling (1996 and 2007), and Budny et al. (1991). Between the quasi-static and FSI cases, transient models similar to those proposed by Covas et al. (2004 and 2005b) and Stephens (2008) consider the pipe wall as a linear-viscoelastic material.

3.1.2 Reflection and transmission of water-hammer waves

The general solution of Eqs. (3.1) and (3.2) is the summation of a progressive and a retrograde wave propagating at the wave speed a in opposite directions along the longitudinal axis of pressurized waterways. These waves are generated at any time t by local excitation that moves variables h and q away from their steady-state values.

At pipes or tunnel junctions characterized by a change of the hydro-acoustic parameters (the flow area A and/or the wave speed a), an incident wave is reflected and transmitted. Fig. 3.1 shows the time behavior of a theoretical rectangular wave front propagating in water and crossing two junctions that limit a pipe reach having a wave speed value a_2 lower than the rest of the pipe (a_1). For steel-lined pressure tunnels, such a decrease of the wave speed can be the consequence of partial or total loss of the stiffness of the exterior support of the steel liner which is provided by the surrounding backfill concrete and rock mass. This reach will be called "weak reach" throughout this report.

According to Fig. 3.1, an incident pressure wave of magnitude $(h_i - h_0)$ is divided into transmitted and reflected waves when crossing junction 1. For a uniform cross-section flow area, the magnitude of the transmitted wave $(h_{t1} - h_0)$ is given by (Wylie et al., 1993):

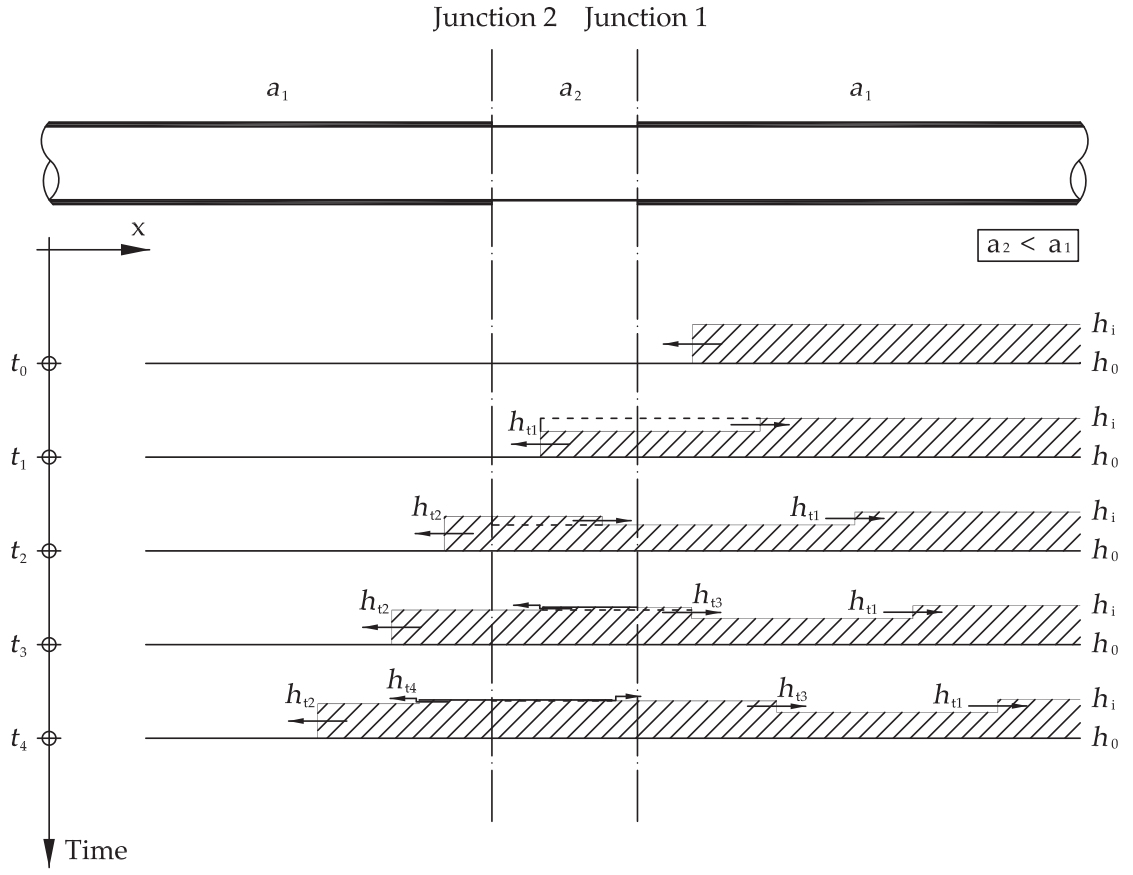

Figure 3.1: Theoretical time behavior of a rectangular pressure wave front crossing two junctions that bound a pipe's reach having a wave speed value lower than the rest of the pipe.

$$h_{t1} - h_0 = \frac{2}{1 + \dfrac{a_1}{a_2}} \, (h_i - h_0) \tag{3.3}$$

where, h_0, h_i and h_{t1} are the steady-state, incident and transmitted piezometric heads, respectively. The same phenomenon is reproduced when the pressure wave crosses the downstream end of the weak reach (junction 2). According to the direction of the first incident wave h_i, junctions 1 and 2 are called the upstream and downstream ends of the weak reach. A generalized transmission formula at the n^{th} boundary of the weak reach can be written as follows (Wylie et al., 1993):

$$h_{tn} - h_0 = 2^n \prod_{j=1}^{n} \frac{1}{1 + \dfrac{a_{j+1} A_j}{a_j A_{j+1}}} \, (h_i - h_0) \tag{3.4}$$

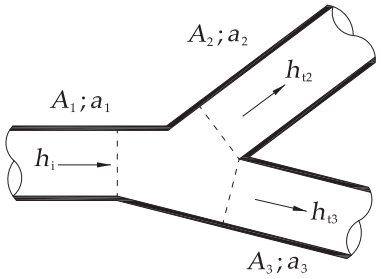

Figure 3.2: Transmitted pressure waves crossing Y junctions of three pipes having different cross-section area and wave speeds.

in which, A_{j+1} and A_j are the cross-section area and a_{j+1} and a_j are the wave speeds in reaches (j+1) and (j), respectively.

At a junction of three or more branches (Fig. 3.2), the magnitude of the transmitted waves to each branch having different cross-section area and wave speeds is (Parmakian, 1963):

$$h_{t2} - h_0 = h_{t3} - h_0 = \frac{\dfrac{2\,A_1}{a_1}}{\dfrac{A_1}{a_1} + \dfrac{A_2}{a_2} + \dfrac{A_3}{a_3}} \; (h_i - h_0) \tag{3.5}$$

where, h_{t2} and h_{t3} are the transmitted heads to the two downstream branches of the pipe.

3.1.3 Water-hammer wave speed

The quasi-static wave speed can be estimated from references such as Halliwell (1963), Streeter (1963), Rieutord (1982), and Wylie et al. (1993). The classical theory of water-hammer predicts pressure wave propagation inside a frictionless closed cylinder with uniform cross section at a wave speed given by the following general formula (Wylie et al., 1993):

$$a = \sqrt{\frac{1}{\rho_w \left(\dfrac{1}{K_w} + \dfrac{1}{A} \dfrac{\mathrm{d}A}{\mathrm{d}p_i} \right)}} \tag{3.6}$$

where, $\mathrm{d}A$ is the variation of the cross-sectional area A of the cylinder caused by the variation of the internal water pressure $\mathrm{d}p_i$ and K_w is the bulk modulus of water. In steel-lined pressure tunnels and shafts considering neither the fluid–structure interaction (FSI) nor the dynamic effect of the tunnel wall, the ratio $\mathrm{d}A/\mathrm{d}p_i$ is a constant value which depends on the geometrical and mechanical characteristics of the steel liner and on the state (cracked or uncracked) of the

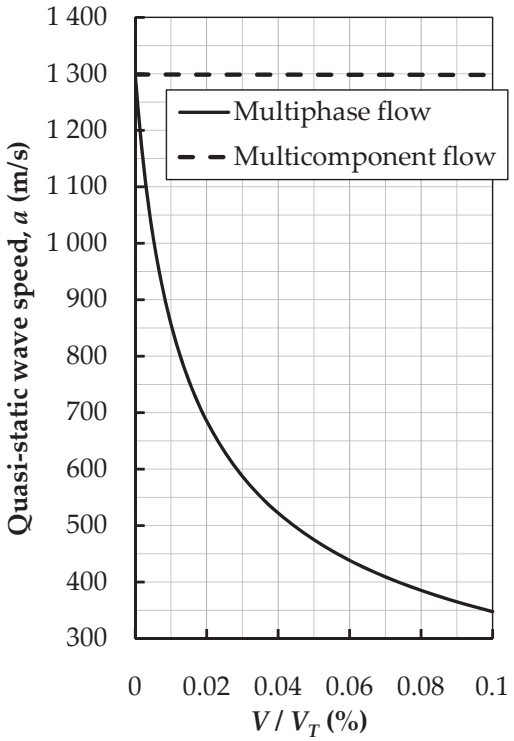

Figure 3.3: Theoretical variations of the quasi-static wave speed as a function of the air and sediment contents inside the flow mixture.

surrounding backfill concrete and rock mass. More details regarding this dependency are presented in Chapter 4.

The bulk modulus and density of water and, thus, the wave speed are influenced by the presence of air and sediments in water (Wylie et al., 1993). An example of the variations of the quasi-static wave speed as a function of the ratio (V/V_T) for a multiphase (air-liquid) and for a multicomponent (sediment-liquid) mixture is shown in Fig. 3.3. V_T is the total reference volume of the multiphase or the multicomponent mixture and V is the volume of air or sediment inside the mixture. Figure 3.3 shows that the presence of small percentage of dissolved air in the fluid can drastically change the wave speed value. An air content of 0.1 % leads to a relative decrease of the wave speed of about 74 %. The presence of suspended sediment inside the flow has a very small impact on the wave speed. Even for a high sediment concentration of 1.5 g/l $(V/V_T = 0.057\,\%)$, the wave speed is rather constant and equal to 1 298 m/s.

In FSI case, the wave speed becomes frequency-dependent. Additional details and discussion are given in Chapter 4. For the model proposed by Covas et al. (2004 and 2005b), the wave speed is defined in terms of the creep-compliance function and is a time-dependent parameter that decreases during the transient event.

3.1.4 Wave dissipation

The energy dissipation of water-hammer wave is caused mainly by the inelastic behaviour of the pipe or shaft wall and by the wall shear stress effect. The inelastic behaviour is related to the mechanical properties of the shaft wall and to the fluid wave frequency (Chapter 4 and Hachem and Schleiss, 2011g). The wall shear stress τ_w (given in Eq. (3.2)) is the summation of a quasi-steady and an unsteady friction components. The former is estimated using expressions such as the Darcy-Weisbach and Hazen-Williams formulae and the latter is obtained from empirical-based models such in Daily et al. (1956), Shuy (1996), Vardy and Brown (1997), Brunone et al. (1991), and Bergant et al. (2001) or from physically-based models such in Zielke (1968), Vardy et al. (1993), and Vardy and Brown (1995). The wave dissipation due to steady or unsteady friction becomes important if the dimensionless parameter Γ is in the order of 1 or higher (Ghidaoui et al., 2005). This parameter is given by the following formula:

$$\Gamma = \xi \left(\frac{L\, M\, f_{\mathrm{D-W}}}{2\, d_i} + \frac{T_d}{L/a} \right) \tag{3.7}$$

where, ξ is a positive real number used in the time scale $(\xi\, L/a)$, M is the Mach number (v_0/a) in which v_0 is the steady-state flow velocity, $f_{\mathrm{D-W}}$ is the Darcy-Weisbach steady-state friction factor, and T_d is the radial diffusion time scale.

3.2 Signal processing

3.2.1 Signal classification

Time histories can be broadly categorized as shown in Fig. 3.4. In contrary of the random or stochastic processes, deterministic signals are those whose behaviour can be predicted exactly. The classification of data as being deterministic or random must be made on the basis of knowledge of the physical situation. Often signals are modeled as being the sum of both types where the deterministic signal is embedded in random noise. The transient signals are limited in time and are considered as being the most common type involved in vibration engineering problems.

3.2.2 System identification

The system identification is an approach used to characterize a physical system in a quantified way. The object of this quantification is that it reveals information about the process and accounts for its behaviour based on measurements of input $i(t)$ and output $o(t)$ signals. For systems that are linear (superposition property) and time invariant (if the input is shifted by a certain time t, then the response will also be shifted by the same amount of time), the identification can be done

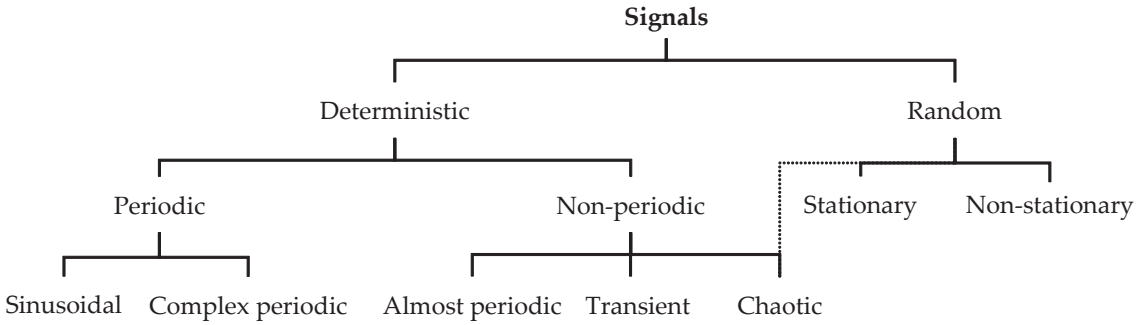

Figure 3.4: Classification of signals (after Shin and Hammond (2008)).

through their impulse response, $h(t)$. This is is expressed by the convolution of $i(t)$ and $h(t)$ according to the following abbreviation:

$$o(t) = h(t) * i(t) \tag{3.8}$$

By taking the Fourier transform of the convolution, Eq. (3.8) is transformed to the simple product

$$O(f) = H(f)\, I(f) \tag{3.9}$$

in which, f denotes frequency and $I(f)$, $H(f)$ and $O(f)$ are the Fourier transforms of $i(t)$, $h(t)$ and $o(t)$, respectively. In this frequency domain, the system is characterized by the frequency response function, $H(f)$. Following on from this, the relationship between the input and output energy spectra is

$$|\, O(f)\,|^2 = |\, H(f)\,|^2\ |\, I(f)\,|^2 \tag{3.10}$$

If the Laplace transform $\mathcal{L}$ is used, then a similar argument gives:

$$O(ss) = H(ss)\, I(ss) \tag{3.11}$$

where, $ss = \sigma + \mathrm{i}\,\omega$ is complex in which ω is the angular frequency $(= 2\pi f)$. The ratio $H(ss) = O(ss)/I(ss)$ is called the transfer function of the system. The relationships between the impulse response function $h(t)$, the frequency response function $H(f)$, and the transfer function $H(ss)$ are shown in Fig. 3.5.

The ultimate objective of the system identification is to estimate the frequency response function $H(f)$ of the system considered as linear and time invariant (LTI) with stationary random input signal. The best estimator when both input are output are affected by noise, is the total least squares estimator, $H_T(f)$, given by the following expression (Shin and Hammond, 2008):

$$H(f) \approx H_T(f) = \frac{\hat{S}_{oo}(f) - \hat{S}_{ii}(f) + \sqrt{\left[\hat{S}_{ii}(f) - \hat{S}_{oo}(f)\right]^2 + 4\left|\,\hat{S}_{io}(f)\,\right|^2}}{2\,\hat{S}_{oi}(f)} \tag{3.12}$$

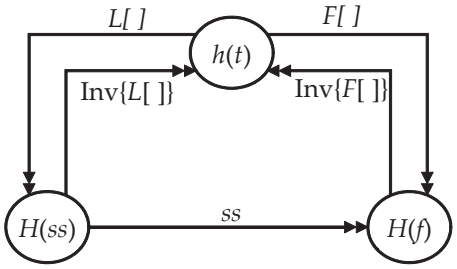

Figure 3.5: Relationship between $h(t)$, $H(f)$, and $H(ss)$.

where, $\hat{S}_{ii}(f)$ and $\hat{S}_{oo}(f)$ are the estimator for the power spectral density function of $i(t)$ and $o(t)$, respectively, and $\hat{S}_{io}(f)$ (resp. $\hat{S}_{oi}(f)$) is the estimator of the cross-spectral density between $i(t)$ (resp. $o(t)$) and $o(t)$ (resp. $i(t)$). These estimators are given as follows:

$$\hat{S}_{ii}(f) = \frac{1}{Nb} \sum_{m=1}^{Nb} \frac{| I_m(f) |^2}{T} \tag{3.13}$$

$$\hat{S}_{io}(f) = \frac{1}{Nb} \sum_{m=1}^{Nb} \frac{I_m^*(f)\, O_m(f)}{T} \tag{3.14}$$

in which, Nb is the number of signals (the number of times the experiment is replicated), the index m implies each sample realization that corresponds to each sample time history of length T, and the superscript * denotes the conjugate. The cross-spectral density functions are complex valued where $| S_{io}(f) |$ is the measure of association of amplitude in $i(t)$ and $o(t)$ at frequency f, and $arg[S_{io}(f)]$ shows lags/leads (or phase difference) between $i(t)$ and $o(t)$ at frequency f.

It should be mentioned here that, in general, all practical processes are non-stationary, thus the assumption of stationary input signal is only an approximation. This assumption is acceptable when we have an ensemble of data where it is possible to perform the average across the ensemble. In case of single record of data, the averaging will be performed along time (Welch's method, Welch (1967)) and the stationarity is a necessary condition for the time average to be meaningful.

To measure the degree of linear association between the input and output signals, the ordinary coherence function (or simply the coherence function) is generally used. It is defined as

$$C_{io}^2(f) = \frac{| \hat{S}_{io}(f) |^2}{\hat{S}_{ii}(f)\, \hat{S}_{oo}(f)} \tag{3.15}$$

The coherence function is unity if the input and output signals are linearly related. Conversely, if it is zero, the two signals are uncorrelated. Possible departures from linear relationship include: (i) the noise affecting both input and

output signals, (ii) the input and output signals are also related non-linearly, and (iii) the output signal is also induced by other inputs.

3.2.3 Fast Fourier Transform

The Fourier analysis is a family of mathematical techniques based on decomposing signals into sinusoids (Smith, 1997). The discrete Fourier transform (DFT or to simply $\mathcal{F}$) is the family member used to change N digitized signal points in the time domain to $(N/2+1)$ points signal in the frequency domain. The horizontal axis of the latter domain is normally labeled as a fraction of the sampling frequency f_{sam}. The ratio $\left(f_{\text{samp}}/N\right)$ is known as the resolution of $\mathcal{F}$. The $\mathcal{F}$ of an input sequence of samples $x(n)$ is the output component $X(m)$ (or spectrum) defined as (Lyons, 1997):

$$X(m) = \sum_{n=0}^{N-1} x(n)\, \mathrm{e}^{-\mathrm{i}\, 2\, \pi\, n\, m/N} \tag{3.16}$$

where, m is the index of the DFT output in frequency domain, n is the index in the time domain of the input sample, and i is the complex number $\sqrt{-1}$. The transformation procedure is reversible through the Inverse DFT or $\mathcal{F}^{-1}$ process given by:

$$x(n) = \frac{1}{N} \sum_{m=0}^{N-1} X(m)\, \mathrm{e}^{\mathrm{i}\, 2\, \pi\, n\, m/N} \tag{3.17}$$

The most efficient algorithm for calculating the $\mathcal{F}$ is the Fast Fourier Transform (FFT) that operates with N value that is a power of two. Windowing is an efficient technique to reduce the $\mathcal{F}$ leakage by forcing the amplitude of the input sequence at both the beginning and the end of the sample interval to go smoothly towards a single common amplitude value. The Hanning windowing type was used in this report.

The RMS magnitude of the $\mathcal{F}$ of $X(m)$ is given by the following equation:

$$|\, X(m)\, | = \sqrt{\mathrm{Re}\left[X(m)\right]^2 + \mathrm{Im}\left[X(m)\right]^2} \tag{3.18}$$

in which, Re [ ] and Im [ ] are the Real and Imaginary parts of the complex number $X\,(m)$, respectively.

3.2.4 Cross-correlation

The cross-correlation (or cross-covariance) function is one of the most important concepts in signal processing, and is applied to various practical problems such as estimating time delays in a system (e.g. radar systems and leak detection).

The cross-correlation technique is a measure of similarity of two signals as a function of a time-lag applied to one of them. It is also known as a sliding dot

product or inner-product. For discrete functions, the cross-correlation coefficients are obtained from the following equation (Lang, 1987):

$$(S1 \star S2)(n) = \sum_{m=m_1}^{m_2} S1^*(m)\ S2(n+m) \tag{3.19}$$

where, $S1$ and $S2$ are two arbitrary signals, $S1^*$ is the complex conjugate of $S1$, m_1 and m_2 are the lower and upper limits of the signal time interval, respectively.

3.2.5 Wavelet Transform

The wavelet analysis transform is used to retain information coming from the time domain analysis. Unlike the Fourier Transform, the wavelet technique is able to capture both rapid local changes and large fluctuation in the signal rather than giving only averaged information over the entire time domain (Mallat, 1992). Wavelets are often compared to a microscope for their ability to reveal particular aspects of the signal at different scales just by "adjusting the focus".

Wavelets are mathematical functions that decompose a signal into its constituent parts using a set of wavelet basis functions. The family of basis functions used for wavelet analysis is created both by dilations (scaling) and translations (in time) of a mother wavelet (Mallat, 1990). The continuous Wavelet Transform coefficients $\mathrm{Wf}(u,s)$ are obtained by convolving the signal $S(t)$ with the translations u and dilations s of the complex conjugate $\Psi^*_{u,s}$ of the mother wavelets $\Psi_{u,s}$, according to the following equation:

$$\mathrm{Wf}(u,s) = \int_{-\infty}^{+\infty} S(t)\ \Psi^*_{u,s}\ \mathrm{d}t \tag{3.20}$$

where the mother wavelets $\Psi_{u,s}$ are generated by:

$$\Psi_{u,s}(t) = \frac{1}{\sqrt{s}}\,\Psi\left(\frac{t-u}{s}\right) \tag{3.21}$$

For discrete signals, the reconstruction of the signal $S(t)$ is performed by using the inverse wavelet transform:

$$S(t) = \sum_{j\in\mathbb{Z}}\sum_{k\in\mathbb{Z}} \mathrm{Wf}(k,j)\ \Psi_{k,j}(t) \tag{3.22}$$

where j is the scale index or the decomposition level $\left(s = 2^j\right)$ and k is the time index $\left(u = k\cdot 2^j\right)$. By fixing j and summing over k, the detail coefficient at level j, D_j, is defined by:

$$D_j(t) = \sum_{k\in\mathbb{Z}} \mathrm{Wf}(k,j)\ \Psi_{k,j}(t) \tag{3.23}$$

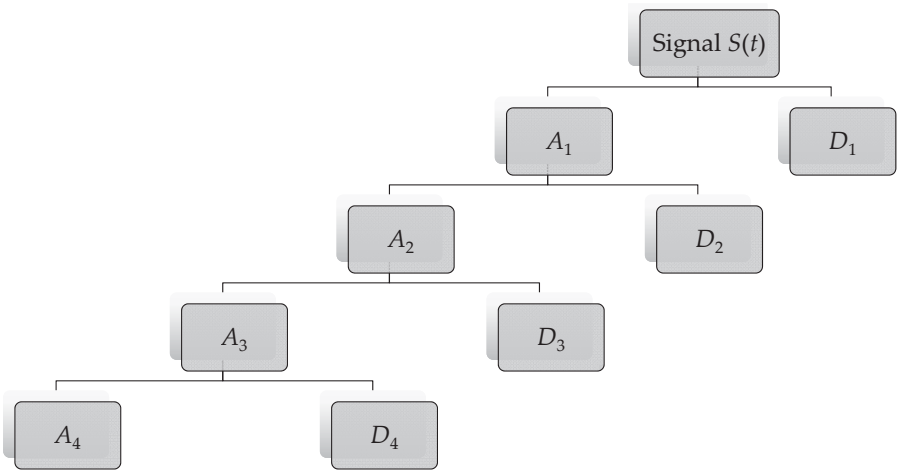

Figure 3.6: Wavelet decomposition tree up to level 4 where, A_1, A_2, A_3, and A_4 are the approximations and D_1, D_2, D_3, and D_4 are the details.

The signal $S(t)$ is thus the sum of its wavelet details at different levels j. By considering a reference decomposition level J, the approximation coefficient at this level is:

$$A_J(t) = \sum_{j>J} D_j(t) \tag{3.24}$$

So, the wavelet decomposition technique is the splitting of the original signal into approximation and detail coefficients. At each decomposition level the signal is passed through a pair of high-pass and low-pass filters. The former gives the high-frequency signal components, known as detail coefficients while the latter gives the low-frequency components or the approximation coefficients. A wavelet decomposition tree up to level 4 is shown in Fig. 3.6, where A_i and D_i are the i$^{\text{th}}$-level approximation and detail coefficients, respectively. After j levels of decomposition, the original signal $S(t)$ can be expressed as:

$$S(t) = A_j + \sum_{i=1}^{j} D_i \tag{3.25}$$

In this work, the *Daubechies* wavelet (db10), shown in Fig. 3.7, is used for the family of basis functions. The numerical index refers to the order or number of coefficients of the wavelet. The db10 does not have an explicit expression. Its central frequency, f_{cent} is equal to 0.68421 Hz. For a sampling time step of $1/f_{\text{samp}}$, the scale is associated to a pseudo-frequency, f_a by

$$f_a = \frac{f_{\text{cent}} f_{\text{samp}}}{s} \tag{3.26}$$

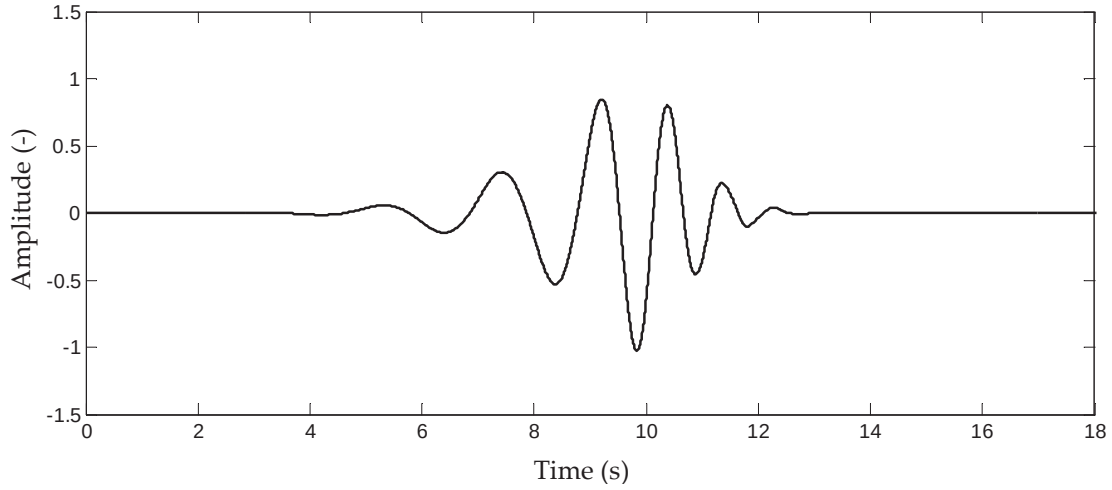

Figure 3.7: The *Daubechies* (db10) wavelet basis.

3.3 Uncertainty analysis

The uncertainty or margin of error of a measurement is the degree of inaccuracy between the measured and the true values of a variable. It is defined as being the sum of two types of error: the systematic (or bias) error and the random (or precision) error. The former error is the degree of closeness of measurements to the true value while the latter error is the degree to which repeated measurements under unchanged conditions show the same results. The uncertainty is stated by giving a range of values of the variable X likely to enclose its true (or best) value, X_{best}, with a certain level of confidence C (in %). The following symmetrical notation is thus proposed (Coleman and Steele, 1999):

$$X_{best} \pm U_X \tag{3.27}$$

in which, U_X is the uncertainty in X that corresponds to the confidence level C.

The Gaussian distribution has been found to describe more real cases of experimental and instrument variability than any other distribution and is the one assumed in the approach recommended in the ANSI/ASME standard (ANSI, 1998).

Each of the measurement systems that is used to measure the value of an individual variable X_i is influenced by a large number of elemental error sources. The material properties that we obtain from references also have uncertainties. These errors propagate through the data reduction equation and yield the bias and precision errors in the experimental results.

For the following general data reduction equation R, of J measured variables X_j

$$R = R(X_1, X_2, \ldots, X_J) \tag{3.28}$$

the uncertainty U_R for the 95 % confidence interval is (Coleman and Steele, 1999):

$$U_R^2 = B_R^2 + P_R^2 \tag{3.29}$$

where,

$$B_R^2 = \sum_{i=1}^{J} \left(\frac{\partial R}{\partial X_i} \right)^2 B_i^2 + 2 \sum_{i=1}^{J-1} \sum_{k=i+1}^{J} \left(\frac{\partial R}{\partial X_i} \right) \left(\frac{\partial R}{\partial X_k} \right) B_{ik} \tag{3.30}$$

and

$$P_R^2 = \sum_{i=1}^{J} \left(\frac{\partial R}{\partial X_i} \right)^2 P_i^2 \tag{3.31}$$

The B_R and P_R are the systematic and random uncertainties, respectively, of the result R, B_i and P_i are the systematic and random uncertainties, respectively, of the variable X_i, and B_{ik} is the covariance estimation for the systematic errors in X_i and X_k.

For situation in which the measurements of different variables share no common elemental error sources, the covariance terms are null. In the other case where the systematic uncertainty are not independent of each other, the B_{ik} value is approximated by the equation

$$B_{ik} = \sum_{m=1}^{n} (B_i)_m (B_k)_m \tag{3.32}$$

where, n is the number of elemental error sources that are common for X_i and X_k. Typical examples of this case occur when different variables are measured using the same transducer or when the variables are measured using different transducers which have been calibrated against the same standard. In the absence of calibration, the instrument systematic uncertainty should be obtained from the manufacturer's information. This accuracy specification will usually consider factors as gain, linearity and zero errors. These factors should be taken as a systematic uncertainty when no other information is available.

In the experimental field, values for some of the variables in the data reduction equation are not measured but rather are found from reference sources such the case for the material properties. All the errors (both random and systematic) in the experimental property data are consider into a systematic error. This generally means estimating a property uncertainty band based on the data scatter from different experiments.

When the experimental results are available, the random uncertainty determined from the propagation Eq. (3.31) can be obtained by the direct method which uses the standard deviation of results, S_R, of M multiple tests. The random uncertainty for large-sample ($M > 10$) is thus obtained according to the formula

$$P_{\overline{R}} = 2 \frac{S_R}{\sqrt{M}} \tag{3.33}$$

and the uncertainty in the average result $\overline{R}$ is then:

$$U_{\overline{R}} = \sqrt{\left(B_{\overline{R}}^2 + P_{\overline{R}}^2\right)} \tag{3.34}$$

Chapter 4

Mathematical model enhancement

This chapter focuses on the analysis of the wave speed propagation in rock-bored steel-lined tunnels and shafts. The purpose of it is to give: (i) a review of relevant contributions in deriving the wave speed formulae with clear definition of hypothesis and constraints, and (ii) to extend the use of the FSI model, derived by Kuiken (1984), to the field of steel-lined tunnels and shafts. Some examples with a sensitivity analysis of the main parameters are also provided in order to compare the results obtained in the frequency domain with the classical approaches presented in Chapter 2. The major parts of this chapter have been published in Hachem and Schleiss (2011g).

4.1 Radial deformation of steel-lined pressure tunnels

4.1.1 Quasi-static case

As discussed in Chapter 2, the deformation of radial symmetrical multilayer systems is generally derived from compatibility conditions at the interfaces (Talobre, 1967). In the case of steel-lined pressure tunnels, three layer interfaces of radius r_c, r_a and r_f, as shown in Fig. 2.2, exist. The compatibility of radial deformation at these three interfaces can be written as follows:

$$\left\{ \begin{array}{rcll} u(r=r_c) - \Delta r_0 & = & u_r^c(r=r_c) & \text{with } \Delta r_0 \geq 0 \\ u_r^c(r=r_a) & = & u_r^{\text{crm}}(r=r_a) & \\ u_r^{\text{crm}}(r=r_f) & = & u_r^{\text{rm}}(r=r_f) & \end{array} \right. \tag{4.1}$$

where superscript s is related to steel liner, c to the backfill concrete, and crm and rm to the near- and far-field zones of the rock mass. The subscript r indicates deformations in the radial direction. In this chapter, when the kinematic and dynamic effects of water and steel liner are considered (Fluid-Structure Interaction phenomenon) under internal pressure, the steel liner is assumed to be in permanent contact with the backfill concrete and the gap Δr_0 can be thus ignored.

For any layer j, considered as a thick circular cylinder in axisymmetrical behaviour and with elasticity modulus E_j, interior radius r_{j-1}, and exterior radius r_j, the two general equations governing the deformation of this layer under internal p_{j-1} and external pressures p_j subject to uniform longitudinal strain ε_l, or uniform longitudinal stress σ_l, are (Halliwell, 1963; Timoshenko and Gere, 2009):

$$u_r^j(r) = \frac{1}{E_j}\frac{r_j^2\, r_{j-1}^2}{r_j^2 - r_{j-1}^2}\left[\frac{1+v_j}{r}\left(p_{j-1}-p_j\right) + \left(1+v_j\right) r\left(\frac{p_{j-1}}{r_j^2} - \frac{p_j}{r_{j-1}^2}\right)\right] - \frac{v_j\,\sigma_l\, r}{E_j} \tag{4.2}$$

$$\varepsilon_l = \frac{\sigma_l}{E_j} - \frac{2\,v_j\, r_j^2\, r_{j-1}^2}{E_j\left(r_j^2 - r_{j-1}^2\right)}\left(\frac{p_{j-1}}{r_j^2} - \frac{p_j}{r_{j-1}^2}\right) \tag{4.3}$$

In plain strain conditions $(\varepsilon_l = 0)$, Eq. (4.3) becomes

$$\sigma_l = \frac{2\,v_j\, r_j^2\, r_{j-1}^2}{r_j^2 - r_{j-1}^2}\left(\frac{p_{j-1}}{r_j^2} - \frac{p_j}{r_{j-1}^2}\right) \tag{4.4}$$

In the following discussion, uncracked materials or layers are homogenous, elastic with axisymmetrical behaviour modeled according to thick-walled cylinder theory (Timoshenko and Gere, 2009) while cracked layers cannot transfer tensile stresses (layers with radial cracks).

The displacements $u_r^j(r)$, of the different layers shown in the 2-D calculation model of Fig. 2.2, can be written as:

- Steel liner

$$u_r^s\left(r = r_c\right) = \frac{1+\nu_s}{E_s}\frac{r_c}{r_c^2 - r_i^2}\left[\left(1-2\,v_s\right)\left(p_i\, r_i^2 - p_c\, r_c^2\right) + \left(p_i - p_c\right) r_i^2\right] \tag{4.5}$$

- Uncracked backfill concrete

$$u_r^c\left(r = r_a \text{ or } r_c\right) = \frac{1+v_c}{E_c}\frac{r}{r_a^2 - r_c^2}\left[\left(1-2\,v_c\right)\left(p_c\, r_c^2 - p_a\, r_a^2\right) + \left(p_c - p_a\right) r^2\right] \tag{4.6}$$

- Cracked backfill concrete

$$u_r^c\left(r = r_a\right) = u_r^c\left(r = r_c\right) + \frac{\left(1-v_c^2\right)\, p_c\, r_c}{E_c}\ln\left(\frac{r_c}{r_a}\right) \tag{4.7}$$

$$\text{with,}\quad p_c\, r_c = p_a\, r_a \tag{4.8}$$

- Uncracked near-field rock zone

  In this case, the entire rock mass (near- and far-field) is treated as an infinite uncracked layer ($r_f \to \infty$). The displacements u_r^{rm} at the interior face of the rock mass layer is

$$u_r^{\mathrm{rm}}\left(r = r_a\right) = \frac{1+v_r}{E_{\mathrm{rm}}}\, p_a\, r_a \tag{4.9}$$

- Cracked near-field rock zone

$$u_r^{\mathrm{crm}}\left(r = r_f\right) = u_r^{\mathrm{crm}}\left(r = r_a\right) + \frac{\left(1+v_r^2\right) p_a\, r_a}{E_{\mathrm{rm}}} \ln\left(\frac{r_a}{r_f}\right) \tag{4.10}$$

$$\text{with,} \quad p_a\, r_a = p_f\, r_f \tag{4.11}$$

- Uncracked infinite far-field rock zone when the near-field rock is considered as cracked

$$u_r^{\mathrm{rm}}\left(r = r_f\right) = \frac{1+v_r}{E_{\mathrm{rm}}}\, p_f\, r_f \tag{4.12}$$

Note that Eq. (4.8) assuming cracked backfill concrete is derived from the theory of thick-walled cylinder by putting the tensile stress σ_t equal to zero in the general equation: $\sigma_t - \sigma_r - r\,\mathrm{d}\sigma_r/\mathrm{d}r = 0$ and then by integrating it between the two layers' borders where $\sigma_r = p_c$ at $r = r_c$ and $\sigma_r = p_a$ at $r = r_a$. Variables σ_t and σ_r stand, respectively, for the tensile and radial stresses in the cylinder wall and $d\sigma_r/dr$ for the first derivative of σ_r relative to the radius r measured from the tunnel axis. The same procedure is used to obtain Eq. (4.11) for cracked near-field rock zone. The far-field rock zone was assumed as homogeneous, isotropic and elastic with a mean elastic deformation modulus E_{rm}.

4.1.2 General case considering kinematic and dynamic effects of water and steel-lined wall

Compared to the conventional uncoupled water-hammer analysis, the FSI may lead to: higher or lower extreme dynamic pressures and steel wall stresses, change in the natural frequencies of the system, and more damping and dispersion in the pressure and stress histories (Kuiken, 1988). That is why an enhanced FSI model is needed. The dispersion results from a frequency-dependent wave speed built from different frequencies traveling at different speeds. This makes difficult to identify the exact location of the wave front.

Denoting the axial displacement of the steel liner by u_l^s, the linearized boundary conditions at the water-liner interface using the no-slip condition are

$$v_l = \frac{\partial u_l^s}{\partial t}, \quad v_r = \frac{\partial u_r^s}{\partial t} \tag{4.13}$$

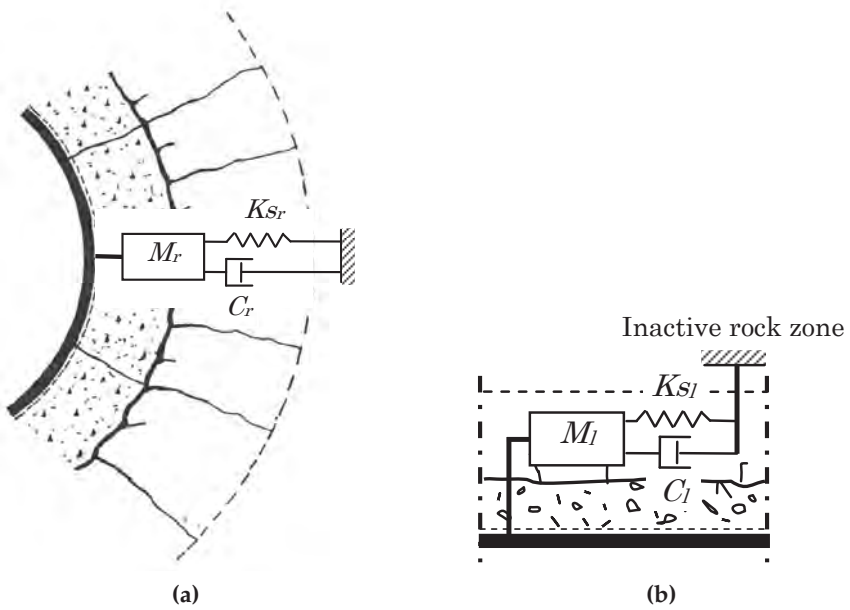

Figure 4.1: Enhanced calculation model for steel liners with axisymmetrical behaviour, (a) transverse cross-section, (b) longitudinal profile.

where v_l and v_r are, respectively, the water velocities in the axial x and radial r directions and t is the time. The first boundary condition concerning the velocity v_l is not needed in non-viscous fluid approximation (Rubinov, 1971).

The effect of the backfill concrete and the surrounding rock mass is mechanically modeled by a spring, a dashpot, and a lumped additional mass (Kelvin model). This conceptual model is represented in Fig. (4.1). The model input coefficients are Ks_r, C_r and M_r representing, respectively, (per unit area) the spring stiffness coefficient, the damping coefficient of the dashpot, and an additional mass. The same mechanical model is used to represent longitudinal liner-rock interaction with Ks_l, C_l, and M_l as coefficients.

The enhanced model can be described by the six-equation (3-mode) model of the FSI problem which was established first by Atabeck (1968) and generalized by Kuiken (1984). The adaptation of these equations gives:

- For the fluid without body forces in the axial x and radial r directions, the linearized equations of motions (Eqs. (4.14) and (4.15)), of continuity (Eq. (4.16)) and the thermodynamic constitutive equation for the density (Eq. (4.17)) are respectively:

$$\rho_0 \frac{\partial v_l}{\partial t} = -\frac{\partial p}{\partial x} + \mu \left(\frac{\partial^2 v_l}{\partial r^2} + \frac{1}{r}\frac{\partial v_l}{\partial r} + \frac{\partial^2 v_l}{\partial x^2} \right) + \left(\kappa + \frac{1}{3}\mu \right) \left(\frac{\partial^2 v_r}{\partial r \partial x} + \frac{1}{r}\frac{\partial v_r}{\partial x} + \frac{\partial^2 v_l}{\partial x^2} \right) \quad (4.14)$$

$$\rho_0 \frac{\partial v_r}{\partial t} = -\frac{\partial p}{\partial r} + \mu \left(\frac{\partial^2 v_r}{\partial r^2} + \frac{1}{r}\frac{\partial v_r}{\partial r} + \frac{\partial^2 v_r}{\partial x^2} - \frac{v_r}{r^2} \right) + \left(\kappa + \frac{1}{3}\mu \right) \left(\frac{\partial^2 v_r}{\partial r^2} + \frac{1}{r}\frac{\partial v_r}{\partial r} - \frac{v_r}{r^2} + \frac{\partial^2 v_l}{\partial x \partial r} \right) \tag{4.15}$$

$$\frac{\partial p}{\partial t} + \rho_0 \left(\frac{\partial v_r}{\partial r} + \frac{v_r}{r} + \frac{\partial v_l}{\partial x} \right) = 0 \tag{4.16}$$

$$\mathrm{d}p = c_T^2 \, \mathrm{d}p \tag{4.17}$$

- For the steel liner, the equations of motion in an initially stressed field are (Flügge, 1973)

$$\rho_s \, e \, \frac{\partial^2 u_l^s}{\partial t^2} = \frac{\partial \sigma_l^+}{\partial x} + F_x + \sigma_l^0 \frac{\partial^2 u_l^s}{\partial x^2} - \frac{\sigma_r^0}{r_i} \frac{\partial u_r^s}{\partial x} \tag{4.18}$$

$$\rho_s \, e \, \frac{\partial^2 u_r^s}{\partial t^2} = -\frac{\sigma_r^+}{r_i} + F_r + \sigma_l^0 \frac{\partial^2 u_r^s}{\partial x^2} + \frac{\sigma_r^0}{r_i} \frac{\partial u_l^s}{\partial x} \tag{4.19}$$

where ρ is the unit mass of water in excess of the steady-state unit mass ρ_0, p is the water pressure in excess of the steady-state pressure p_0, μ, and κ are, respectively, the dynamic and the bulk viscosities of water, ρ_s is the unit mass of steel, e the thickness of the liner, σ_r^+ and σ_l^+ are, respectively, the perturbation stresses in the circumferential and axial directions, σ_r^0 and σ_l^0 are the initial radial and longitudinal stresses in the liner evaluated per unit length, and c_T is the speed of sound in unconfined water equal to $(K_w/\rho_w)^{0.5}$, where K_w is the bulk modulus of water and ρ_w is the unit mass of water when the FSI is not considered. The forces F_x and F_y represent the resultant of hydrodynamic forces and forces applied by the surrounding backfill concrete on the liner, respectively, in the axial and radial directions. These forces for the Kelvin model presented in Figs. 4.1a and 4.1b, are specified by

$$F_x = -\mu \left[\frac{\partial v_l}{\partial r} + \frac{\partial v_r}{\partial r} \right]_{r=r_i} - M_l \frac{\partial^2 u_l^s}{\partial t^2} - C_l \frac{\partial u_l^s}{\partial t} - Ks_l \, u_l^s \tag{4.20}$$

$$F_r = \left[p - 2\,\mu \frac{\partial v_r}{\partial r} - \left(\kappa - \frac{2}{3}\,\mu \right) \left(\frac{1}{r} \frac{\partial r v_r}{\partial r} + \frac{\partial v_l}{\partial x} \right) \right]_{r=r_i} - M_r \frac{\partial^2 u_r^s}{\partial t^2} - C_r \frac{\partial u_r^s}{\partial t} - Ks_r \, u_r^s \tag{4.21}$$

Finally, the liner stress-strain relations for membranes are

$$\sigma_r^+ = B\,\frac{u_r^s}{r_i} + B_{(12)}\,\frac{\partial u_l^s}{\partial x} \tag{4.22}$$

$$\sigma_l^+ = B_{(12)}\,\frac{u_r^s}{r_i} + B\,\frac{\partial u_l^s}{\partial x} \tag{4.23}$$

where B and $B_{(12)}$are defined in Eq. (4.30).

The unknowns to be solved are v_l, v_r, p, u_l^s, and u_r^s. They are assumed to vary harmonically in x and t with a real constant angular frequency ω according to the following expressions in which the superscript ^ indicates the amplitude of the periodic quantities and c denotes the complex propagation velocity

$$[v_l, v_r, p] = [\hat{v}_l(r), \hat{v}_r(r), \hat{p}(r)]\,\mathrm{e}^{\mathrm{i}\,\omega\,(t-x/c)} \tag{4.24}$$

$$[u_l^s, u_r^s] = [\hat{u}_l^s, \hat{u}_r^s]\,\mathrm{e}^{\mathrm{i}\,\omega\,(t-x/c)} \tag{4.25}$$

Any non-sinusoidal variable can be treated as the combination of an infinite number of harmonic components using Fourier transformation. In linear theory, small sinusoidal amplitude motions of the liner wall are considered.

By substituting Eq. (4.24) into Eqs. (4.14)-(4.16), and using Eq. (4.17), the following expressions for $\hat{v}_l(r)$, $\hat{v}_r(r)$, and $\hat{p}(r)$ can be written

$$\begin{cases} \hat{v}_l(r) = \dfrac{\phi_1\,\hat{p}_0}{\rho\,c_0}\left[k\,\mathrm{J}_0\left(\mathrm{i}\,\beta\,\zeta\,k\,r/r_i\right) + D\,\mathrm{F}_0\left(\left(\mathrm{i}^3\alpha^2 - k^2\beta^2\right)^{0.5}\,\dfrac{r}{r_i}\right)\right] \\ \hat{v}_r(r) = \dfrac{\phi_1\,\hat{p}_0}{\rho\,c_0}\left[\zeta\,k\,\mathrm{J}_1\left(\mathrm{i}\,\beta\,\zeta\,k\,r/r_i\right) + 0.5\,\mathrm{i}\,\beta\,k\,D\,\mathrm{F}_1\left(\left(\mathrm{i}^3\alpha^2 - k^2\beta^2\right)^{0.5}\,\dfrac{r}{r_i}\right)\right] \\ \hat{p}(r) = \hat{p}_0\,\mathrm{J}_0\left(\mathrm{i}\,\beta\,\zeta\,k\,r/r_i\right) \end{cases} \tag{4.26}$$

where $\hat{p}_0$ is the reference pressure amplitude of water at $r = 0$, D an integration constant, and c_0 is the reference wave speed (defined in Eq. (4.48)), and the functions $\mathrm{F}_n\left(\lambda\,r/r_i\right)$ are defined by

$$\mathrm{F}_n\left(\lambda\,r/r_i\right) = 2^n\,n!\,\frac{\mathrm{J}_n\left(\lambda\,r/r_i\right)}{\lambda^n\,\mathrm{J}_0\left(\lambda\right)} \tag{4.27}$$

$\mathrm{J}_0(y)$ and $\mathrm{J}_1(y)$ are, respectively, the zero- and first-order first-kind Bessel functions. In Eq. (4.26), the various dimensionless parameters are

$$\begin{cases} k = \dfrac{c_0}{c}, \quad \alpha = r_i \left(\dfrac{\omega\,\rho_0}{\mu}\right)^{0.5}, \quad \alpha' = \alpha \left(\dfrac{\omega\,\rho_0}{\kappa}\right)^{0.5}, \quad \beta = \dfrac{\omega\, r_i}{c_0}, \quad \beta' = \dfrac{\omega\, r_i}{c_T} \\ \beta_{0T} = \dfrac{c_0}{c_T}, \quad \zeta^2 = 1 - \dfrac{\beta_{0T}^2}{k^2\,\phi_1}, \quad \phi_1 = 1 + \dfrac{\mathrm{i}\,\beta'^2}{\alpha'^2} + \dfrac{4\,\mathrm{i}\,\beta'^2}{3\,\alpha^2} \end{cases} \tag{4.28}$$

The first two homogeneous equations needed to solve the problem are derived from substitution of Eq. (4.26) into Eqs. (4.20) and (4.21). These latter equations with Eqs. (4.22) and (4.23) are then injected into Eqs. (4.18) and (4.19). The other two equations are derived from the substitution of Eqs. (4.24) and (4.26) into the kinematic boundary condition (4.13). A non-trivial solution for the five unknowns plus the constant of integration D is possible if the determinant is equal to zero. The following dispersion equation for an isotropic and elastic steel liner is thus obtained:

$$\begin{aligned} &k^6(\zeta^2 F_{1\beta}(1) - F_{1\alpha}(1))\beta^2 B'_{22}\sigma_l'^0 + k^4[(\zeta^2 F_{1\beta}(1) - F_{1\alpha}(1))(B'_{22}B^0_{11} - B^{02}_{12} + K'_l\sigma_l'^0) \\ &\quad - 0.5\zeta^2 F_{1\beta}(1)F_{1\alpha}(1)\beta^2\sigma_l'^0] + k^2[F_{1\alpha}(1)(B^0_{12} + \phi_4 B^0_{21} - 0.5B^0_{11}\zeta^2 F_{1\beta}(1)) \\ &- 2\phi_4 B'_{22} + (K'_l/\beta^2)B^0_{11}(\zeta^2 F_{1\beta}(1) - F_{1\alpha}(1))] + \phi_4[F_{1\alpha}(1) - 2(K'_l/\beta^2)] = 0 \end{aligned} \tag{4.29}$$

where

$$\begin{cases} B'_{22} = \dfrac{B + \sigma^0_l}{\rho\, r_i\, c_0^2}, \quad B = \dfrac{E_s\, e}{1 - v_s^2}, \quad \sigma_l'^0 = \dfrac{\sigma^0_l}{\rho\, r_i\, c_0^2}, \\ B^0_{11} = B'_{11} + K'_r - \dfrac{2\,\mathrm{i}\,\beta^2}{\alpha}, \quad B'_{11} = \dfrac{B}{\rho\, r_i\, c_0^2}, \\ K'_{r,l} = \dfrac{r_i}{\rho\, c_0^2}[K s_{r,l} + \mathrm{i}\,\omega\, C_{r,l} - \omega^2(M_{r,l} + \rho_s\, e)], \quad B^0_{21} = B^0_{12} = B'_{12} - \dfrac{2\,\mathrm{i}\,\beta^2}{\alpha^2}, \\ B'_{12} = \dfrac{B_{(12)} - \sigma^0_r}{\rho\, r_i\, c_0^2}, \quad B_{(12)} = \dfrac{E_s\, e\, \nu_s}{1 - v_s^2}, \\ \phi_4 = \dfrac{\phi_2 + (2\,\mathrm{i}\,\beta'^2/\alpha^2)}{\phi_1}, \quad \phi_2 = 1 - \dfrac{\mathrm{i}\,\beta'^2}{\alpha'^2} + \dfrac{2\,\mathrm{i}\,\beta'^2}{3\,\alpha^2} \end{cases} \tag{4.30}$$

and $F_{1\alpha}\,(r/r_i)$ and $F_{1\beta}\,(r/r_i)$ stand. respectively, for the first members of

$$\begin{cases} F_{n\alpha}(r/r_i) = \mathrm{F}_n\left((\mathrm{i}^3\alpha^2 - k^2\beta^2)^{0.5}(r/r_i)\right);\ n = 0, 1 \\ F_{n\beta}(r/r_i) = \mathrm{F}_n\left(\mathrm{i}\,\beta\,\zeta\,k\,(r/r_i)\right);\ n = 0, 1 \end{cases} \tag{4.31}$$

The complete solution is finally obtained for a linear combination of the forward and backward propagation mode for infinitely long tunnels and shafts. Using Eqs. (4.26), the linear combination of the solution (4.20) for each mode gives

$$\begin{cases} v_l(r) = \dfrac{\phi_1\,\hat{p}(r_i)}{\rho\,c_0}\,k\left[F_{0\beta}(\dfrac{r}{r_i}) + D^{'}F_{0\alpha}(\dfrac{r}{r_i})\right]\left[C_1\cos(\frac{\omega\,x}{c}) + C_2\sin(\frac{\omega\,x}{c})\right]\mathrm{e}^{\mathrm{i}\omega t} \\ v_r(r) = \dfrac{\phi_1\,\hat{p}(r_i)}{2\,\rho\,c_0}\beta k^2\left[\zeta^2\mathrm{F}_{1\beta}(\dfrac{r}{r_i}) - D^{'}F_{1\alpha}(\dfrac{r}{r_i})\right]\left[-C_1\sin(\frac{\omega\,x}{c}) + C_2\cos(\frac{\omega\,x}{c})\right]\mathrm{e}^{\mathrm{i}\omega t} \\ p(r) = \hat{p}(r_i)\,F_{0\beta}(\dfrac{r}{r_i})\left[-C_1\sin(\frac{\omega\,x}{c}) + C_2\cos(\frac{\omega\,x}{c})\right]\mathrm{e}^{\mathrm{i}\omega t} \end{cases} \tag{4.32}$$

where, the complex constants C_1 and C_2 are determined, for each mode, by boundary conditions at two different sections of the steel-lined tunnel, and the mode-dependent factor $D^{'}$ is defined by

$$D^{'} = -\frac{D}{k\,\mathrm{J}_0(\mathrm{i}\,\beta\,\zeta\,k)} = \frac{\left[\left(B_{11}^0 + k^2\beta^2\sigma_l^{'0}\right)\zeta^2F_{1\beta} - 2\,B_{12}^0\right]k^2 - 2\,\phi_4}{\left[\left(B_{11}^0 + k^2\beta^2\sigma_l^{'0}\right)F_{1\alpha} - 2\,B_{12}^0\right]k^2} \tag{4.33}$$

The radial and longitudinal displacements of the steel liner or penstock wall result from the summation of the mode solutions. For each mode, the solution is

$$\begin{cases} u_r^s(x,t) = 0.5\,r_i\,k^2\left(\zeta^2F_{1\beta}(1) - D^{'}F_{1\alpha}(1)\right)\left(\dfrac{\phi_1\,p(r_i)}{\rho\,c_0^2}\right) \\ u_l^s(x,t) = -\mathrm{i}\,r_i\,\dfrac{k}{\beta}\left(1 - D^{'}\right)\left(\dfrac{\phi_1\,p(r_i)}{\rho\,c_0^2}\right) \end{cases} \tag{4.34}$$

4.2 Water-hammer wave-speed expressions without fluid-structure interaction

4.2.1 General expressions

In plain strain conditions and considering the hypothesis of linear elasticity and small deformations with $r_i \approx r_c$ (thin-walled liners are considered), Eq. (3.6) can be written as follows:

$$a = \sqrt{\frac{1}{\rho_w\left(\dfrac{1}{K_w} + \dfrac{2}{r_i}\dfrac{\mathrm{d}u_r^s(r_i)}{\mathrm{d}p_i}\right)}} \tag{4.35}$$

in which $(\mathrm{d}u_r^s(r_i)/\mathrm{d}p_i)$ is the first derivative of u_r^s relative to the internal pressure p_i at the layer interface of radius r_i.

4.2.1.1 Case 1: Backfill concrete and near-rock mass zone are uncracked

For this case, the transmitted load to the rock is first determined as a function of p_i, Δr_0, and the materials characteristics by solving the system of the compatibility of deformation (4.1) using Eqs. (4.5), (4.6) and (4.9). The radial deformation of the steel liner, $u_r^s(r_c)$ and its derivative according to p_i are then computed from Eq. (4.5).

The complete expression of water-hammer wave speed is obtained by replacing the following expression of $(\mathrm{d}u_r^s(r_i)/\mathrm{d}p_i)$ in Eq. (4.35):

$$\frac{\mathrm{d}u_r^s(r_c)}{\mathrm{d}p_i} = \frac{B_1}{B_2 + B_3} \tag{4.36}$$

where

$$B_1 = 2(1+\nu_c)(1-\nu_s^2)r_c r_i^2[E_c(1+\nu_r)((1-2\nu_c)r_c^2 + r_a^2) - E_{\mathrm{rm}}(1+\nu_c)(1-2\nu_c)(r_c^2 - r_a^2)],$$

$$B_2 = E_s(r_c^2 - r_i^2)[E_{\mathrm{rm}}(1+\nu_s)^2(2\nu_c - 1)(r_c^2 - r_a^2) - E_c(1+\nu_c)(1+\nu_r)((2\nu_c - 1)r_c^2 - r_i^2)],$$

$$B_3 = E_c(1+\nu_s)[(2\nu_s - 1)r_c^2 - r_i^2)((1+\nu_r)(r_c^2 - r_a^2) - E_{\mathrm{rm}}(1+\nu_c)(r_c^2 - (2\nu_c - 1)r_a^2)]$$

4.2.1.2 Case 2: Backfill concrete is cracked while rock mass is not

Eqs. (4.5), (4.7), (4.8) and (4.9) are used to solve the system of Eqs. (4.1) for p_c, p_a and $u_r^s(r_c)$. The following expression of $(\mathrm{d}u_r^s(r_c)/\mathrm{d}p_i)$ is then replaced in Eq. (4.35).

$$\frac{\mathrm{d}u_r^s(r_c)}{\mathrm{d}p_i} = \frac{B_4}{B_5 + B_6} \tag{4.37}$$

where

$$\begin{aligned} B_4 &= 2(\nu_s^2 - 1)r_c r_i^2[E_c(1+\nu_r) - (1-\nu_c^2)E_{\mathrm{rm}}\ln(r_c/r_a)], \\ B_5 &= E_c[E_{\mathrm{rm}}(1+\nu_s)((2\nu_s - 1)r_c^2 - r_i^2) - E_s(1+\nu_r)(r_c^2 - r_i^2)], \\ B_6 &= (1-\nu_c^2)E_{\mathrm{rm}}E_s(r_c^2 - r_i^2)\ln(r_c/r_a) \end{aligned}$$

4.2.1.3 Case 3: Backfill concrete and near-rock zone are cracked

For this case, the expression of $(\mathrm{d}u_r^s(r_c)/\mathrm{d}p_i)$ is obtained by replacing E_c by $(E_c E_{\mathrm{crm}})$ and $(1-\nu_c^2)\ln(r_c/r_a)$ by $[(1-\nu_c^2)E_{\mathrm{crm}}\ln(r_c/r_a)+(1-\nu_r^2)E_c\ln(r_a/r_f)$ in Eq. 4.37. This yields to the following expression:

$$\frac{\mathrm{d}u_r^s(r_c)}{\mathrm{d}p_i} = \frac{B_7}{B_8+B_9} \tag{4.38}$$

where

$$B_7 = 2(\nu_s^2-1)r_c r_i^2[E_c E_{\mathrm{crm}}(1+\nu_r) - E_{\mathrm{rm}}((1-\nu_c^2)E_{\mathrm{crm}}\ln(r_c/r_a)+(1-\nu_r^2)E_c\ln(r_a/r_f))],$$

$$\begin{aligned} B_8 &= E_c E_{\mathrm{crm}}[E_{\mathrm{rm}}(1+\nu_s)((2\nu_s-1)r_c^2-r_i^2)-E_s(1+\nu_r)(r_c^2-r_i^2)], \\ B_9 &= E_{\mathrm{rm}}E_s(r_c^2-r_i^2)((1-\nu_c^2)E_{\mathrm{crm}}\ln(r_c/r_a)+(1-\nu_r^2)E_c\ln(r_a/r_f)) \end{aligned}$$

As discussed in Chapter 2, this case of the calculation scheme can be considered as the most realistic case. In fact, the backfill concrete with low tensile strength is normally cracked, and the close rock field is disturbed and cracked as a result of excavation and the change in the stress field around the tunnel. Only radial compressive stresses can be transmitted in these cracked zones. The water-wave-velocity expression for this case is referred in this work as the "complete quasi-static expression" which is valid for wave-speed calculation in frictionless circular steel-lined tunnel with axisymmetrical behaviour. The complete quasi-static expression neglects fluid-structure interaction.

4.2.2 Comparison of calculated wave speeds for Cases 1, 2, and 3

For comparison of Cases 1, 2 and 3, three configurations with different elasticity modulus for the far-field rock zone ($E_{\mathrm{rm}} = 5\,\%$, $10\,\%$, and $20\,\%$ of E_s) were analyzed by using the following input values:

$E_s = 210\,000\,\mathrm{MPa};\ E_c = 21\,000\,\mathrm{MPa};\ E_{\mathrm{crm}} = 0.5\,E_{\mathrm{rm}}$

$\upsilon_s = 0.30;\ \nu_c = 0.20;\ \nu_{\mathrm{rm}} = 0.25$

$r_a = 1.2\,r_i;\ r_f = 1.25\,r_a;\ K_w = 2\,200\,\mathrm{MPa};\ \rho_w = 1\,000\,\mathrm{kg/m^3}$

In Fig. 4.2, the quasi-static wave speeds for the three cases are given. The relative differences of Cases 1 and 2 compared to Case 3 are indicated as a function of (r_i/e) for the three (E_{rm}/E_s) ratios. If the near-rock mass zone is considered as uncracked with cracked backfill concrete (Case 2), it can be seen that the wave speed is higher, compared to the cracked layers case (Case 3). This augmentation of wave speed is 1-1.5 % for thick steel liners and 1.5-4 % for thin steel liners.

If the backfill concrete and the near-rock field are both considered as uncracked (Case 1), the overestimation of the wave speed, compared to Case 3, is between 2 and 8 % for thin steel liners. For thick liners, the overestimation is between 1 % and 2.5 %. The highest differences in the computed values of the wave speed are observed for relatively weak rock-mass moduli.

4.2.3 Comparison with other simplified expressions

4.2.3.1 Jaeger's formula

Jaeger (1972, 1977) published the following formula to estimate the pressure wave velocity in steel-lined pressure tunnels:

$$a = \sqrt{\frac{1}{\rho_w \left(\frac{1}{K_w} + \frac{2\, r_c (1 - \lambda_{11})}{E_s (r_c - r_i)} \right)}} \tag{4.39}$$

where

$$\lambda_{11} = \frac{r_c^2 / (E_s e)}{(r_c^2 / (E_s e)) + (r_a^2 - r_c^2 / (2\, E_c r_a)) + (\nu_r (1 + 1/\nu_r) r_c / E_{\mathrm{rm}})}$$

This formula was derived from the same hypothesis as the Case 2 model. The steel liner is treated as a thin circular cylinder and the mean radial deformation of the backfill concrete is taken into account. However, the steel and concrete Poisson ratios are ignored.

The quasi-static wave speeds calculated according to Jaeger's formula for different (E_{rm}/E_r) ratios and their relative differences compared to Case 3 are shown on Fig. 4.3a. Jaeger's relation overestimates the water-hammer velocity relative to the complete quasi-static expression. The maximum relative difference reaches 3.5 % for $r_i/e \approx 130$ and $E_{\mathrm{rm}}/E_s = 0.05$.

4.2.3.2 Parmakian's formula

Parmakian (1963) proposed a formula considering a steel liner surrounded by uncracked and infinite rock mass. The influence of the backfill concrete and the steel Poisson ratio are ignored. The same relation has also been used by Chaudhry (1987). It is given as follows:

$$a = \sqrt{\frac{1}{\rho_w \left(\frac{1}{K_w} + \frac{2\, r_i (1 + \nu_r)}{E_{\mathrm{rm}} r_i} + E_s e\, (1 + \nu_r) \right)}} \tag{4.40}$$

Fig. 4.3b shows that the wave speed values computed by Parmakian's relation are higher than values obtained from the complete quasi-static expression. For $E_{\mathrm{rm}}/E_s = 0.05$, the wave speed is overestimated by 3-4.6 % for $r_i/e \approx 150$.

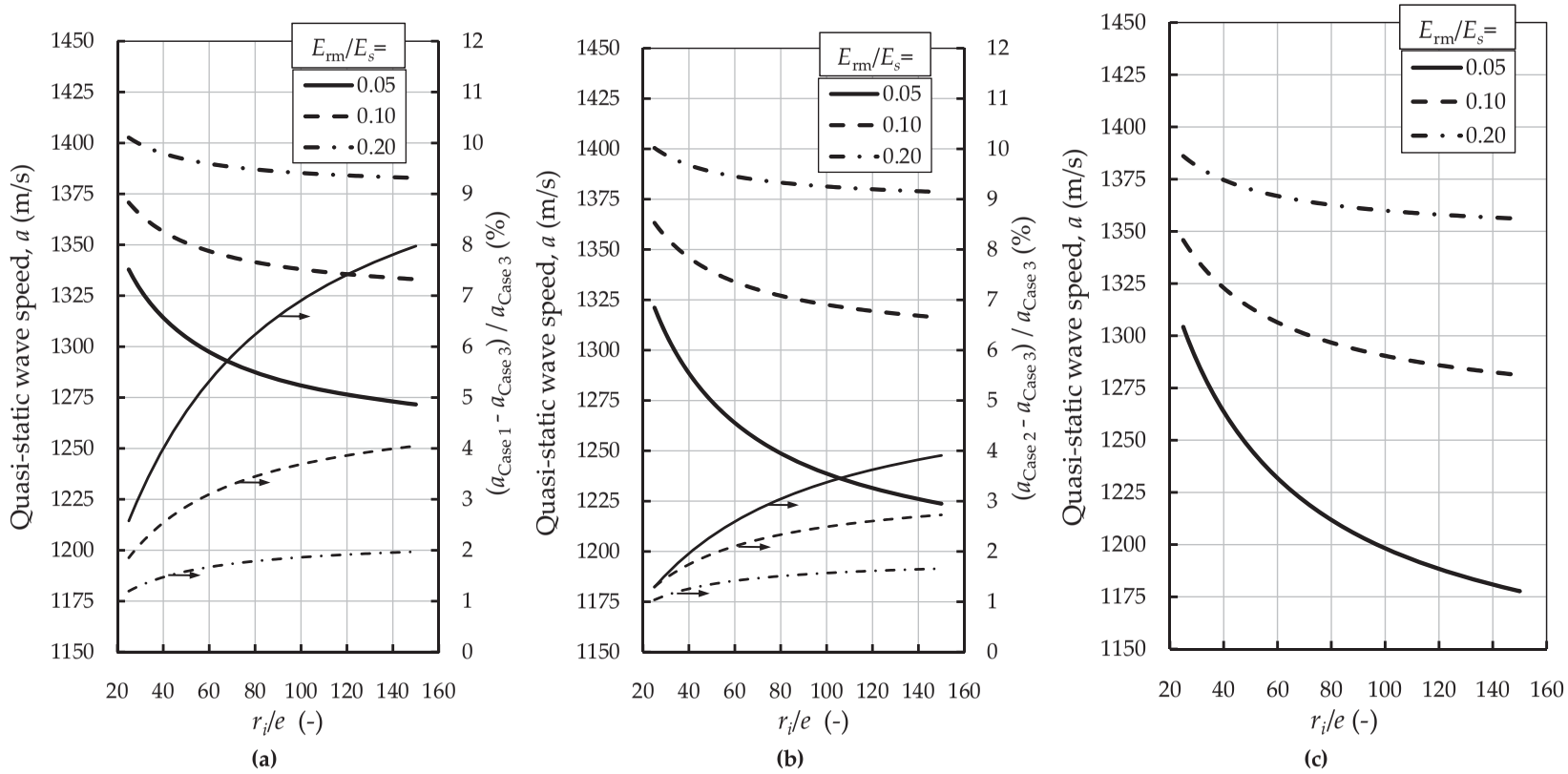

Figure 4.2: Quasi-static wave speeds and relative differences compared to Case 3 (right-hand scale) calculated by the formulae of the Cases 1, 2 and 3 as a function of the ratio of internal tunnel radius to steel-liner thickness for different values of E_{rm}/E_s ratio. (a) Case 1: Backfill concrete and the near-rock mass zone are uncracked (Eqs. (4.35) and (4.36)), (b) Case 2: Backfill concrete is cracked while the rock mass is not (Eqs. (4.35) and (4.37)), (c) Case 3: Backfill concrete and the near-rock zone are cracked (Eqs. (4.35) and (4.38)).

4.2.3.3 Halliwell's formula

Halliwell (1963) derived a formula for the wave speed assuming an uncracked concrete and rock mass surrounding the steel liner. The same Poisson ratios for steel, concrete and rock are considered. Salah et al. (2001) generalized Halliwell's formula using different Poisson ratios for each material.

Halliwell's wave speed equation is written as follows:

$$a = \sqrt{\frac{1}{\rho_w \left(\frac{1}{K_w} + \frac{2\, r_c (1-\nu^2)(1-\lambda_{12})}{E_s (r_c - r_i)} \right)}} \tag{4.41}$$

where

$$\lambda_{12} = \frac{(1-\nu)\, r_c}{(1-\nu)\, r_c + \frac{E_s (r_c - r_i)}{E_c} \frac{E_c (r_a^2 + r_c^2 (1-2\nu)) + E_{\mathrm{rm}} (1-2\nu)(r_a^2 - r_c^2)}{E_c (r_a^2 - r_c^2) + E_{\mathrm{rm}} (r_c^2 + r_a^2 (1-2\nu))}}$$

and $\nu_s = \nu_c = \nu_r = \nu$.

The wave speed and relative differences computed from Halliwell's formula are shown on Fig. 4.3c. This formula gives wave speed values of approximately 7.5 % higher than the complete quasi-static expression for $r_i/e \approx 150$ and $E_{\mathrm{rm}}/E_s = 0.05$ assuming $\nu = 0.3$.

4.2.3.4 Special case of open-air penstocks and unlined pressure tunnels

(a) Open-air penstocks

The pressure wave speed relation for a longitudinally blocked penstock can be derived from Eq. (4.36) of Case 1 by putting $r_a = r_c$ and by replacing ν_c, ν_r, E_c and E_{rm} by zeros and $(r_c + r_i)$ by $2\, r_i$. Considering the longitudinal boundary conditions of the penstock, Halliwell (1963) generalized the formula and Streeter (1963) corrected it in the case of penstocks that can freely slip in the longitudinal direction as follows:

$$a = \sqrt{\frac{1}{\rho_w \left(\frac{1}{K_w} + \frac{2\, r_i\, \lambda_{13}}{E_s\, e} \right)}} \tag{4.42}$$

where

$$\lambda_{13} = \begin{cases} 1 - 0.5\, \nu_s & \text{if the penstock can freely slip in the longitudinal direction,} \\ 1 & \text{if the penstock has expansion joints over its entire length,} \\ 1 - \nu_s^2 & \text{if the penstock is blocked in the longitudinal direction} \end{cases}$$

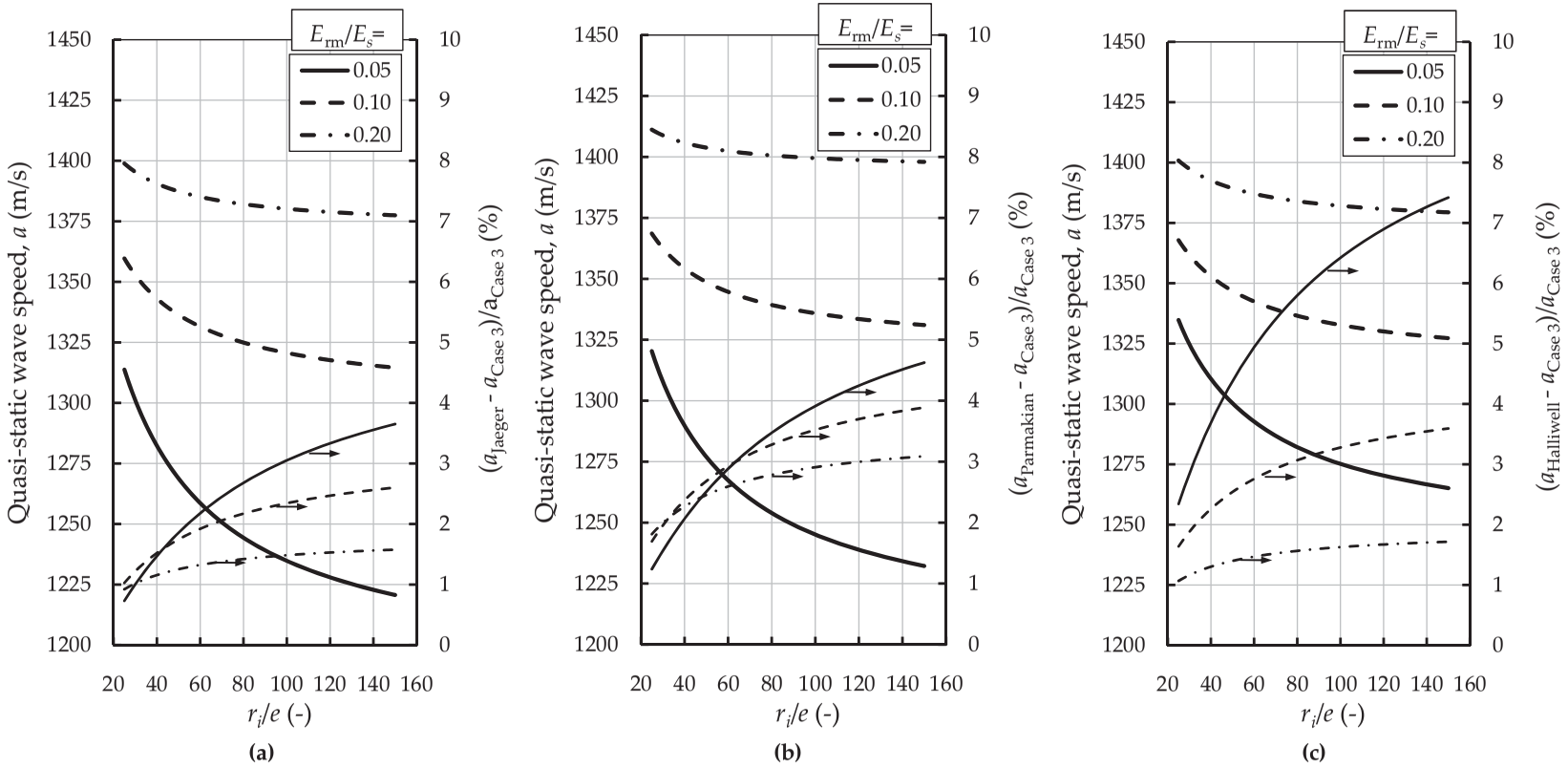

Figure 4.3: Quasi-static wave speeds and relative differences compared to Case 3 (right-hand scale) as a function of the ratio of internal tunnel radius to steel-liner thickness for different values of E_{rm}/E_s ratio. (a) Jaeger's formula (Eq. (4.39)), (b) Parmakian's formula (Eq. (4.40)), and (c) Halliwell's formula (Eq. (4.41)).

(b) Unlined pressure tunnels

The wave speed in an unlined pressure tunnel can be deduced from Case 1 by putting $r_a = r_c = r_i$ and by setting ν_s, ν_c, E_s and E_c equal to zero. Then, the wave speed can be written as

$$a = \sqrt{\frac{1}{\rho_w \left(\frac{1}{K_w} + \frac{2\,(1+\nu_r)}{E_{\mathrm{rm}}} \right)}} \tag{4.43}$$

The same relation has been proposed by Parmakian (1963) while in Jaeger (1977), ν_{rm} has also been set equal to zero. Jaeger's approximation leads to a wave speed overestimation of 3.5 % for $E_{\mathrm{rm}} = 10\,000\,\mathrm{MPa}$ and $\nu_r = 0.25$.

4.2.4 Definition of an apparent rock mass modulus

The purpose of the definition of such apparent rock mass modulus is to simplify the complicated expression of the quasi-static wave speed of the complete quasi-static expression (Case 3). The backfill concrete and the near- and far-rock masses are replaced by an equivalent homogeneous rock mass with an apparent elasticity modulus, E_{app}. This latter is defined such that the transmitting load ratio from steel to the equivalent rock mass is the same as in Case 3. The apparent rock mass modulus can be obtained by equating the wave velocity expressions in Cases 1 or 2 (with $r_a \to r_c$ and E_{rm} replaced by E_{app}) with wave velocity in Case 3 (with $r_a \to r_c$)

$$a(\text{Case 1 or 2}) = a(\text{Case 3}) \tag{4.44}$$

Eq. (4.44) leads to two expressions defining, respectively, E_{app} and a as follows:

$$E_{\mathrm{app}} = \frac{E_{\mathrm{rm}}\,E_{\mathrm{crm}}}{E_{\mathrm{crm}} - E_{\mathrm{rm}}\,(1-\nu_r)\,\ln(r_c/r_f)}, \tag{4.45}$$

$$a = \sqrt{\frac{1}{\rho_w \left[\frac{1}{K_w} + \frac{4\,(\nu_s^2-1)(1+\nu_r)\,r_c\,r_i}{E_{\mathrm{app}}(1+\nu_s)[(2\nu_s-1)r_c^2 - r_i^2] - E_s(1+\nu_r)(r_c^2-r_i^2)} \right]}} \tag{4.46}$$

4.3 Water-hammer wave-speed expressions considering fluid-structure interaction

4.3.1 General expressions

By considering the water as a compressible non-viscous fluid $(\mu = \kappa = 0)$ and by neglecting the initial longitudinal stress in the steel liner $(\sigma_l^0 = 0)$, the dispersion

Eq. (4.29) can be simplified as follows:

$$[(B_{22}^{'}+K_{r}^{'})K_{l}^{'}+k^{2}\beta^{2}(B_{22}^{'2}+B_{22}^{'}K_{r}^{'}-B_{12}^{'2})](k^{2}\beta^{2}-\beta^{'2})F_{1}(\mathrm{i}(k^{2}\beta^{2}-\beta^{'2})^{0.5}) = 2\beta^{2}(K_{l}^{'}+k^{2}B_{22}^{'}\beta^{2}) \quad (4.47)$$

The reference velocity c_0 can be taken, as in Kuiken (1984), equal to

$$c_{0}=\sqrt{\frac{1}{\rho_{w}\left(\frac{1}{K_{w}}+C\,\frac{2\,r_{i}}{E_{s}\,e}\right)}} \quad (4.48)$$

where

$$C=\frac{1-\nu_{s}^{2}}{1+(K_{r}/B)}, \quad (4.49)$$

and

$$K_{r}=r_{i}^{2}\left[Ks_{r}+i\,\omega\,C_{r}-\omega^{2}\,(M_{r}+\rho_{s}\,e)\right] \quad (4.50)$$

ω is the real angular frequency $(=2\,\pi\,f)$ of the continuous excitation of frequency f.

If Ks_r is taken equal to $(p_c/u_r^s(r_c))$, calculated according to Case 3, and if ω is very small, c_0 is equal to the complete quasi-static wave speed. When ω approaches infinity, c_0 becomes the speed of sound in unconfined water $(K_w/\rho_w)^{0.5}$.

The solutions of the quadratic dispersion Eq. (4.47) occur in pairs $(\pm k)$ where each $\pm k$ solution is associated to a particular mode of oscillation with waves propagating in positive and negative directions along x. The modes with small values of the imaginary part of k are the propagating modes, whereas the modes with high values of the imaginary part of k decay rapidly according to the following expression:

$$[v_{l},v_{r},p]=[\hat{v}_{l}(r),\hat{v}_{r}(r),\hat{p}_{i}(r)]\,\mathrm{e}^{\mathrm{i}\omega(t-x/c)}=[\hat{v}_{l}(r),\hat{v}_{r}(r),\hat{p}_{i}(r)]\,\mathrm{e}^{-\Delta_{i}x/\lambda_{i}}\,\mathrm{e}^{i\omega(t-x/c_{i})} \quad (4.51)$$

where λ_i is the wave length of the i^{th} wave mode, c_i is the phase velocity (c_{pi}) or the group velocity (c_{gi}), and Δ_i is the logarithmic decrement of the i^{th} wave mode. The phase velocity of a traveling wave form may or may not correspond to a particular physical entity and does not necessarily correspond to the speed at which energy or information is propagating. That is why the phase velocity might go to infinity and be higher than the speed of sound in unconfined water. Hence, the energy of the wave propagates with the group velocity when this later is smaller than the phase velocity. The parameters of Eq. (4.51) with the equivalent reference wave speed are defined by

$$\lambda_{i}=2\,\pi\,\frac{c_{i}}{\omega},$$

$$\text{Phase velocity, } c_{pi} = \frac{1}{\mathrm{Re}[k/c_0]}, \quad \text{Group velocity, } c_{gi} = \frac{\mathrm{d}\omega}{\mathrm{d}(\omega\, Re[k/c_0])},$$
$$\Delta_i = -2\,\pi\,\frac{\mathrm{Im}[k/c_0]}{\mathrm{Re}[k/c_0]}, \quad c_{0\mathrm{eq}} = \frac{\mathrm{Re}[c_0]^2 + \mathrm{Im}[c_0]^2}{\mathrm{Re}[c_0]} \tag{4.52}$$

Rubinov and Keller (1971, 1978) showed that, for the non-viscous fluid approximation, two modes (called tube modes) can only propagate at low frequencies (with or without cut-off bands) and an infinite number of acoustic modes propagate at high frequencies. For open-air penstocks, the first acoustic mode begins to propagate at an angular frequency of $(\beta_{01} c_T / r_i)$, where β_{01} is the first positive root of the Bessel function J_0 $(= 2.40483)$. For example, the lower cut-off frequency of the first acoustic mode of a penstock of radius $r_i = 1.75\,\mathrm{m}$ is equal to 2 038.25 rad/s (or 324.4 Hz).

In the low-frequency range solution of Eq. (4.47), the tube mode with the lowest propagation velocity at low frequencies is the longitudinal compression mode in water (water-hammer or Young mode), while the higher propagation velocity corresponds to the axial stress wave mode in the steel walls of liners and penstocks (precursor or Lamb mode). The axial stress waves result from the coupling of the radial expansion and contraction of the liner or penstock walls and the Poisson's ratio of the steel. The stress waves in return generate pressure fluctuations in the enclosed water. This coupling is known as the ''Poisson coupling'' (Skalak, 1956). Tijsseling et al. (2008) re-calculated the solution of Skalak's four-equation model and gave an analytical expression for water-hammer and precursor quasi-static wave speeds in open-air penstocks. The general solution of the Poisson coupling problem has been solved exactly by Li et al. (2003) and by Tijsseling (2003).

Tijsseling (1996) has classified the one-dimensional FSI models according to their basic equations and physical variables involved to derive their dispersion equations. According to this classification and by ignoring the radial movement of water, the enhanced model can be considered as a six-equation model (3-mode solutions) where the unknown variables are: the pressure and axial velocity of water, axial stress, axial velocity, hoop stress, and radial velocity in the steel liner or penstock wall.

The wave speed results of the two tube modes (water-hammer and precursor modes) and the first acoustic mode, evaluated according to Eqs. (4.47) and (4.52), are shown in Fig. 4.4 for steel-lined pressure tunnels with the following parameters: $r_i = 1.75\,\mathrm{m}$, $(p_i/e) = 100$, $\rho_s = 7\,850\,\mathrm{kg/m^3}$, $\rho = \rho_0 = \rho_w = 1\,000\,\mathrm{kg/m^3}$, $E_s = 210\,000\,\mathrm{MPa}$, $f_y = 580\,\mathrm{MPa}$, $\rho_r = 2\,200\,\mathrm{kg/m^3}$, $E_c = E_{\mathrm{rm}} = 21\,000\,\mathrm{MPa}$, $E_{\mathrm{crm}} = 10\,500\,\mathrm{MPa}$, $\zeta = 10\,\%$, $\mu = \kappa = 0$, $\sigma_l^0 = 0$, and $\sigma_r^0 = 0.5\,f_y\,e$. It can be seen (Fig. 4.5b) that the motion of the liner wall is primarily radial for the water-hammer mode and primarily longitudinal for the precursor mode. The logarithmic decrement coefficients plotted versus ω are shown in Fig. 4.5a. The

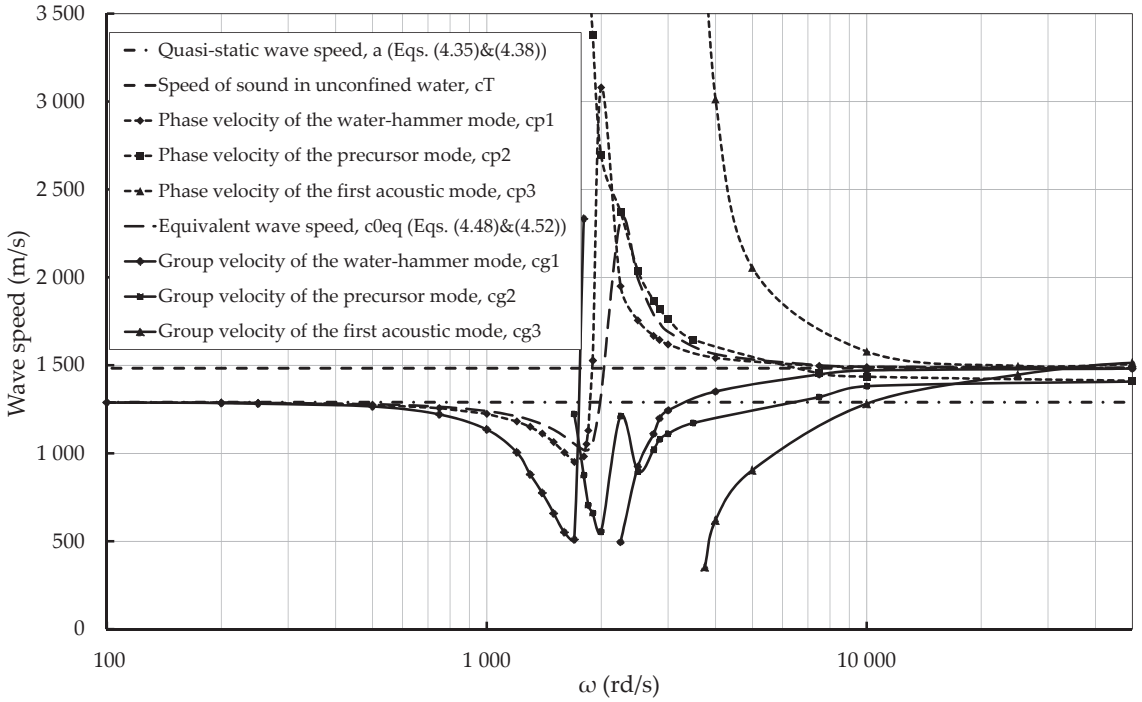

Figure 4.4: Three modes' phase and group wave speeds as a function of the angular frequency ω for an isotropic steel-lined tunnel having the input parameters shown in Section 4.3.1. The speed of sound in unconfined water, the wave speeds calculated according to quasi-static and equivalent reference approaches are also shown.

radial and longitudinal mechanical coefficients of the surrounding rock mass are taken as follows:

$$\begin{cases} M_r = M_l = \rho_r \left(r_f - r_c\right), \\ Ks_r = Ks_l = \dfrac{p_c}{u_r^s(r = r_c)} \\ C_r = C_l = 2\,\zeta\, M_r \sqrt{Ks_r / M_r} \end{cases} \quad \text{of Case 3,} \tag{4.53}$$

in which the inactive rock zone is considered at radius $r = r_f$.

For the water-hammer mode, the group velocity is below the phase velocity for all ω values except in the narrow frequency band $1\,700 - 1\,900\,\text{rad/s}$. The group velocity represents then the wave speed of the propagating energy and can be compared to quasi-static wave speed, a, and to the speed of sound in unconfined water, c_T. For frequencies lower than 800 rad/s, the relative difference, $(c_{g1} - c_{0\text{eq}})/c_{g1}$, between the group velocity, c_{g1} and a is less than 5 %. This difference increases considerably and reaches 150 % for $\omega = 1\,700\,\text{rad/s}$. A cut-off frequency band exists around 2 000 rad/s. The water-hammer mode starts to propagate again in the high-frequency range (higher than 2 250 rad/s) with a group velocity that goes up from 500 m/s to reach asymptotically c_T. Near 1 700 rad/s,

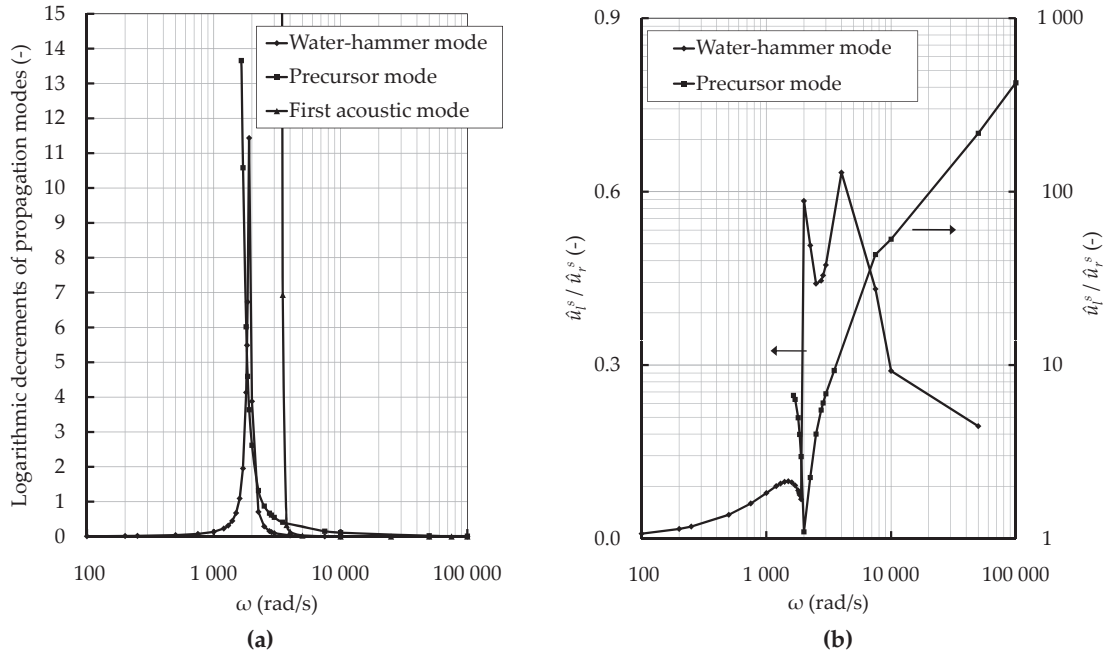

Figure 4.5: (a) The logarithmic decrement coefficients (Eq. (4.52)) of the three propagation modes shown in Fig. 4.4, (b) The amplitude ratios of the longitudinal to radial displacements $(\hat{u}_l^s / \hat{u}_r^s)$ of the liner wall for the two tube modes shown in Fig. 4.4.

the maximum attenuation coefficient is reached.

For the precursor mode, the low cut-off frequency is around 1 600 rad/s and the wave speed (equal to the group velocity) decreases rapidly when ω increases in the intermediate frequency range (between 1 600 and 2 000 rad/s) and reaches, for large ω, a rather constant value between the quasi-static and c_T wave speeds. Fig. 4.6a shows the variation of the precursor wave speed mode (phase and group velocities) as a function of ω for $C_l = 0$ and $Ks_l = 0.001\, Ks_r$, $0.01\, Ks_r$ and Ks_r. The cut-off frequency depends on the longitudinal stiffness constraint of the liner and can be used as an indicator to detect the presence and intensity of such constraint.

The first acoustic mode begins to propagate at an angular frequency near 3 300 rad/s. This frequency is 1.7 times higher than in open-air penstocks. This cut-off frequency depends on the radial constraint of the steel liner (Fig. 4.6b) and varies close to the second mode of rigid tubes ($\beta_{11} c_T / r_i = 3\,247.6$ rad/s). β_{11} is the first positive root of the Bessel function J_1 ($\beta_{11} = 3.83171$). The phase and group velocities of this mode approach c_T when ω becomes very high.

4.3.2 FSI problem in the case of open-air penstocks

For open-air penstocks ($K_r = 0$), Eq. (4.48) becomes equal to (4.42) when λ_{13} is equal to $(1 - v_s^2)$. The solutions of Eq. (4.47) for the two tube modes and the first acoustic mode are given in Fig. 4.7. The water-hammer mode has a cut-off fre-

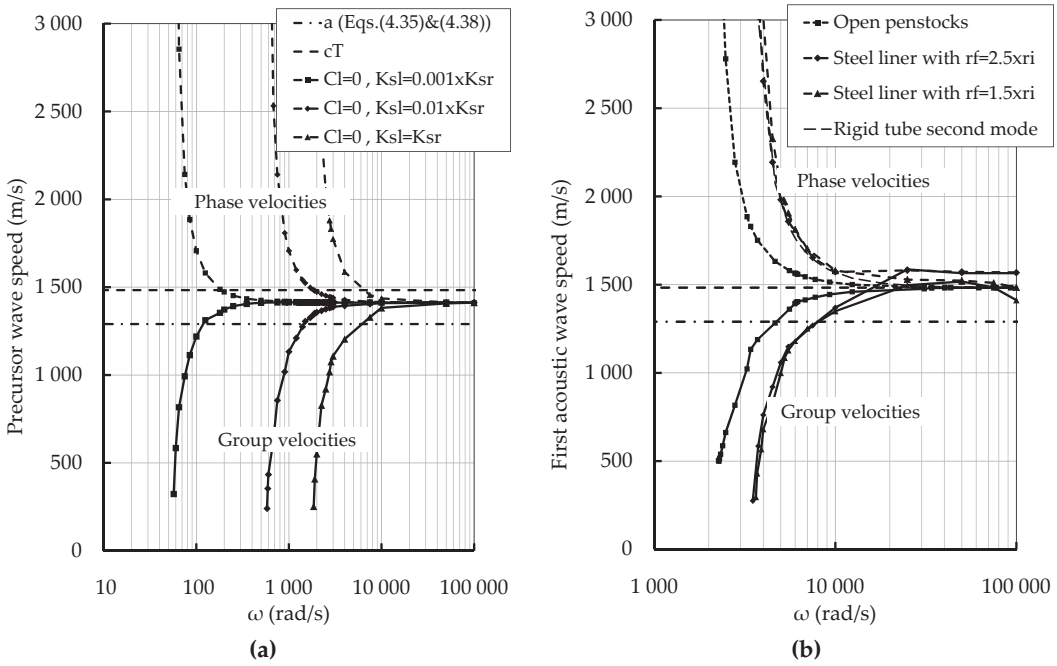

Figure 4.6: (a) The variation of the precursor phase and group wave speeds (Eqs. (4.47) and (4.52)) versus ω for different longitudinal stiffness constraints of a steel liner with $C_l = 0$ and with the other input parameters similar to those given in Section 4.3.1, (b) The variation of the first acoustic phase and velocity wave speeds (Eqs. (4.47) and (4.52)) versus ω for different radial stiffness constraints characterized by two different values of the internal radius of the crack rock zone (r_f) and with the other input parameters similar to those given in Section 4.3.1.

quency equal to $(1/r_i)(E_s/\rho_s)^{0.5}$. The precursor mode propagates for all values of ω and is very well estimated by Skalak's formula for frequencies lower than 1 200 rad/s and higher than 7 500 rad/s. In the intermediate frequency range the maximum relative difference, $(c_{g2} - a_{\text{Skalak}})/c_{g2}$, can reach 20 %. The first acoustic mode presents a lower cut-off frequency equal to 2 038.25 rad/s $(\beta_{01} c_T/r_i)$.

The classical expression (4.42) of the quasi-static wave speed has been also modified by Stuckenbruck et al. (1985). They ignore radial inertia and consider only the axial inertial forces in the pipe wall. This approach leads to a constant real wave velocity and causes a reduction of the classical wave speed of about 7 % for high values of $(2\,r_i/e)$.

For thin-walled viscoelastic pipes, a complex-valued and frequency-dependent wave speed has been formulated by Suo and Wylie (1990a). The classical expression (4.42) was extended by replacing E_s by a complex frequency-dependent Young's modulus, $E_s(\omega)$, of the viscoelastic material.

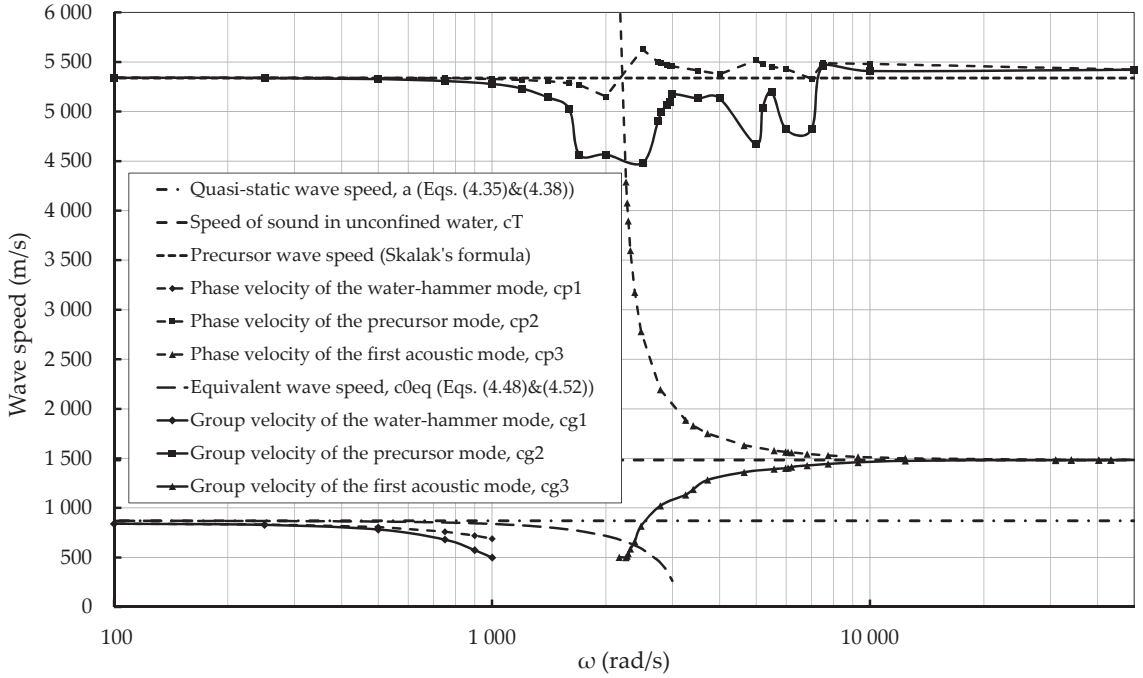

Figure 4.7: Comparison between the variation of the quasi-static wave speed, the speed of sound in unconfined water, the equivalent reference wave speed, and the phase and group wave speeds of the three propagation modes versus the angular frequency for an open-air penstock having the input parameters given in Section 4.3.1.

4.3.3 FSI problem in the case of unlined pressure tunnels

As can be seen from Eq. (4.30), the properties of the surrounding materials are included in $K_r^{'}$ and $K_l^{'}$ expressions. For unlined pressure tunnels in rigid rock mass, $K_r^{'}$ and $K_l^{'}$ goes to infinity (similar to a strongly constrained liner), resulting in the rigid dispersion approximation written as follows:

$$(\beta^2 k^2 - \beta'^2/\phi_1)\, F_1(\mathrm{i}(\beta^2 k^2 - \beta'^2/\phi_1)^{0.5}\, 1) - \beta^2 k^2\, F_1(\mathrm{i}(\beta^2 k^2 - \mathrm{i}^3\, \alpha^2)^{0.5}\, 1) = 0 \tag{4.54}$$

In this case, the propagation modes are only acoustic and occur because the fluid is compressible. The roots of Eq. (4.54) are

$$c_j = \omega\, r_i\, ((\omega\, r_i/c_T^2) - \beta_{1j}^2)^{-0.5}, \quad j = 0, 1, 2, \ldots, \tag{4.55}$$

where β_{1j} is the jth positive root of the Bessel function (J1). The reference velocity c_0 given in (4.48) becomes equal to the wave speed c_T which is the first root ($j = 0$) of Eq. (4.55).

The hydraulic transients in unlined pressure tunnels have been studied by Fanelli (1973) and Suo and Wylie (1990b) without considering the complete FSI problem. The rock mass has been treated as an infinite homogeneous and isotropic

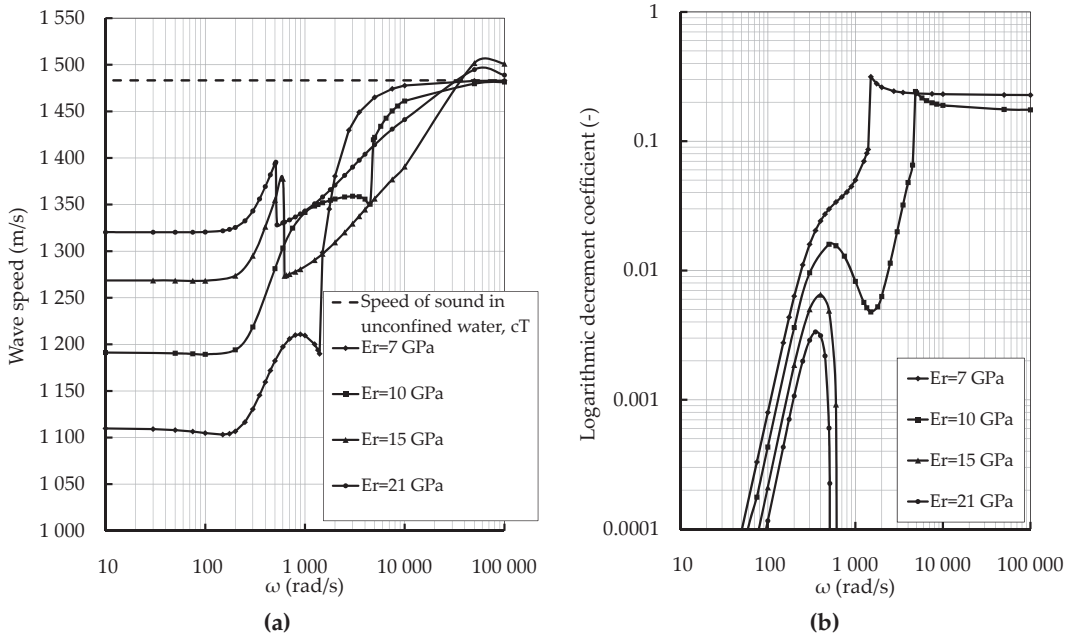

Figure 4.8: The variation of: (a) The water-hammer wave speed (Eqs. (4.47) and (4.52)), (b) The logarithmic decrement coefficient (Eq. (4.52)) versus the radial frequency in an unlined pressure tunnel having the following input parameters: $r_i = 1.75\,\mathrm{m}$, $\rho_r = 2\,200\,\mathrm{kg/m^3}$, and $E_{\mathrm{rm}} = 7\,000$, $10\,000$, $15\,000$, and $21\,000\,\mathrm{MPa}$.

cylinder and only the dynamic effect of the rock mass has been taken into account. This leads to a complex-valued and frequency-dependent wave speed. Fig. 4.8a and Fig. 4.8b shows, respectively, the variation of the equivalent wave speed and the logarithmic decrement coefficient (Eq. (4.52)) versus the radial frequency in an unlined pressure tunnel with the following input parameters: $r_i = 1.75\,\mathrm{m}$, $\rho_r = 2\,200\,\mathrm{kg/m^3}$, and $E_{\mathrm{rm}} = 7\,000$, $10\,000$, $15\,000$, and $21\,000\,\mathrm{MPa}$. The equivalent wave speeds are bounded between the quasi-static (Eq. (4.43)) and the c_T wave speeds and have no cut-off frequencies. They decrease slightly at low frequencies, increase rapidly when ω increases with abrupt change of value at intermediate frequencies, and approach asymptotically c_T when the frequency goes to infinity. The decrement coefficient increases rapidly for ω between 50 and $100\,\mathrm{rad/s}$ and reaches its maximum value for ω around 300 and $400\,\mathrm{rad/s}$ for hard rock. For relatively weak rock, the coefficient continues increasing with increasing ω, and reaches a constant value at high frequency.

4.4 Conclusions

In this chapter, general applicable approaches for estimating the quasi-static and frequency-dependent water-hammer wave speed in steel-lined pressure tunnels and shafts were analyzed. The external constraints and assumptions of these

approaches have been discussed and the reformulated formulae have been compared to commonly used expressions. An enhanced theoretical model for the steel-liner has been proposed as a basis of future development, including, for example, the application of fracture mechanics, to assess the response of high-strength steel which is used as lining for shafts of new hydro plants. The following assumptions have been considered: (i) frictionless and axisymmetrical waterways, (ii) linearization of equations of water motion, (iii) linear elastic behaviour of the steel-liner and pipe wall, and (iv) infinitely long waterways.

Compared to the "complete quasi-static expression" (Eqs. (4.35) and (4.38)), the wave speed in steel-lined pressure tunnels with cracked backfill concrete and uncracked near-rock zone (Eqs. (4.35) and (4.37)) is overestimated by 4 % for thin steel liners and by 1.5 % for thick steel liners. If all layers are uncracked (Eqs. (4.35) and (4.36)), the wave speed is overestimated up to 8 % for thin steel liners and up to 2.5 % for thick steel liners. The highest differences are observed for relatively weak rock mass moduli. The "complete quasi-static expression" was also compared to other formulas in literature. For thin steel liners and weak rock mass modulus, Jaeger's and Parmakian's relationships (Eqs. (4.39) and (4.40), respectively) overestimate the water-hammer velocity (Eqs. (4.35) and (4.38)) by approximately 3-4.5 %, while in Halliwell's formula (Eq. (4.41)) this overestimation reaches 7.5 %.

For practical applications, the above wave speed differences can be tolerated because of the uncertainty in the estimation of the rock mass characteristics and the presence of air in the water. Nevertheless, the dynamic pressures obtained from classical water-hammer theory are not overly affected by such differences in wave speed. Depending on the system stiffness, the FSI may lead to higher extreme dynamic pressures with higher frequencies. Therefore, further investigations of results of the enhanced model proposed herein are required with laboratory experiments and in-situ measurements. They will allow the validation of some cases presented herein and the comparison of a calculated transient event in the time and frequency domains, respectively.

The FSI problem with the phase, group and reference wave velocities (Eqs. (4.48) and (4.52)) has been analyzed. The dispersion equation was also solved through a numerical example. The phase and group velocities of the water-hammer mode, precursor mode, and first acoustic mode were evaluated in function of the angular frequency of the transient excitation.

For the water-hammer mode inside steel-lined pressure tunnels and open-air penstocks, FSI results show that the equivalent reference velocity is a good approximation of the phase and group velocities in low (80 Hz) and high (800 Hz) frequency ranges with no significant wave attenuation. In the intermediate frequency range, the maximum relative difference of the wave velocities in steel-lined tunnels relative to the quasi-static case reaches 150 %, and the maximum attenuation coefficient is reached. In the intermediate frequency range, the precursor mode has a cut-off frequency and decreases rapidly when ω increases

from 255 to 320 Hz. This mode reaches, for large ω, a constant value between the quasi-static wave speed and speed of sound in unconfined water, c_T. The cut-off frequency is dependent on the longitudinal distribution of the stiffness of the liner. It can be used as an indicator to detect the presence and intensity of such local weak stiffness. In the case of open-air penstocks, the water-hammer mode presents a high cut-off frequency around 150 Hz, while the precursor mode propagates for all values of the angular frequency and can be well estimated by Skalak's formula.

In steel-lined pressure tunnels, the first acoustic mode begins to propagate at an angular frequency near 3 300 rad/s (525 Hz). This cut-off frequency depends on the radial constraint of the steel liner and varies closely with the second mode of rigid tubes. The wave velocity of this mode approaches the speed of sound when the angular frequency becomes very large.

For the special case of unlined pressure tunnels with constant wave speed, Jaeger's equation overestimates the wave speed by 3.5 % compared to the "complete quasi-static expression". Another approach was adopted by Suo and Wylie (1990b) considering the rock mass as an infinite homogeneous and isotropic cylinder and taking only the dynamic effect of the rock mass into account. Using the FSI formulations, the results show that the equivalent wave speed is bounded between the quasi-static wave speed and the speed of sound in unconfined water and has no cut-off frequencies. It decreases slightly at low frequencies, increases rapidly when ω increases with abrupt change of value at intermediate frequencies, and approaches asymptotically c_T when the frequency goes to infinity. For the numerical cases studied, the decrement coefficient, in the case of hard rock, increases rapidly for small ω, reaches a maximum value, and then decreases. For relatively weak rock, the coefficient continues increasing with increasing ω, approaching a constant value at high frequencies.

Chapter 5

Laboratory experimental set-up

The description and design of the test facility are described in this chapter. The facility was built in purpose to enhance the monitoring methods for steel-lined pressure shafts and tunnels. If the hypothesis of an axi-symmetrical deformation of the multilayer system (steel-concrete-rock) of the pressure shaft presented in Chapter 2 is accepted, the shaft can be modeled by a single-layer system of the test pipe. Water-hammer events are generated inside the test pipe by closing a shut-off valve at its downstream end. For the detection of longitudinal stiffness heterogeneity, different geometric configurations of the steel test pipe were examined by changing systematically the position of an aluminum and PVC pipe reach of 1 and 0.5 m long. Some additional information in french language can be found in (Buchs, 2010).

5.1 Design of the experimental set-up

5.1.1 Main construction constraints

Before discussing the design and presenting the description of the experiments, it is important to list the main construction constraints of the test facility.

The test rig, called "PF4", is an existing installation in the Laboratory of Hydraulic Machines (LMH) of the Ecole Polytechnique Fédérale de Lausanne (EPFL). It is an independent close hydraulic loop which includes a water supply reservoir, a variable speed pump, a supply conduit, an air vessel, and a small Francis turbine connected downstream to the supply reservoir. The pump, the supply reservoir, a small part of the supply steel conduit, and the air vessel have been kept in place and used for the construction of the new test set-up. All the other parts of the existing installation have been dismantled except the imposing steel frame which supported the turbine and its generator. This steel frame did not consist an obstacle to the new construction. A collection of photos of the old configuration of the test rig is given in Section B.1 of Appendix B.

Thus, the new experimental set-up shown in Fig. 5.1, has been built by adapt-

ing the old one. The two major constraints during construction were the following: (i) a restricted horizontal distance between the supply reservoir and the air vessel, and (ii) a difference in altitude between the input and output orifices of the supply reservoir and the air vessel. The limited horizontal distance has dictated the length of the new test pipe to be around 7.5 m while the difference of altitude of 0.63 m has imposed the use of two elbows to connect the downstream end of the test pipe to the supply reservoir.

5.1.2 The characteristics of existing components of the experimental set-up

5.1.2.1 Pump

The variable speed pump of the test rig is of type "Sulzer G7 200-500" with a maximum rotation speed of 1 000 rpm. The characteristic curves of this pump are shown in Fig. 5.2 for four rotation speeds, $n_p = 390$, 700, 850, and 1 000 rpm. The pump is operated by an electrical board with a manual potentiometer to adjust its rotation speed. An electrical switch placed at the output of the pump, shuts it down when overpressure inside the supply conduit exceeds the 2 bars.

5.1.2.2 Supply reservoir

The supply reservoir is made of steel and has a cylindrical form of 2.8 m height and 1.6 m in diameter. Its capacity is equal to 5.1 m^3. The diameter of its input and output holes is equal to 150 mm. A vertical distance of 705 mm separates the axis of these holes. The curves which relate the reservoir height to reservoir capacity and some detail drawings are given in Section B.2 of Appendix B.

5.1.2.3 Pressurized air vessel

The air vessel is a cylindrical tank having a water capacity of 1 m^3 and an input and output orifice of 160 mm in diameter. The maximum admissible internal pressure inside the vessel is limited to 2 bars. Some detail drawings can be found in Section B.3.

5.1.3 Description and design of new components

5.1.3.1 Water supply conduit

The existing steel conduits at the high-pressure side of the pump has been extended by a 10 m long PVC supply pipe of 150 mm of internal diameter. The existing air purge valve situated at the intersection of the steel supply conduits (Fig. B.1b) has been preserved and used to evacuate the captured air inside the test rig. The water flow discharge that has been used to design the new components of the experimental set-up was equal to 65 l/s (see the hydraulic design paragraph in Section 5.1.3.3). This design discharge generates a moderate steady-state flow

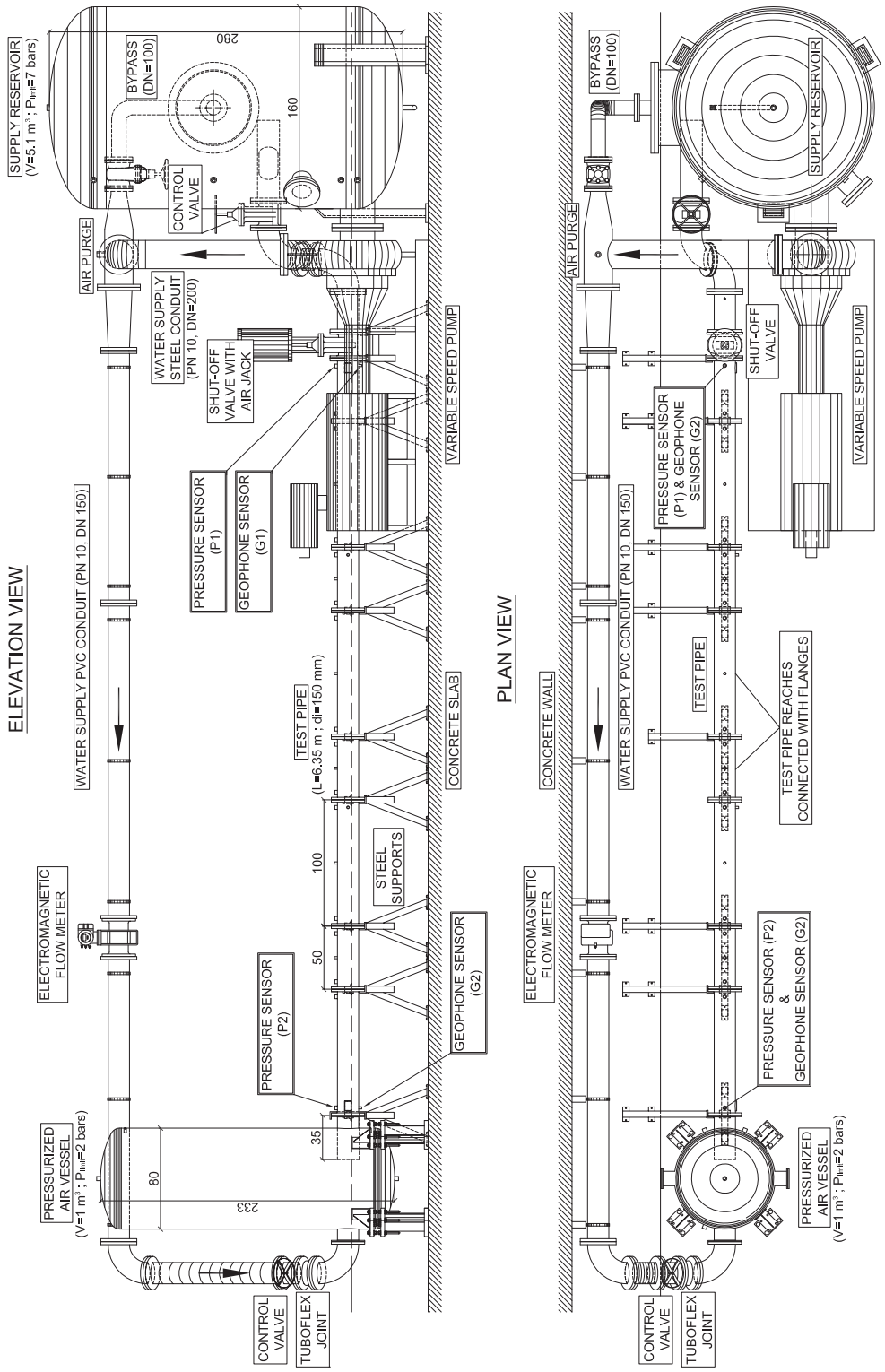

Figure 5.1: Elevation and plan views of the experimental facility.

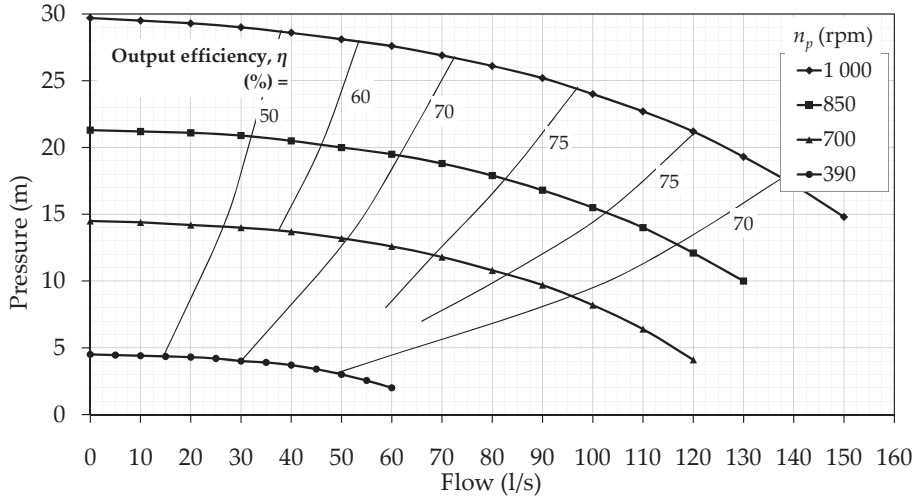

Figure 5.2: Characteristic curves and efficiency of the test rig pump for four rotation speeds, $n_p = 390$, 700, 850, and 1 000 rpm.

velocity of 3.68 m/s inside the PVC supply conduit. A control and security valve, type "hawle 4 000, flange slider, PN16" followed by an elastic deformable joint, type "TUBOFLEX, GUKO DN150, PN16, 100 lg, Mod.5B", have been placed at the downstream end of the supply conduit. This latter is protected against water-hammer by the pressurized air vessel. Figs. B.5a and B.5b show two photos of this part of the test facility.

5.1.3.2 Shut-off valve

The shut-off valve is a "vonRoll*hydrotec*" slide gate valve of type "5 000 plus PN10 EN-GJS-500-7" (Fig. B.6a). The upper cover part of the valve and the sliding core axis have been adapted to receive a pneumatic air jack of type "SMC C95SDB 125-150/00106209" (Fig. B.6b). The pneumatic jack has been equipped with an electro-distributor valve and the volume of air needed to activate it has been provided by an air compressor with a constant pressure of 10 bars. The opened and closed states of the shut-off valve are detected by two "Baumer FHDK 07N6901" infrared diffuse sensors and a small cantilever plate fixed on the sliding axis of the valve (Fig. B.6b). The points representing the measured closure times and their mean and mean$\pm$standard deviation lines are shown in Fig. 5.3 for the 330 tests that have been carried out on the different configurations of the test pipe. The mean and standard deviation of the closure time of the shut-off valve are 0.228 s and 0.0044 s, respectively. The closure time is considered slow relative to the characteristic time of the test pipe. The latter is equal to $(2\,L_p)/a = 0.01$ s, in which $L_p = 6.45$ m is the length of the test pipe between the vertical axis of the shut-off valve and the pressurized air vessel (Section 5.1.3.3) and $a = 1\,292$ m/s is the theoretical wave speed inside the steel test pipe estimated from Eq. (4.42) with

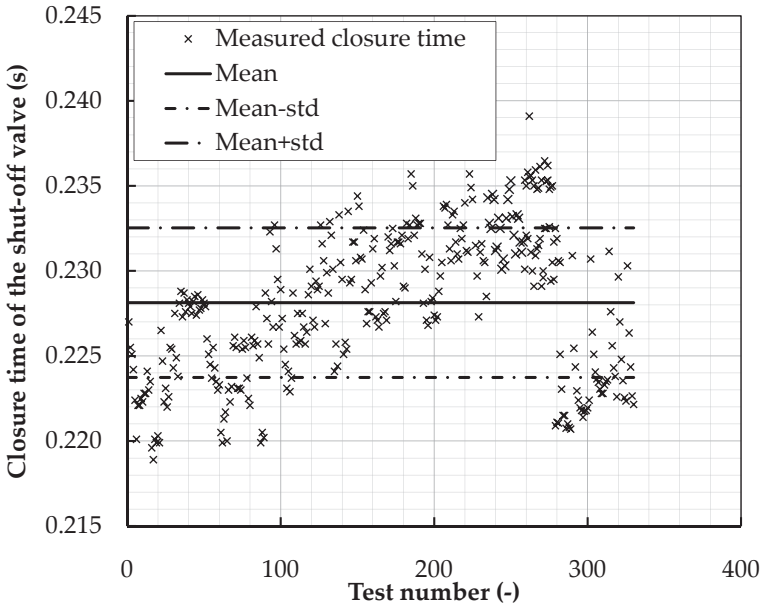

Figure 5.3: Closure time of the shut-off valve, their mean and mean±standard deviation measured from the 330 tests carried out on the test pipe.

$\lambda_{13} = (1 - \nu_s^2) = 0.91$ and $K_w = 2\,200$ MPa. The value of the other parameters needed in Eq. (4.42) can be found in Table 5.1.

A series of no-flow tests has been carried out to study the behaviour of the shut-off valve. These tests have revealed the presence of an important pressure drop followed by high-amplitude and high-frequency fluctuations. The pressure drop is probably caused by the compression and expansion of an air pocket captured inside the upper cover of the valve during the filling up of the test pipe. The important fluctuations which follow the pressure drop are probably generated by the deformation, friction and/or vibration of the internal core of the valve. Fig. 5.4 shows a typical no-flow pressure record measured at 16.5 cm upstream from the shut-off valve axis. This figure shows also the time at the beginning and at the end of the valve closure manoeuvre.

Table 5.1: Length, wall thickness, material characteristics, and the theoretical wave speed (Eq. (4.42)) of the steel, aluminum and PVC pipe reaches.

Material	Length (m)	Wall thickness (mm)	Unit mass (kg/m^3)	Elastic modulus (MPa)	Equivalent steel thickness (mm)	Theoretical wave speed (m/s)
Steel	0.5 - 1	4.5	7 850	210 000	4.500	1 292
Alu	0.5 - 1	5.0	2 700	69 000	1.640	1 085
PVC	0.5	5.0	1 400	3 000	0.071	324

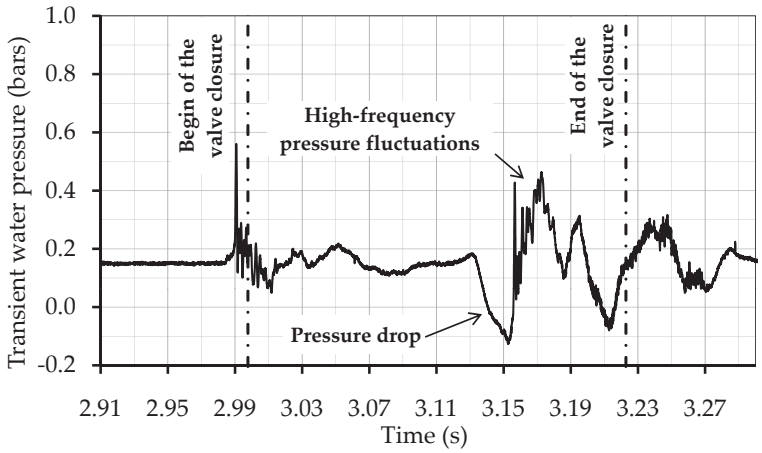

Figure 5.4: Typical record of the measured transient pressure in no-flow condition inside the test pipe acquired at 16.5 cm upstream from the vertical axis of the shut-off valve. The time at the beginning and at the end of the valve closure is also shown.

5.1.3.3 Test pipe

Description

The test pipe has been prepared from standard black longitudinally welded pipes of quality P235TR1 (Ac 37.0) EN 10217-1. It has an internal diameter of 150 mm, a wall thickness of 4.5 mm, and a length of 6.35 m measured from the upstream side of the shut-off valve to the air vessel. It is divided into several steel reaches 0.5 m and 1 m long, fitted together with O-ring joints and flanges having an external diameter of 285 mm and a thickness of 24 mm. The flanges are also used to fix the test pipe rigidly along its length by using steel supports in both horizontal and vertical directions. These supports minimize any longitudinal and lateral movements of the pipe during the tests.

The shut-off valve, which is described in Section 5.1.3.2, is followed by a 0.12 m long pipe reach. This reach is equipped with a purge valve of 2.54 cm in diameter. It is followed by two elbows, an elastic TUBOFLEX joint, and a second control valve located at the entrance of the supply reservoir. The total length of the test pipe made up of all these pieces (including the shut-off valve) is about 1.88 m. All the steel reaches of the test pipe have been protected against oxidation by using the hot-dip galvanizing process. A global view of the steel test pipe and its downstream end are shown in Figs. B.7a and B.7b of Appendix B.

The 0.5 m and 1 m aluminum reaches used to simulate the weak part inside the test pipe, are made up of standard pipes of type EN AW-6 082 (AlMgSi1) T651. They have an internal diameter of 150 mm and a wall thickness of 5 mm. For the PVC reaches, it was difficult to find standard tubes of 150 mm of internal diameter. Therefore, the PVC reaches have been prepared from grey standard PVC RAL 7 011 which has an external diameter of 160 mm and a wall thickness

of 7.7 mm. A material layer 2.7 mm thick has been removed from the internal part of the standard PVC tube at the LCH mechanical workshop. The available mechanical machine was not able to deal with pieces longer than 0.5 m. Therefore, only three PVC reaches of 0.5 m length have been prepared (Figs. B.8). Table 5.1 shows the length, wall thickness, unit mass, elasticity modulus, and the theoretical wave speed of the test pipe reaches made of steel, aluminum, and PVC materials. The wave speed is determined from Eq. (4.42) with $\lambda_{13} = (1 - \nu_s^2) = 0.91$ and $K_w = 2\,200$ MPa. The equivalent steel thicknesses of the aluminum and PVC reaches determined from the equation $e_{\text{eq. steel}} = (E_{\text{alu,PVC}} / E_{\text{steel}})\, e_{\text{alu,PVC}}$ are also shown in Table 5.1. The detail drawings and dimensions of steel, aluminum, and PVC reaches are depicted in Table 5.2.

Hydraulic design

For the steady-state design flow of 65 l/s, the velocity inside the test pipe, v_l, is equal to 3.68 m/s and the flow is turbulent with a Reynolds number $(\rho_w v_l d_i / \mu) = 460\,000$, in which $\rho_w = 1\,000\,\text{kg/m}^3$ and $\mu = 0.0012$ Pa.s. The steady-state pressure at the upstream end of the test pipe is around 0.21 bar.

The unsteady hydraulic design of the test rig has been done by using the computer software package "HYTRAN v3.2.3" (HYTRAN, 2004). This software is developed for analyzing the HYdraulic TRANsients in pipelines and has drag-and-drop facilities which enable on-screen construction of a pipe network in either plan or profile views. Some of the selectable boundary tools include pumps, turbines, air vessels, vacuum relief valves, pressure regulating valves, and demands. A method of characteristics-based solver generates pressure and flow rate histories at the boundary nodes and along the pipelines. A column separation indicator warns the user when cavitation is detected. HYTRAN divides the shortest pipe reach into a given specified number of equal-length sub-reaches and creates internal nodes in all pipes according to this length. The software determines the computation time-step by dividing the sub-reach length by the computed or user introduced wave speed of all the pipe reaches. In order to have a discrete number of sub-reaches in all pipes, the algorithm sets up a fixed computational grid by adjusting their wave speeds. The smallest pipe length which can be introduced in the software is equal to 1 m.

Fig. 5.5 shows the numerical model scheme of the experimental facility. The supply reservoir is modeled by two separate reservoirs (at nodes 1 and 9) to consider the difference in altitude between its input and output holes. The pump is placed at node 2 and the pressurized air vessel at node 10. The pipes 5 and 16 represent the new supply conduit without considering the control valve and the elastic joint. The test pipe between the air vessel and the shut-off valve is modeled by a series of 1 m long reaches numbered from 10 to 15. The shut-off valve is placed at the downstream end of reach 15 (at node 8). The two elbows and the elastic joint at the downstream part of the test pipe are modeled by one single pipe (pipe 8). The transient pressure results at the upstream and downstream

Table 5.2: Detail drawings and dimensions of the steel, aluminum and PVC pipe reaches.

Material	Number of pieces	Detail drawings
Steel	4 pieces of 50 cm length 4 pieces of 100 cm length	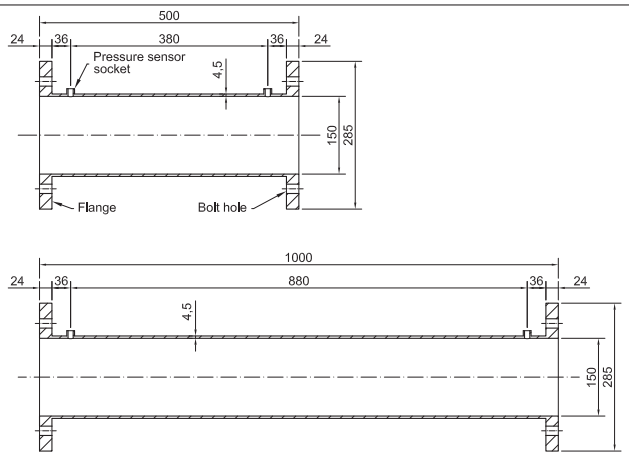
Alu	3 pieces of 50 cm length 3 pieces of 100 cm length	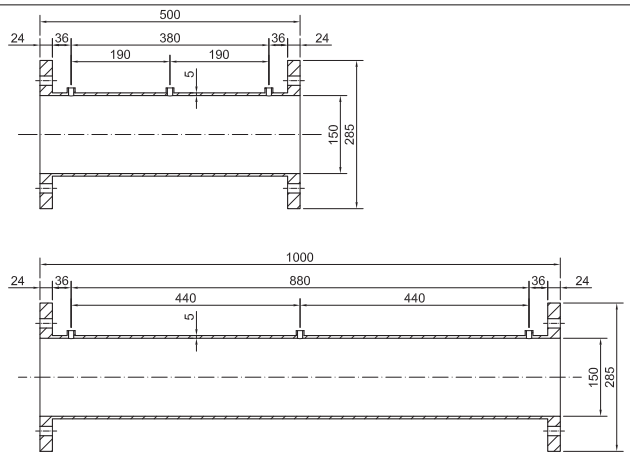
PVC	3 pieces of 50 cm length	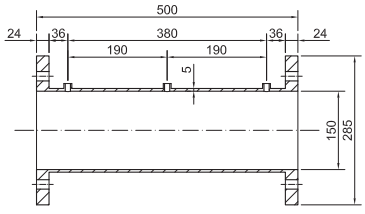

sides of the shut-off valve obtained from the closure of the shut-off valve in 0.22 s are given in Fig. 5.6a. This figure shows also the flow discharge and the ratio of opened to maximum cross-section area of the valve. After 1.48 s from the end of the closure manoeuvre, the valve is totally re-opened in 0.5 s. The computed air pressure and water level inside the air vessel are shown in Fig. 5.6b. The pressure head and discharge at the pump output during the overall valve manoeuvre are given in Fig. 5.6c.

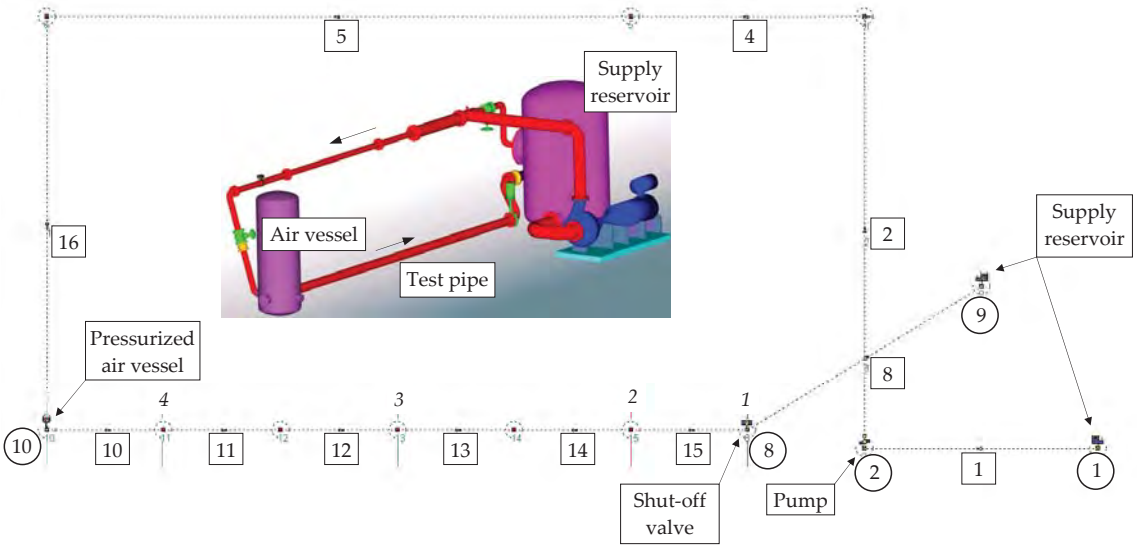

Figure 5.5: Numerical model scheme and a 3D view of the experimental facility.

The results show that the maximum transient pressure inside the test pipe at the upstream side of the valve is equal to 3.9 bars while the minimum pressure occurs downstream the valve and is around -0.85 bar. The maximum air pressure inside the vessel is below the maximum admissible value of 2 bars. The minimum pump flow discharge is around 0.02 m^3/s and the maximum pressure head at the pump output is equal to 1.79 bars.

For the test pipe of total length $L_T = 8.23$ m measured between the supply reservoir and the air vessel, the wave dissipation due to steady or unsteady friction can be neglected since the dimensionless parameter Γ determined from Eq. (3.7) is equal to $0.042 \ll 1$ for the first full wave cycle where ξ is set equal to 4.

Natural frequencies

The modal analysis concerns the test pipe between the air vessel and the shut-off valve. This analysis is important to distinguish between the observed experimental frequencies that are related to the pressure reflections and those induced by the structural oscillation of the test pipe with or without the aluminum and PVC reaches.

Any structure with mass and elasticity will possess one or more natural frequencies of vibration (Blevins, 1979). The natural frequencies are the result of cyclic exchange of kinetic and potential energy within the structure. The modal analysis determines the vibration characteristics (natural frequencies and mode shapes) of a structure or a machine component.

The natural frequencies and mode shapes of the first 10 oscillation modes of the test pipe filled with water have been calculated using ANSYS software (ANSYS, 2008). The test pipe was modeled by using SOLID186 element type. The

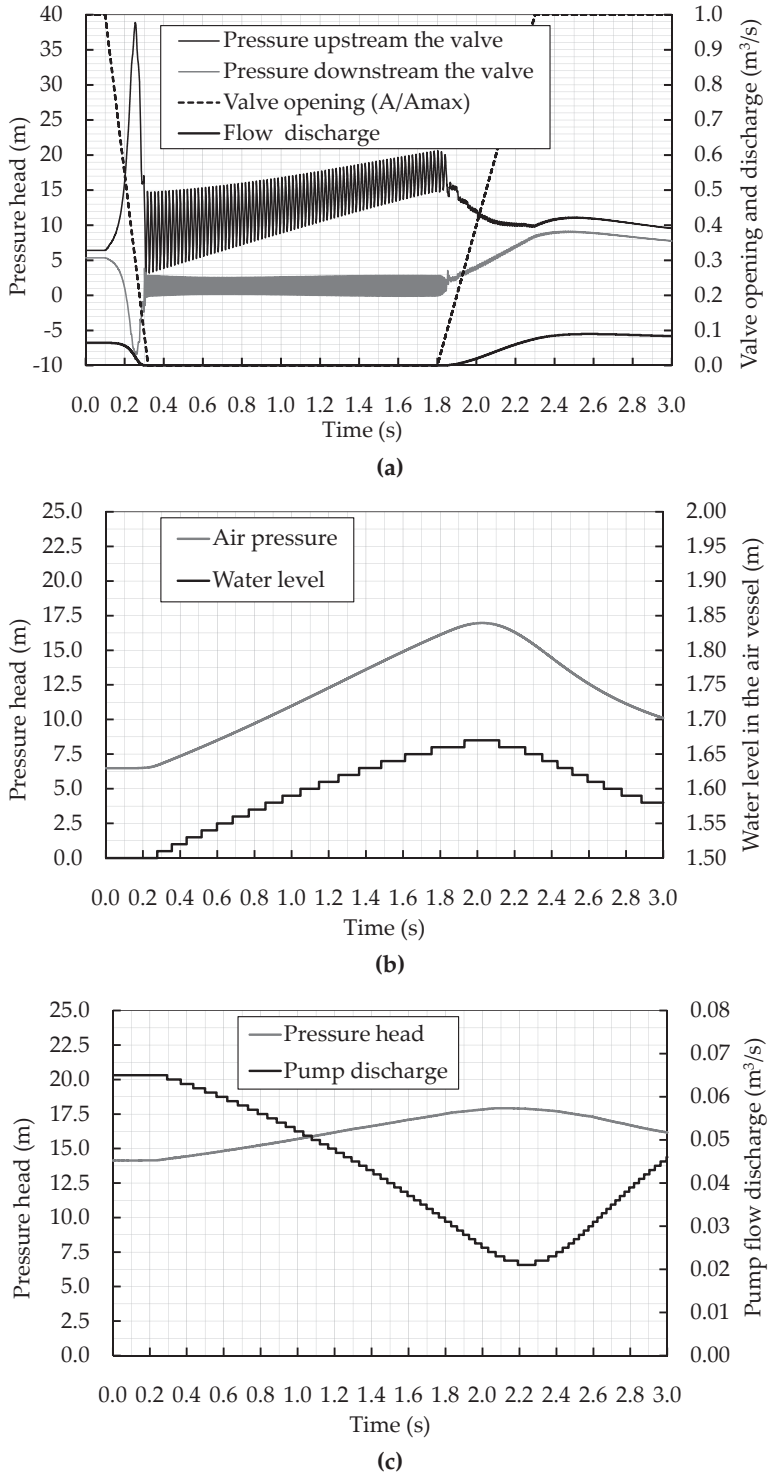

Figure 5.6: Numerical model results, (a) pressure transient at both upstream and downstream sides of the shut-off valve (right-hand scale), the closure and opening manoeuvres of the valve, and the flow discharge inside the model (left-hand scale), (b) air pressure and water level inside the pressurized air vessel, (c) pressure head and discharge at the pump output.

water inside the pipe was of type FLUID30 which can interact with the wall of the test pipe. The vertical supports were modeled by zero displacement constraints in the vertical and axial directions while the horizontal ones by zero displacement in the lateral horizontal direction. The both ends of the pipe including the two upstream and downstream faces of the fluid were considered as totally blocked without displacements nor rotations movements.

Figs. 5.7 show the 10 mode shapes of the steel test pipe without weak reaches. The natural frequencies for each of these modes and for "Steel+PVC" pipe configurations (configurations defined in Section 5.2) are shown in Fig. 5.8. The bubble size is proportional to the mass participation factor of each mode. Inside the frequency interval of interest $[f_{\min}, f_{\max}]$ in which $f_{\min} = a/(2\,L_T) = 78.5\,\text{Hz}$, $f_{\max} = a/(2\,\text{L}_{\min}) = 478\,\text{Hz}$, and $L_{\min} = 1.35\,\text{m}$ (the closest distance of the weak reach boundary to the air vessel), modes 2 to 5 for the "Steel+PVCs" configurations have very low participation mass with small differences between their frequencies. These modes correspond to the radial deformations of the PVC reach and show significant frequency decrease compared to the "Steel" configuration. The natural frequency of the 6^{th} mode is more or less the same for all PVC configurations. The first mode is a horizontal deformation of the pipe located mainly at the fourth pipe flask (air vessel side, Fig. 5.1) and is caused by the absence of horizontal support in the physical set up (site constraint caused by the presence of the existing steel frame). For this mode, the participation factor is high and the maximum difference of frequencies for the different pipe configurations is around 100 Hz. Nevertheless, the 1^{st} mode frequencies for the PVC configurations (189 Hz for "Steel+PVC1", 96 Hz for "Steel+PVC2", and 214 Hz for "Steel+PVC3") do not appear as peak frequencies in the experimental $\mathcal{F}$ graphs (Fig. 6.14) in Section 6.2.2.3 of Chapter 6. Therefore, it may be concluded that the observed experimental frequencies are related to the pressure reflections and not to the structural oscillation modes of the test pipe with or without the PVC reaches.

5.2 Test pipe configurations

As it was discussed in the description paragraph of Section 5.1.3.3, the weak reaches are modeled by using pipe wall materials having different $(E \cdot e)$ values than the rest of the test pipe, where E is the Young modulus and e is the thickness of the pipe wall. Aluminum and PVC reaches of $(E \cdot e) = 345\,\text{MN/m}$ and $15\,\text{MN/m}$, respectively, have been used. This consists in a local drop of stiffness of the pipe wall relative to steel of about 63 % in the aluminum case and near 98 % in the PVC case. A total number of 144 tests have been carried out on the twelve test pipe configurations shown in Fig. 5.9. For each configuration, 12 repetitive tests have been performed.

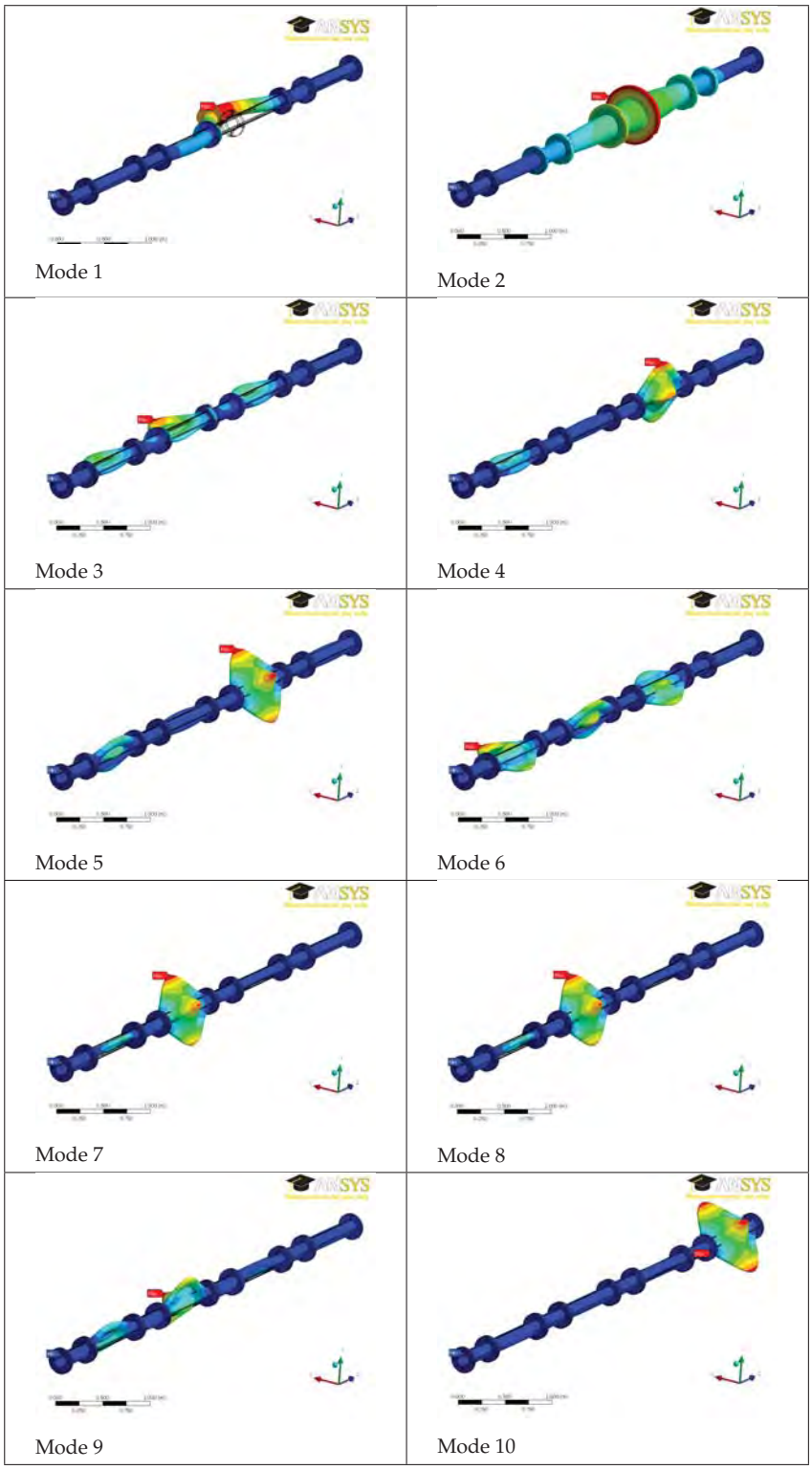

Figure 5.7: Natural mode shapes (10 first modes) of the "Steel" configuration of the test pipe determined from numerical modal analysis.

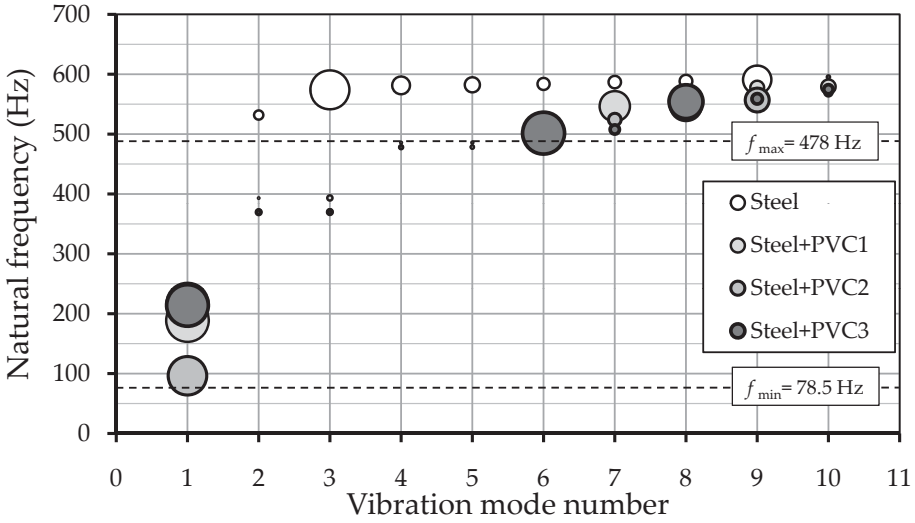

Figure 5.8: Natural frequencies of the test pipe determined from numerical modal analysis for the "Steel" and "Steel+PVC" pipe configurations as defined in Section 5.2.

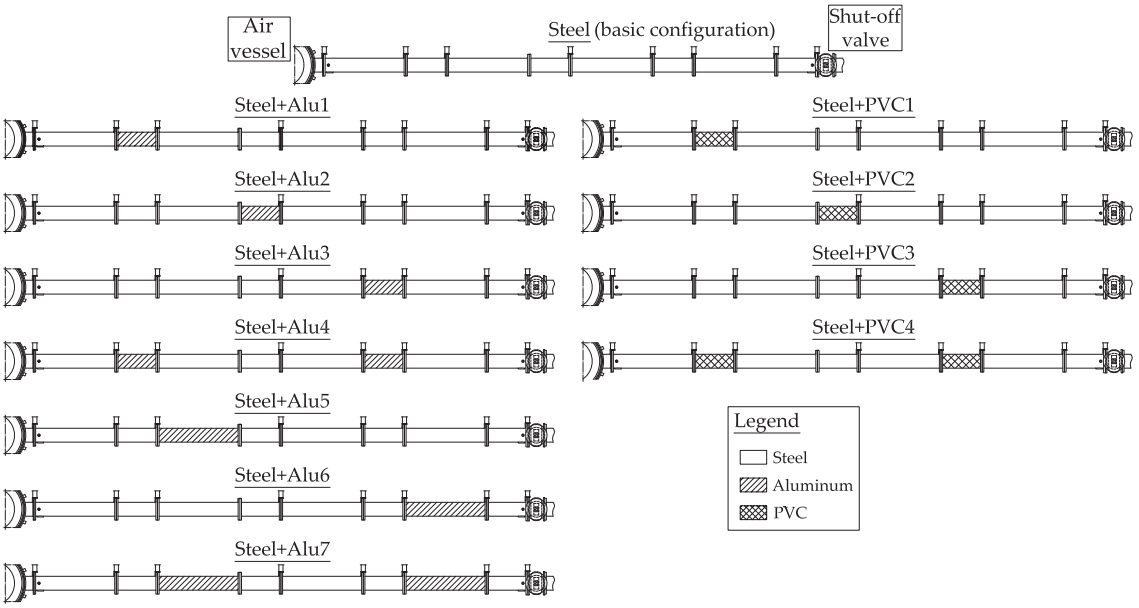

Figure 5.9: The twelve different configurations of the test pipe.

5.3 Test instrumentation and data acquisition

In the following paragraphs, the test instrumentation and measurement techniques to control the set-up facility and acquire data during tests are presented. They include the sensors description and calibration, the signal conditioning, the data acquisition hardware and software, and the data storage procedure.

5.3.1 Pressure sensors

A total number of eight calibrated pressure transducers of type "kulite HKM-375(M)-7-BAR-A" with an absolute pressure range of 7 bars and a maximum error of 0.5 % have been used to measure the pressure transients inside the test pipe. The DC electrical excitation current of 12 V needed for these sensors has been provided by a linear AC/DC power supply of type "GWinstek, GPD-3303S". These sensors have been calibrated in LMH by using a high precision (± 0.1 %) "Huber" transducer. The calibration procedure and results are given in Appendix C.

5.3.2 Geophones

The geophone is relatively a simple sensor that has a suspended moving coil around a permanent magnet (Figs. 5.10a and 5.10b). When the coil moves relative to the magnet, a voltage is induced in the coil according to Faraday law. The induced voltage is proportional to the relative coil-magnet velocity and the proportionality factor is known as the sensitivity G. This type of sensors is cheap, passive (no need for power supply), and has good linearity. It is usually used in seismologic survey to detect refraction and/or reflection from subsurface formations after generating a surface disturbance by explosives or other means. It has been also used in leak detection monitoring of shallow underground pipelines by allowing users to scan the entire length of the inspected pipelines and to hear the noise coming up from the leak (Mays, 2000).

Two geophones of type "I/O Sensor Nederland, SM-6 4.5 Hz 3 500 Ω" having the response curves shown in Fig. 5.10c have been used in the experimental set-up. They have been screwed on the lower exterior face of the test pipe wall (Fig. 5.1). These geophones are unidirectional and have different sub-categories depending on their use in the horizontal (SM-6/HB), vertical upward (SM-6/UB), and vertical downward (SM-6/SB) directions. The latter type has been used to measure the radial vibration of the test pipe wall at its both ends (Fig. 5.1). Table 5.3 shows the test pipe configurations and the number of repetitive tests in which the geophones data are available.

5.3.3 Flow meter

A "Proline Promag 50, Endress+Hauser" electromagnetic flow meter with analogue output signal (in mA) has been mounted on the new supply conduit to

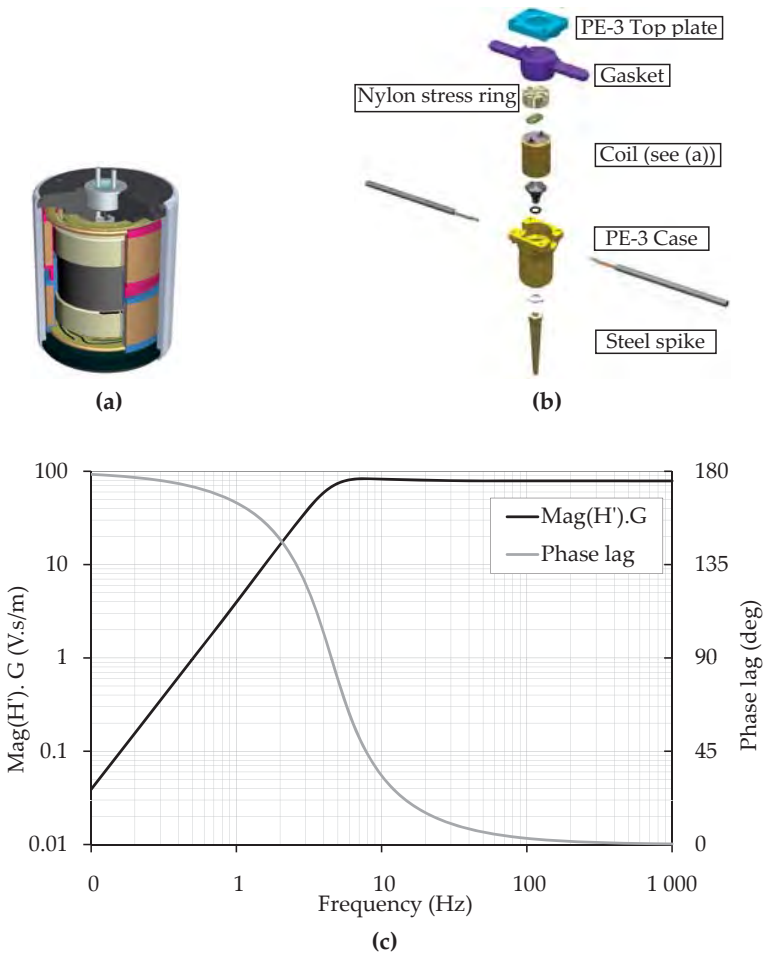

Figure 5.10: Geophone sensor, (a) photo of the moving coil, (b) the different components of the "SM-6/SB 4.5 Hz 3500 ohm" geophone type, (c) geophone response curves where Mag($H^{'}$) is the magnitude of the complex function $H^{'}$ (Appendix D) (source: www.iongeo.com).

measure the steady-state flow inside the facility (Fig. B.5a). The output electric current is transformed first to voltage through a 500 Ω resistor and then to flow in l/s according to the linear relation: $q\,(\mathrm{l/s}) = -10\,q\,(\mathrm{Volt}) + 21.5$.

5.3.4 Control equipments for the shut-off valve

As it was stated earlier in Section 5.1.3.2, the shut-off valve is equipped with a pneumatic air jack which is activated by an electro-distributor valve. The latter is controlled by the LabVIEW software through the acquisition card. An electrical signal $(0 - 10\,\mathrm{V})$ sent from the analog output channel of the acquisition card, switches on a 220 V electric relay which opens the input valve of the electro-distributor. After a defined duration, a second voltage signal is sent again from the card to a second relay to activate the output of the electro-distributor valve.

Table 5.3: Availability of the geophone data for each test pipe configuration.

Test pipe configuration	Geophone data availability	Number of tests
Steel	✓	6
Steel+Alu1	✓	6
Steel+Alu2	✓	6
Steel+Alu3	✓	6
Steel+Alu4	✗	-
Steel+Alu5	✗	-
Steel+Alu6	✓	6
Steel+Alu7	✗	-
Steel+PVC1	✓	6
Steel+PVC2	✗	-
Steel+PVC3	✓	6
Steel+PVC4	✗	-

The opened and closed states of the shut-off valve are detected by the two infrared diffuse sensors which are supplied by 12 VDC current. When the small cantilever plate fixed on the sliding axis of the valve is in front of the upper diffuse sensor (Fig. B.6b), the infrared beam is reflected back to the sensor and the output voltage is zero. It changes to 12 V when the cantilever plate leaves its position. The lower sensor reacts in the same manner as the upper one. The output signals of the two diffuse sensors are sent to LabVIEW software via the analog inputs of the acquisition card.

5.3.5 Acquisition card

The acquisition card is a "NI-USB-6259 M series" with 32 analogue input channels (16-bit, 1.25 MS/s) and 4 analogue output channels (16-bit, 2.8 MS/s). The maximum voltage range of the input and output signals is ± 10 V. This card is a USB high-speed multifunction DAQ module optimized for accuracy (range accuracy$=$ 1.92 mV) at fast sampling rates. A full technical description of this type of acquisition card can be found on the website: www.ni.com. During the tests, the sampling frequency, f_{samp}, has been taken equal to 20 kHz.

5.3.6 Data acquisition software

The data acquisition software uses the LabVIEW (Laboratory Virtual Instrumentation Engineering Workbench) programming platform developed by National Instruments. It is a very efficient tool to automate the usage of processing and measuring equipment in laboratory experimental facilities. The programming language used in LabVIEW is a dataflow programming language based on a graphical block diagram on which the programmer connects different function-

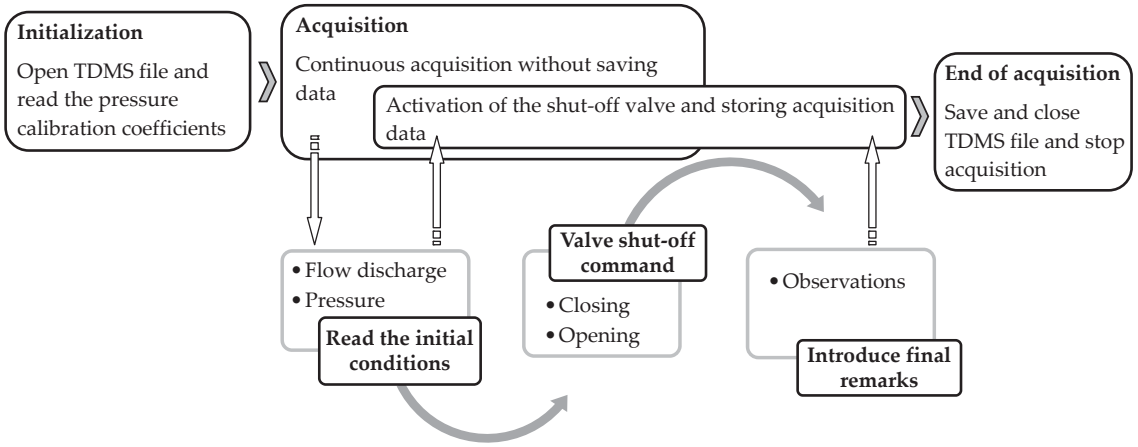

Figure 5.11: Scheme of the bloc diagram of the acquisition LabVIEW code for the experimental tests.

nodes by drawing wires. The information carried out by variables propagate through these wires from downstream towards upstream nodes. Each node executes its code as soon as all its input data become available. LabVIEW programs/subroutines are called Virtual Instruments (VIs). The interaction between the user and the software is provided by a user interface called front panel.

The main part of the acquisition program has been prepared during a Master project (Bustamante, 2009) carried out at the Laboratory of Hydraulic Constructions. The block diagram of the acquisition code is summarized in Fig. 5.11. It is composed of three main sequences:

- **Initialization:** The acquisition code starts with the opening of a data storage file of format TDMS and asks the user to assign a name and a save path to it. TDMS file type is a binary-based format which has a small disk footprint and can stream data at high speed. It is structured using three levels of hierarchy: file, group, and channel as shown in Fig. 5.12. At each level of the hierarchy, it is possible to store an unlimited number of custom scalar properties. Each level accepts an unlimited number of custom-defined attributes to achieve well-documented and search-ready data files. The TDMS files can be read by many applications such as Microsoft Excel, OpenOffice, and DIAdem. During initialization, the software reads the calibration coefficients of the pressure sensors.

- **Acquisition sequence:** It is the central part of the acquisition software. Once the TDMS file is initialized, the data acquisition is launched automatically according to initial default sample rate and sample buffer size. The acquisition type is continuous and the sample rate and buffer size can be adjusted in an interactive way. The front panel button of the valve closure and data

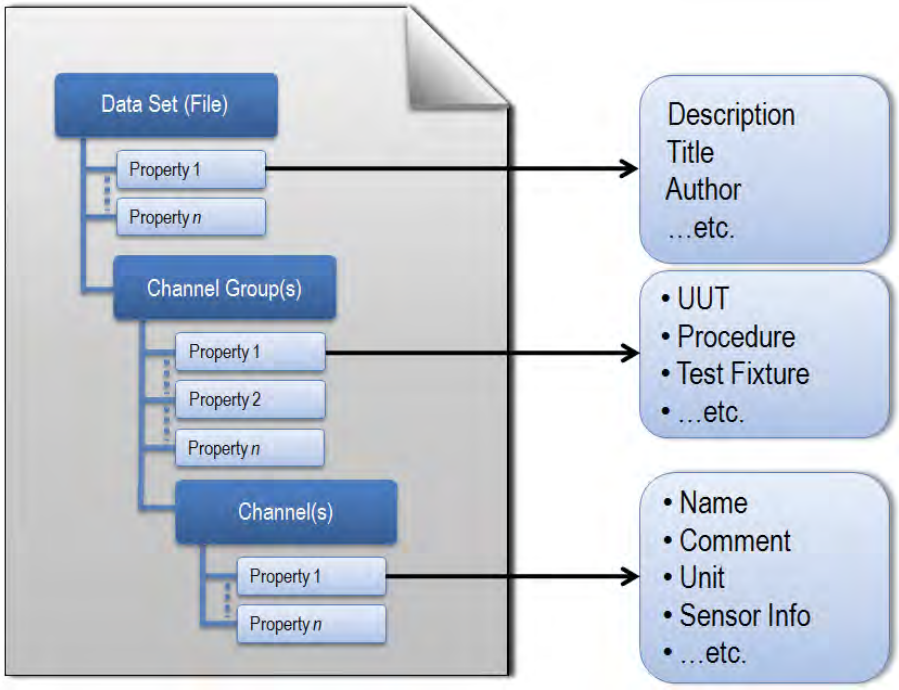

Figure 5.12: TDMS file hierarchy and attributes (source: www.ni.com).

storage sub-sequence will become active after the insertion and validation of some data file attributes and test parameters. Two groups of test parameters should be manually introduced and validated while the third one needs only to be validated. The third group contains the steady-state discharge (read from the flow meter) and the steady-state pressure at the upstream end of the test pipe (read from the pressure sensor P2 (Fig. 5.1)). The three groups of the test parameters can be listed as follows:

Group 1
- Operator name
- Number of the carried out test
- Photo of the pipe configuration that is being tested
- Material type of the pipe reaches used in the test
- Positions of sensors along the test pipe

Group 2
- Pump speed
- Duration in which the shut-off will be closed
- Acquisition sample rate and buffer size
- Acquisition duration after the end of the valve opening

Group 3
- Initial discharge
- Initial pressure head

- **Saving and closing the data file:** The acquisition code ends automatically after the collapse of the duration from the end of the valve opening manoeuvre. The user can write eventual final remarks and activate the "write and close" button which closes the data storage file and stops the acquisition sequence. The data have been saved in two TDMS groups. The first group contains the output signals of all sensors in Volt while in the second group the signals have been converted to the appropriate units according to their calibration laws.

A print screen of the front panel of the acquisition program is shown in Fig. 5.13.

5.4 Test procedure

The test procedure for each series of 12 tests carried out on each of the test pipe configuration begins with the closing of the two control valves. This is followed by the dewatering of the test pipe through the two purge valves. The first purge valve is placed directly at the downstream side of the shut-off valve while the second one is situated at the bottom of the air vessel. During the emptying of the test pipe, the air pressure inside the vessel is balanced with the atmospheric pressure by opening the 1/2 inch diameter valve placed at the top of the air vessel. Once the test pipe is empty, the two purge valves are closed.

The next step is the construction of the test pipe configuration. The bolts connecting the pipe reach which needs to be replaced are unscrewed, as well as, all the bolts which are used to fix the pipe flanges to the supports situated downstream from this reach. This downstream part of the pipe is pushed towards the supply reservoir by using screws connected to the vertical supports. The pipe reach is replaced and all the parts of the test pipe are fitted again together and to the horizontal and vertical supports.

The slowly filling of the test pipe with water is done by opening the two control valves of the test rig. The volume of water lost during the dewatering of the pipe is recovered by the laboratory supply conduit connected to the supply reservoir. During filling, the valve placed at the top of the air vessel is closed once the water level reaches a pre-defined mark. The filling procedure ends when the water surface inside the supply reservoir reaches the level of 2 m measured from the top of the floor slab. The air pressure inside the vessel is around 0.15 bar.

The pump is started up and its rotation speed is adjusted to have a flow discharge in the test rig equal to 6 l/s. The air purge valve placed at the highest point of the existing supply conduit is opened for a duration of around 1 minute. At the end of this step, a steady-state flow regime is established inside the experimental facility.

The final step of the test procedure is the generation of water-hammer inside the test pipe. The acquisition software is launched by using a notebook computer connected to the acquisition card through a USB cable. The test parameters are

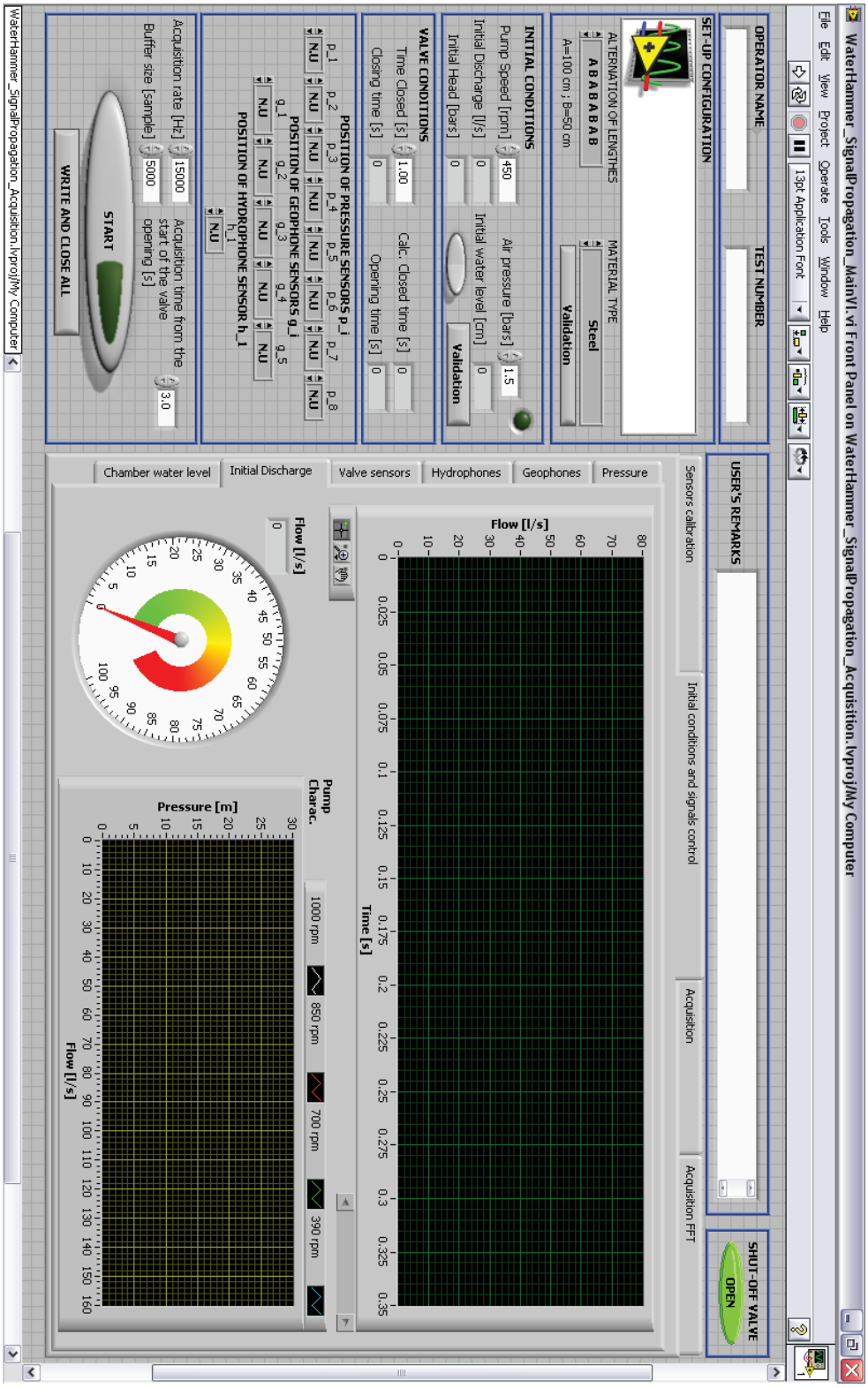

Figure 5.13: Front panel of the acquisition program for the experimental tests.

introduced and validated according to the procedure described in Section 5.3.6. The pressure inside the air compressor is set manually to 10 bars and the "Start" button of the LabVIEW front panel is pushed. This button activates the shut-off valve closing and opening manoeuvres and the storing of the acquired data.

The data files were stored inside directories named according to the dates in which the tests have been carried out. These tests directories are saved within other mother directories which have the names of the corresponding test pipe configurations shown in Fig. 5.9.

Chapter 6

Analysis of the experimental data

In this chapter, the experimental results are presented, analyzed and discussed. New monitoring approaches for detecting, locating and quantifying structurally weak reaches of steel-lined pressure tunnels and shafts are presented. These approaches are based on assessing the pressure and vibration records acquired at the both ends of the multi-reach test pipe. The weak reaches arise from local deterioration of the backfill concrete and the rock mass surrounding the liner. The change of wave speed generated by the weakening of the radial liner supports creates reflection boundaries for the incident pressure waves.

The first section presents the experimental results of pressures and vibrations. Two signal windows for the data analyses are defined.

In the second section, a monitoring approach based on the generation of transient pressure with a steep wave front is proposed. It analysis the reflected pressure and vibration signals using the Fast Fourier Transform and wavelet decomposition methods. The influence of local drop of wall stiffness of pressurized waterways on the pressure wave speed and wave dissipation during transients is also investigated.

The third section introduces a second processing procedure based on assessing transients generated by the progressive stoppage of the flow by the shut-off valve.

The fourth section presents the uncertainty analysis for the test results and the fifth section formulates the conclusions of the chapter.

Different parts of the monitoring methods presented in this chapter have been published in Hachem and Schleiss (2011a and 2011b) and as conference papers in Hachem and Schleiss (2010, 2011f, and 2011d).

6.1 Experimental output data

Figures 6.1a, 6.1b, and 6.1c show, respectively, the outputs of the diffuse sensors (in Volt), the flow discharge inside the supply conduit (in m^3/s), and the pressure signals P1 and P2 (in bars) for one experiment carried out on the "Steel"

configuration of the test pipe. The flow discharge inside the test rig is rather constant between the beginning of the test and the re-opening of the shut-off valve. It decreases to around 60 l/s at the end of the acquisition time. The pressure P1 reaches its maximum value of 3.2 bars at the end of the closure manoeuvre of the valve. The closure and the re-opening of the shut-off valve are followed by pressure transients with low frequency ($f \approx 26\,\text{Hz}$) caused by the mass oscillation between the air vessel and the supply reservoir. After the end of the valve closure, the two elbows and the elastic joint between the shut-off valve and the supply reservoir vibrate. This induces an important pressure variation inside the test pipe. Therefore, only the test measurements that are acquired before this peak are relevant, and therefore, they have been analyzed herein.

Typical time histories of normalized pressures (P1 and P2) and geophones (G1 and G2) are shown in Figs. 6.2a and 6.2b. The pressure signals inside the window W1 are generated at the beginning of the valve closure by the external pressure excitation caused by the impact of the air inside the jack of the valve. These pressure fluctuations die out after 0.045 s from the beginning of the valve closure. This defines the lower time border of a second window, W2, in which the progressive stoppage of the flow by the valve generates water-hammer pulsations inside the test pipe. The upper time border of W2 was fixed after 0.16 s from the start of the valve closure. Beyond this time, the series of no flow tests has revealed the presence of an important pressure drop followed by high-amplitude and high-frequency fluctuations caused mainly by the valve (Section 5.1.3.2).

6.2 Monitoring approach based on steep front transient waves

6.2.1 Pressure excitations

The transient pressure excitations inside the water must have enough energy in the wave front to interact with the surrounding walls of the structure even after dissipation during longitudinal propagation. In a hydropower plant, such excitations are generated by the change of the flow rate at the pumps or turbines. Consequently, a water-hammer propagating along the conveying system occurs (Chaudhry, 1987; Parmakian, 1963). These excitations are repeated many times a day when synchronizing the energy production to the grid demand. Therefore, with a monitoring method based on processing of this type of water transient pressure, a large data base can be acquired. Depending on the flow rate change, a water-hammer with steep front can be generated. Nevertheless, the localization of weak zones becomes difficult for rather slow changes of flow rate. In this case, the rising front slope of the incident pressure wave becomes less steep as well as the slopes of the partially reflected pressure signal coming back from the weak reach boundaries.

Another artificial type of water pressure excitation could be produced by an explosive shock wave generated in water near the reservoir's intake structure

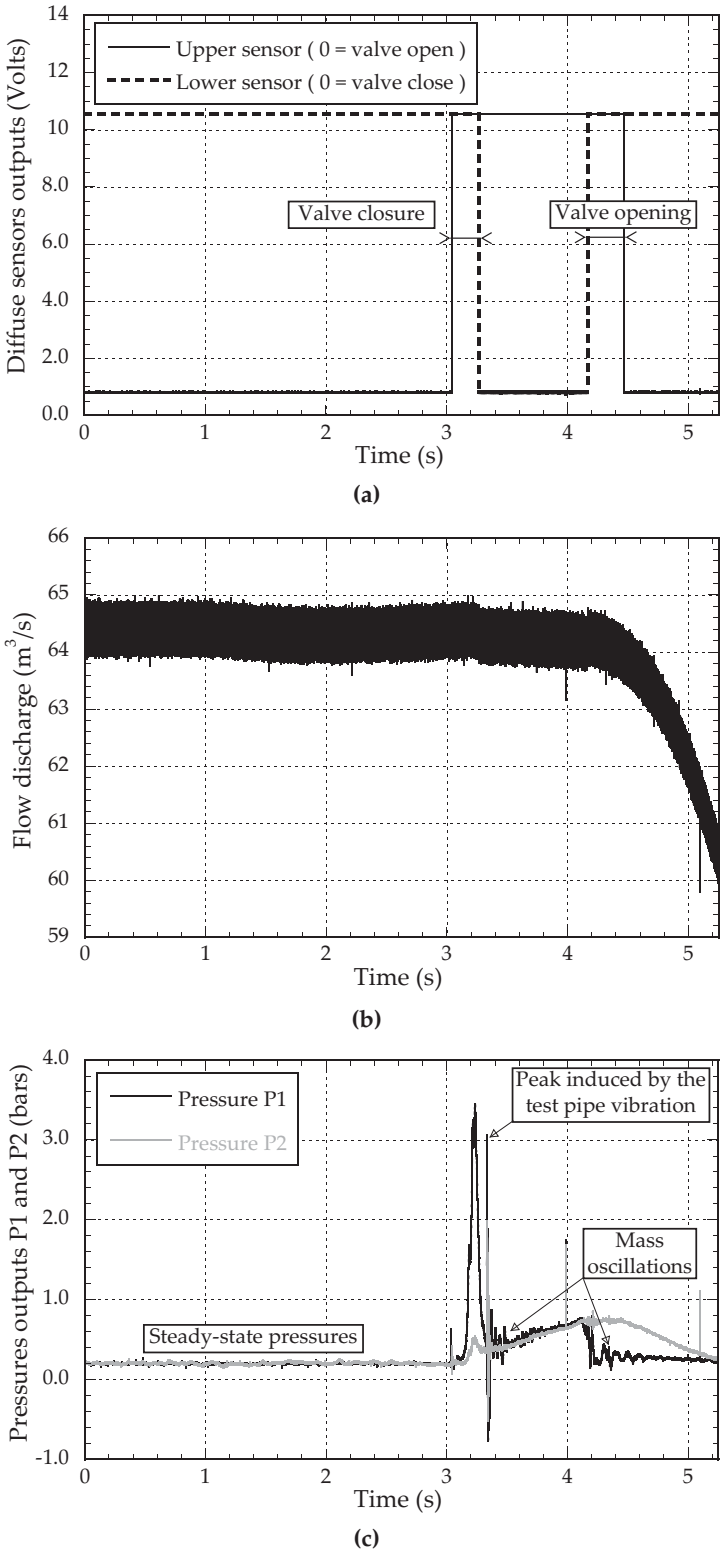

Figure 6.1: Output test records for "Steel" pipe configuration, (a) diffuse sensors of the shut-off valve, (b) flow discharge, and (c) pressures P1 and P2 at the both ends of the test pipe.

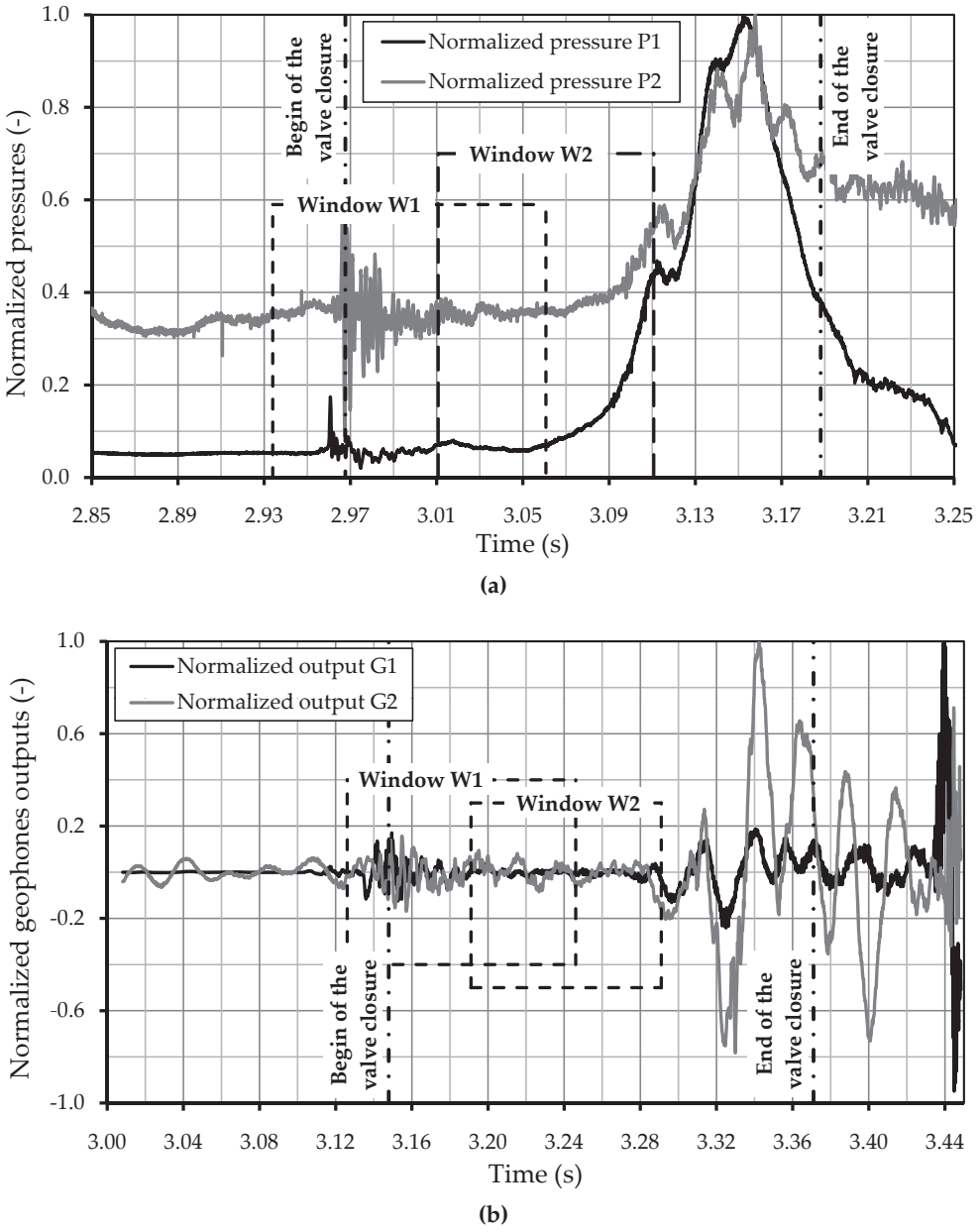

Figure 6.2: Typical records of the experimental transient data at the both ends of the test pipe, (a) pressures and (b) geophones outputs.

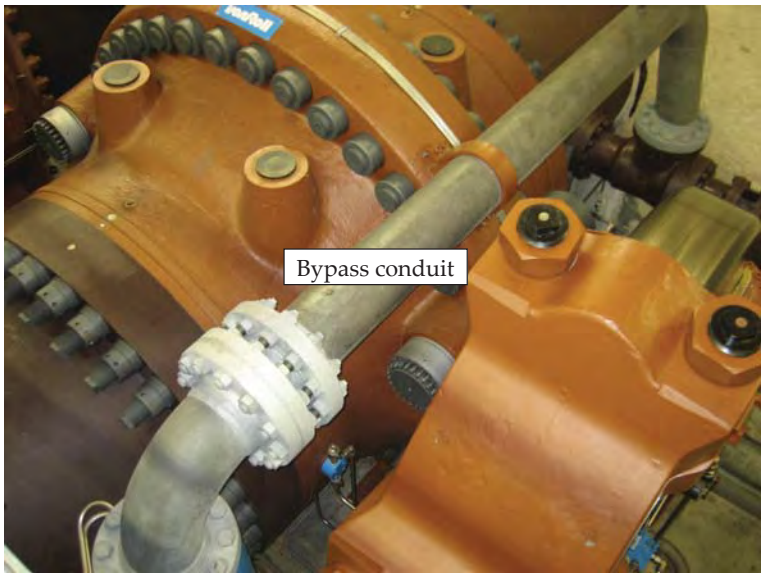

Figure 6.3: Spherical control valve and its bypass conduit in Grimsel II power plant (photo: F. Hachem).

or near the tunnel–shaft junction inside the surge tank. This type of excitation is more risky and complicated to produce than the water-hammer phenomenon resulting from normal operations. Furthermore, the monitoring of shafts and tunnels would have only a limited number of in-situ data measurements. The main advantage of such artificial excitation, in comparison to water-hammers, is the possibility of generating an incident wave with a steep front, allowing more accurate localization of the weak zones.

In hydro plants, the inlets of turbines are generally equipped with spherical control valves (Fig. 6.3). These valves are bypassed by conduits which are used to balance the water pressure between their both sides before starting the opening manoeuvres. The generation of transients with steep wave front could be also generated by a rapid shut-off valve placed on these bypasses.

In this section, the processing of the transient pressure of laboratory experimental data produced by a steep wave excitation is analyzed.

6.2.2 Localization of the weak reach based on wave timing

The location of a weak reach of steel-lined pressure tunnel can be determined on the basis of the timing of pressure wave reflections that occur at the boundaries of this reach. The travel times of these transient waves can be found by using pressure measurement sampled at high frequency at two points of the waterway. For steel-lined pressure tunnels and shafts, these points are restricted to the accessible reaches of the steel liner. They are normally located inside the valves chambers situated downstream of the reservoir intake, downstream of the surge tank, and

at the entrance of the power house. The travel times are then transformed to distances or wave path lengths using the simple formula:

$$l = \frac{a\,t}{2} \tag{6.1}$$

where, l is the distance between the pressure sensor and the boundary of the weak reach, a is the front wave speed in water and t is the travel time that an incident wave needs to travel from the pressure sensor towards the boundary of the weak reach and to come back, after reflection, to the same sensor's position. In order to localize the weak reach, a good estimation of the front wave speed and of the incidence–reflection travel time is required.

6.2.2.1 Estimation of the front wave speed based on pressures data

Three time-based approaches are used to estimate the time needed by the water wave front to travel from the upstream pressure position (P1) to the downstream one (P2). The upstream and downstream nomenclatures for pressure positions or data, P1 and P2, are defined according to the direction of the first incident wave h_i (Fig. 3.1). The values of the front wave speed are then extracted by dividing the known distance separating the two sensors by the estimated travel time.

The first approach extracts the time that separates the maximum values of the front pressure measurements. The second approach determines, for each pressure record, the time at the intersection point of two regression lines correlating the steady-state and the first front pressure data, respectively. The third approach uses the cross-correlation technique (Section 3.2.4) to calculate the time-lag which separates the front wave lobes of P1 and P2 data.

A unique value of the front wave speed is finally retained for each test. It is the one of the three wave values obtained from the three approaches which is bounded by the two others (median value). The maximum relative difference between the wave speed values computed according to the three methods is around 11 %.

For comparison purpose, the same procedure presented above has been applied to estimate three reference wave speeds inside the different pipe reaches made of steel, aluminum and PVC materials (Fig. 6.4). The data acquired from two pressure sensors placed inside the pipe reach at 60 mm from each of its end have been used. The results are in very good agreement with the theoretical values determined from Eq. (4.42). Also, the geometric mean of the wave speed inside each test pipe configuration was determined based on the reaches' lengths and the estimated mean wave speeds shown on Fig. 6.4. These geometric means are depected as dashed lines in Figs. 6.7 and 6.26.

In Fig. 6.5a eight records of the transient water pressure, P1, for the eight "Steel" and "Steel+Alu" configurations of the test pipe are shown. These transient pressures are caused by the impact of the pressurized air on the jack piston. This excitation is transmitted to water inside the test pipe by means of the jack

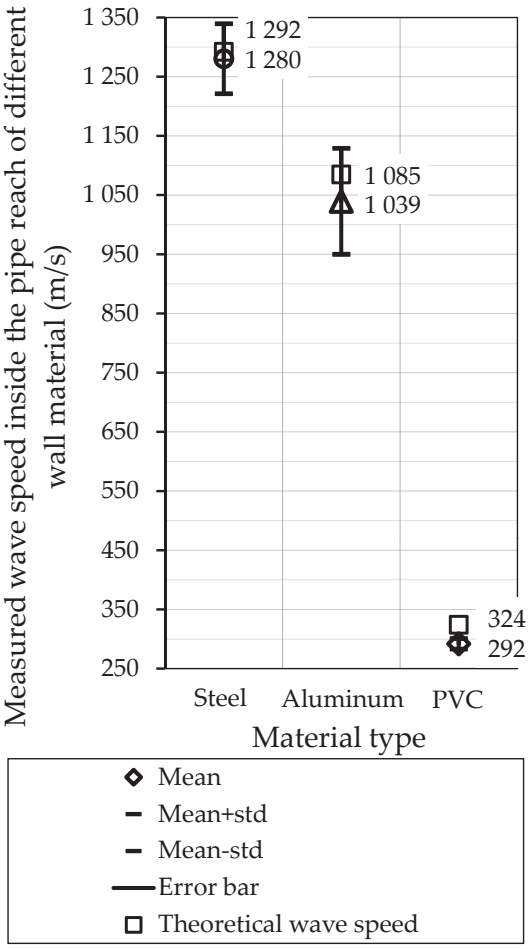

Figure 6.4: Mean and standard deviation of wave speed estimated by pressure measurements inside three pipe reaches made of steel, aluminum and PVC materials. The theoretical wave speed values given in Table 5.1 are also shown.

axis. Fig. 6.5b depicts the eight pressure signals, P2, for the same tests. The pressure histories P1 and P2 for the "Steel+PVC" configurations are shown in Figs. 6.6a and 6.6b, respectively.

The front wave speeds a of all the 144 tests have been computed using the three approaches presented in Section 6.2.2.1. In Fig. 6.7, the mean and the standard deviation of a for each pipe configuration are shown. The highest standard deviation value of 42.3 m/s corresponds to the "Steel+Alu4" configuration. This value is relatively high and it is caused by the low wave speed $(1\,050\,\mathrm{m/s})$ computed from the first test data of the series of 12 tests carried out on this configuration. For each series of experiments, the lowest speed value is obtained from the pressure data of the first test of the series. This phenomenon is due probably to a very small percentage of air which has been captured inside the test pipe and has disappeared when overpressure of the first water-hammer test have occurred.

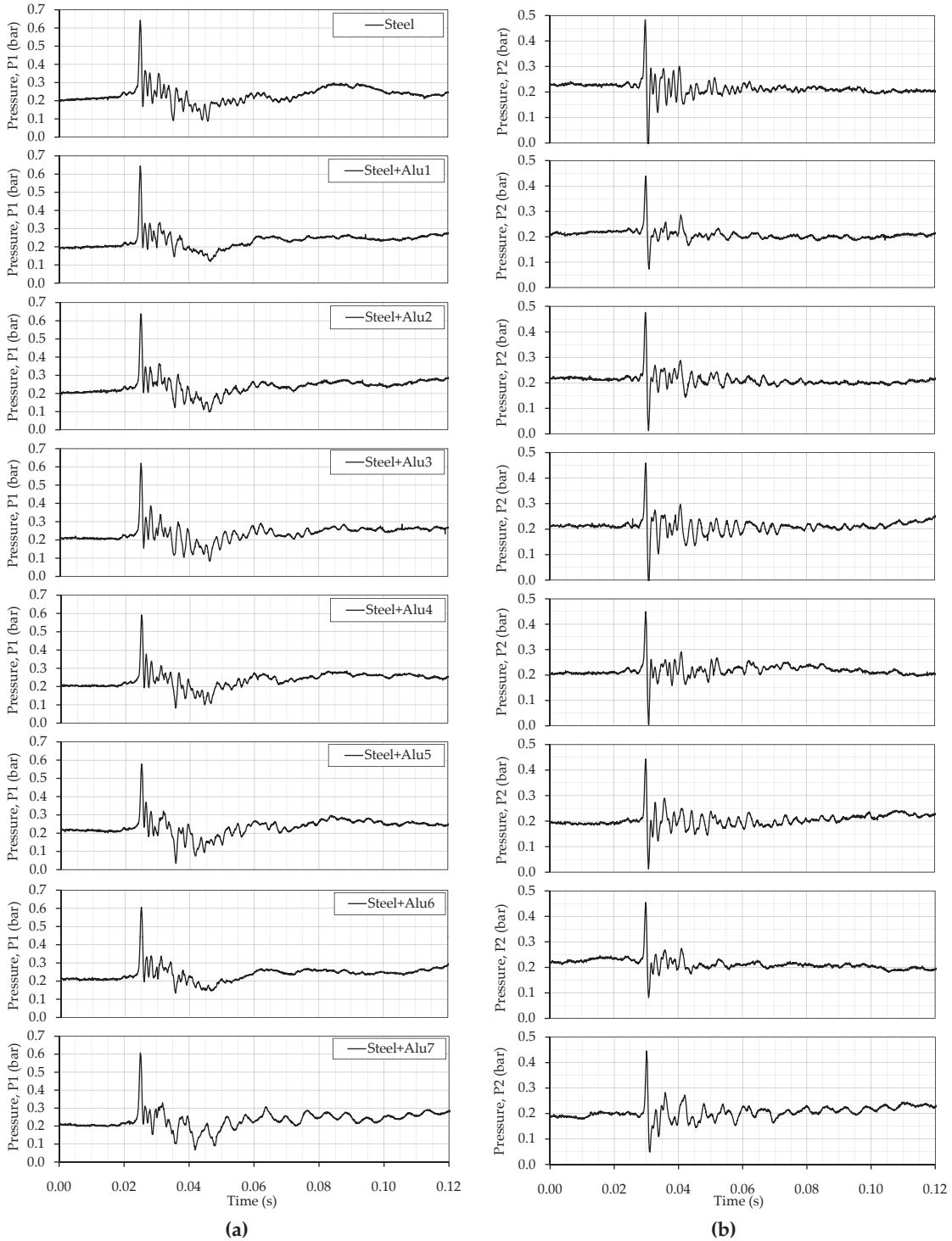

Figure 6.5: Example of pressure records for the "Steel" and "Steel+Alu" configurations of the test pipe, (a) P1 pressures and (b) P2 pressures.

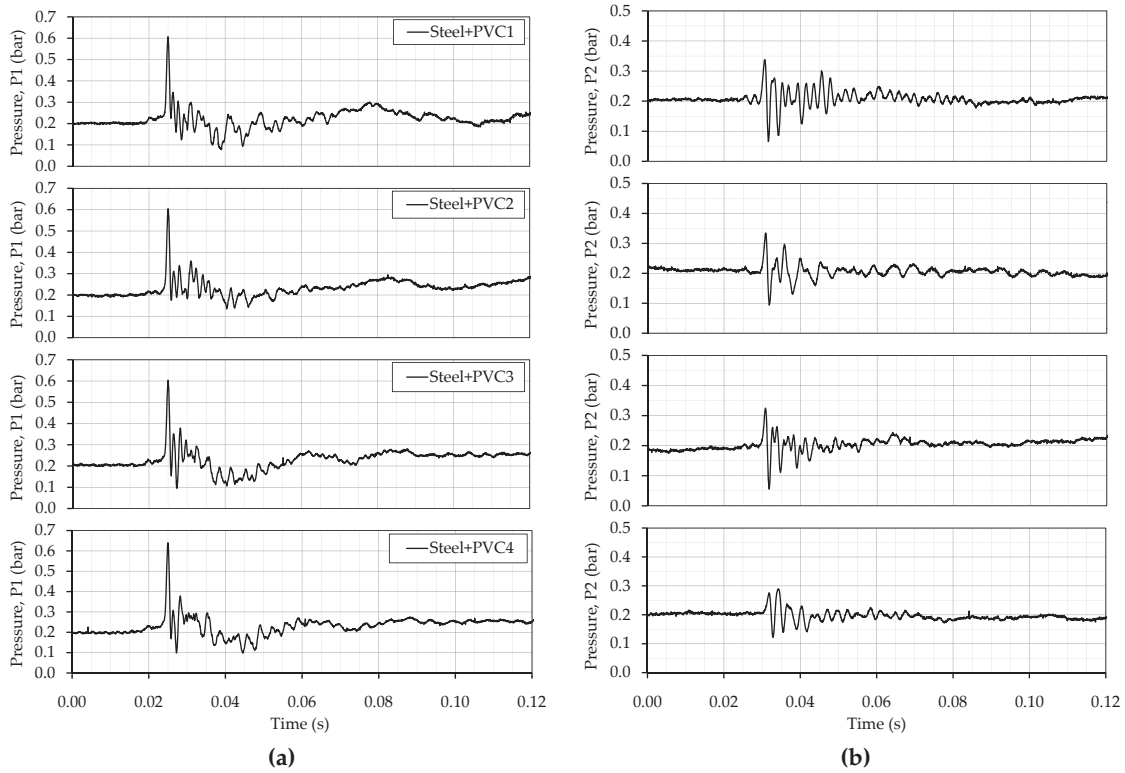

Figure 6.6: Example of pressure records for the "Steel+PVC" configurations of the test pipe, (a) P1 pressures and (b) P2 pressures.

For all the test pipe configurations, the geometric means of the wave speed are higher than the estimated wave speed values.

Based on the low to moderate values of the standard deviation and the clear differences observed between the mean wave speed of "Steel" and "Steel+PVC" configurations (16 % for the "Steel+PVC1, 2, and 3" and 30 % for "Steel+PVC4"), it may be concluded that the wave speed computed according to the three approaches using the dynamic pressure records at both ends of the test pipe can be considered as a global indicator of large changes in the stiffness of the pipe wall. These relative changes $[(E \cdot e)_{\text{Steel}} - (E \cdot e)_{\text{PVC}}]/(E \cdot e)_{\text{Steel}}$ are around 98 %. This conclusion is consistent with previous statements in the literature (Hunaidi, 2006b). For the test pipe configurations with one 50 cm long aluminum reach having a $(E \cdot e)$ value equal to 345 MN/m, the drop of the wave speed values relative to the "Steel" configurations is small (around 1.6 %). In case of configurations with two 50 cm long or one 100 cm long aluminum reaches, the drop of wave speed is around 4.1 %. It reaches 6.5 % for the "Steel+Alu7" configuration.

The wave speed differences for each test pipe configuration relative to the basic "Steel" case are plotted in Fig. 6.8 as a function of the variable X defined as

$$X = L_{\text{WR}}/L_T + [(E \cdot e)_{\text{Steel}} - (E \cdot e)_{\text{WR}}]/(E \cdot e)_{\text{Steel}} \tag{6.2}$$

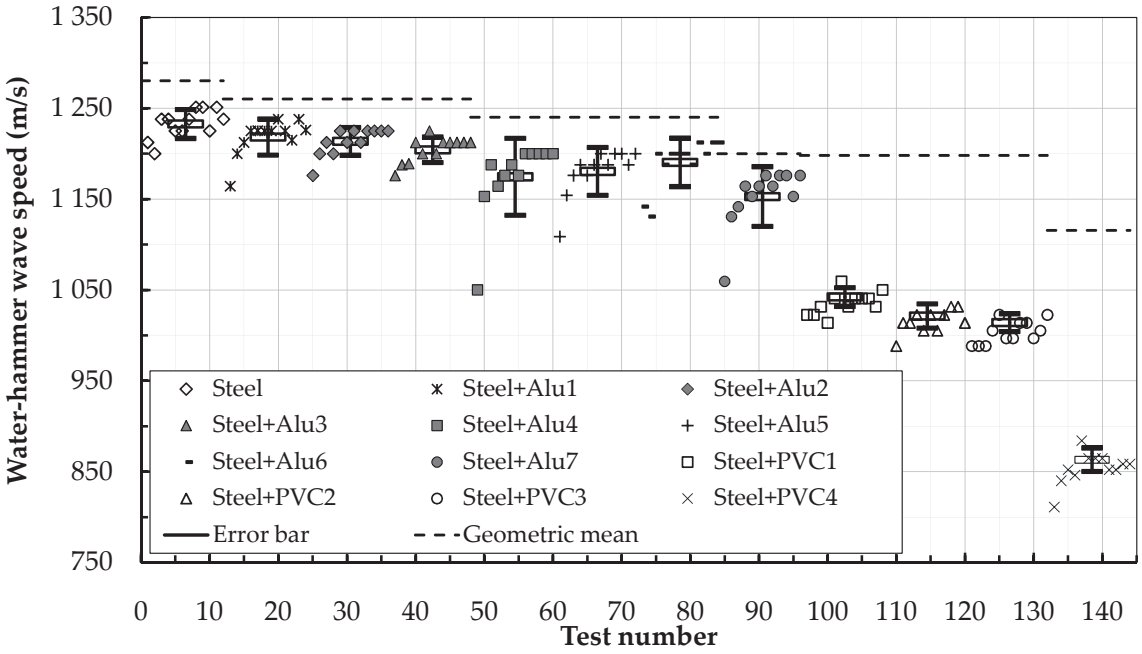

Figure 6.7: Water-hammer wave speed estimated from the pressure records in case of steep wave front shown in Figs. 6.5 and 6.6.

This variable indicates the importance of the stiffness weakness of the pipe wall.

An exponential regression line ($R^2 = 0.981$) with its 95 % confidence boundaries have been determined from wave speed data of all the pipe configurations except the "Steel" and "Steel+PVC4". The points relative to these configurations (0 % and 30 %) were used to verify the accuracy of the empirical formula

$$Y = 0.05157\, e^{5.537\, X} \tag{6.3}$$

in which, Y is the relative difference of the measured mean wave speed $(a_{\text{Steel}} - a_{\text{WR}})/a_{\text{Steel}}$.

6.2.2.2 Estimation of the front wave speed based on geophones data

The radial vibrations of the pipe wall were determined from the measurement of the two geophones G1 and G2 fixed on the exterior surface of the test pipe (Fig. 5.1). Hunaidi (2006a) developed an acoustic method based on cross-correlating two accelerometer signals to determine the wave speed in a water distribution pipe reach in purpose to extract its mean wall thickness from standard theoretical wave speed formulae (e.g. Eq. (4.42)). The advantage of the method developed herein consists in using geophones instead of relatively expensive accelerometers and their signal conditioning hardware.

The wave speed values obtained from processing the geophone output signals G1 and G2 measured inside window W1 (Fig. 6.2b) are compared to those esti-

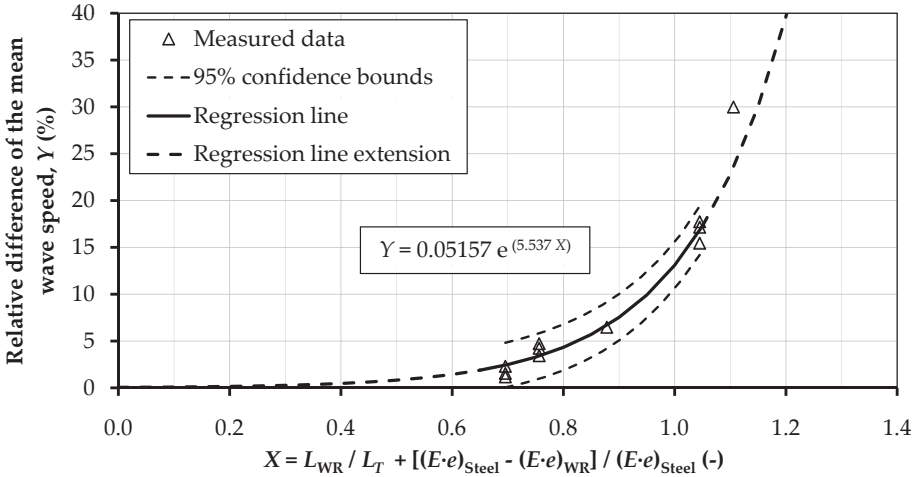

Figure 6.8: Empirical law relating the relative difference of the wave speed Y (defined in Eq. (6.3)), to the importance of the stiffness weakness of the pipe wall X (defined in Eq. (6.2)).

mated from pressure signals in Section 6.2.2.1. This comparison covers the test pipe configurations shown in Table 5.3.

The analysis starts by decomposing the two geophone signals using *Daubechies* (db10) mother wavelet (Section 3.2.5). Fig. 6.9a shows the time history of the detail D_4 for the geophone output G1 given in Fig. 6.2b. A significant amplitude increase can be observed at time $t_{1\max}$ when the wave front crosses the pipe section at G1. The full decomposition scheme is given in Figs. E.5 and E.6.

The signal detail is transformed to pipe surface displacement, u_r^s, according to the following transfer function, $H(f)$, obtained from the second order differential equation of motion of the damped mass of the geophone sensor (Appendix D):

$$H(f) = \frac{\mathcal{F}\left(\mathrm{G1}, 2\,[\mathrm{in\,Volts}]\right)}{\mathcal{F}\left(u_r^s\,[\mathrm{in\,m}]\right)} = \frac{-2\,\pi\,\mathrm{i}\,f^3\,G}{f_0^2 - f^2 + 2\,\mathrm{i}\,\zeta_G\,f_0\,f} \tag{6.4}$$

where f_0 is the natural frequency $(= 4.5\,\mathrm{Hz})$ and ζ_G is the damping ratio $(= 0.58)$ of the geophones, respectively.

The maximal computed radial displacement at time $t_{1\max}$ is compared to the theoretical radial displacement of the pipe wall determined according to the following tube formula without considering any longitudinal displacement

$$u_r^s = \frac{\triangle p\, r_i^2\,\left(1 - v_s^2\right)}{E_s\, e} \tag{6.5}$$

where $\triangle p$ is the pressure increase value at the wave front, r_i is the internal radius of the test pipe $(= 0.075\,\mathrm{m})$, v_s is the Poisson's ratio of steel $(= 0.3)$, and E_s and e are the elastic modulus and wall thickness of the steel pipe, respectively (Table 5.2).

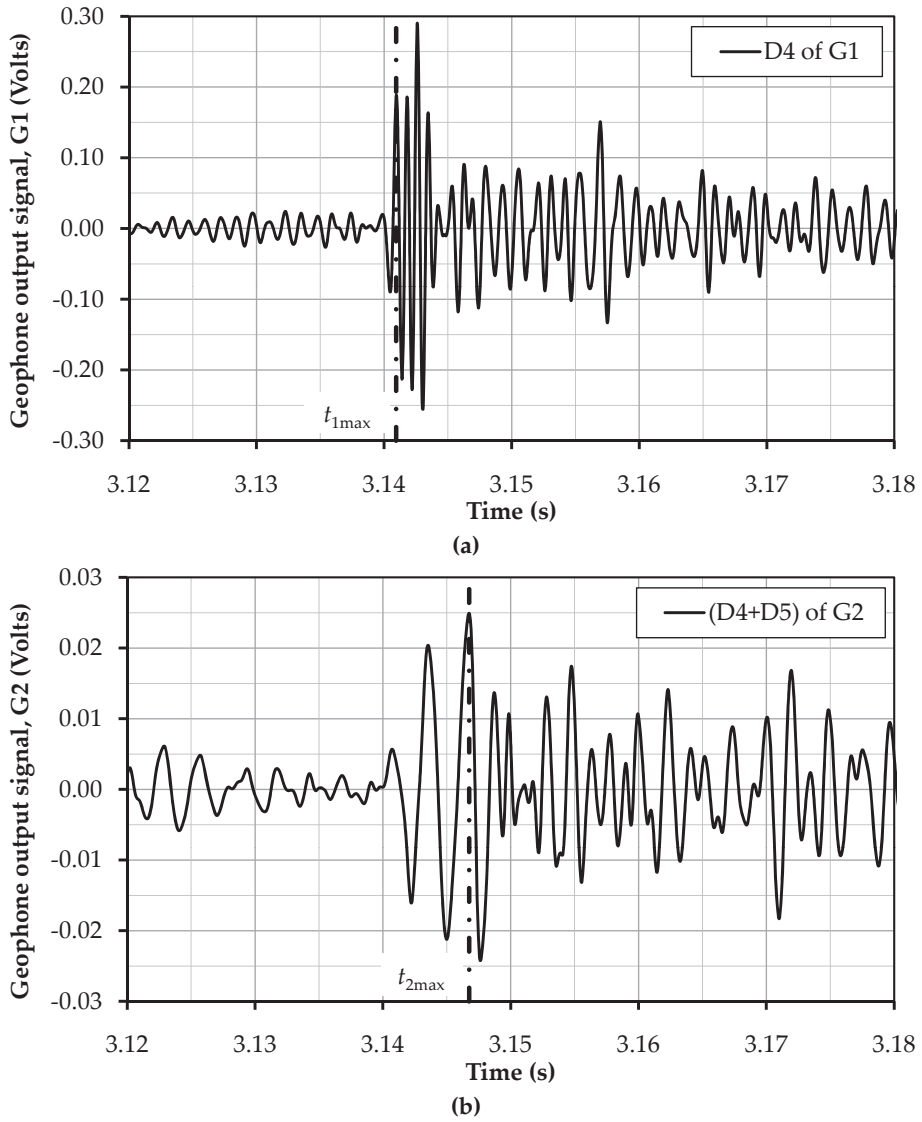

Figure 6.9: Wavelet details components of the geophones output signals shown in window W1 of Fig. 6.2b, (a) D_4 for geophone G1, (b) $(D_4 + D_5)$ for geophone G2.

The relative differences between the theoretical and computed radial deformations of the pipe wall are depicted in Fig. 6.10 for the six repetitive tests carried out on each of the seven pipe configurations. This comparison shows globally good agreement between the theoretical and computed deformations with a relative mean error around 18 % and proves that detail D_4 contains the most important part of the radial component of the pipe wall displacement. High relative differences are detected for the 6 tests carried out on the "Steel+Alu3" configuration (mean error = 38 %). The maximum relative difference reaches 74 % for one test on the "Steel+Alu6" case. It should be mentioned here that the geophones are very sensitive to pipe vibrations. These vibrations induce fluctuations in the geophones output signals before the significant amplitude increase caused by the water overpressure at time $t_{1\max}$. This can explain the high relative differences detected in some tests.

At geophone G2, the summation of details D_4 and D_5 was considered to identify the arrival time, $t_{2\max}$, of the water-hammer pressure wave (Fig. 6.9b). The full decomposition graphs are shown in Appendix E (Figs. E.7 and E.8). The time $t_{2\max}$ is determined from the first peak time of record $(D_4 + D_5)$ that gives a wave speed value between 800 and 1 400 m/s. The wave speed is computed according to Eq. (6.1) with $2l = L_{\mathrm{P1,P2}} = 5.88$ m and $t = t_{2\max} - t_{1\max}$. In Fig. 6.11, the comparison between the wave speeds estimated by the proposed geophone based method and pressure approach are shown for seven test pipe configurations. The wave speeds obtained from the geophone signals for the "Steel" configuration are about 80 m/s higher than those estimated from pressure measurements. The comparison points for the other pipe configurations lie close to the symmetric line except two points, one for the "Steel+PVC3" and the other for the "Steel+Alu6" configurations. In the latter configuration, the comparison points are also scattered and lie above the symmetric line.

In general, the results show good agreement between the two methods. The discrepancy in water-hammer wave speed in case of "Steel" configuration is probably caused by the interference of geophones with the stress waves traveling at high speed inside the test pipe wall. These waves are considerably attenuated by the presence of the PVC reach along the pipe. The scattering results for the "Steel+Alu6" pipe configuration are probably induced by the vibration of the test pipe.

6.2.2.3 Estimation of the incident-reflection travel time

A first approximation of the incident–reflection travel time is obtained by the Fast Fourier Transform $(\mathcal{F})$ applied to the pressure records P1 and P2. The $\mathcal{F}$ gives a global representation of the frequency content of these signals over the entire time domain. For the configurations with weak reach, peaks should occur at frequencies which correspond to the wave reflections issuing from the weak reach boundaries (Fig. 6.12).

In the second approach, the results of the $\mathcal{F}$ approximation combined with

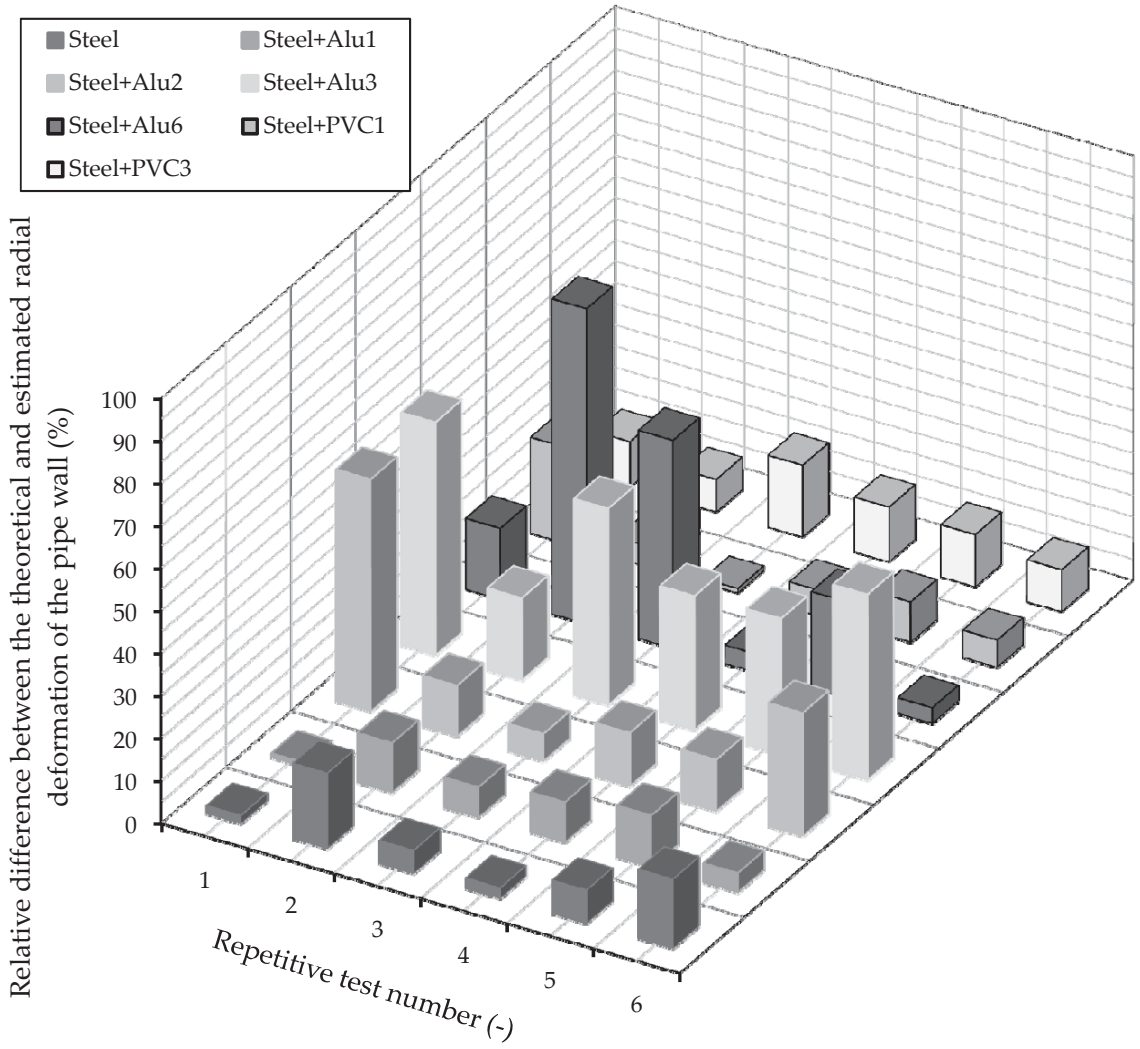

Figure 6.10: Relative differences between the theoretical and computed radial deformations of the pipe wall at section G1 for the six repetitive tests carried out on each of the seven pipe configurations.

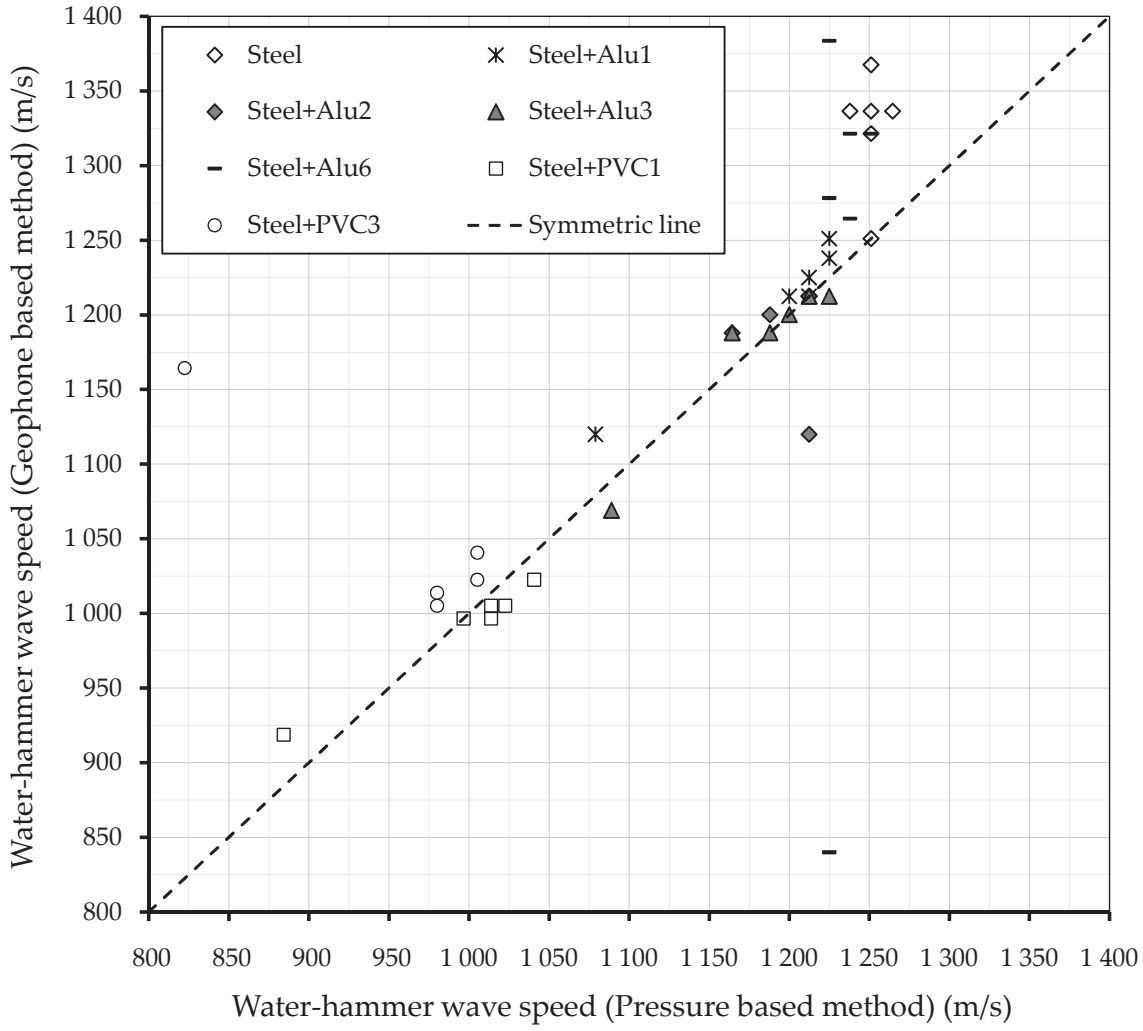

Figure 6.11: Comparison between the estimated wave speeds obtained by processing the geophone signals and the pressure records with steep wave front for seven different configurations of the test pipe.

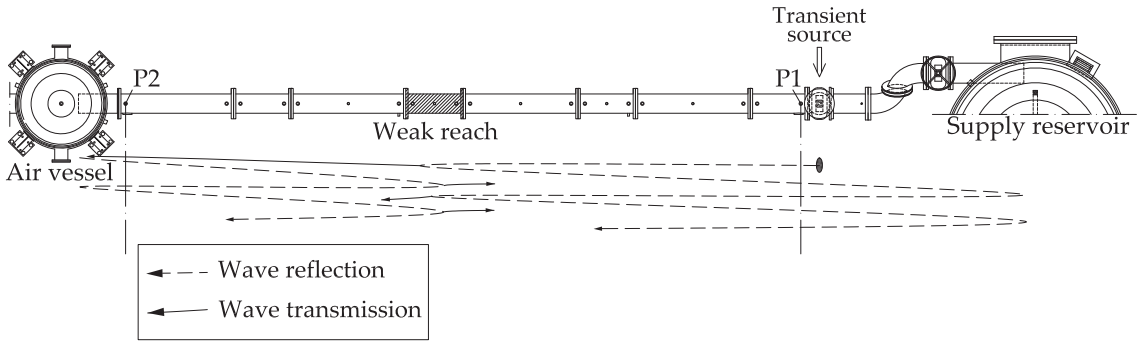

Figure 6.12: Schematic plan view of the transmission-reflection water-hammer waves generated by a source (the shut-off valve) inside the test pipe.

the wavelet transform and decomposition techniques (Section 3.2.5) are used to localize more accurately the boundaries of the weak reach. One pressure record is sufficient to estimate the incident–reflection travel time between the pressure sensor's position and these boundaries.

$\mathcal{F}$ approach

The $\mathcal{F}$ with Hanning windowing has been used (Lyons, 1997). The normalized RMS $\mathcal{F}$ density spectrums of all the tests signals P1 and P2 inside window W1 have been computed. The normalization is obtained by dividing all the $\mathcal{F}$ magnitudes by the maximum magnitude computed in the frequency interval $[75\,\text{Hz}, 500\,\text{Hz}]$. This interval was defined to include the frequencies $f_{\min}$ and $f_{\max}$ given in the natural frequencies paragraph of Section 5.1.3.3. Figs. 6.13 and 6.14 show an example of the normalized $\mathcal{F}$ for the P1 (Figs. 6.13a and 6.14a) and P2 (Figs. 6.13b and 6.14b) signals shown in Figs. 6.5 and 6.6. For the "Steel" configuration, the mean $\mathcal{F}$ curve of the 12 tests has been considered.

The $\mathcal{F}$ records of the test configurations with Aluminum reach (Figs. 6.13a and 6.13b) are very similar to those for "Steel" configuration. This is due to the small magnitude of the wave that is reflected backwards from the Aluminum reach boundaries. In fact, Fig. 6.15 gives the theoretical values of the ratio between water-hammer transmission and reflection as a function of the ratio between the elasticity modulus of the weak reach and the other parts of the test pipe (Hachem and Schleiss, 2011c). PVC reaches having an $E_{\text{WR}}/E_{\text{steel}} = 0.014$ generate reflections of up to 38 % of the incident wave. In the case of Aluminum reaches, these reflections are around 1 %. This low ratio induces difficulties in detecting and capturing the reflection pressure signals especially in high dissipative media and in presence of noise. Therefore, the localization of such reaches using the $\mathcal{F}$ approach was not possible.

The $\mathcal{F}$ curves of "Steel+PVCs" show significant differences in their pattern compared to the "Steel" configuration. These differences are induced by the pres-

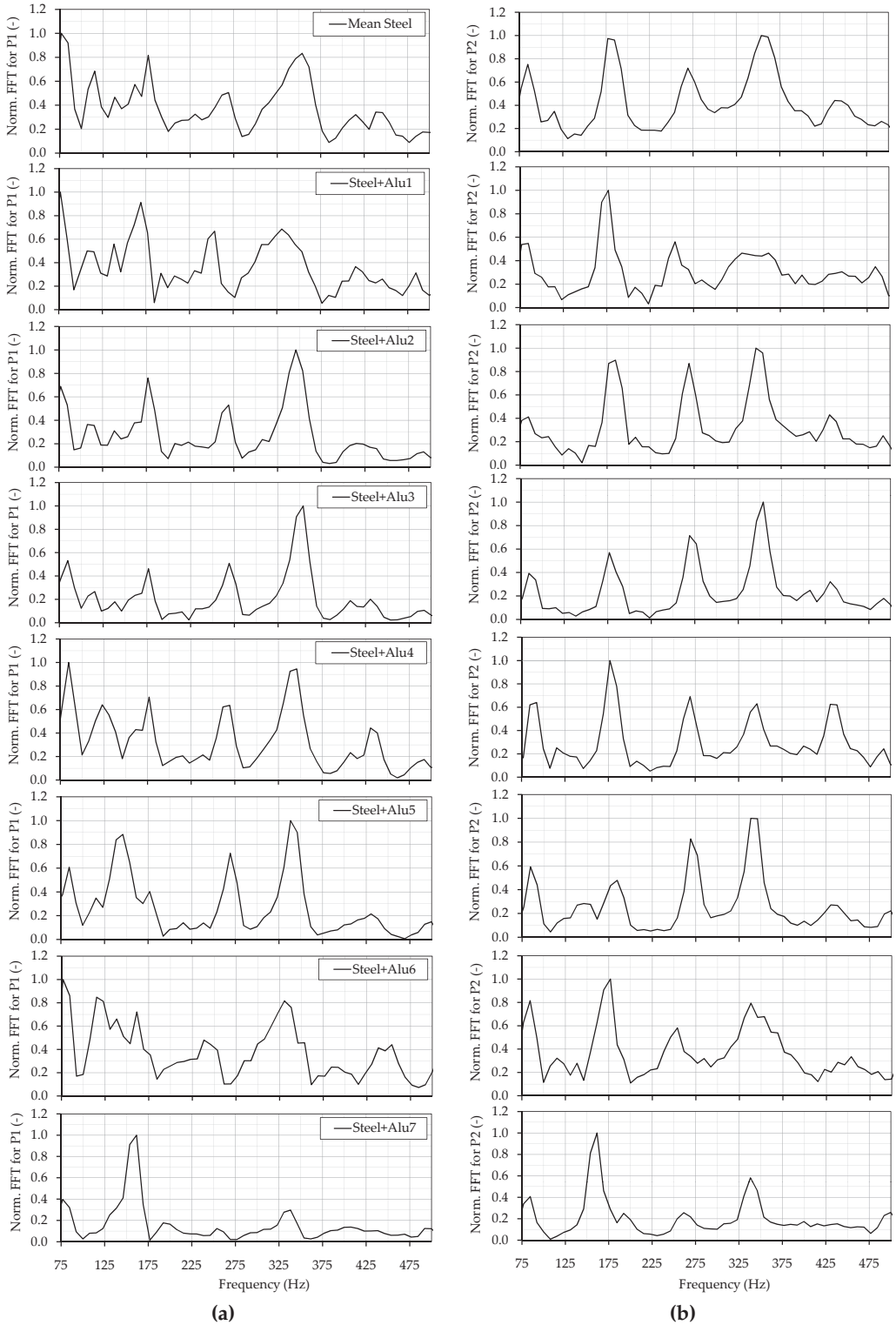

Figure 6.13: Normalized Fast Fourier Transform of the "Steel" and "Steel+Alu" test pipe configurations, (a) $\mathcal{F}$ of the P1 records as shown on Fig. 6.5a and (b) $\mathcal{F}$ of the P2 records as shown on Fig. 6.5b. The mean $\mathcal{F}$ curve of the 12 tests has been taken for the "Steel" configuration.

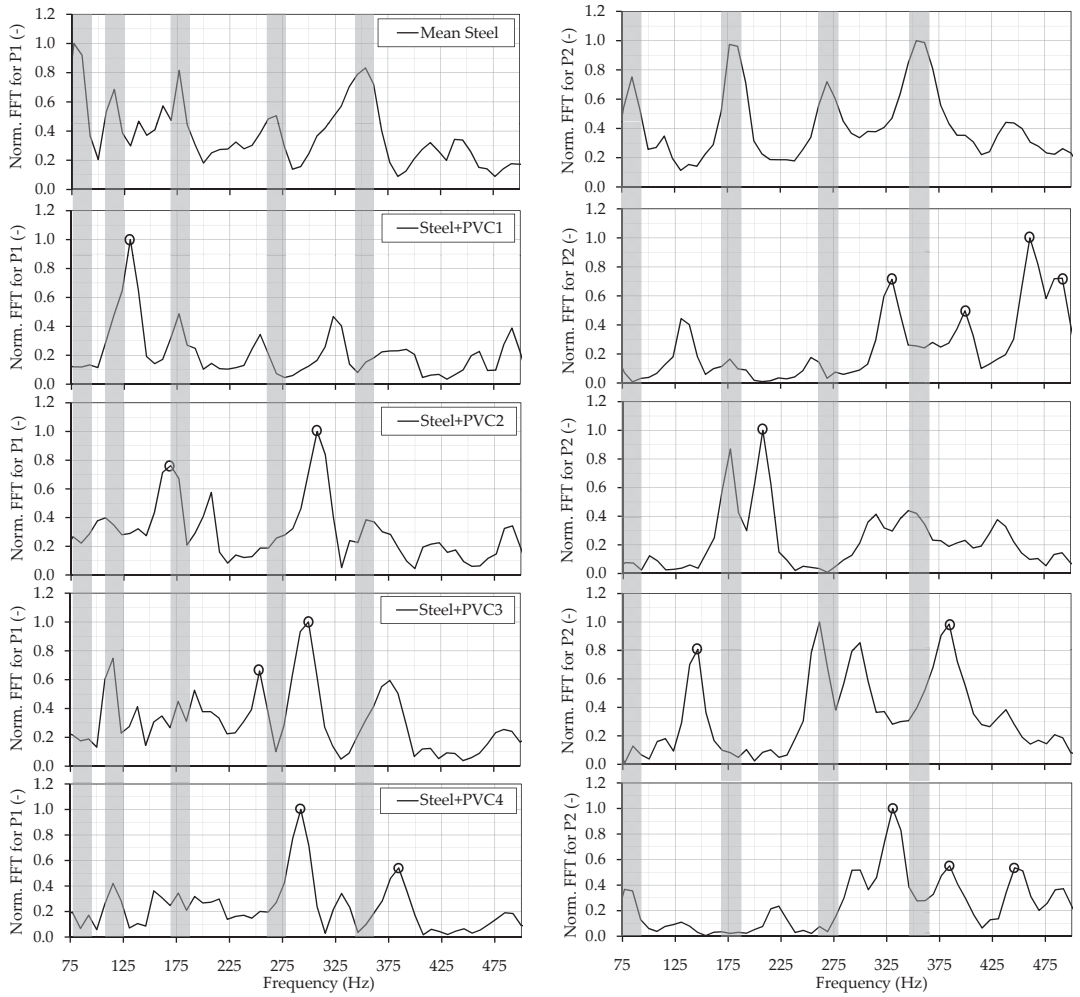

Figure 6.14: Normalized Fast Fourier Transform of the "Steel" and "Steel+PVC" test pipe configurations, (a) $\mathcal{F}$ of the P1 records as shown on Fig. 6.6a and (b) $\mathcal{F}$ of the P2 records as shown on Fig. 6.6b. The mean $\mathcal{F}$ curve of the 12 tests has been taken for the "Steel" configuration.

sure reflection generated by the weak reach inside the test pipe. The frequency that corresponds to the weak reach for each pipe configuration is identified after discarding the $\mathcal{F}$ peaks of the "Steel+PVCs" records that have the same frequencies as peaks of the "Steel" configuration (see the grey bands shown in Figs. 6.14a and 6.14b). For each configuration, the $\mathcal{F}$ peaks that have lower normalized magnitude among those that figures at the same frequencies for P1 and P2 are also discarded. One of the many remaining P1 $\mathcal{F}$ peaks (marked by circles in Fig. 6.14) should be chosen. This is done by using couples of P1 and P2 peak frequencies to compute the fundamental frequency of the test pipe in the Reservoir-Pipe-Reservoir (RPR) system with one weak reach, f_{fund}, according to the following

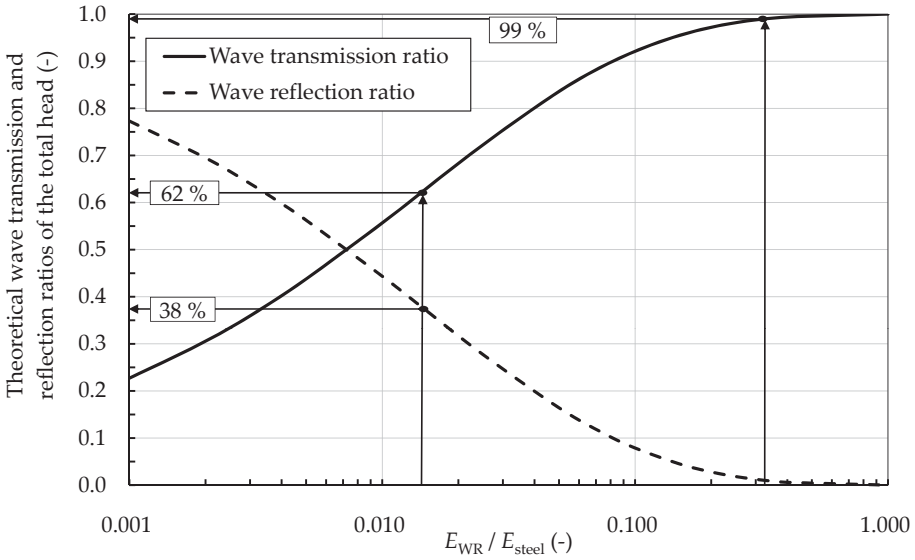

Figure 6.15: Theoretical ratios of wave transmission and reflection as a function of the ratio of the elasticity modulus of the weak reach and the other stretches of the test pipe.

equation:

$$f_{\text{fund}} = \frac{f_{\text{max,P1}}\, f_{\text{max,P2}}}{f_{\text{max,P1}} + f_{\text{max,P2}}} \tag{6.6}$$

where $f_{\text{max,P1}}$ and $f_{\text{max,P2}}$ are the $\mathcal{F}$ maximum peaks of P1 and P2, respectively. The frequencies f_{fund} are then compared to the theoretical value $f_{\text{min}} = a/(2L_T) = 75\,\text{Hz}$ in which $a = 1\,232.7\,\text{m/s}$ is the mean wave speed of the 12 tests carried out on the "Steel" pipe configuration and computed according to the procedure described in Section 6.2.2.1. The pair of frequencies which gives the nearest f_{fund} relative to the theoretical value is retained. Table 6.1 gives the values of these pairs of frequencies from the $\mathcal{F}$ records shown in Figs. 6.14. Fig. 6.16 depicts the theoretical 75 Hz line and the f_{fund} values as a function of the $f_{\text{max,P1}}$ frequencies for all the 48 tests carried out on the "Steel+PVC" configurations. It can be seen that the computed fundamental frequencies for the "Steel+PVC1, 2, and 3" configurations are close to the theoretical value of 75 Hz which indicates the presence of only one weak reach inside the test pipe. For the "Steel+PVC4" case, the f_{fund} values are very high relative to the 75 Hz line. This can be an indicator of the presence of two or more weak reaches along the test pipe.

The estimation of the incident-reflection travel distances, L_1 and L_2 between the weak reach and the downstream and upstream reservoirs, respectively is done according to Eq. (6.1) using the mean wave speed of the "Steel" configuration ($a = 1\,232.7\,\text{m/s}$). These travel distances and the error relative to the real paths length are presented in Table 6.2.

The FFT approach can roughly predict the position of the weak reach with one path length relative to the pressure sensors. Over the 48 tests carried out on

Table 6.1: Retained pairs of frequencies from Figs. 6.14 for each "Steel+PVC" test pipe configuration.

Test pipe configuration	$f_{max,P1}$	$f_{max,P2}$
Steel+PVC1	130	330
Steel+PVC2	161	207
Steel+PVC3	254	146
Steel+PVC4	292	331

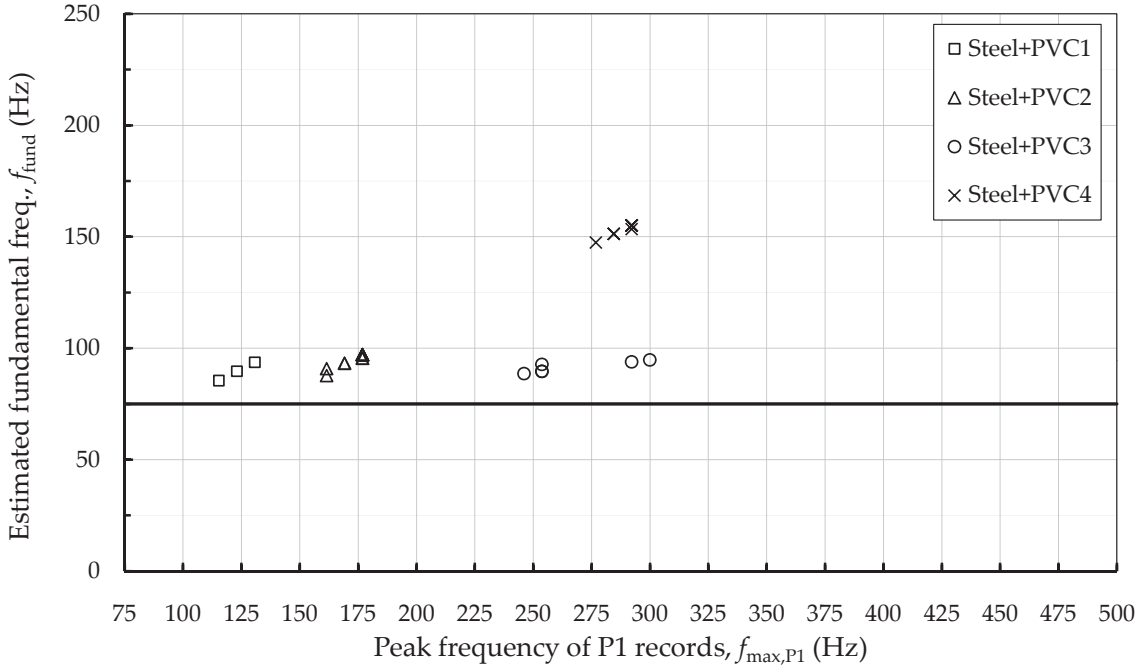

Figure 6.16: Estimated fundamental frequencies of the test pipe configurations with PVC reaches computed from Eq. (6.6) as a function of the $\mathcal{F}$ maximum peak of P1 ($f_{max,P2}$).

Table 6.2: Estimated distances between the middle of the weak reach and the downstream (supply reservoir) and upstream (air vessel) reservoirs obtained from the $\mathcal{F}$ approach for the four test pipe configurations "Steel+PVC1, 2, 3, and 4".

Test pipe config.	Path	Real path length to the middle of the weak reach (m)	Estimated inc.-ref. travel time (s)	Estimated paths length L_1 and L_2 (m)	Relative error on the path length (%)
Steel+PVC1	Sup. res.-WR*	6.63	0.007692	4.74	28.5
	Air vessel-WR	1.60	0.003030	1.87	16.9
Steel+PVC2	Sup. res.-WR	5.13	0.006211	3.83	25.3
	Air vessel-WR	3.10	0.004831	2.98	3.9
Steel+PVC3	Sup. res.-WR	3.63	0.003937	2.43	33.1
	Air vessel-WR	4.60	0.006849	4.22	8.3
Steel+PVC4	Sup. res.-WR	3.63**	0.003425	2.11	41.9
	Air vessel-WR	1.60**	0.003021	1.86	16.3

* WR stands for Weak Reach, ** the path length to the nearest WR is considered

the "Steel+PVC" configurations, the error in predicting the position of the weak reach relative to the real position of its middle varies from 3.2 % to 22.2 % for the air vessel-WR path and from 19.4 % to 43.4 % for the supply reservoir-WR path. The relatively high error on the supply reservoir-WR path is probably induced by the reflections from the two elbows and the elastic joint downstream from the shut-off valve. Therefore, the L_2 distance and the total length of the test pipe were used to correct L_1 for the three "Steel+PVC1, 2, and 3" as follows:

$$L_{1\,\mathrm{corr}} = L_T - L_2 \tag{6.7}$$

The estimated distance between the pressure sensor P1 and the weak reach was then computed by subtracting from $L_{1\,\mathrm{corr}}$ the known length $(= 1.94\,\mathrm{m})$ of the test pipe measured between the pressure sensor position P1 and the supply reservoir. The mean travel distances and mean error relative to the real path length are presented in Table 6.3. The mean incident-reflection travel time between P1 and the middle of the weak reach is also presented.

Wavelet approach for detecting one weak reach

To localize more accurately the weak reach inside the "Steel+PVC1, 2, and 3" configurations, the wavelet transform and decomposition techniques presented in Chapter 3, are applied to pressure signal P1 (Figs. E.1 and E.2 in Appendix E). In low dispersion media, the shifts in the water pressure signals caused by reflections have a slope values close to the front slope of the incident wave. To capture accurately these shifts in the time domain, an appropriate decomposition level with a pseudo-frequency (Eq. (3.26)) near but higher than the quarter-frequency

Table 6.3: Mean values of the corrected path length and the incident-reflection travel time between the pressure sensor P1 and the middle of the weak reach for the three test pipe configurations "Steel+PVC1, 2, and 3".

Test pipe config.	Path	Real path length (m)	Mean $L_{1\,corr}$ (m)	Mean estimated path length (m)	Mean estim. incident-reflection travel time (s)	Mean rel. error on the path length (%)
Steel+PVC1	P1-WR	4.69	6.37	4.43	0.00718	5.6
Steel+PVC2	P1-WR	3.19	5.29	3.35	0.00544	5.7
Steel+PVC3	P1-WR	1.69	3.84	1.90	0.00308	12.2

of the wave front should be used. The latter frequency is estimated according to the following equation:

$$f_{1/4} = \frac{1}{4\,(t_{max} - t_{int})} \tag{6.8}$$

where t_{max} is the time of the maximum front pressure and t_{int} is the time of the intersection point of two regression lines correlating respectively the steady-state and the first front pressure signal. The mean quarter-frequency of the steep incident waves generated during laboratory tests is equal to 357 Hz (period of 2.8 ms). From Eq. (3.26) it can be concluded that level 4 (with a pseudo-frequency of 641.4 Hz) should be used. Detail D_4 associated with approximation A_4 is then investigated in order to find the incident–reflection travel time.

Figs. 6.17 gives an example of the normalized graphs (normalization relative to their maximum values) of A_4 and D_4 for the three P1 pressure records with one PVC reach shown in Fig. 6.6a. A window between times 0.02 s and 0.05 s of the wavelet decomposition-level 4 is shown. The two slopes that limit the negative pressure shifts caused by reflections from the weak reach boundaries are time-located by two positive peaks of D_4. The shifts themselves mark A_4 with minimum peaks. Therefore, the incident–reflection travel time of each weak reach boundary corresponds to the difference between the maximum peak time of D_4 that bounds a minimum peak of A_4 and the time when the pressure wave front passes through P1. The time t_{int} of the front wave pressure P1 is taken as the time origin to locate the upstream boundary. The time t_{max} at the maximum pressure of the wave front is considered as the origin of time to locate the downstream boundary. The incident-reflection travel time between the pressure sensor P1 and the weak reach estimated from the $\mathcal{F}$ approach (Table 6.3) is used to localize the adequate A_4 minimum peak relative to the maximum pressure of the wave front. The maximum peaks of D_4 that bound this A_4 minimum correspond to the two slopes of the negative shifts caused by reflections from the weak reach boundaries. The D_4 maximum peaks are marked by vertical lines on Figs. 6.17. The estimated values of the incident–reflection times, the position of the weak reach boundaries, and the relative error are given in Table 6.4.

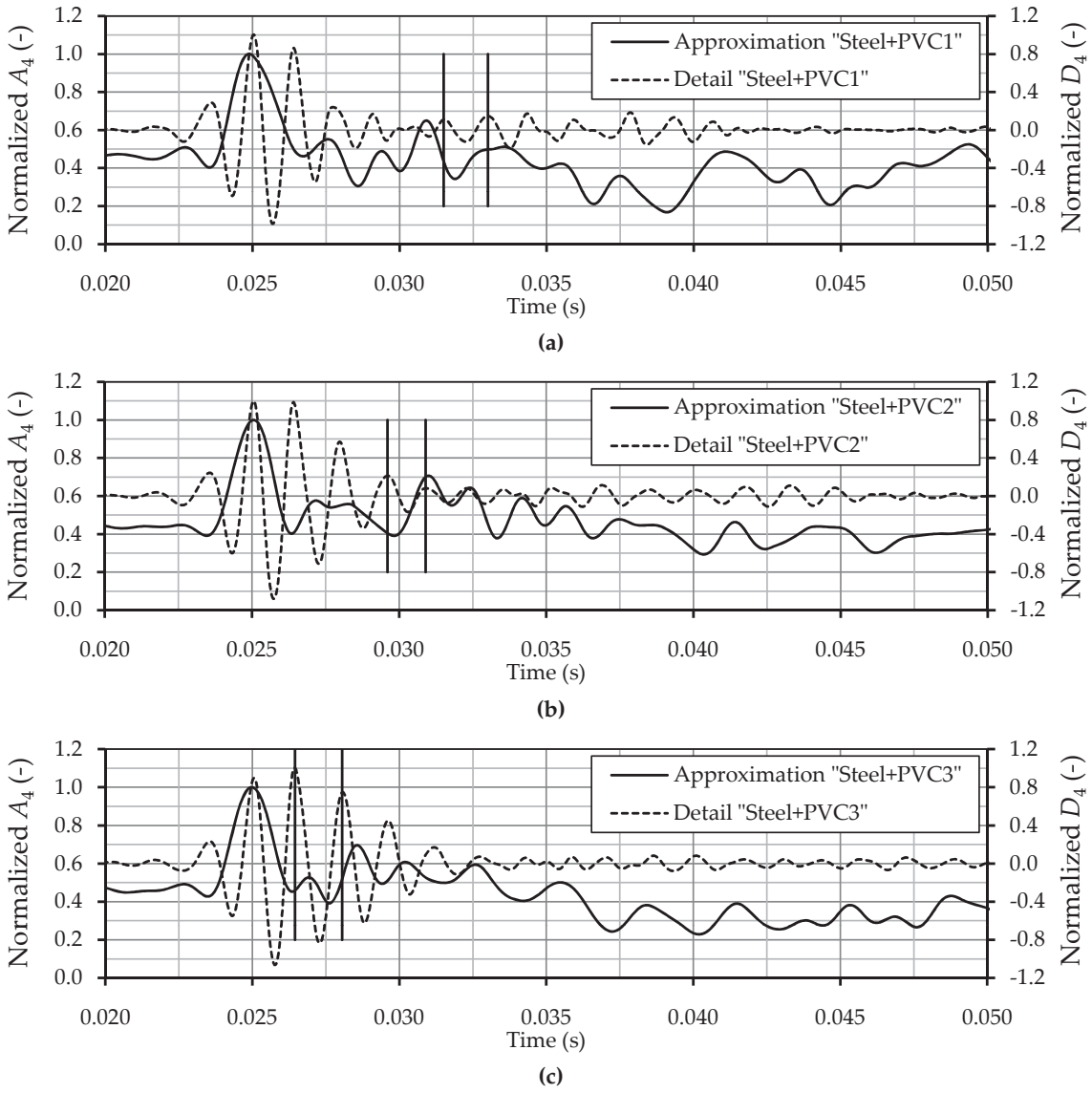

Figure 6.17: Normalized wavelet approximation A_4 and detail D_4 of the transient pressures P1 shown in Fig. 6.6a, (a) for "Steel+PVC1" , (b) for "Steel+PVC2", and (c) for "Steel+PVC3" test pipe configurations. The D_4 maximum peaks of interest are marked by vertical lines in the figures.

Table 6.4: Estimated distances between the weak reach boundaries and the pressure sensor P1 obtained from the wavelet decomposition approach for the three test pipe configurations "Steel+PVC1, 2, and 4".

Test pipe config.	Path	Real path length (m)	Estimated incident-reflection travel time (s)	Estimated path length (m)	Relative error on the path length (%)
Steel+PVC1	P1-UWR*	4.44	0.00729	4.49	1.2
	P1-DWR**	4.94	0.00800	4.93	0.2
Steel+PVC2	P1-UWR	2.94	0.00536	3.30	12.3
	P1-DWR	3.44	0.00590	3.64	5.7
Steel+PVC3	P1-UWR	1.44	0.00222	1.37	5.1
	P1-DWR	1.94	0.00305	1.88	3.1

* UWR stands for the Upstream boundary of the Weak Reach

** DWR stands for the Downstream boundary of the Weak Reach

The transformation of the incident–reflection time to distance for the upstream and downstream boundaries is performed with the mean front wave speed of the "Steel" configuration ($a = 1\,232.7\,\mathrm{m/s}$). The errors on distances relative to the real values vary between 0.2 % and 12.3 %. In Figs. 6.18a and 6.18b, the means and the standard deviations of distances between the boundaries of the weak reach and the position of the pressure sensor P1 are given. These statistical parameters are computed using the data of the 36 tests in which one PVC weak reach is used. The highest relative error of about 14 % occurs when localizing the weak reach in the middle of the test pipe. The relative mean error for the localization of the upstream and downstream boundaries of "Steel+PVC1," "Steel+PVC2" and "Steel+PVC3" configurations are significantly small and are equal to 1.3 %, 5.9 % and 5.4 %, respectively.

6.2.3 Estimation of the stiffness of the weak reach

The stiffness $(E \cdot e)_{\mathrm{WR}}$ of the weak reach of the test pipe can be estimated using the wave speed relation for pipes and open penstocks (Eq. (4.42)). This relation can be written, after rearrangement, as follows:

$$(E \cdot e)_{\mathrm{WR}} = \frac{2\, r_i\, \lambda_{13}}{\dfrac{1}{\rho_w\, a_{\mathrm{WR}}^2} - \dfrac{1}{K_w}} \tag{6.9}$$

where a_{WR} is the front wave speed in the confined water inside the weak reach. The only unknown parameter in Eq. (6.9) is a_{WR}. It can be calculated by using the estimated value of the wave speed between sensors P1 and P2 and the estimated

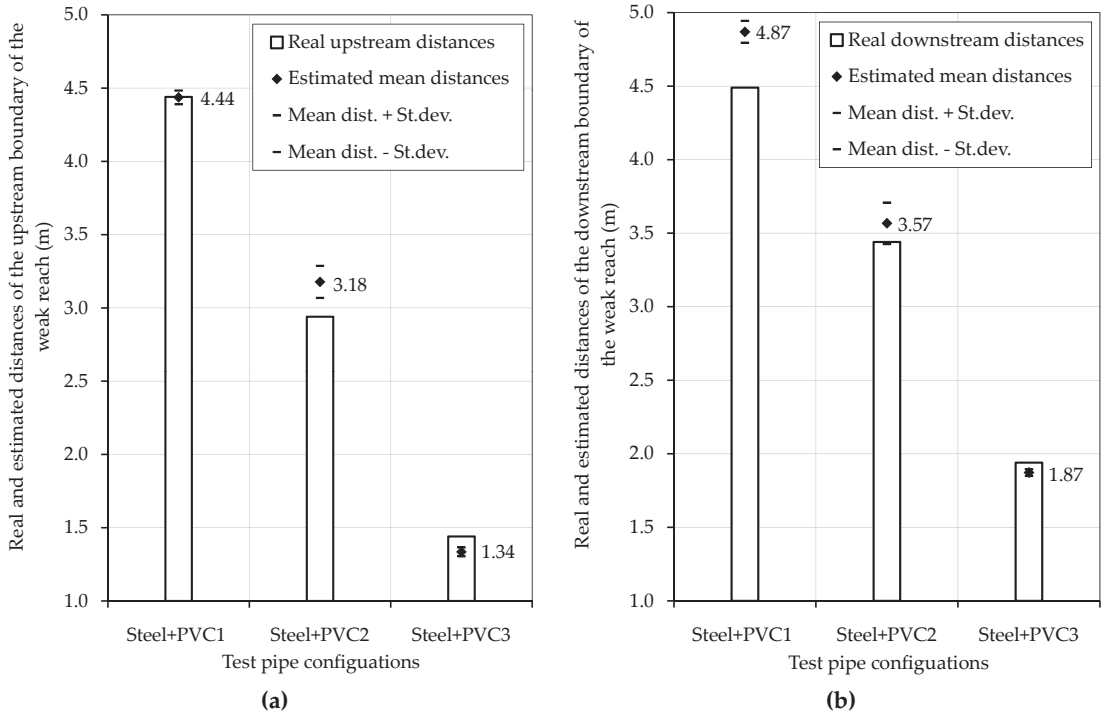

Figure 6.18: Comparison between the real and the mean estimated distances separating the weak reach boundaries from the sensor position P1. The standard deviations of these distances computed for all the 36 tests with PVC reach are also shown, (a) for the upstream and (b) for the downstream boundaries.

length of the weak reach. This is done according to the following equation:

$$a_{\mathrm{WR}} = \frac{l_{\mathrm{WR}}}{\dfrac{L_{\mathrm{P1,P2}}}{a_{\mathrm{P1,P2}}} - \dfrac{(L_{\mathrm{P1,P2}} - l_{\mathrm{WR}})}{a_{\mathrm{basic}}}} \tag{6.10}$$

where, l_{WR} is the estimated length of the weak reach, $a_{\mathrm{P1,P2}}$ is the estimated front wave speed of the test pipe configuration with weak reach, $L_{\mathrm{P1,P2}}$ is the distance separating the two sensors positions, and a_{basic} is the mean front wave speed of the basic test pipe configuration.

The real and estimated stiffness of the weak reach for the tested pipe configurations are given in Fig. 6.19a for the pressure records with PVC reach shown in Figs. 6.6a and 6.6b. The big differences between the stiffness of "Steel" and "Steel+PVCs" configurations make the log scale for the vertical axis of Fig. 6.19a necessary to show clearly the points relative to the configurations tested. Also the estimated mean stiffness of the "Steel" configuration can be seen. It is determined by averaging the values obtained from Eq. (6.9) in which a_{WR} is replaced by the steel front wave speed between P1 and P2. The real stiffness for this configuration is the product of the steel Young's modulus of 210 000 MPa and the thickness of the steel pipe wall of 4.5 mm. In Fig. 6.19a, the following input values have been used: $r_i = 75\,\mathrm{mm}$; $K_w = 2\,200\,\mathrm{MPa}$; $\rho_w = 1\,000\,\mathrm{kg/m^3}$; $\nu_s = 0.3$; $\nu_{\mathrm{PVC}} = 0.4$; $\lambda_{13} = 1 - v_{s,\mathrm{PVC}}^2$.

In Fig. 6.19b, the mean and the standard deviation of the stiffness of the weak reach is shown for each test pipe configuration. A maximum relative mean error of about 29 % is observed for the "Steel" test pipe configuration. For the "Steel+PVC1, 2 and 3" configurations, these relative mean errors are 12.3 %, 21.8 % and 20.6 %, respectively.

6.2.4 Estimation of the wave dissipation factor induced by the transmission and reflection phenomena at the weak reach boundaries

For the pressure front wave generated in window W1 of Fig. 6.2a, a total number of six pressure sensors were used to measure the water transient inside and at the upstream and downstream ends of the Aluminum and PVC reaches. Three sensors were placed inside the weak reach (one in the middle and two at 60 mm from each of its end, Fig. 6.20), one upstream and two downstream from it. For each "Steel+PVC" and "Steel+Alu" configuration, the six sensors were displaced to follow the position of the weak reach along the pipe. The pressure sensors at sections S1 and S2 were used to record the global wave dissipation along the test pipe.

Figure 6.21a gives the theoretical and measured pressure head ratios between the transmitted and incident waves, as it is defined in Eq. (3.4), for three different reaches made of steel, aluminum, and PVC materials. In presence of PVC reach, the measured results show that the front wave looses around 44 % of its

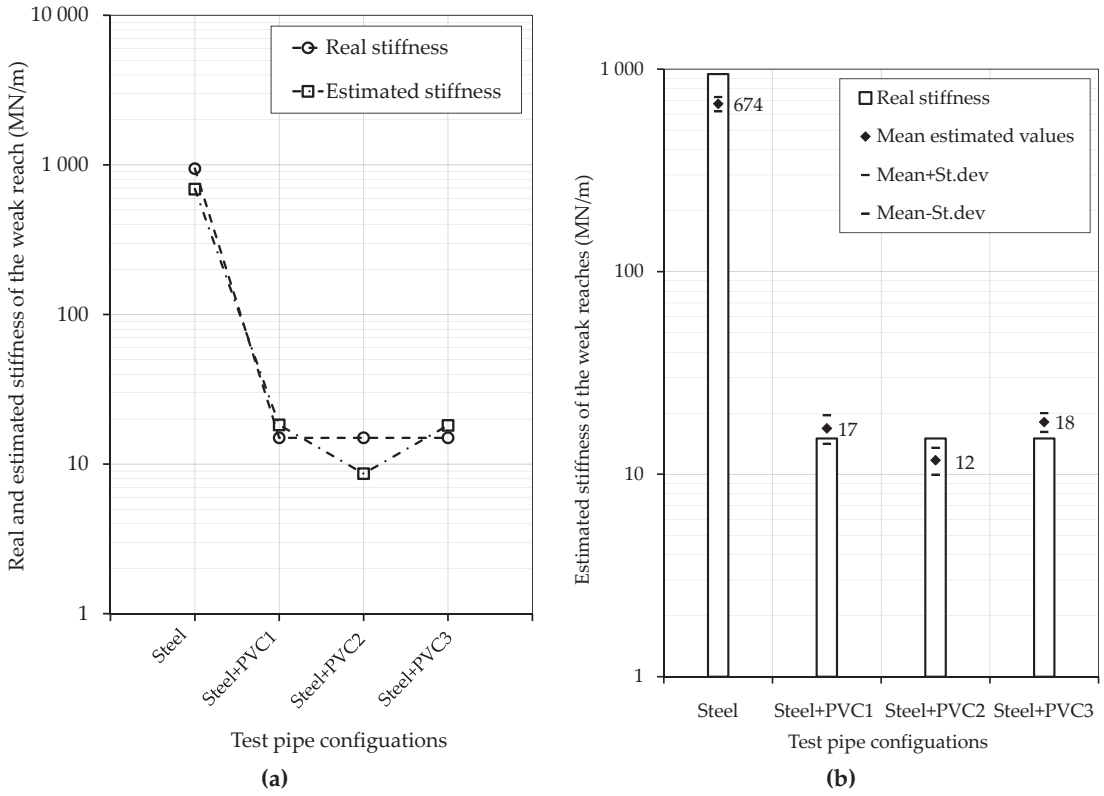

Figure 6.19: Real and estimated stiffness of the weak reach, (a) for the test pipe configurations whose pressure records are given in Figs. 6.6a and 6.6b, (b) the mean and the standard deviations for each of the "Steel" and "Steel+PVC" test pipe configuration.

magnitude when it enters the weak reach. The reflection coming back from the downstream border amplifies the wave front by about 32 % (Fig. 6.21b). The wave continues its downstream propagation with a dissipation slope higher than in steel and aluminum cases. The measured ratios inside the weak reach are 20 % higher than the theoretical values obtained from Eq. (3.4). The higher downstream slope and the difference between the theoretical and measured pressure ratios are probably caused by the inelastic behavior of the PVC reach. For the aluminum reach, the same wave behavior is observed with less dissipation and less amplification when entering and leaving the reach, respectively. The additional wave dissipation induced by the aluminum and PVC reaches is confirmed by the measurement of the total dissipation factor of the entire test pipe.

Figure 6.22 shows the relative dissipation ratios between P1 and P2 for all the test pipe configurations (Fig. 5.9). Significant and proportional differences (+44 % in "Steel+PVC1,2,3" and +77 % in "Steel+PVC4") between the "Steel" and the "Steel+PVCs" configurations can be observed. Such differences could not be identified in the "Steel+Alu" cases.

It should be mentioned that it was difficult to extract similar information re-

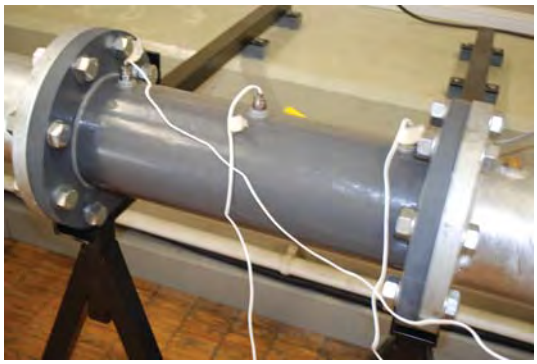

Figure 6.20: Photo of the PVC reach equipped with three pressure sensors.

garding the wave dissipation by using the geophones or the pressure records situated within window W2.

6.3 Monitoring approach based on the progressive stoppage of the flow by the shut-off valve

6.3.1 Estimation of the wave speed based on pressures data

The pressure signals inside the window W2 of Fig. 6.2a do not have a clear wave front that can be easily identified and followed as in their first parts (Window W1). Therefore, a new procedure to estimate the wave speed from the pressure records is proposed in this section. It is validated by a series of experimental tests carried out on the pipe configurations shown in Fig. 5.9.

The procedure starts with decomposing each signal P1 and P2 into an approximation A_J and several details D_i components using the wavelet decomposition technique (Figs. E.9 to E.12). The *Daubechies* (db10) mother wavelet is used. The details D_4 to D_7 for each pressure signal are then summed together to construct two new signals S(P1) and S(P2). This construction filters the signals with a band-pass filter of low and high frequencies of 72 and 486 Hz, respectively. This interval was defined to include the frequencies $f_{\min}$ and $f_{\max}$ which correspond to the incident-reflection travel time between the supply reservoir and the air vessel and to waves propagating between the closest distance of the weak reach boundary to the air vessel, respectively. The signals S(P1) and S(P2) of the pressure records given in window W2 of Fig. 6.2a are shown in Fig. 6.23.

The procedure continues with the computation of the energy content history of signal S(P1) using the floating Root Mean Square (RMS) or the Singular Value Decomposition (SVD) method (Trefethen, 1997 and Yang et al., 2006). The RMS

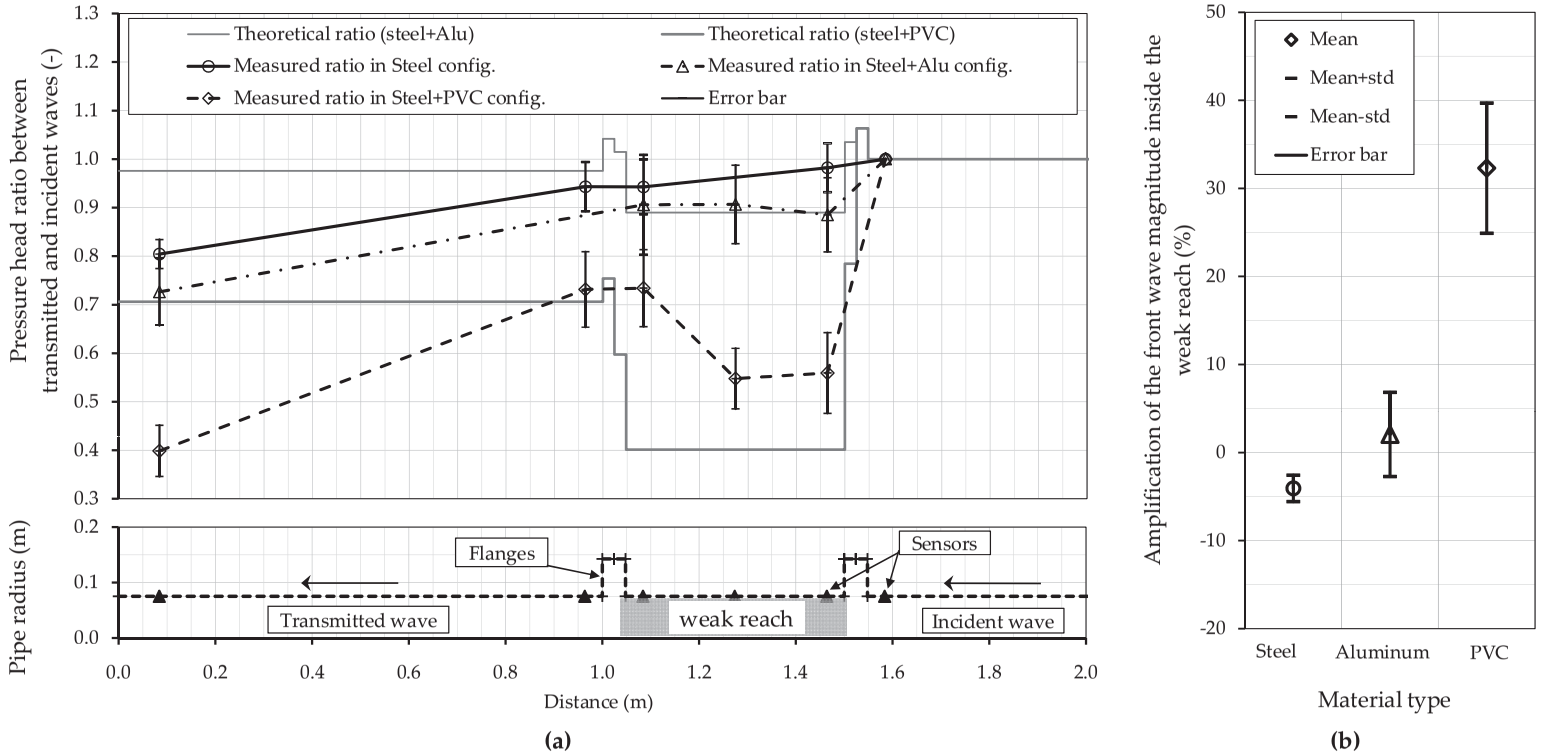

Figure 6.21: (a) local theoretical and experimental dissipation ratios of the pressure wave front encountered by the weak reach, and (b) means and standard deviations of the amplifications of the wave front magnitude inside the weak reach for different materials types.

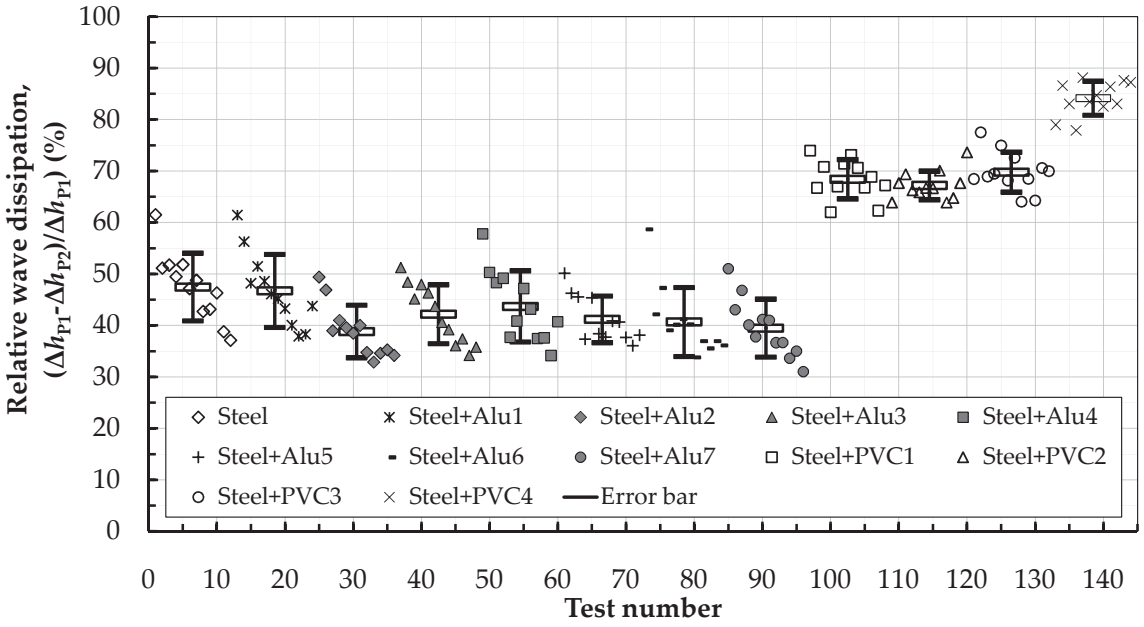

Figure 6.22: Relative dissipation ratios between measurement records P1 and P2 estimated from the pressure with steep wave front shown in Figs. 6.5 and 6.6.

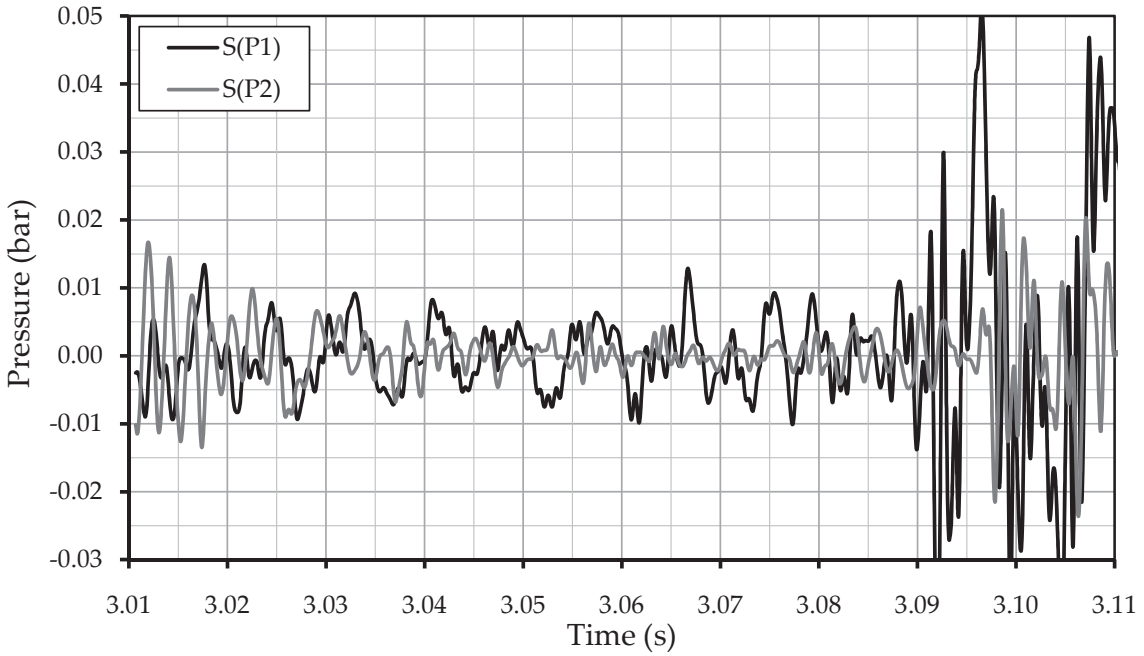

Figure 6.23: Pressure signals S(P1) and S(P2) constructed by summing the wavelet details from D_4 to D_7 of the pressure records given in window W1 of Fig. 6.2a.

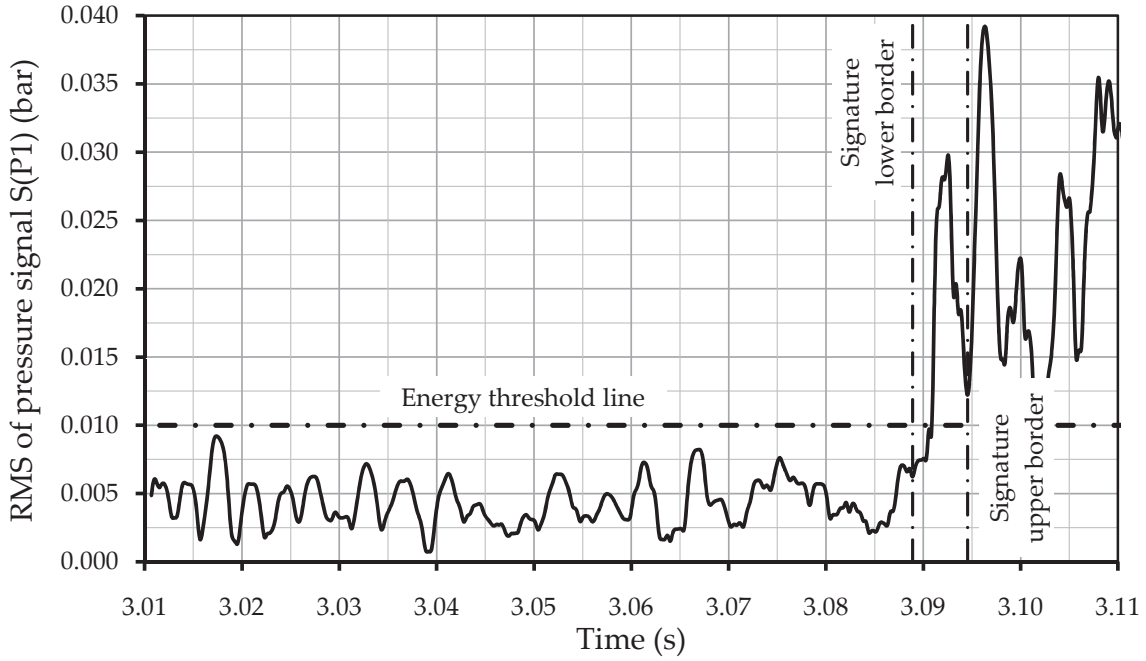

Figure 6.24: Floating Root Mean Square of the S(P1) signal shown in Fig. 6.23 including the energy threshold line and the borders of the S(P1) pressure signature.

method has been applied by using the following equation:

$$\mathrm{RMS}_i = \sqrt{\frac{1}{N_{\mathrm{RMS}}} \sum_{i=j}^{j+N-1} sp_i^2} \tag{6.11}$$

in which, sp_i is the discrete pressure values of the signal S(P1), and N_{RMS} is a real parameter that defines the resolution of the RMS and represents the number of pressure points inside a one period interval. The high-frequency, $f_{\max} = 478\,\mathrm{Hz}$ is used to determine the value of N_{RMS} according to the formula:

$$N_{\mathrm{RMS}} = \frac{1}{f_{\max}} f_{\mathrm{samp}} \approx 42 \tag{6.12}$$

The RMS curve shows positive shifts at times when an important pressure energy package crosses the measurement section P1. A RMS threshold line of 0.01 bar was chosen to define a portion or a signature of the S(P1) signal. This signature is limited by the times of the two minimum peaks of the first RMS lobe that has a positive shift that crosses the threshold line. The RMS curve, the energy threshold line, and the signature borders of the S(P1) pressure records given in Fig. 6.2a are shown on Fig. 6.24.

The procedure ends with a cross-correlation between the signature of pressure S(P1) and the pressure S(P2). For discrete functions, the cross-correlation

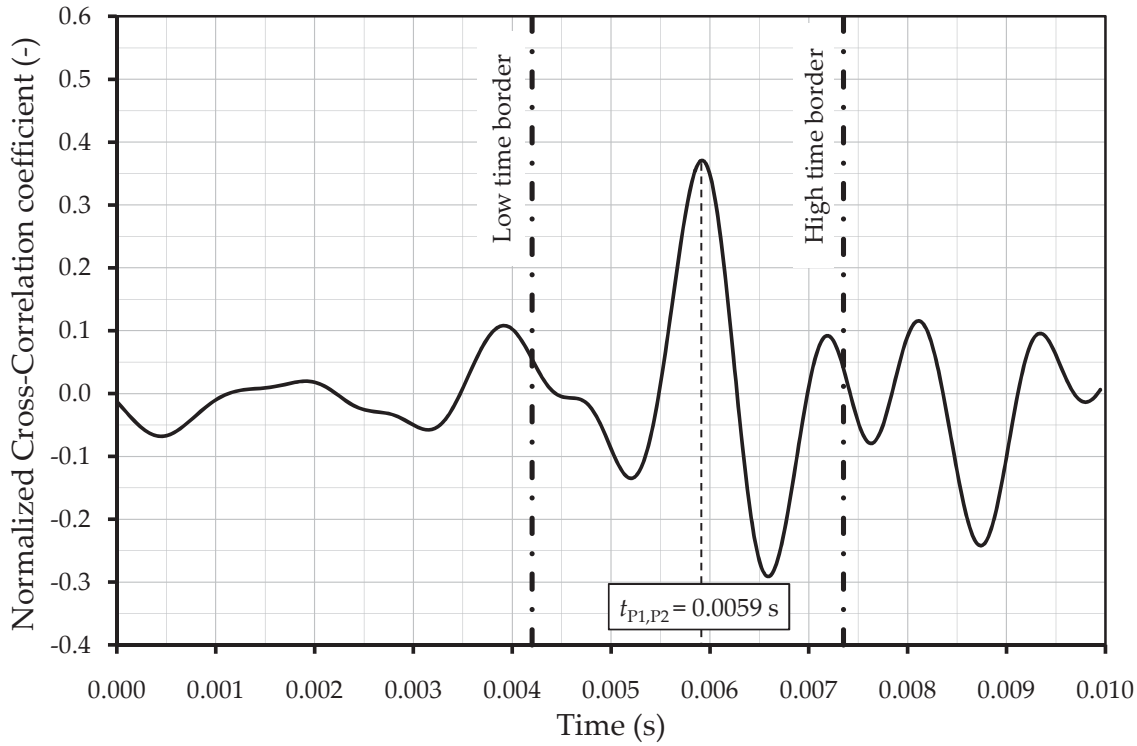

Figure 6.25: Normalized Cross-Correlation of the pressure signature of S(P1) and the S(P2) signal shown in Fig. 6.23.

is defined in Eq. (3.19). The estimated travel-time of the water-hammer wave speed between the two measurement pressure sensors P1 and P2 corresponds to the time-lag at the maximum positive peak of the cross-correlation curve identified between two time borders obtained from the logical wave speed values of 1 400 m/s and 800 m/s according to the relations: $t_{\text{Lower border}} = {}^{5.88}/_{1\,400} = 0.0042$ s and $t_{\text{Higher border}} = {}^{5.88}/_{800} = 0.00735$ s.

The result of the cross-correlation of the signals given in Fig. 6.2a is shown on Fig. 6.25. The peak time, $t_{\text{P1,P2}}$ is equal to 0.0059 s and can be easily transformed to wave speed according to Eq. (6.1) with $2\,l = L_{\text{P1,P2}} = 5.88$ m.

The estimated values of the wave speed between sensors P1 and P2 determined according to the procedure described in this section for signals in window W2 are shown in Fig. 6.26. The means and standard deviations of each 12 tests which correspond to each pipe configuration are also shown. These wave speeds are given for all the 144 tests that have been carried out on the twelve configurations of the test pipe. As in case of steep pressure excitation, the geometric means of the wave speed are higher than the estimated mean wave speed values in all the test pipe configurations.

The mean and standard deviation of the wave speeds estimated from steep pressures in Section 6.2.2.1 and those obtained from the progressive stoppage of the flow by the shut-off valve are compared in Figs. 6.27. Fig. 6.27a shows a very good agreement between mean values estimated by the two pressure based methods with a maximum relative difference around 5 % for the configuration "Steel+PVC4". The scattering of estimated wave speeds is lower in case of steep wave front than in case of progressive stoppage of flow (Fig. 6.27b). In the former case the mean and maximum values of the standard deviation are 20 m/s and 42 m/s, respectively, while in the latter case the maximum standard deviation reaches 73 m/s with a mean value of 40 m/s.

It should be mentioned that the geophones signals inside the window W2 could not be analyzed by the herein proposed method due to the long dissipation time of the output signal generated in window W1.

6.3.2 Estimation of the location of weak reach using $\mathcal{F}$ approach

The pressure records P1 and P2 inside the window W2 of Fig. 6.2a are considered to estimate the incident–reflection travel times between the weak reach and the air vessel. As in Section 6.2.2.3, the $\mathcal{F}$ approach was used to localize one PVC reach inside the "Steel+PVC1, 2, and 3" test pipe configurations. For each of these pipe configuration, the mean of the normalized $\mathcal{F}$ (with Hanning windowing) for P1 and P2 has been computed. The normalization is obtained by dividing all the $\mathcal{F}$ magnitudes by the maximum magnitude computed in the frequency interval [75 Hz , 500 Hz]. Figs. 6.28a and 6.28b depict the average curves of the normalized $\mathcal{F}$ for P1 and P2 signals, respectively, acquired from the "Steel" and "Steel+PVCs" configurations. The identification procedure of the $\mathcal{F}$ peaks is similar to the one presented in Section 6.2.2.3. For "Steel+PVC1" configuration,

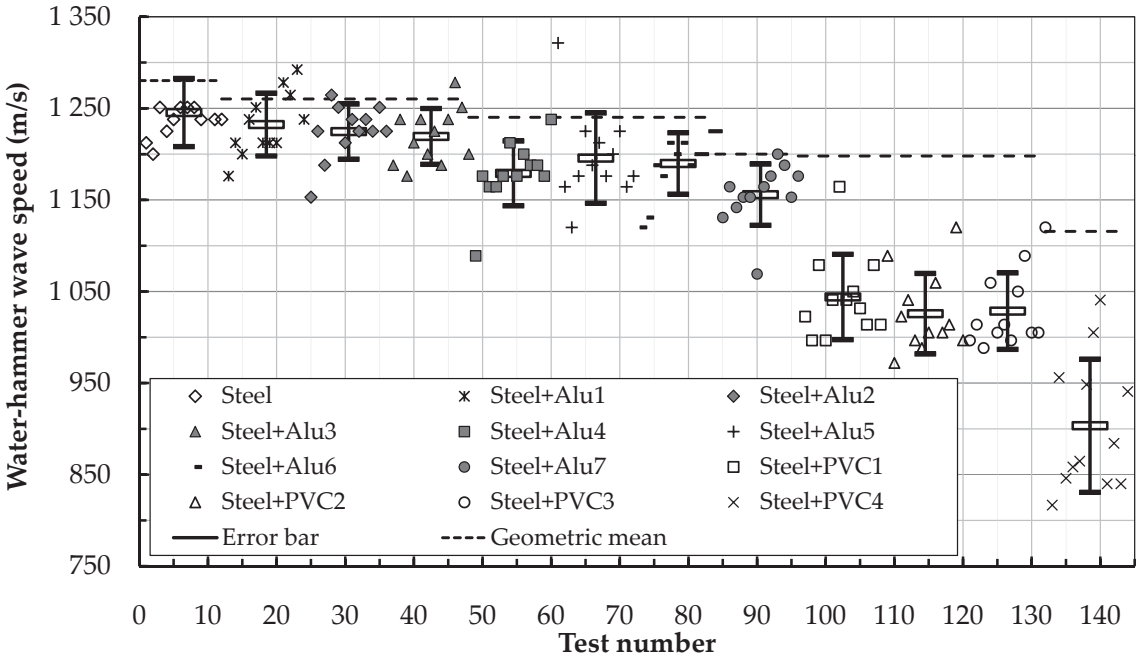

Figure 6.26: Water-hammer wave speed estimated from the pressure records generated by the progressive stoppage of flow by the shut-off valve (signals inside the window W2 of Fig. 6.2a).

the frequencies are $f_{\text{max,P1}} = 120\,\text{Hz}$ and $f_{\text{max,P2}} = 330\,\text{Hz}$. For "Steel+PVC2" and "Steel+PVC3" configurations, the only remaining frequencies of the $\mathcal{F}$ of P2 records after discarding peak frequencies of the "Steel" configuration are 210 Hz and 140 Hz, respectively. For these configurations, Eq. (6.6) has not been used to identify the frequency peaks.

The estimation of the incident-reflection travel distance, L_2 between the weak reach and the air vessel was done by using the mean wave speed of the "Steel" configuration ($a_{\text{steel}} = 1\,245.5\,\text{m/s}$), as it was estimated in Section 6.3.1, and the identified fundamental frequencies from the $\mathcal{F}$ of P2. The travel distances and the errors relative to the real path lengths are presented in Table 6.5. The error in estimating the position of the weak reach relative to the real position of its middle section varies from 3.3 % to 18.1 %.

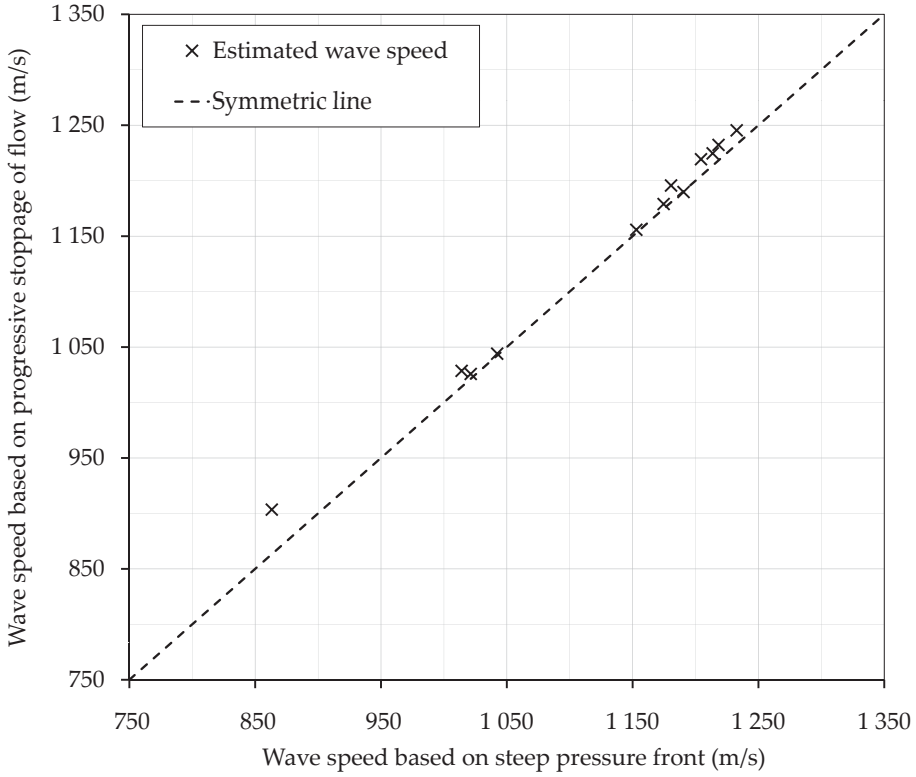

(a)

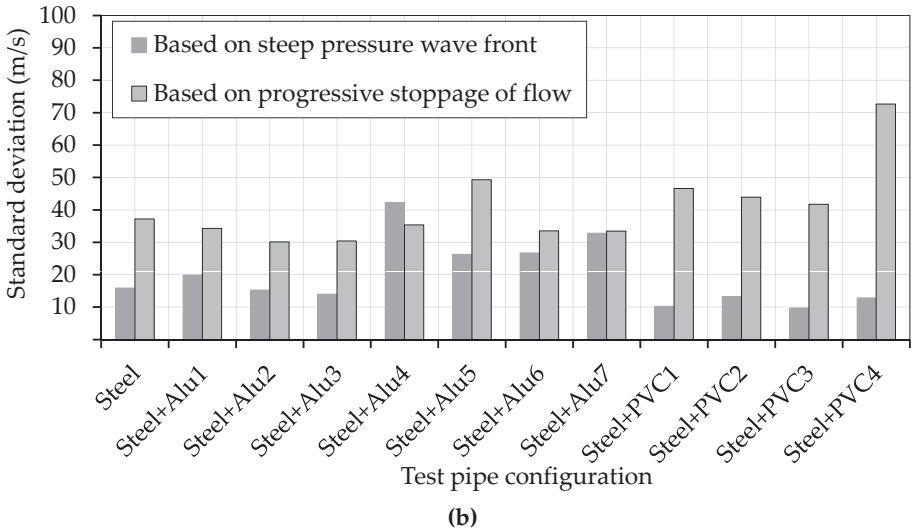

(b)

Figure 6.27: Comparison between the estimated wave speeds obtained by processing the pressure records with steep wave front and those generated by progressive stoppage of flow by the shut-off valve for the twelve configurations of the test pipe, (a) mean and (b) standard deviation.

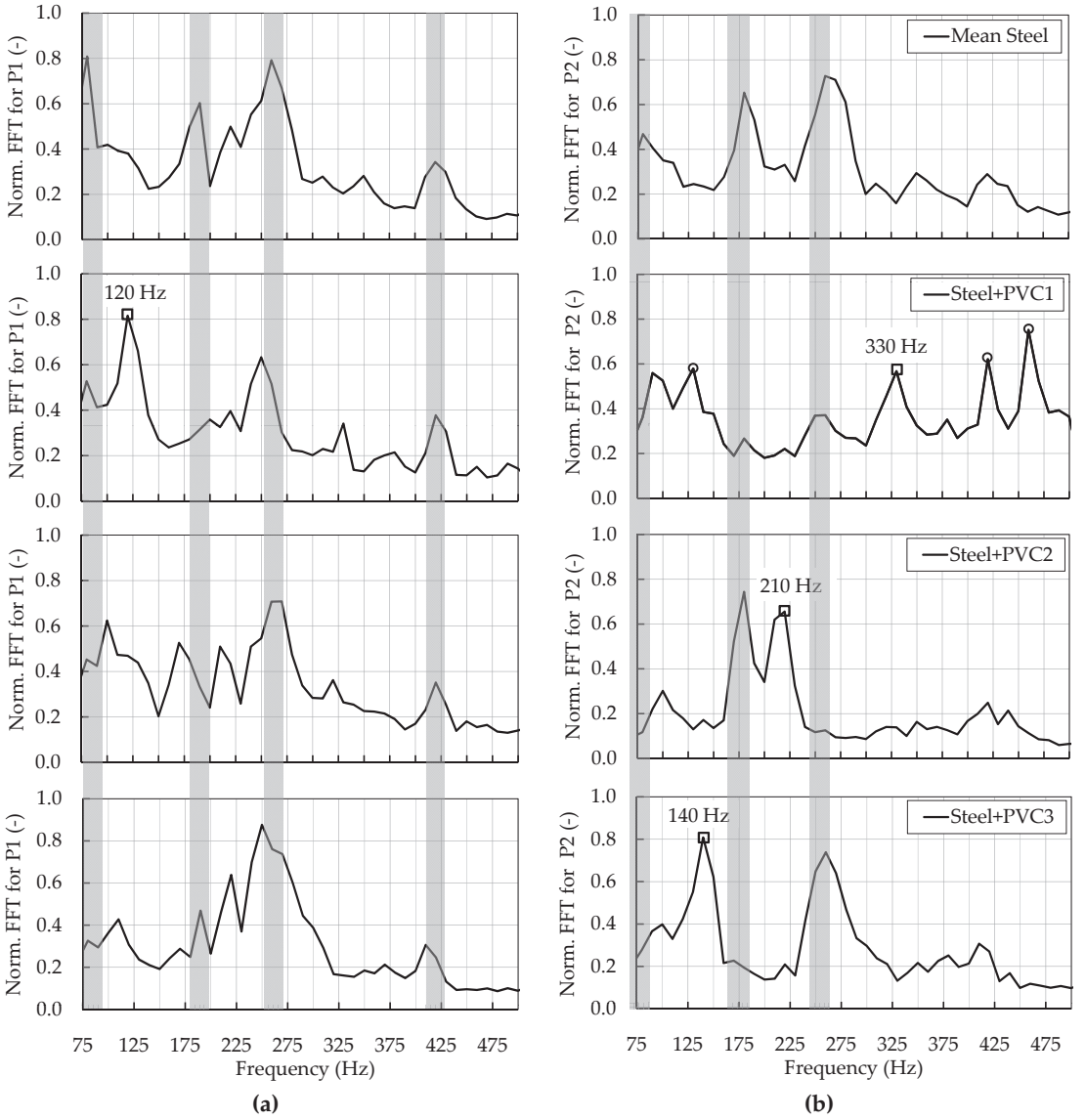

Figure 6.28: The mean normalized Fast Fourier Transform of the "Steel" and "Steel+PVC" test pipe configurations for pressures generated by the progressive stoppage of flow by the shut-off valve, (a) $\mathcal{F}$ of the P1 records and (b) $\mathcal{F}$ of the P2 records.

Table 6.5: Estimated distances between the middle of the weak reach and sensor P2 obtained from the $\mathcal{F}$ approach for the three test pipe configurations "Steel+PVC1,2, and 3".

Test pipe config.	Path	Real path length L_2 (m)	P1 peak frequency $f_{max,P2}$ (Hz)	Estimated L_2 path length (m)	Relative error on the path length (%)
Steel+PVC1	Air vessel-WR	1.60	330	1.89	18.1
Steel+PVC2	Air vessel-WR	3.10	210	2.97	4.2
Steel+PVC3	Air vessel-WR	4.60	140	4.45	3.3

6.4 Monitoring based on the system identification approach

6.4.1 Estimation of the wave speed based on pressures data

In the system identification approach, the entire length of the pressure signals P1 and P2, shown inside the windows W1 and W2 of Fig. 6.2a, are considered. These signals are filtered by using *Daubechies* (db10) mother wavelet where details D_4 to D_7 were summed together to construct the filtered signals. For each test carried out on the "Steel" and "Steel+PVCs" test pipe configurations, the filtered signals P1 and P2 are cross-correlated according to Eq. (3.19). In Fig. 6.29, an example of the cross-correlation results versus the time lag for each pipe configuration is given. The first peak observed for each configuration (marked by circle on Fig. 6.29) gives the wave travel time between sensors P1 and P2. The wave speeds are then estimated from Eq. (6.1) (with $2l = 5.88\,\text{m}$) and their mean values for the 12 tests carried out on each of the "Steel" and "Steel+PVCs" configurations are compared to the mean values obtained from the steep pressure front presented in Section 6.2.2.1. This comparison is shown in Fig. 6.30 where a very good agreement is found for the "Steel" and "Steel+PVC1, 2 and 3" cases with a maximum error of 1.6 % for the "Steel+PVC3" configuration. For the "Steel+PVC4" case, the cross-correlation results give low wave speeds with a mean value around 625.5 m/s. These low values are generated by the high time lag which corresponds to the first maximum peak of the cross-correlation curve of "Steel+PVC4" pipe configuration (0.0095 s on Fig. 6.29). For this configuration, the first peak should theoretically occur near 0.0065 s. This was not the case due probably to the interference between the incident and reflected water-hammer waves inside the test pipe.

6.4.2 Identification of the system by the frequency response function $H(f)$

The frequency response function has been computed from Eq. (3.12) for the "Steel" and "Steel+PVCs" test pipe configurations. Figs. 6.31 and 6.32 show the magnitude and phase of $H(f)$, respectively, within the frequency band of inter-

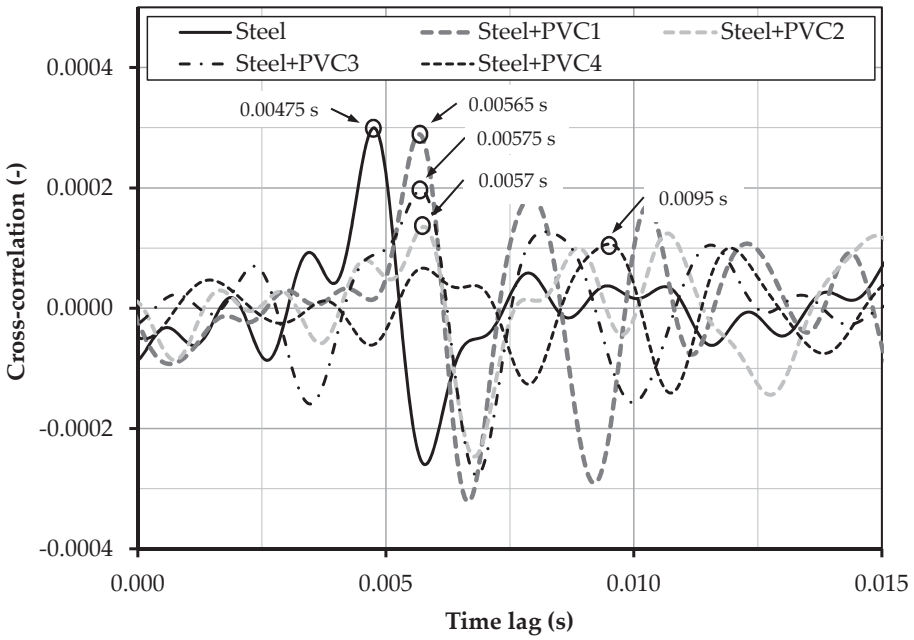

Figure 6.29: Example of cross-correlation results of the entire pressure signals P1 and P2 enclosed in windows W1 and W2 of Fig. 6.2a for the "Steel" and "Steel+PVCs" test pipe configurations. The time lag at the first maximum peak for each pipe configuration is also shown.

est [75 Hz,475 Hz]. For the "Steel" configuration, the fundamental frequency f_1 which corresponds to the first peak of $H(f)$ inside the frequency band, is equal to 93.75 Hz. This frequency yields to a wave speed of 1 543.13 m/s estimated from the test pipe path between the air vessel and the main reservoir ($L_T = 8.23$ m). As it was discussed in Section 6.2.2.3, the high value of the wave speed is induced by the error in the wave path length where the two elbows and the elastic joint downstream from the shut-off valve generate wave reflections and modify the total path length from which the wave speed is estimated. The harmonics $2f_1$,$3f_1$, and $4f_1$ are easily identified from the response function of the "Steel" configuration. The time delay between sensors P1 and P2 can be also identified from the slope of the phase graphs of $H(f)$ (Fig. 6.32) according to the following formula:

$$\text{delay} = -\text{slope}/2\pi \tag{6.13}$$

The wave speed can then be estimated from the the test pipe path between the air vessel and the main reservoir. For the "Steel" configuration, the wave speed estimated from the phase is equal to 1 555.07 m/s.

For the "Steel+PVCs" configurations, a significant change in the response function is observed in each case (Fig. 6.31) relative to the "Steel" basic configuration. Two fundamental peaks f_1 and f_2 are observed for the pipe configurations with one PVC reach. The other peaks can be identified as the second and third har-

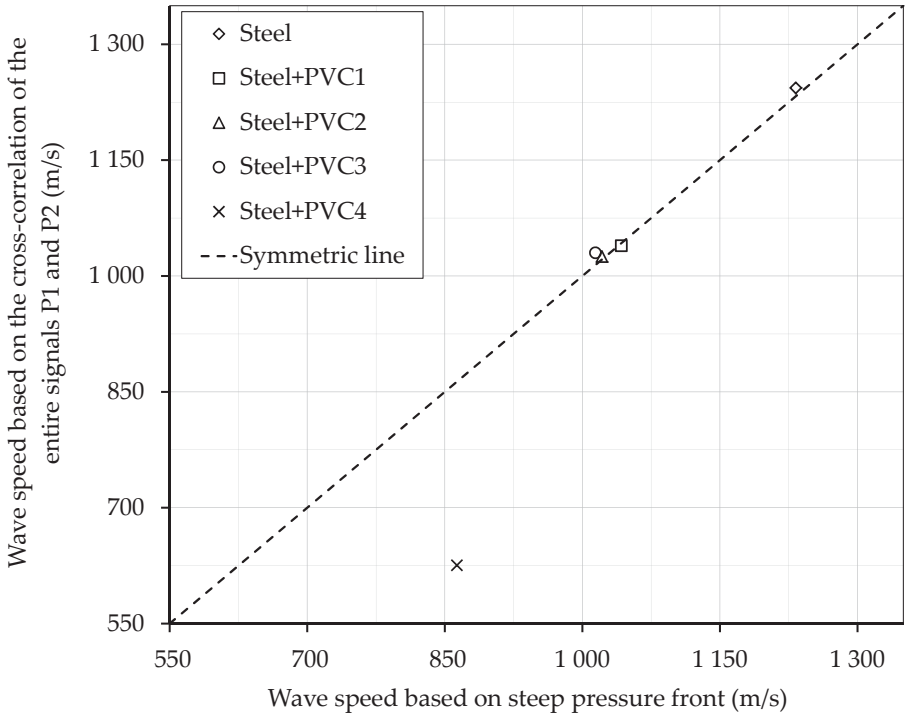

Figure 6.30: Comparison between the mean values of the estimated wave speeds obtained by processing the pressure data with steep wave front and those determined from the cross-correlation results of the entire pressure signals P1 and P2.

monics of f_1 and f_2. For the "Steel+PVC1", the frequency f_1 corresponds to the travel path between the weak reach and the supply reservoir while f_2 is the frequency of the incident-reflection wave between the weak reach and the air vessel. A similar pattern of the response function is observed for the "Steel+PVC3" configuration in which f_1 and f_2 are the frequency of the travel paths WR-air vessel and WR-supply reservoir, respectively. Thus, it is not possible to distinguish the configurations "Steel+PVC1 and 3" from each other by using the frequency response function approach. The identification of only two fundamental frequencies inside the frequency interval of interest indicates the presence of one weak reach along the test pipe. This is not the case for the "Steel+PVC4" configuration where another fundamental frequency ($f_2 = 225\,\text{Hz}$) has been detected. The latter corresponds to the wave path between the two weak reaches.

The coherence charts for the "Steel" and "Steel+PVCs" configurations are determined from Eq. (3.15) and are shown in Fig. 6.33. The coherence function $C_{io}^2(f)$ is above 0.5 within the frequency band [125 Hz,475 Hz]. Between 75 Hz and 125 Hz, the coherence drops below 0.5. This important deviation from linearity is probably due to the interaction of the water-hammer mode with the first vibration mode of the test pipe (Figs. 5.7 and 5.8). Systematical drops of coherence functions are also observed at the fundamental frequencies. This is caused by the bias error which can be reduced by improving the resolution (Shin and Hammond, 2008).

6.5 Uncertainties

In this section, the uncertainty analysis of the experimental test results is carried out according to the theoretical background presented in Section 3.3. This includes the estimation of uncertainties in the wave speed and the weak reach location in both cases of transient pressure excitations (steep front waves and waves induces by the progressive stoppage of the flow) and in the wave dissipation ratio and the weak reach stiffness in case of steep front waves.

6.5.1 Uncertainty in the wave speed value

Case of steep front waves

The wave speed inside the test pipe has been estimated according to Eq. (6.1) by substituting $2l$ by the distance between the two pressure sensors, $L_{\text{P1,P2}}$, and the time t by the wave travel time $t_{\text{P1,P2}}$. The systematic uncertainties in $L_{\text{P1,P2}}$ and in the time at the pressure peaks P1 and P2 propagate through Eq. (6.1) and yield the bias error B_a in the results. This error is determined from Eq. (3.30) which becomes after rearrangement as follows:

$$B_a = \frac{1}{t_{\text{P2}} - t_{\text{P1}}} B_{L_{\text{P1,P2}}} \tag{6.14}$$

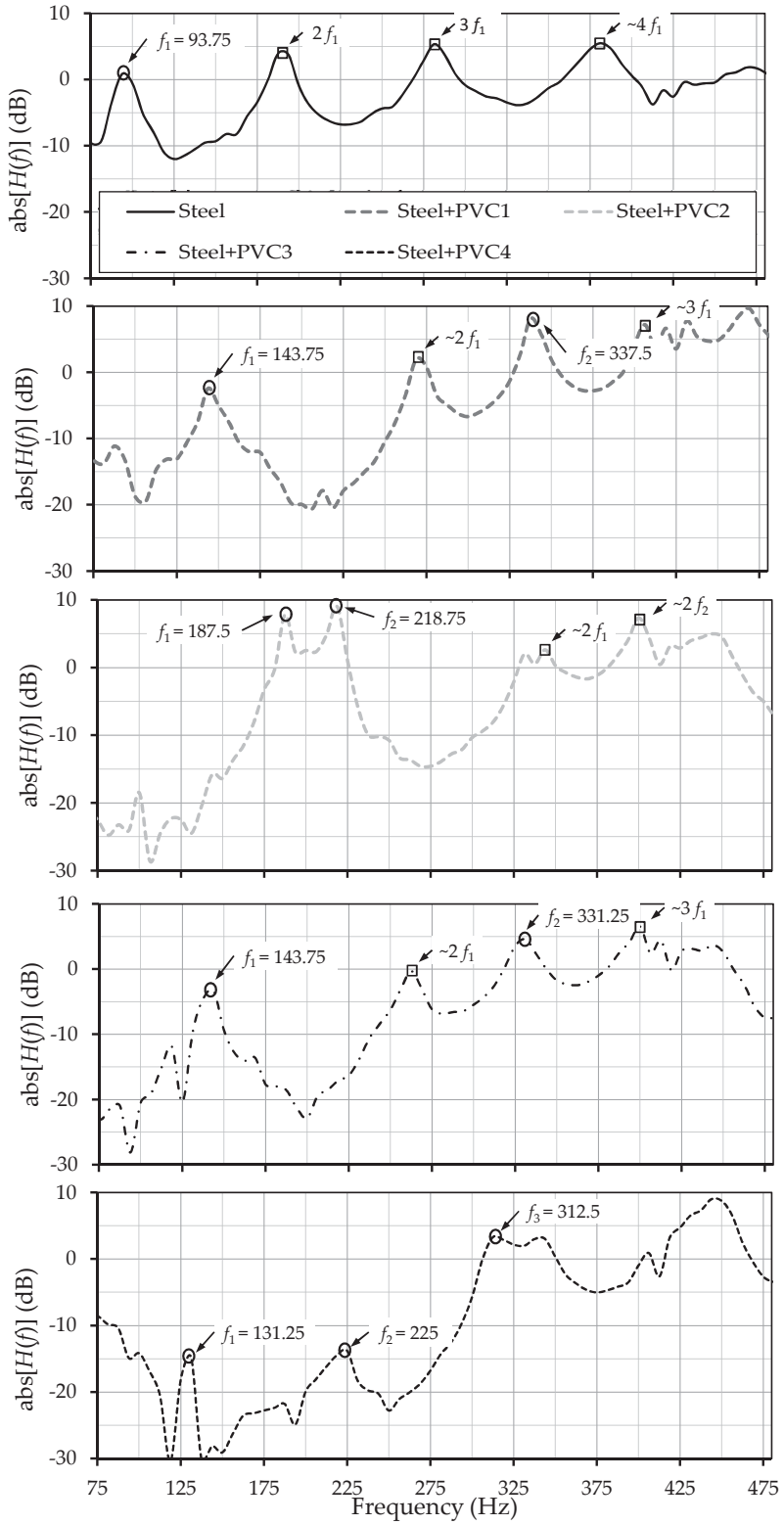

Figure 6.31: Magnitude spectrum of the frequency response function $H(f)$ estimated from Eq. (3.12) for the "Steel" and "Steel+PVCs" test pipe configurations. The fundamental and harmonic frequencies for each pipe configuration is also depicted.

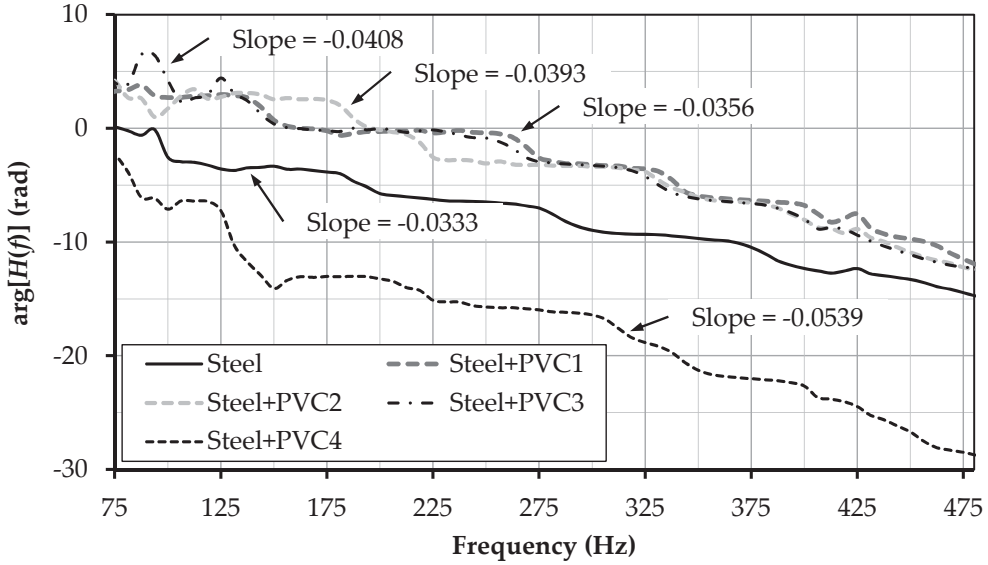

Figure 6.32: Phase spectrum of the frequency response function $H(f)$ for the "Steel" and "Steel+PVCs" test pipe configurations. The slopes of the best fitted lines of phase values between frequencies 75 Hz and 475 Hz for each pipe configuration is also shown.

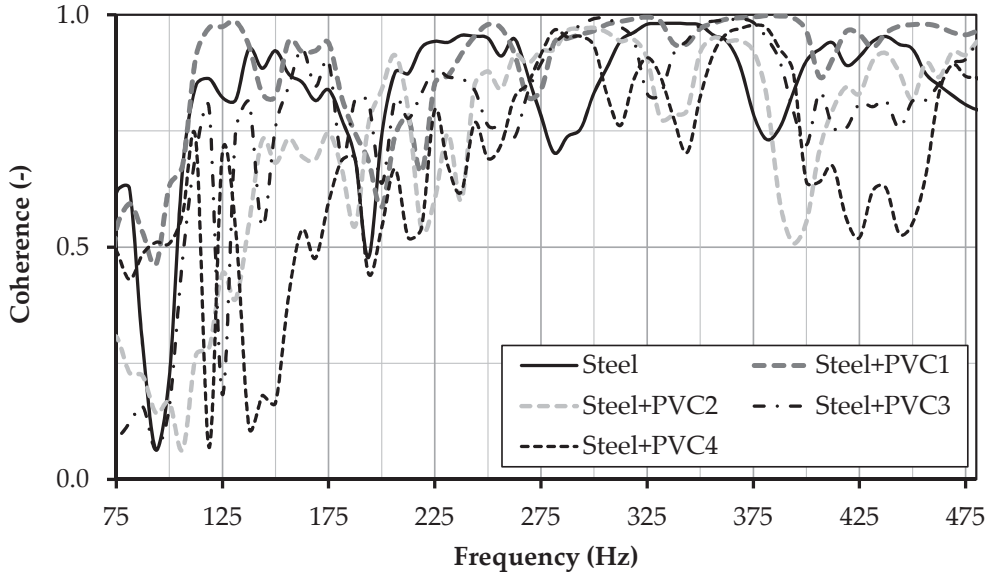

Figure 6.33: Coherence function for the "Steel" and "Steel+PVCs" test pipe configurations between frequencies 75 Hz and 475 Hz.

The terms containing $B_{t_{P1}}$ and $B_{t_{P2}}$ add to zero in Eq. (3.30), therefore, the systematic uncertainty in the time at pressure peaks measurements has no effect on the systematic uncertainty of the wave speed value. This occurs because: (i) the bias errors $B_{t_{P1}}$ and $B_{t_{P2}}$ are considered as equal since the pressure transducers are of the same type, (ii) the partial derivatives with respect to t_{P1} and t_{P2} are equal in magnitude but opposite in sign, and (iii) the entire systematic uncertainties estimated for t_{P1} and t_{P2} are correlated with each other since the pressure transducers have been calibrated by using the same "Huber" transducer. The uncertainty $B_{L_{P1,P2}}$ associated with the readability of a meter ruler is taken equal to 1 mm. It is the least scale division of the ruler used.

The random uncertainty is determined directly from Eq. (3.33) for the 12 experimental results ($M = 12$) carried out on each of the 12 configurations of the test pipe. Fig. 6.34 shows the uncertainties in the wave speed which are obtained from Eq. (3.34) in case of steep front wave excitations.

The uncertainty varies between 7.3 m/s and 24.9 m/s with a mean value of 13.2 m/s and a standard deviation of 5.4 m/s. The low uncertainty values compared to the clear differences observed between the mean wave speed of "Steel" and "Steel+PVC" configurations confirm the conclusion formulated in Section 6.2.2.1 and stating that the wave speed can be considered as a global indicator of large changes in the stiffness of the pipe wall.

Case of waves generated by the progressive stoppage of the flow by the shut-off valve

In this case, the wave speed has been determined from Eq. (6.1) after the estimation of the travel time using the procedure presented in Section 6.3.1. Therefore, it is difficult to calculate the systematic error in the travel time by using the propagation method. The hypothesis of a bias error of 1 % of the travel time obtained from the cross-correlation analysis is thus proposed. The systematic error in the wave speed value is determined from Eq. (3.30) by considering the travel time as a measured variable. This yields to the following equation:

$$B_a = \left[\frac{1}{t_{P1,P2}^2} B_{L_{P1,P2}}^2 + \frac{L_{P1,P2}^2}{t_{P1,P2}^4} B_{t_{P1,P2}}^2 \right]^{1/2} \tag{6.15}$$

The random uncertainty $P_{\overline{a}}$ is estimated by the direct method which uses the experimental results of the test pipe. The uncertainties in the wave speed in the case of progressive stoppage of the flow inside the test pipe, are shown in Fig. 6.34.

In this case, the uncertainty in the wave speed values is higher than the case of steep wave front. It varies between 21.3 m/s and 42.9 m/s with a mean value of 26.3 m/s and a standard deviation of 6.0 m/s. The differences in wave speed values (Fig. 6.26) of about 200 m/s for "Steel+PVC1, 2, and 3" configurations and 350 m/s for "Steel+PVC4" configuration still be considered high enough to confirm the conclusion formulated in Section 6.2.2.1.

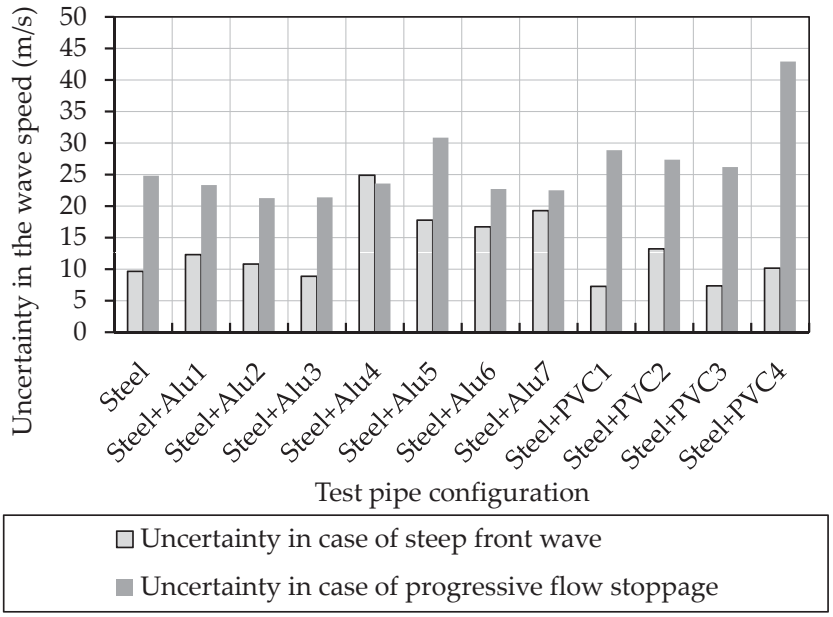

Figure 6.34: Uncertainties in the experimental results of the wave speed in both cases of steep front wave and progressive stoppage of the flow. The results are shown for the 12 configurations of the test pipe.

6.5.2 Uncertainty in the longitudinal coordinate of the weak reach position

Case of steep front waves

When pressure waves with steep front were generated inside the test pipe of the experimental facility, it was possible to estimate the position of the upstream and downstream boundaries of the PVC reach. The wavelet technique was used to estimate the incident-reflection travel time of water-hammer waves between the sensor P1 and the boundaries of the weak reach. The positions of these boundaries have been determined from Eq. (6.1). Therefore, the systematic errors in the wave speed and in the travel time values propagate through this equation according to the following expression:

$$B_l = \left[\frac{t_{\mathrm{P1,P2}}^2}{4} B_a^2 + \frac{a_{\mathrm{steel}}^2}{4} B_{t_{\mathrm{P1,P2}}}^2 \right]^{1/2} \tag{6.16}$$

Similar to the case of uncertainty analysis of the wave speed, the bias error in the travel time values has been taken equal to 1 % and the precision errors have been estimated from the standard deviations of the results. The uncertainties in the longitudinal coordinate of the weak reach position for the three test pipe configurations with one PVC reach are presented in Fig. 6.35.

For each pipe configuration, the uncertainties in the coordinate values of the upstream and downstream boundaries are, more or less, the same. The smallest

error is observed in the "Steel+PVC3" configuration and is equal to 2.2 cm. The largest one corresponds to the "Steel+PVC2" case with a value of 8.9 cm.

Case of the progressive stoppage of the flow

In this case, the $\mathcal{F}$ approach was used to estimate the incident-reflection travel time of water-hammer wave and to localize one PVC reach along the test pipe. The errors induced by the limited resolution of the $\mathcal{F}$ values have been propagated to the incident-reflection time according to the following equation:

$$B_{t_{\mathrm{P1,P2}}} = \frac{B_f}{f^2} \tag{6.17}$$

The systematic and precision errors in the position of the center of the weak reach have been estimated from Eq. (6.16) and from the standard deviations of the results, respectively. The uncertainties for the three test pipe configurations "Steel+PVC1, 2, and 3" are presented in Fig. 6.35.

For both "Steel+PVC1 and 2" configurations, the uncertainties in the center coordinate values of the weak reach are close to those estimated for the position of the upstream and downstream boundaries in the case of steep wave front. For the "Steel+PVC3" configuration, the uncertainty is particularly high with a value of 18.1 cm. This is induced by the small value of f and the high value of the standard deviation of the results of coordinate L_2. Due to this high uncertainty, the relative error on the path length for the "Steel+PVC3" configuration (shown in Table 6.5) increases from 3.3 % to 7.2 %.

6.5.3 Uncertainty in the relative wave dissipation ratio

The bias error in the relative wave dissipation ratio B_{diss}, is estimated by the following expression obtained from Eq. (3.30):

$$B_{\mathrm{diss}} = \left[\frac{\left(\triangle h_{\mathrm{P2}}\right)^2}{\left(\triangle h_{\mathrm{P1}}\right)^4} + \frac{1}{\left(\triangle h_{\mathrm{P1}}\right)^2} - 2\,\frac{\triangle h_{\mathrm{P2}}}{\left(\triangle h_{\mathrm{P1}}\right)^3} \right]^{1/2} \cdot B_{\triangle h} \tag{6.18}$$

For the pressure sensors, the manufacturer's information states that the uncertainty due to the combined non-linearity, hysteresis and repeatability is typically ± 0.1 % of the full scale output of 100 mV. So, $B_{\triangle h} \approx 0.00585$ bar. The uncertainties in the relative wave dissipation according to Eq. (6.18) are depicted in Fig. 6.36.

The uncertainty in the dissipation values is low and varies between 1.6 % and 4.1 % with a mean value of 3.0 % and a standard deviation of 0.9 %. The low uncertainty values confirm the conclusion stating that the wave dissipation ratio is the second global indicator of large changes in the stiffness of the pipe wall.

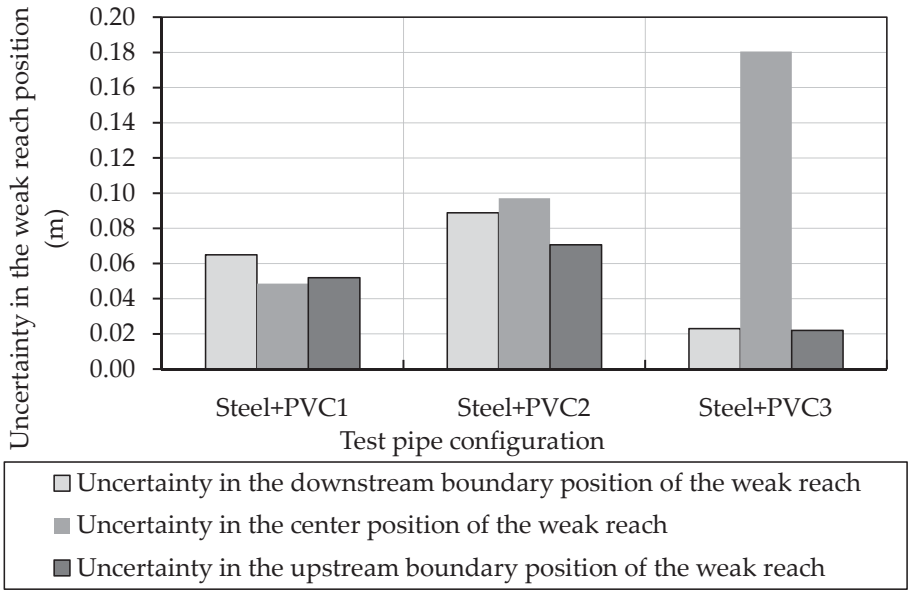

Figure 6.35: Uncertainties in the experimental results of the longitudinal coordinate of the weak reach position for both cases of steep front wave and progressive stoppage of the flow. The results are shown for the three test pipe configurations "Steel+PVC1, 2, and 3".

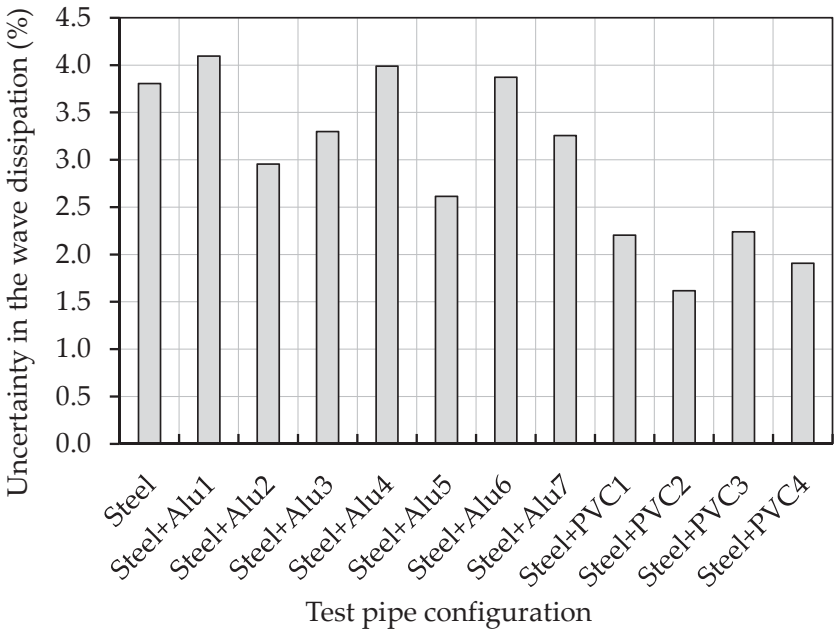

Figure 6.36: Uncertainties in the experimental results of the relative wave dissipation inside the test pipe between sensors P1 and P2. The results are shown for the 12 configurations of the test pipe.

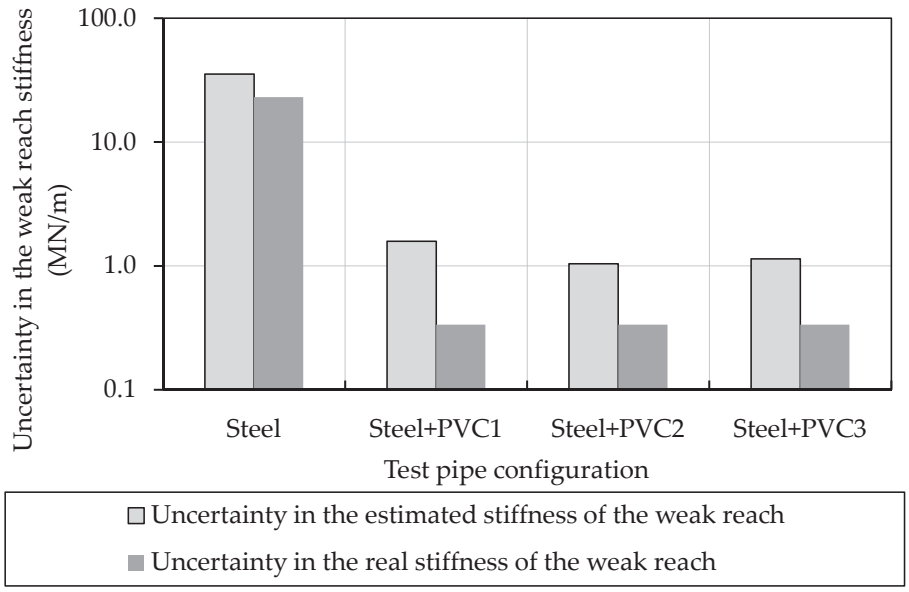

Figure 6.37: Uncertainties in the real and estimated results of the stiffness of the weak reach. The results are shown for the "Steel" and "Steel+PVC1, 2, and 3" test pipe configurations.

6.5.4 Uncertainty in the stiffness of the weak reach

For the estimated values of the stiffness of the weak reach, Eq. (6.9) shows that $(E \cdot e)_{\mathrm{WR}}$ is function of the variables r_i, ρ_w, a_{WR}, and K_w. The systematic errors in the materials properties B_{ρ_w} and B_{K_w} have been taken equal to 0.1 % and 1 % of the nominal values, respectively. The bias error in the radius of the test pipe is 1 mm and those in the wave speed values are estimated from Eq. (6.14). The uncertainties in the estimated stiffness of the weak reach are shown in Fig. 6.37 for the pipe configurations "Steel" and "Steel+PVC1, 2, and 3". This figure shows also the uncertainties in the real stiffness values estimated from Eq. (3.30) with the uncertainty in the elasticity modulus $B_E = 1\,\%$ of the nominal value of the elasticity modulus of the material used and the uncertainty in the wall's thickness, $B_e = 0.1$ mm.

For all the test pipe configurations, the uncertainties in the estimated stiffness values are higher than those in the real stiffness ones. For the "Steel" configuration, the maximum uncertainty in the estimated stiffness is equal to 35.4 MN/m. This consists about 5.3 % of the mean estimated stiffness value of steel material. For the "Steel+PVCs" configurations, the maximum uncertainty is equal to 1.6 MN/m which is 10.3 % of the mean estimated stiffness value of PVC material.

6.6 Conclusion

New procedures for the estimation of the wave speed and the wave dissipation inside pressurized waterways during water-hammer phenomena in presence of local drop of wall stiffness has been proposed. These procedures were validated by a series experimental tests that have been carried out in a multi-reach steel pipe where the weak reaches were physically modeled by exchanging the steel reaches by aluminum and PVC materials. They are based on acquiring and processing pressure and vibration records obtained at two sections of the test pipe. These methods are also able to estimate the position of the weak reach when only one PVC reach is used. They include the wavelet decomposition and filtering techniques and the Fast Fourier Transforms.

For the signal processing procedure based on pressure excitation with steep wave front, the following points may be concluded:

1. The measured water transient pressures at two end positions of the test pipe can be used to predict the front wave speed of an excitation traveling between them. Three different methods were applied to estimate this crucial parameter required in the time–distance transformation process. They are based on: (i) the determination of the time separating the maximum front peaks of the signals, (ii) the time separating the intersection point of the regression line for the steady-state pressure and the regression line for the first pressure front, and (iii) the cross-correlation method. It is shown that this parameter can serve as a global indicator of large changes in stiffness (stiffness decreases down to 98 %) of the pipe wall.

2. The wave speeds have been also computed by using geophone sensors. The results are in very good agreement with those obtained from pressure records using steep waves fronts. The processing of the geophone signals give approximately the same mean error but overestimate the wave speed values in “Steel” configuration by about 80 m/s.

3. It is possible to extract very useful information from the reflected pressure signals induced by the boundaries of a PVC weak reach of the test pipe. The localization routine of the weak reach begins with an $\mathcal{F}$ analysis of the two measured pressure signals. This allows a rough approximation (between 3.2 % and 22.2 %) of the middle position of the weak reach. The time obtained by this approach is used to choose the appropriate peaks in the details and approximations of the wavelet decomposition of one measured signal. This latter analysis predicts very well the position of the weak reach boundaries with a maximum relative mean error of 5.9 %.

4. Once the length of the PVC weak reach is found, the severity of the local stiffness change of the pipe wall can also be estimated by using the standard wave speed equation inside the weak reach. This wave speed is determined

from the predicted length of the weak reach and the estimated front wave speed of the test pipe configuration. The relative mean errors reach a maximum of 20.6 % for the tested configurations with one PVC reach.

5. It was possible to evaluate the wave dissipation factor by using the steep front wave pressures. Significant and proportional dissipation differences of +44 % in "Steel+PVC1,2,3" and +77 % in "Steel+PVC4" relative to the "Steel" configuration have been observed. Such differences cannot be identified for the "Steel+Alu" cases. The wave dissipation factor during transients can be considered as second global indicator of local and large changes in stiffness (stiffness decreases down to 98 %) of the pipe wall.

Regarding the signal processing procedure based on the progressive stoppage of the flow by the shut-off valve, the following conclusions can be mentioned:

1. The estimation of wave speed from pressure records starts with decomposing each signal P1 and P2 into an approximation A_J and several details D_i components using the wavelet approach. It continues with the computation of the energy content history of the filtered pressure signal P1 using the floating Root Mean Square (RMS). The procedure ends by applying the cross-correlation technique between the signature of pressure P1 and the filtered pressure P2 in purpose to estimate the travel-time of the water-hammer wave speed between the two measurement pressure sensors.

2. The mean and standard deviation of the wave speeds estimated from steep pressures and from those obtained from the progressive stoppage of the flow by the shut-off valve show a very good agreement with a maximum relative difference around 5 %. The scattering is lower in case of steep wave front than in case of progressive stoppage of flow. In the former case the mean and maximum values of the standard deviation are 20 m/s and 42 m/s, respectively, while in the latter case the maximum standard deviation reaches 73 m/s with a mean value of 40 m/s.

3. By using the $\mathcal{F}$ analysis for the pressure signals it was possible to localize one weak reach that has a very low stiffness (PVC reach) relative to the steel. The error in estimating the position of such reach relative to the real position of its middle varies from 3.3 % to 18.1 %.

The proposed monitoring procedure is based on a continuous acquisition of the transient pressure signals and calculating the wave speed. Once a significant and persistent drop of the wave speed value is detected, a drop of the wall stiffness is suspected to be occurred somewhere along the shaft. The pressure $\mathcal{F}$s and the frequency response function $H(f)$ should reveal new peaks at frequencies that corresponds to reflections from the weak reaches. The wavelets approach is then used to locate the weakness and to estimate its severity. The actual state of the pipe (i.e. penstock, steel-lined pressure tunnel or shaft) with weak reach will be

then considered as the basic configuration for the future monitoring records. The reflections coming from other irregularities such as galleries and caverns near the tunnel and from partially closed valves can easily be discarded due to their known locations. The air pocket sources have a different pressure print out than the gradual drop of wall stiffness. They are characterized by a drastic and scattered drop of the wave speed. The roughness increase due to corrosion of the steel liner is expected to have minor effect. A local significant change of the cross-section area of the tunnel can be caused, for example, by the yielding of the steel liner after the loosening of its support.

In Chapter 8, the practical application of the proposed method will be tested through a series of in-situ measurements which have been carried out at a pressure shaft of a pumped-storage power plant in Switzerland. These measurements are obtained by dynamic pressure and geophones sensors placed at both ends of the pressure shaft. They give additional information about the steepness, energy and dissipation of water-hammer waves generated during start-up and shut-down of pumps and turbines.

Chapter 7

Prototype measurements

This chapter describes the Grimsel II pumped-storage plant and presents the in-situ monitoring system which was used to acquire the pressure and vibration measurements from the shaft of the high pressure side. The analysis and processing of the in-situ data are given in Chapter 8.

7.1 Description of the site

The Grimsel II pumped-storage power plant is located in the Canton of Bern, in the central part of Switzerland, at an elevation of 1 760 m a.s.l. (Fig. 7.1a). It is in operation since 1982. The plant, owned by Kraftwerke Oberhasli AG (KWO), has an underground powerhouse, equipped with four separated pump-turbine units with a total installed capacity of 350 MW (Figs. F.1a, F.2 and F.4). A 4 km long headrace tunnel with an internal diameter of 6.8 m connects the Lake Oberaar (the upper reservoir) to the vertical 123 m high surge tank of 13 m in diameter. A security butterfly valve (Fig. F.3b) is installed downstream of the surge tank and followed by the steel-lined shaft which has an internal diameter of 3.8 m and a length of about 750 m. The upstream end of the shaft is connected to a 170 m long inclined tunnel of 4.14 m of internal diameter. It is the extension of the pressure shaft excavation (Fig. F.5) and functions together with the main surge tank as an inclined surge shaft. The steel-lined pressure shaft has a slope of 100 % (45^o) and conveys water from El. 2 213 to the powerhouse. An accessible steel-liner reach of about 1.5 m (Fig. 7.2a) is located just upstream of the bifurcation which distributes the water at the high pressure side to the four machines inside the powerhouse. The control and security valves situated in the powerhouse are shown in Figs. F.1b and F.2. On the low pressure side, downstream from the hydraulic machines, a third vertical surge tank, 155 m high with a diameter of 8 m, is connected laterally to the 300 m tailrace tunnel which connects the powerhouse to Lake Grimsel (the lower reservoir).

Fig. 7.1b shows a schematic 3D view of this water conveyance system, including the shaft, the surge tanks and the powerhouse. The locations of the measure-

ment stations S1 and S2 and the lateral cross-section of the steel-lined shaft, are also shown.

7.2 In-situ measurement instrumentation and data acquisition

In this section, the existing and new in-situ acquisition systems and instrumentation are presented. It includes the description of the installed sensors, the signal conditioning and synchronization, the hardware and software of the data acquisition scheme, as well as, the data storage procedure.

7.2.1 The existing monitoring system

The Grimsel II pumped-storage plant is equipped with a monitoring system which allows the following measurements:

- the water levels at the upstream Lake Oberaar and downstream Lake Grimsel
- the water levels at the upstream and downstream vertical surge tanks and inside the inclined surge shaft
- the water pressure at the entrance of the powerhouse (at section S1 of Fig. F.4)
- the water flow discharge of each pump and turbine of the 4 units.

The acquired data of the existing system are transmitted to the command and control center of KWO in Innertkirchen village at a distance of about 20 km from the site. The powerhouse machines and valves are automatically controlled from this center.

The examination of the existing acquired data reveals that the water level measurements inside the vertical surge tank and the inclined shaft are only valid to measure the water mass oscillation and the mean upstream water pressure inside the pressure shaft (Hachem, 2009b). The existing pressure sensors have a maximum sample frequency of 1 Hz which is around the double of the fundamental frequency of the shaft ($= a/4\,L = 0.45\,\text{Hz}$) in which a is the mean value of the theoretical water-hammer wave speed inside the pressure shaft determined from Eq. (4.38) by using the parameters values given in Table (F.1) and L is the length of the pressure shaft between the inclined surge shaft and the dead end of the water distributor inside the powerhouse ($\approx 762\,\text{m}$). These sensors cannot detect water-hammer pulsation and, therefore, new dynamic pressure sensors were needed (Hachem, 2009a,c). The water pressures measured at section S1 at the downstream end of the shaft, present the same problem as for the water level data. For the water flow discharge, the existing acquisition system shown in Fig. F.6, is based on pressure measurements inside a Venturi pipe reach. Its output

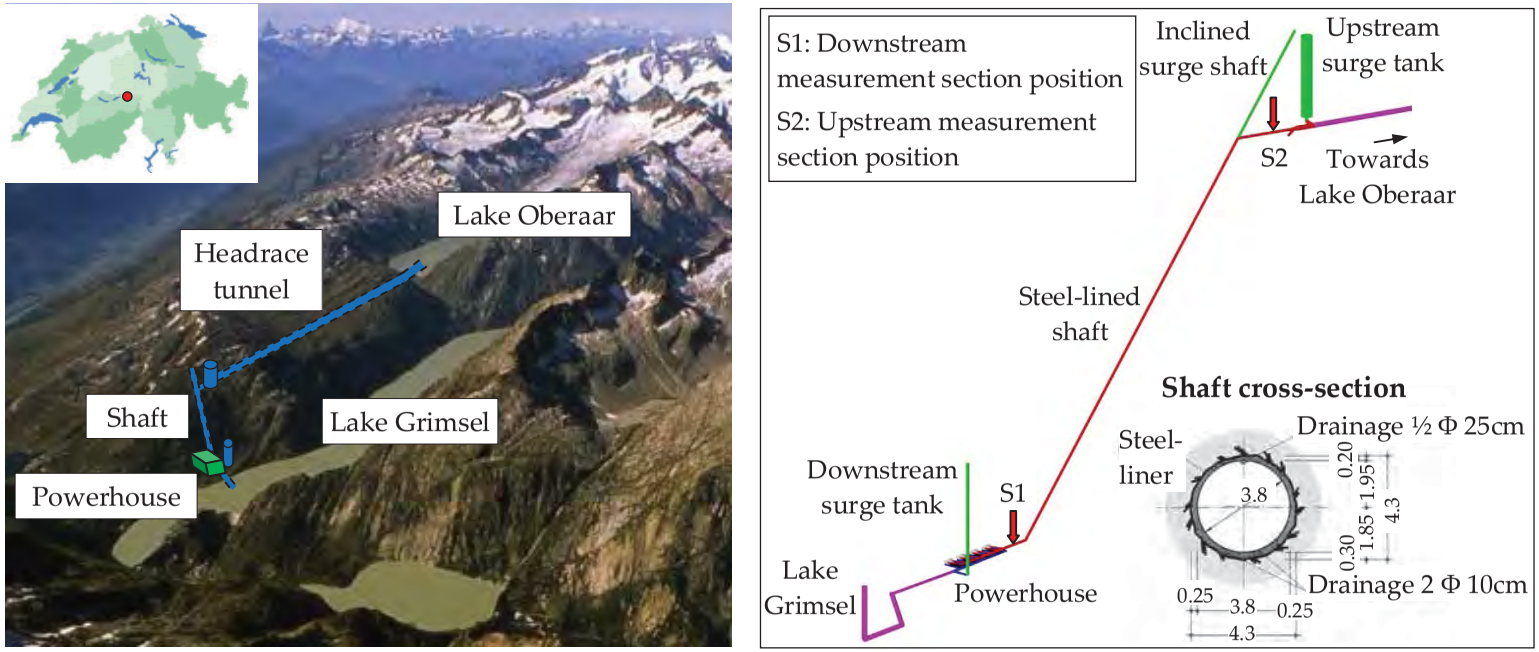

Figure 7.1: Grimsel II pumped-storage scheme, (a) aerial view of the site with the upper and lower reservoir, (b) schematic 3D view of the waterway system with the two positions of the data acquisition systems and a cross-section of the steel-lined shaft.

signal has been used in the new monitoring system to extract the total pump and turbine discharge, q, using the following linear transformation:

$$q\,(\text{in m}^3/\text{s}) = 10\,q\,(\text{in Volts}) \tag{7.1}$$

7.2.2 The new installed monitoring system

7.2.2.1 Pressure sensors

Two dynamic piezoresistive pressure sensors of type "Kistler 4045A" with an absolute pressure range of 100 bars (for the measurement station S1) and 20 bars (for station S2) have been used. The sensitivities of these sensors are equal to 5 mV/bar and 25 mV/bar for the former and latter, respectively. The constant DC electrical excitation current of 24 V needed for these sensors, is provided after transformation of the 48 VDC current available in the powerhouse and in the security valve cavern. These pressure sensors are calibrated by the manufacturer and the output signals, p, are amplified by a "Kistler 4618A2" amplifier type. The calibration laws are:

$$p\,(\text{in bars}) = 10\,p\,(\text{in Volts}) \text{ for the sensor S1} \tag{7.2}$$
$$p\,(\text{in bars}) = 2\,p\,(\text{in Volts}) \text{ for the sensor S2} \tag{7.3}$$

At the measurement section S1 (Fig. F.4), the pressure sensor is screwed inside a hole made in the elbow of the shaft drainage conduit of 150 mm in diameter (Figs. 7.2a and 7.2b). At the measurement section S2 shown in Fig. F.5, the pressure sensor is fixed on the cover plate of the shaft drainage reach of 200 mm in diameter (Figs. 7.3a and 7.3b).

7.2.2.2 Geophones

Two geophones similar to those which have been used in the experimental pipe tests (Section 5.3.2) have been fixed on the exterior face of the steel-liner at the measurement sections S1 and S2 as shown in Figs. 7.4a and 7.4b, respectively. These geophones are unidirectional of vertical upward category (SM-6/UB).

7.2.2.3 Acquisition scheme and synchronization

Each of the two data acquisition systems at S1 and S2 contains one "Kistler" pressure sensor, one "I/O Sensor Nederland, SM-6 4.5 Hz 3 500 Ω" geophone, one "NI-USB-6259 M series" acquisition card (same as the one describe in Section 5.3.5) and one industrial PC (Figs. 7.5a and 7.5b). The total output current of the Venturi measurement system has been transformed to voltage (through a box of electric resistances) and then injected inside the acquisition card at S1. The control command of the valves in the powerhouse, sent from the Innertkirchen control center, are transformed by an electric relay (Fig. 7.6a) to a trigger signal

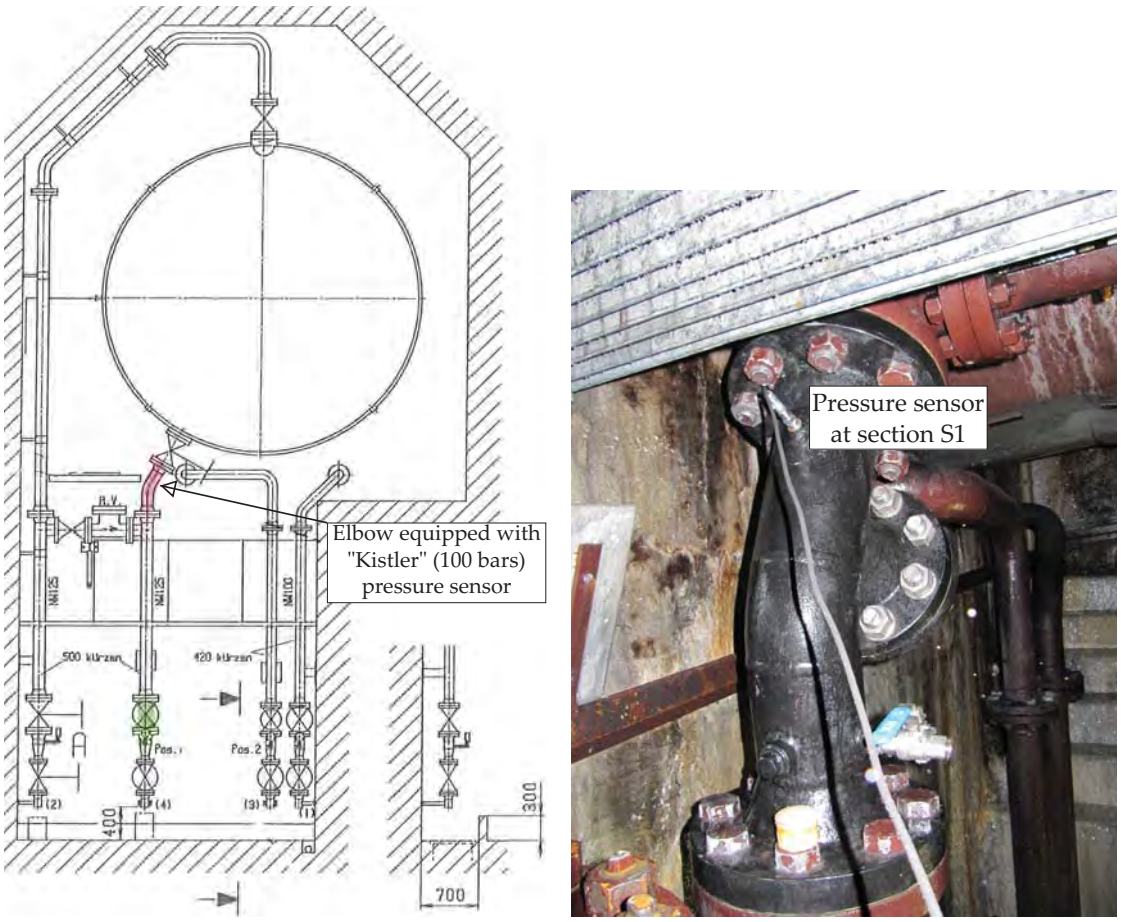

Figure 7.2: Pressure sensor placed at section S1 of the steel-lined shaft of the Grimsel II plant, (a) cross-section view of the shaft at the entrance of the powerhouse with its drainage conduits, (b) photo of the elbow equipped with the pressure sensor.

(a) (b)

Figure 7.3: Pressure sensor placed at section S2 of the steel-lined shaft of the Grimsel II plant, (a) photo of the by-pass drainage reach with its valve ($\Phi = 200\,\mathrm{mm}$), (b) the pressure sensor screwed inside a hole in the cover steel plate of the bypass reach.

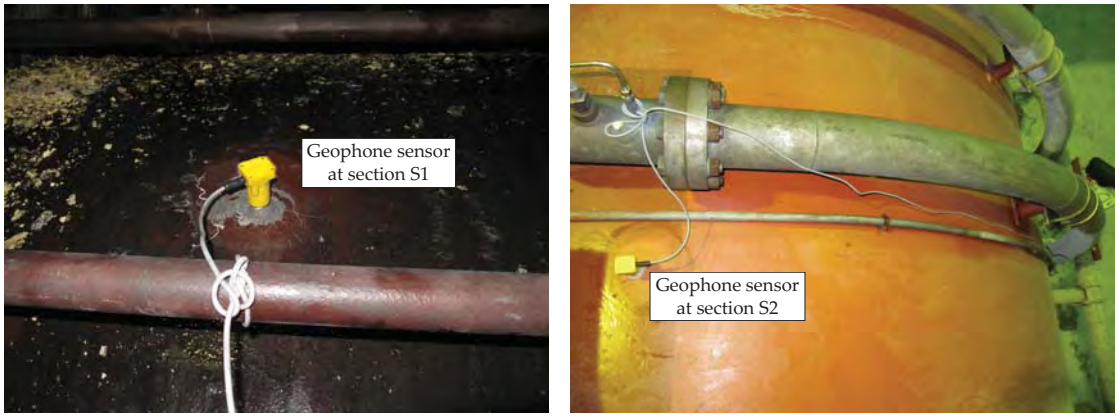

(a) (b)

Figure 7.4: Geophone sensors fixed on the exterior face of the steel-liner of the Grimsel II shaft, (a) at measurement section S1, (b) at measurement section S2.

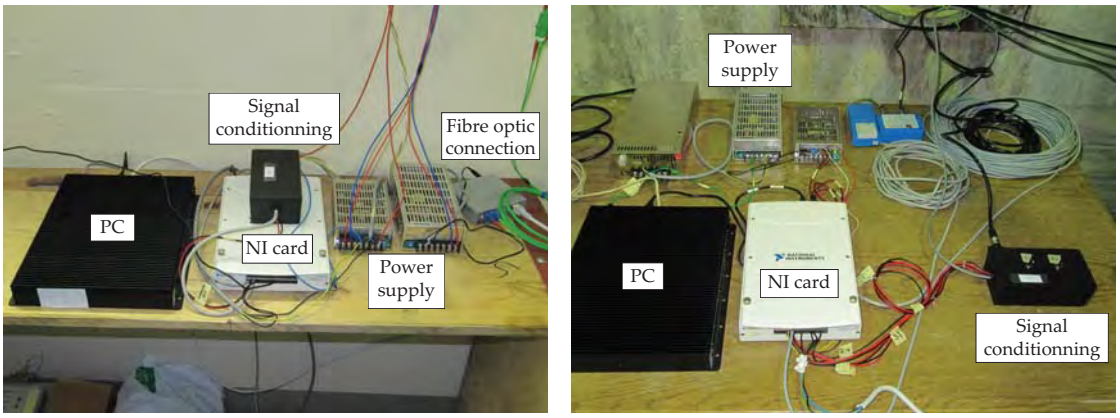

(a) (b)

Figure 7.5: Installed acquisition systems in the Grimsel II plant, (a) at the measurement station S1, (b) at the measurement station S2.

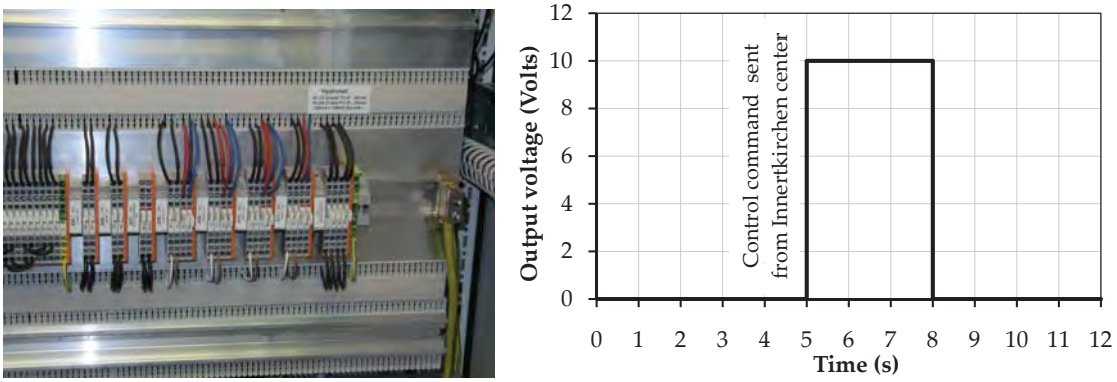

(a) (b)

Figure 7.6: (a) Photo of the electric relay in the Grimsel II powerhouse, (b) the relay output voltage.

of $0 - 10 - 0$ VDC with a plateau of 3 s (Fig. 7.6b). The trigger output signal has been connected to the measurement system at S1.

The synchronization of the two acquisition systems at S1 and S2 is done via a fiber optic cable which connects the two system PCs to the KWO server inside the powerhouse. Every one hour, the internal clocks of the two PCs are automatically synchronized with the KWO server time. The trigger signal acquired at S1 is saved by the acquisition software as a shared variable type (LabVIEW, 2008) and sent to the PC of station S2. This type of network-published variables can be used to write and read across an Ethernet network. Fig. 7.7 illustrates the deployment and hosting process of this type of variables.

The two measurement systems can be controlled via a VPN internet connection (Virtual Private Networking) established by the HydroNet I partner EMPA. The acquired data can be accessed on-line through a secure VPN internet connec-

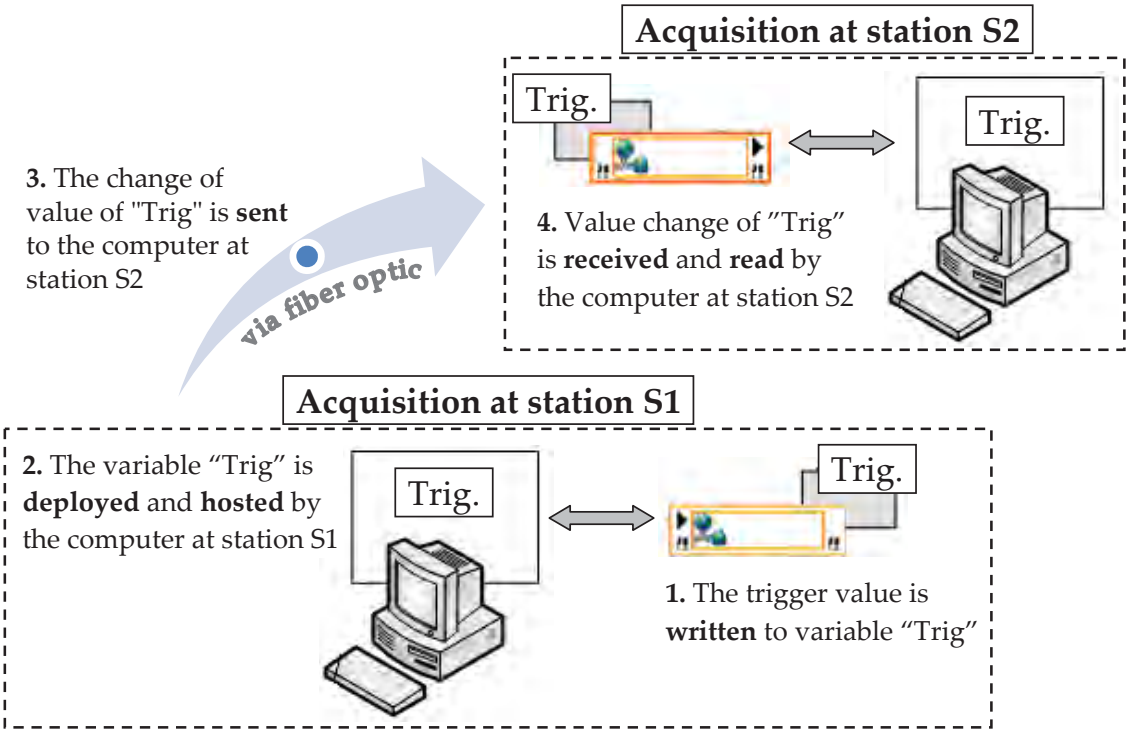

Figure 7.7: Connection scheme of the shared variable of the trigger signal between the two PCs at the measurement stations S1 and S2.

tion.

7.2.2.4 Data acquisition software

The data acquisition software is based on LabVIEW programming platform. The main part of the block diagram of the acquisition code is summarized in Fig. 7.8. The data are acquired continuously in time at a sample frequency of 1 kHz and they are not stored until the trigger signal rises from 0 to 10 V (Fig. 7.6b). The time at the front of the rectangular trigger signal indicates the arrival of the control command from the KWO center. The total storage time has been fixed to 600 s and includes the steady-state and the transient parts of the pressure and vibration signals.

In each PC of the two measurement systems, the storage loop starts by opening a data file of format TDMS (Fig. 5.12) and assigning the date given by the PC clock to the storage directory name. This loop ends automatically after the collapse of the storage duration fixed by the user. A print screen of the front panel for the acquisition stations S1 and S2 is shown in Figs. 7.9 and 7.10, respectively.

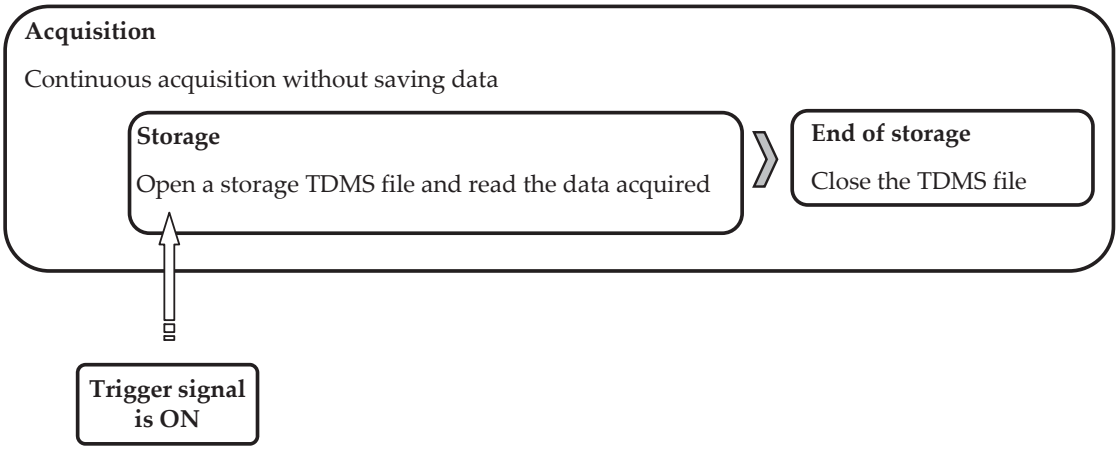

Figure 7.8: Scheme of the bloc diagram of the acquisition LabVIEW code for the in-situ measurements at the Grimsel II plant.

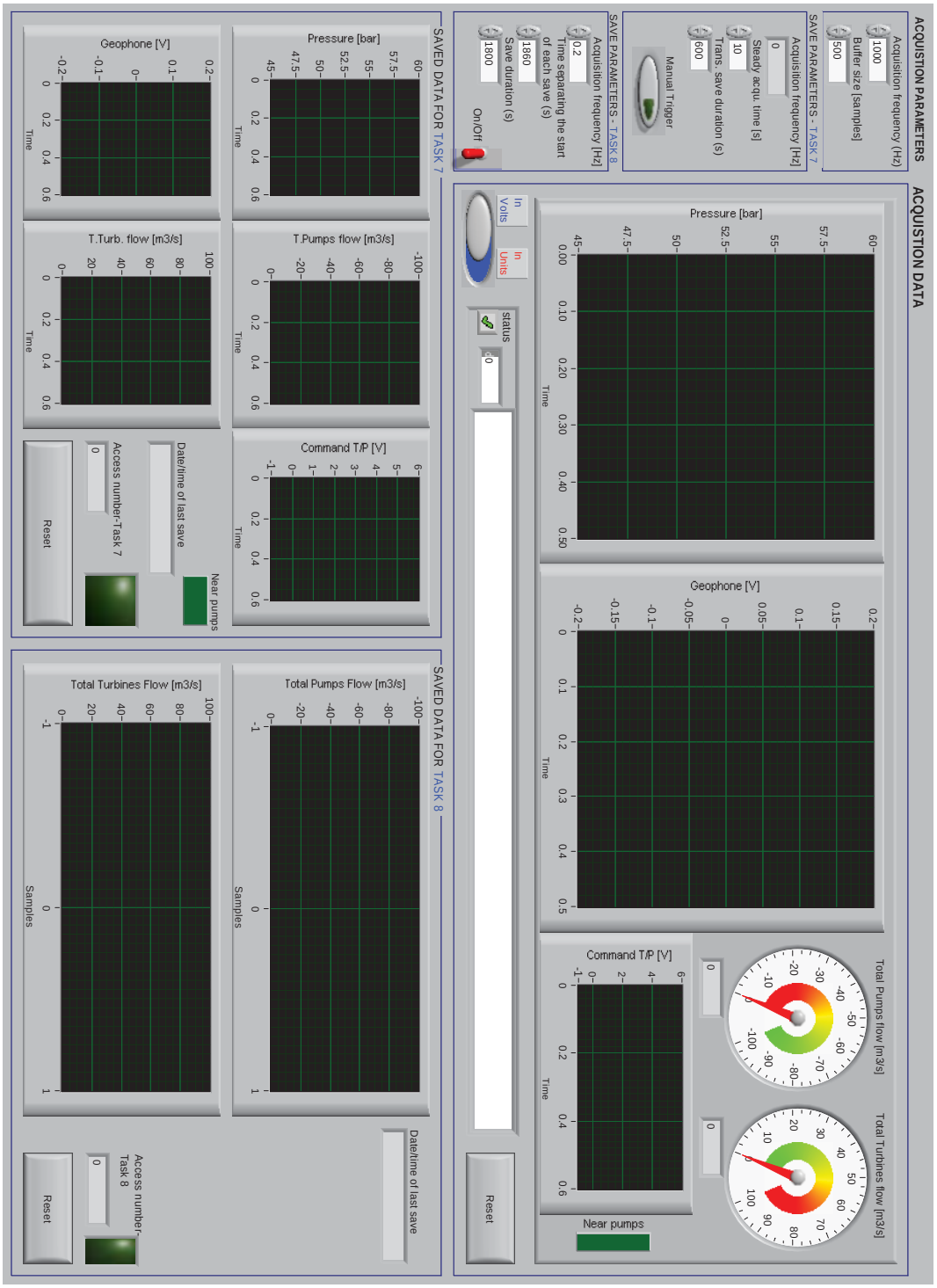

Figure 7.9: Front panel of the acquisition program at station S1.

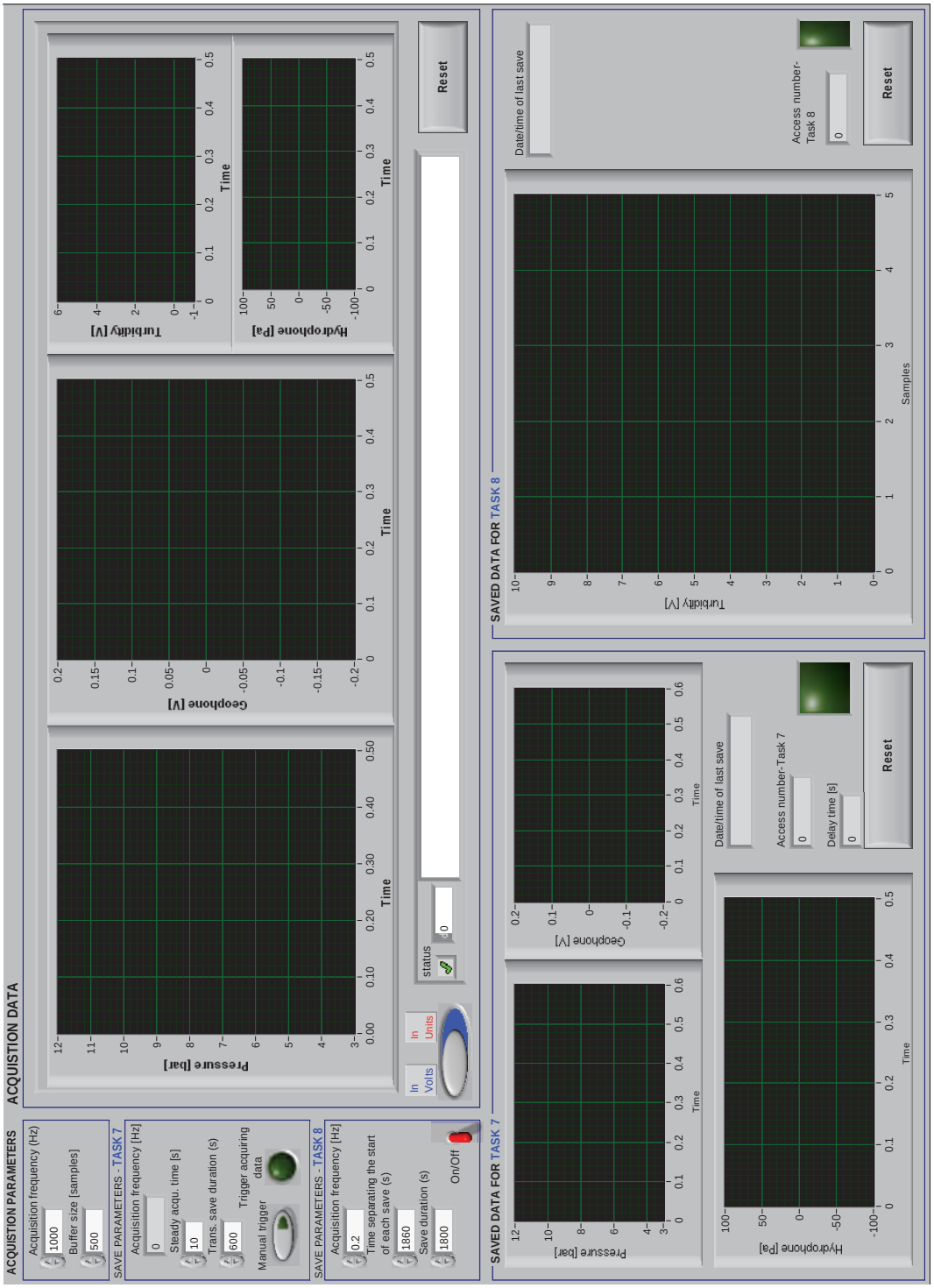

Figure 7.10: Front panel of the acquisition program at station S2.

Chapter 8

Analysis of prototype data

In this chapter, the in-situ measurement data at the Grimsel II plant are presented, analyzed and discussed. The new monitoring approaches proposed in Chapter 6 for detecting, locating and quantifying structurally weak reaches of steel-lined pressure tunnels and shafts are tested. The difficulties encountered during application of these approaches in prototype scale are outlined.

The first section presents in detail the high pressure side of the waterway scheme of the Grimsel II pumped-storage plant and the measured in-situ data of pressures and vibrations.

In the second section, the monitoring approach is applied to the prototype. The practical difficulties of application and uncertainties are also discussed.

The third section introduces the reader to the statistical quality control method. This method is used to establish monitoring charts for the water-hammer wave speed and the wave dissipation coefficient. Finally, some conclusions are given in the fourth and final section.

The major parts of this chapter have been published in Hachem and Schleiss (2011e).

8.1 The layout of the main water-hammer travel paths and the in-situ data measurements acquired from the pressure shaft of the Grimsel II plant

Pumped-storage schemes can store energy in the form of water in purpose to be released through turbines during periods of high electrical demand. The water is pumped from a lower storage reservoir to a higher elevation during off-peak hours. The low-cost energy used for pumping is obtained from nuclear, fossil, wind or solar energy which power output cannot be adjusted to satisfy temporary peak demands. Therefore, pumped-storage plants are very efficient for load balancing. Fig. 8.1 shows the general scheme of such power plants with the schematic histories of pressure transients generated inside the pressure shaft

during one loop of pumping and generating modes.

8.1.1 Layout of the waterway at the high pressure side of the Grimsel II plant

Fig. 8.2 shows in detail a 3D view of the high pressure side of the waterway of the Grimsel II pumped-storage plant with some important point coordinates and paths lengths. Starting from point 1 at the low level end, a bifurcation with eight branches lies between this point and P1 (two branches for each Francis unit). The bifurcation is followed by an inclined steel-lined pressure shaft (between points P1 and 2), a horizontal steel-lined tunnel (from point 2 to point 3), and a concrete-lined headrace tunnel from point 3 towards the Lake Oberaar. The 2-3 reach includes the shut-off security valve at point P2 and a dead end junction (between points 3 and 5) which provides the connection to the future pressure shaft for the power plant extension project. At point 2, a concrete-lined surge shaft is connected to the junction between the horizontal tunnel and the pressure shaft. The vertical surge tank is located at point 4 and is connected to the headrace tunnel by a tunnel reach of 15 m long. At point 8, the pressure shaft travels below a 2.5 m wide ventilation tunnel. The distance between the top of the steel-liner and the bottom of this tunnel is around 2.5 m. In this area, a thick backfill concrete layer (thickness up to 4 m) fills the space between the bottom of the steel liner elbow and the rock. This reach of the pressure shaft is the only place where a significant differences in the wall stiffness of the pressure shaft is detected from the as-built existing drawings. The thickness of the steel-liner varies from 40 mm at point P1 to 16 mm at point 2. The backfill concrete having a thickness of about 25 cm (Fig. 7.1b), fills the space between the steel liner and the surrounding homogeneous granite rock mass.

8.1.2 In-situ output data obtained from normal operating conditions

8.1.2.1 Start-up of pumps and turbines

During the pump start-up, the outlet spherical valve (valve 4 of the pump 7 in Fig. F.2) is kept closed to reduce the electrical load on the motor. When the pump speed reaches the rated speed, the spherical valve is gradually opened. In the Grimsel II pumped-storage plant, the pump start-up is preceded by a start-up and shut-down of the turbine of another Francis unit. This produces the electrical power needed to launch the pump motor. During the turbine start-up, the valve at the bypass conduit of the inlet spherical valve (Fig. 6.3) is first opened to balance the water pressure between its both sides. The inlet valve (valve 4 of the turbine 6 in Fig. F.2) is gradually opened simultaneously with the wicket gates. The latter are kept opened to the breakaway gate position until the unit speed is about 60 % of the rated speed then are closed to speed-no-load position. As soon

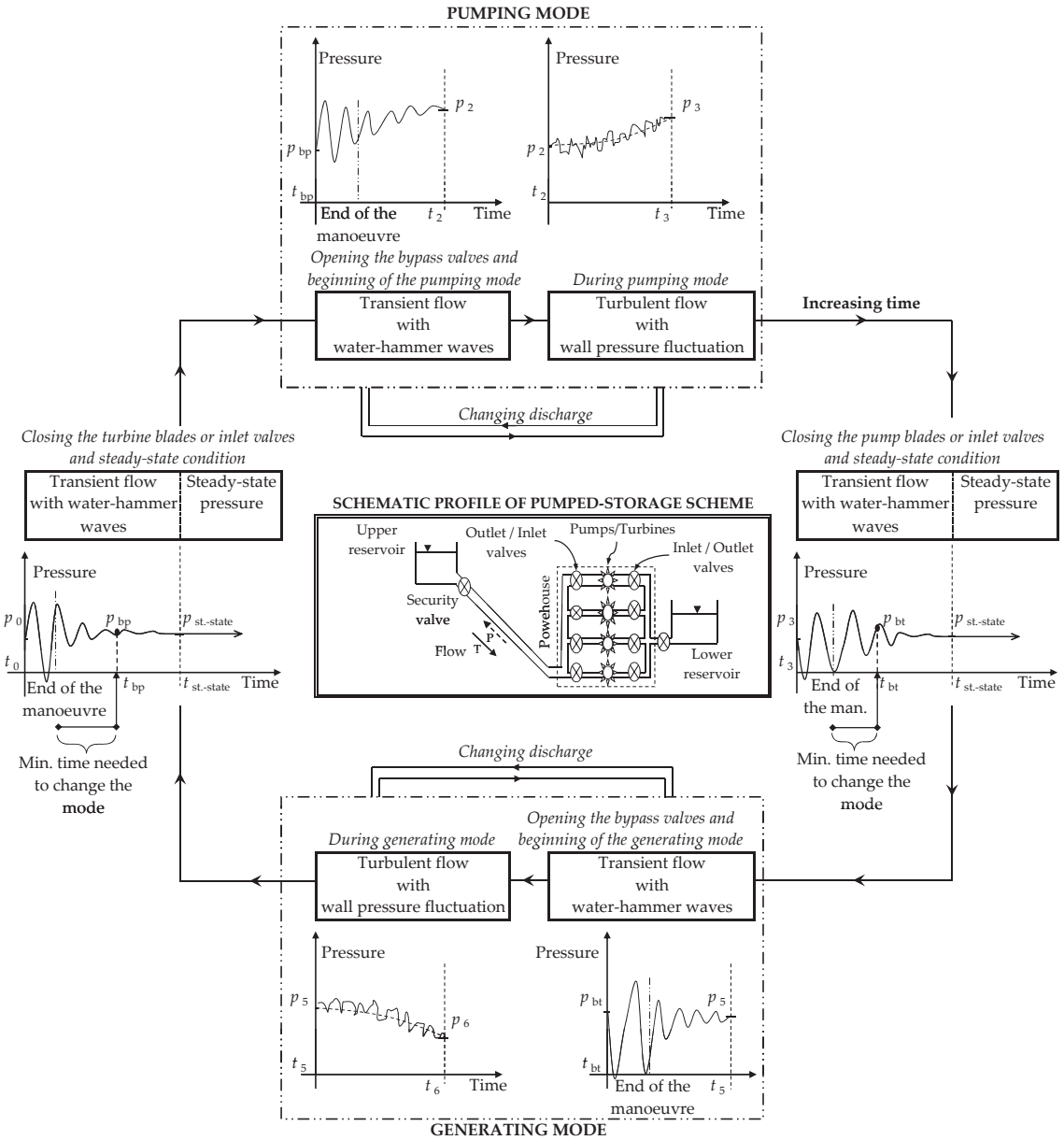

Figure 8.1: General scheme representing the pressure fluctuations histories inside the pressure shaft of pumped-storage power plants during one loop of pumping and generating modes.

Table of coordinates at axis (m)

Point	X	Y	Z
1	0.00	0.00	1763.50
2	578.72	0.00	2211.27
3	689.78	-30.50	2214.87
4	766.28	-42.40	2216.38
5	644.90	-51.45	2214.75
6	709.70	0.00	2336.00
7	779.43	-26.17	2336.00
8	129.83	0.00	1766.93
P1	103.83	0.00	1763.50
P2	639.93	-11.86	2214.70
a	9.89	0.00	1763.50
b	27.00	0.00	1763.50
c	36.89	0.00	1763.50
d	54.00	0.00	1763.50
e	63.89	0.00	1763.50
f	81.00	0.00	1763.50
g	90.89	0.00	1763.50

Table of reaches lengths (m)

Reach	L
1-a, b-c, d-e, f-g	9.89
a-b, c-d, e-f	17.11
g-P1	12.94
P1-8	26.46
8-2	632.05
1-2	762.34
2-P2	64.00
P2-3	49.53
3-4	98.72
3-5	49.53

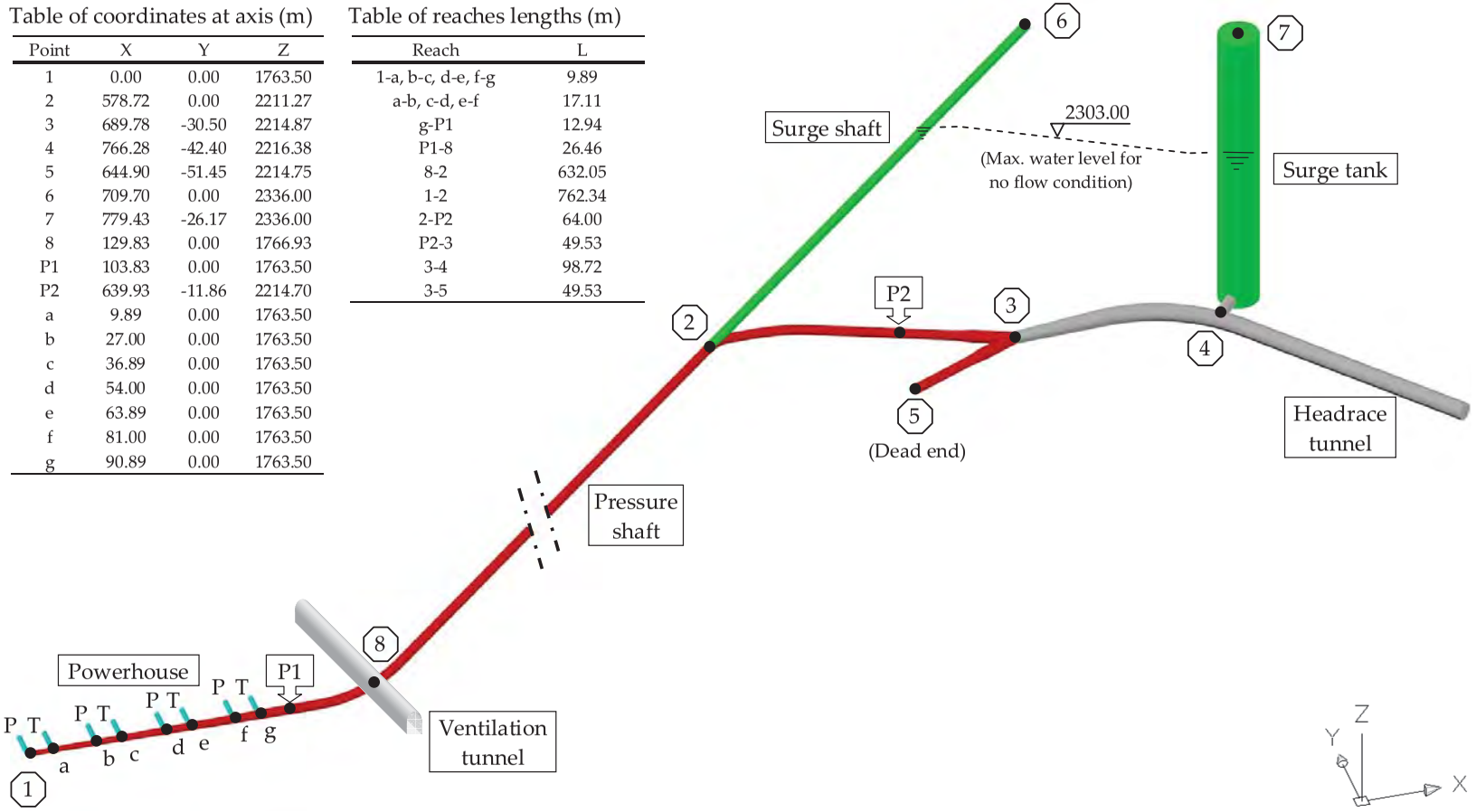

Figure 8.2: 3D schematic view of the high pressure side of the waterway of Grimsel II plant from the bifurcation inside the powerhouse to the downstream end of the headrace tunnel. The coordinates and lengths of the main reaches are given in the Tables.

as the unit reaches the synchronous speed it becomes ready for electric load acceptance. For load acceptance, the wicket gates are opened at the prescribed rate. The manoeuvres of these gates are controlled by the governor system.

Figs. 8.3 show the typical records of the total flow and the water pressures acquired at sections S1 and S2 during the pump start-up of one unit from an initial no-flow condition (the initial total flow in the shaft is zero). The corresponding output records of the geophones are given in Figs. 8.4. Similar graphs are depicted in Figs. 8.5 and 8.6 for pressures and geophones vibrations generated during the start-up of one turbine of the Grimsel II powerhouse.

In both pumps and turbines start-up cases, pressure fluctuations having a maximum amplitude around 1 bar and a frequency near 0.46 Hz are generated by the opening of the pressure balance bypass of the spherical valve. The opening of this valve begins after around 50 s to 80 s from the beginning of the pressure balance procedure. The total flow inside the pressure shaft increases from zero to around 16 m^3/s in about 72 s. In the pump start-up mode, the flow decreases again to zero in around 55 s.

During the pump start-up, the beginning of the turbine shut-down manoeuvre generates a steep positive increase of pressure at S1 of about 1.8 bar in amplitude and 1.5 s in duration. After 12 s from the beginning of the turbine shut-down, the outlet valve of the pump is opened and the total flow changes progressively its direction inside the shaft. Its value increases and reaches $-20\,m^3/s$ in about 50 s (negative discharge indicates pumping flow).

After the end of the pump and turbine start-up manoeuvres, pressure fluctuations having an oscillation period of 220 s ($f = 0.0045$ Hz) are observed. Their amplitude is around 1.5 bar and 0.9 bar for the pump and turbine start-up modes, respectively. The fluctuations are generated by the mass oscillation phenomenon between the upper reservoir (Lake Oberaar) and the surge system (the upstream vertical tank and the inclined shaft). The theoretical value of the maximum amplitude surge, S_{max}, and the mass oscillation period, T_{osc}, of a simplified frictionless model including the surge vertical tank, the headrace tunnel and the upper reservoir of Grimsel II plant are 1.2 bar and 239 s, respectively. These values are computed for a rapid closure of the valve using the following equations (Parmakian, 1963):

$$S_{max} = \frac{q_0}{F}\sqrt{\frac{F\,L_h}{A_h\,g}} \tag{8.1}$$

$$T_{osc} = 2\,\pi\sqrt{\frac{F\,L_h}{A_h\,g}} \tag{8.2}$$

in which q_0 is the steady-state flow of $20\,m^3/s$, F is the cross-sectional area of the vertical surge tank ($= 132.7\,m^2$), L_h is the headrace length from the vertical surge tank to the upper reservoir ($= 3\,900$ m) and A_h is the cross-sectional area of the headrace tunnel ($= 36.3\,m^2$).

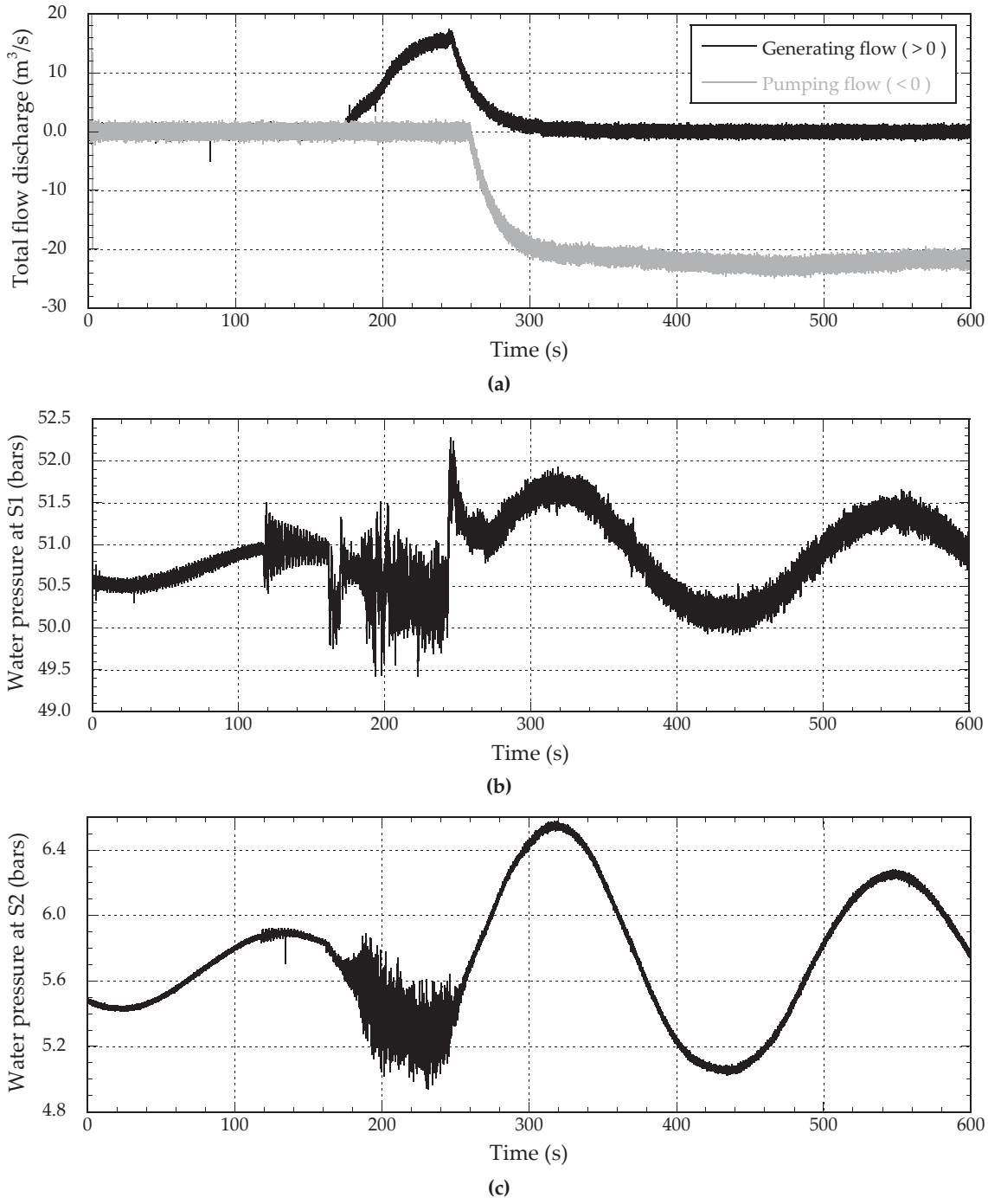

Figure 8.3: Output records of the in-situ measurements acquired from the steel-lined pressure shaft of the Grimsel II power plant during the **start-up of pumps**, (a) total flow discharge, (b) pressure at section S1, and (c) pressure at section S2.

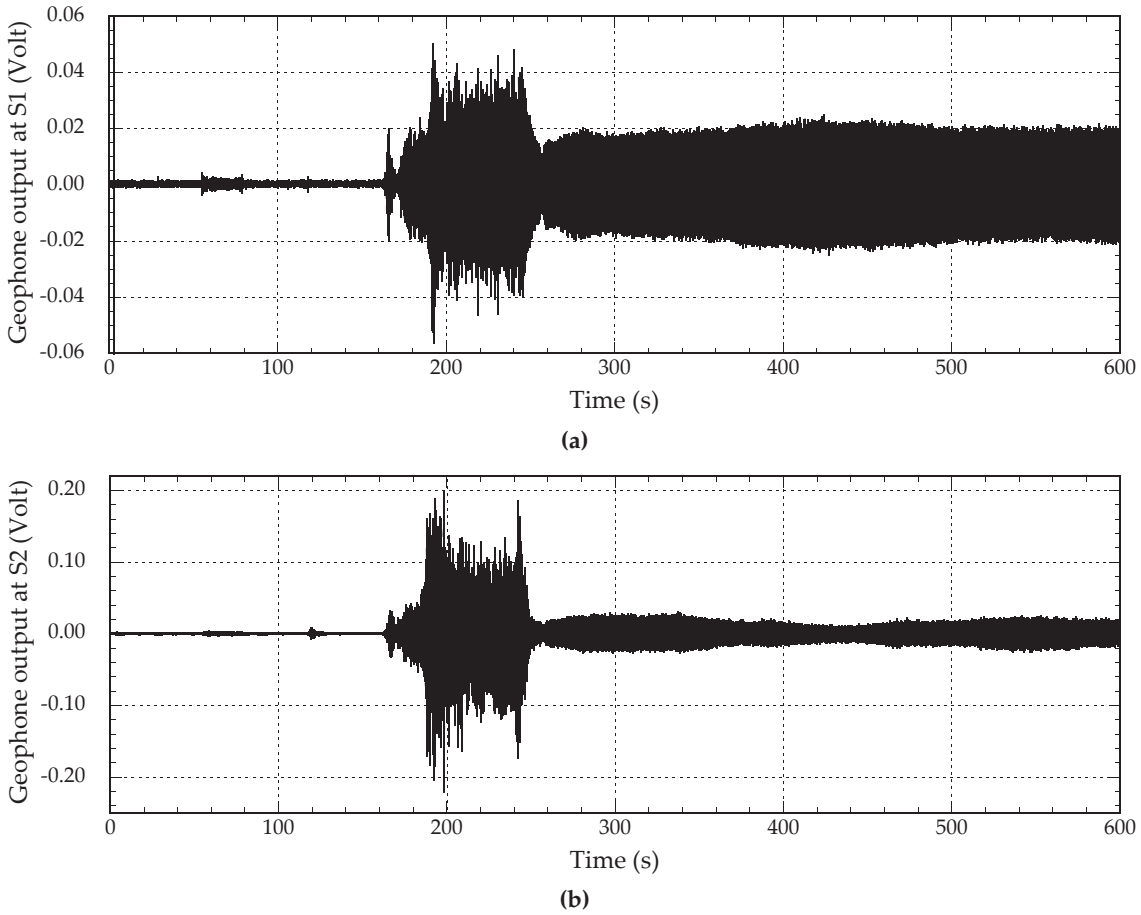

Figure 8.4: Output records of the in-situ measurements acquired from the steel-lined pressure shaft of the Grimsel II power plant during the **start-up of pumps**, (a) geophone output at section S1, and (b) geophone output at section S2.

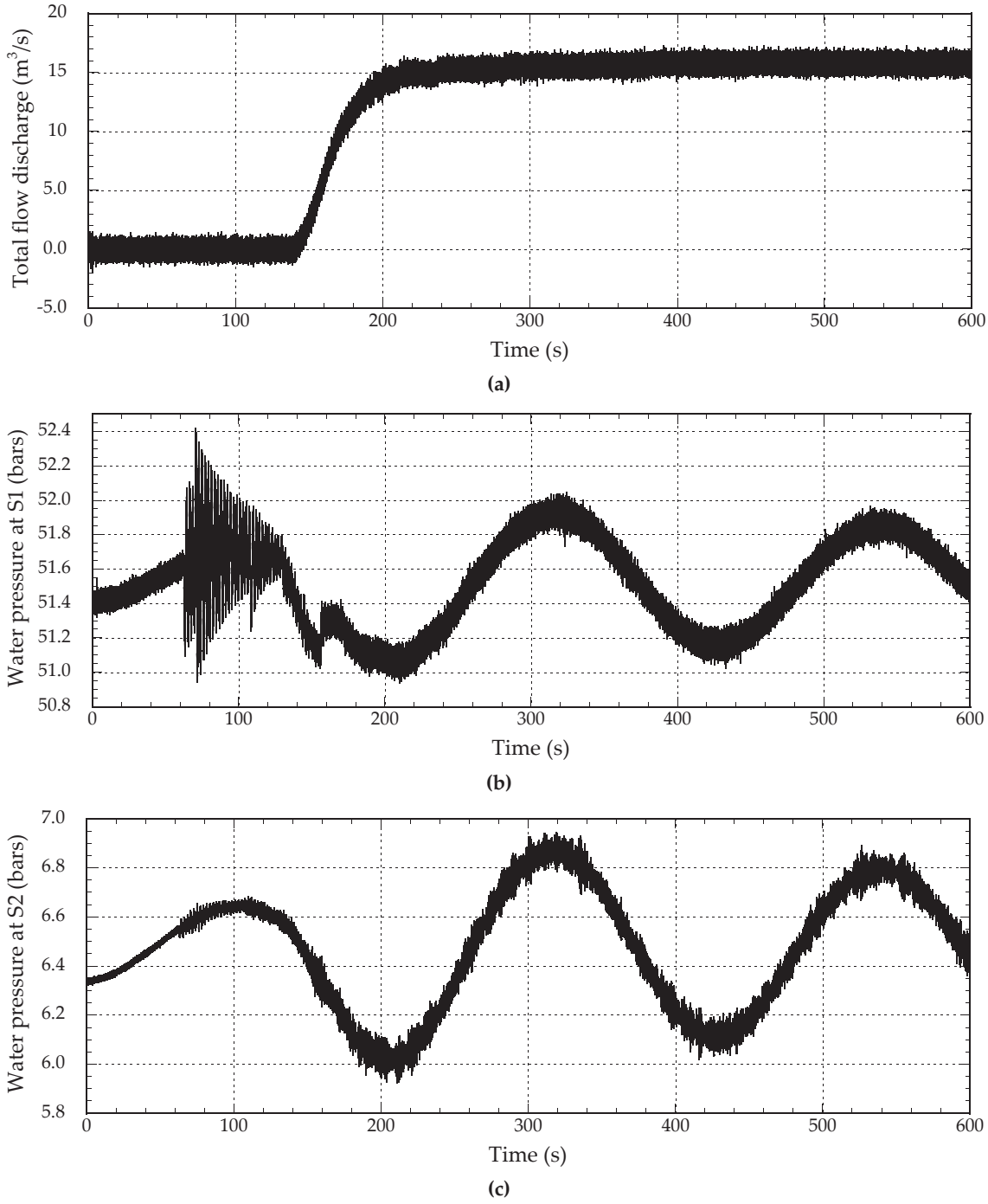

Figure 8.5: Output records of the in-situ measurements acquired from the steel-lined pressure shaft of the Grimsel II power plant during the **start-up of turbines**, (a) total flow discharge, (b) pressure at section S1, and (c) pressure at section S2.

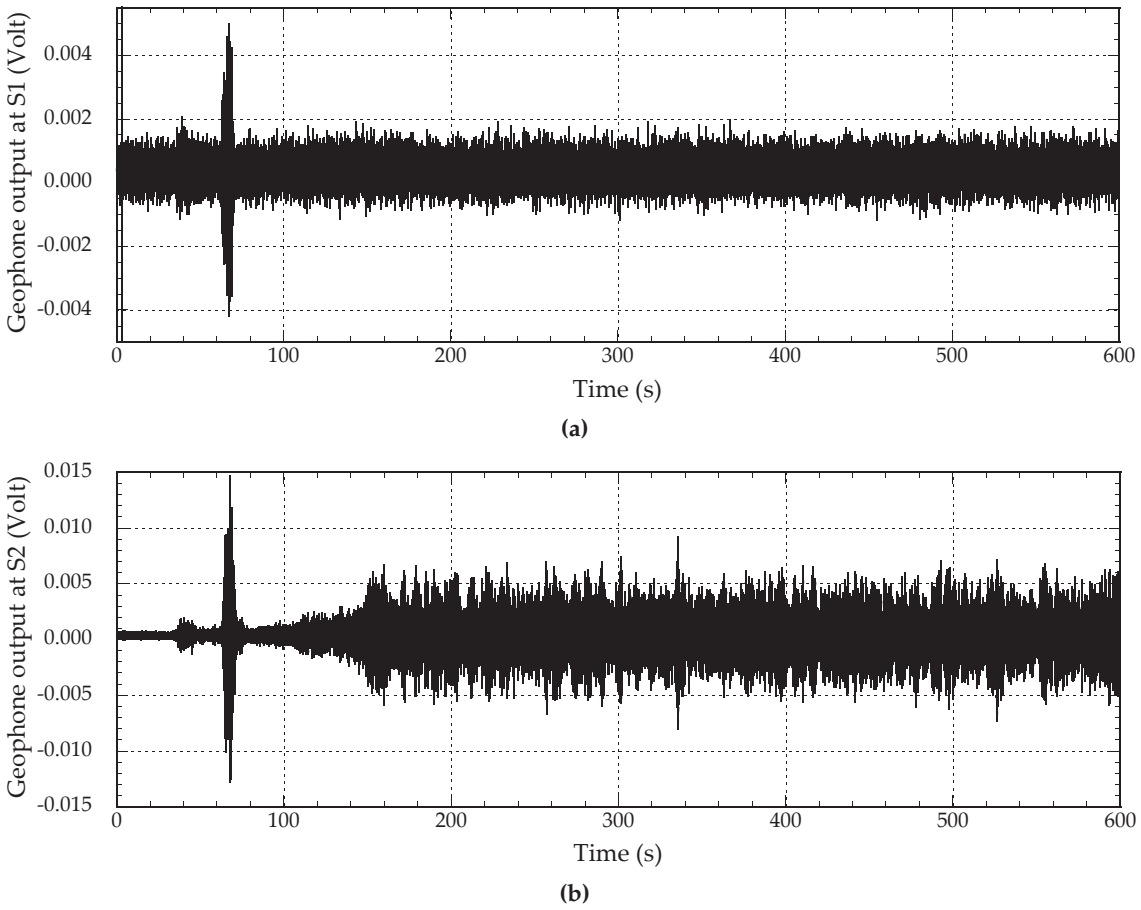

Figure 8.6: Output records of the in-situ measurements acquired from the steel-lined pressure shaft of the Grimsel II power plant during the **start-up of turbines**, (a) geophone output at section S1, and (b) geophone output at section S2.

At the measurement section S2, the pressure fluctuations induced by the bypass opening during the turbine start-up have small amplitude. The main part of energy of the water-hammer waves are reflected back to the powerhouse by the junction at point 2 (Fig. 8.2). During the start-up of the pump motor, high frequency pressure fluctuations of around 100 Hz are detected at both pressure sensors S1 and S2 (Figs 8.3b and 8.3c between times 180 s and 250 s). These pressure fluctuations are probably generated by the fluid-structure interaction between the water, the liner wall and the pump motor. They are not detected by the pressure and geophone sensors during the turbine start-up mode (Figs. 8.5 and 8.6). These perturbations propagate as stress waves inside the steel-liner of the pressure shaft and reach section S2 without significant dissipation. The stress waves generate geophones output with high amplitude at sections S1 and S2 (Figs. 8.4).

The mass oscillation phenomena is not relevant for the monitoring of the pressure shaft. Therefore, the parts of the signals generated by them are ignored. More, the above discussion reveals that the most relevant part of the measurements are those acquired during the opening of the inlet valve. They contain the water-hammer fluctuations which are generated directly after the steady-state condition. This allows to follow the first wave front between sections S1 and S2 to estimate the value of the water-hammer wave speed. Therefore, these parts of the pressure and geophone output signals of 130 000 samples in length are analyzed in detail in Section 8.2.

8.1.2.2 Shut-down of pumps and turbines

During the normal pump shut-down, the spheric outlet valve is first closed slowly and then the power supply of the pump motor is switched off. The normal turbine shut-down mode begins with the electric load rejection of the generator followed by the simultaneous closure of the wicket gates and the spheric inlet valve.

In Figs. 8.7, the typical histories of the total flow and pressures at sections S1 and S2 during the pump shut-down are shown. The corresponding signals of the geophones are given in Figs. 8.8. The output measurement data for the turbine shut-down mode are given in Figs. 8.9 and 8.10. These records are automatically acquired during the shut-down of the last operated unit of the Grimsel II powerhouse (the total flow decreases towards zero).

The closure time of the spheric valve during the pump shut-down is about 70 s. The total flow discharge decreases from $-20\,\mathrm{m}^3/\mathrm{s}$ to zero. At the beginning of the valve closing manoeuvre, an important drop of pressure at section S1 of about 6.5 bars is observed. It propagates upstream towards the surge system and is detected by sensors at section S2. The front steepness of this pressure drop is around 4.5 s. Pressure fluctuations of 2 bars in amplitude and 0.46 Hz in frequency are observed at around 22 s after the time of the minimum pressure peak at S1. At zero flow, the mass oscillation phenomenon between the upper reservoir and the surge systems is observed. The part of the pressure and geophone signals between the times $t = 20\,\mathrm{s}$ and $t = 150\,\mathrm{s}$ in Figs. 8.7 and 8.8 are considered in the

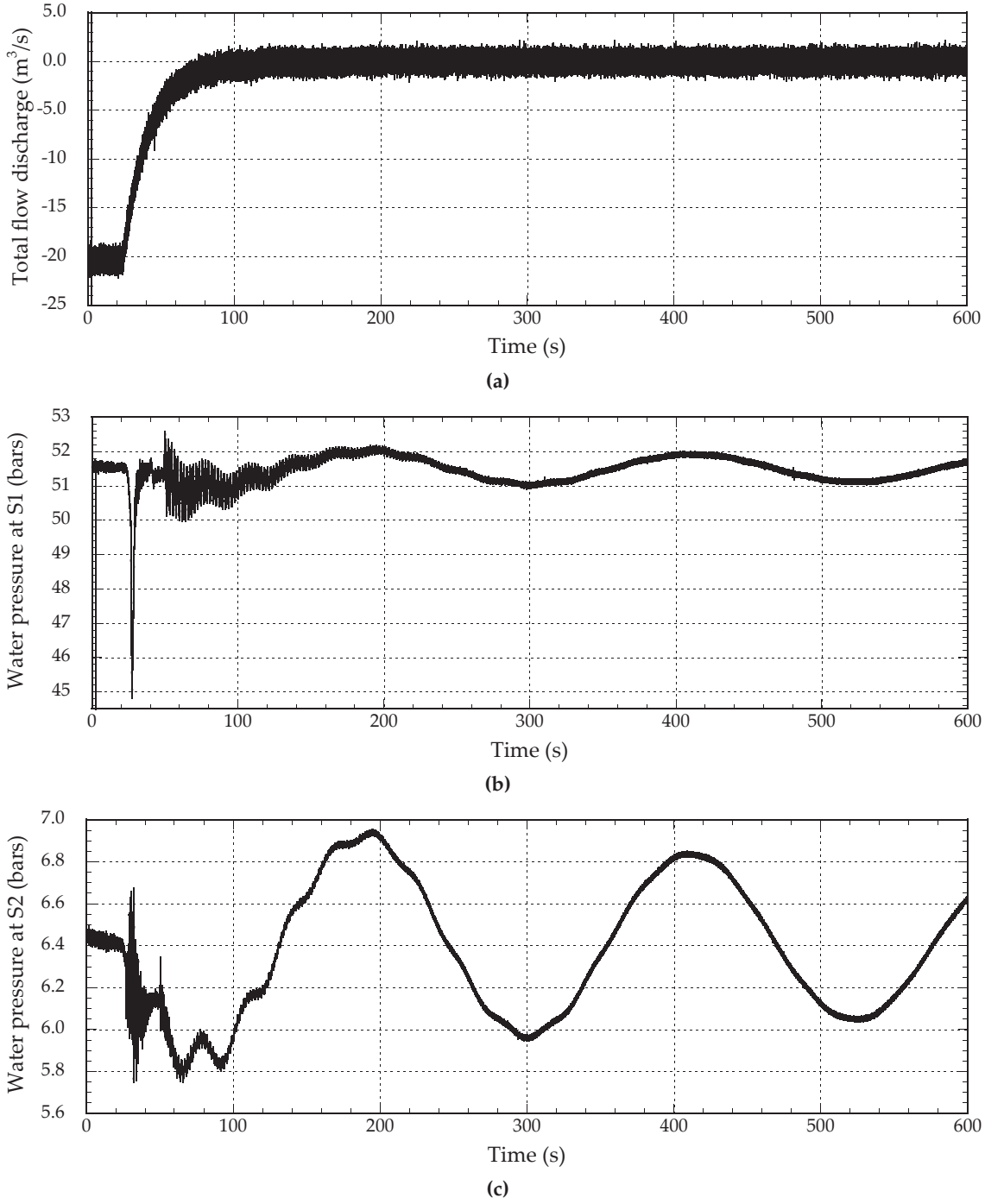

Figure 8.7: Output records of the in-situ measurements acquired from the steel-lined pressure shaft of the Grimsel II power plant during the **shut-down of pumps**, (a) total flow discharge, (b) pressure at section S1, and (c) pressure at section S2.

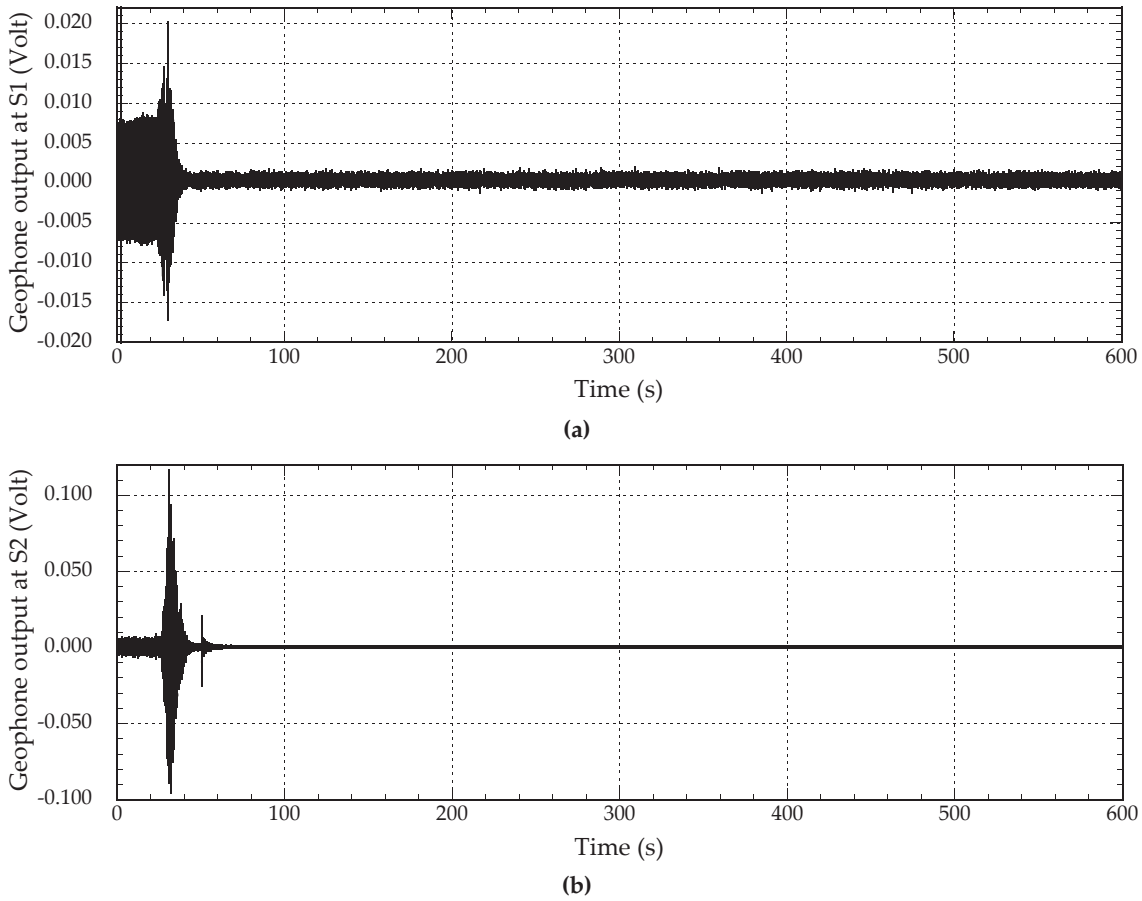

Figure 8.8: Output records of the in-situ measurements acquired from the steel-lined pressure shaft of the Grimsel II power plant during the **shut-down of pumps**, (a) geophone output at section S1, and (b) geophone output at section S2.

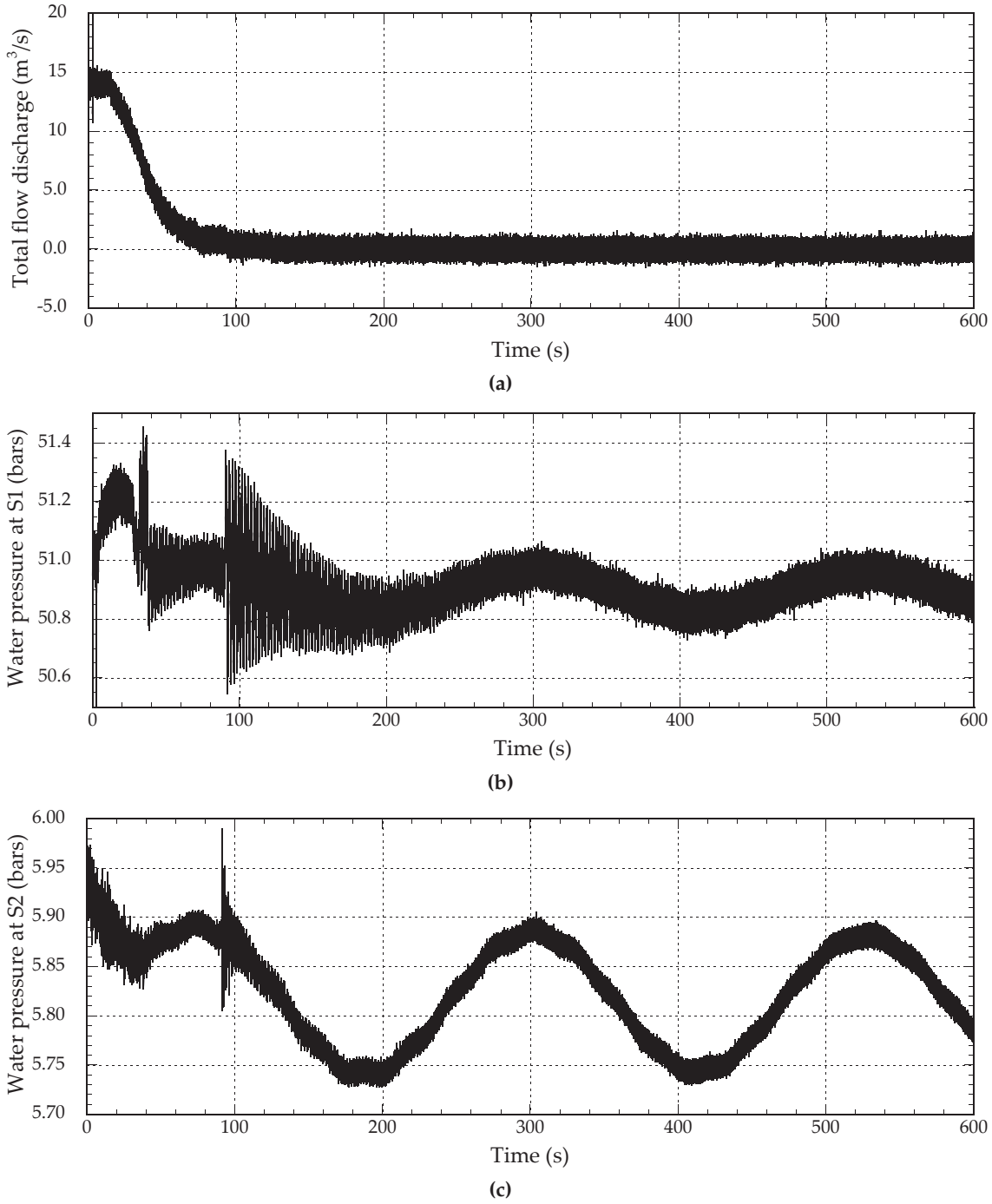

Figure 8.9: Output records of the in-situ measurements acquired from the steel-lined pressure shaft of the Grimsel II power plant during the **shut-down of turbines**, (a) total flow discharge, (b) pressure at section S1, and (c) pressure at section S2.

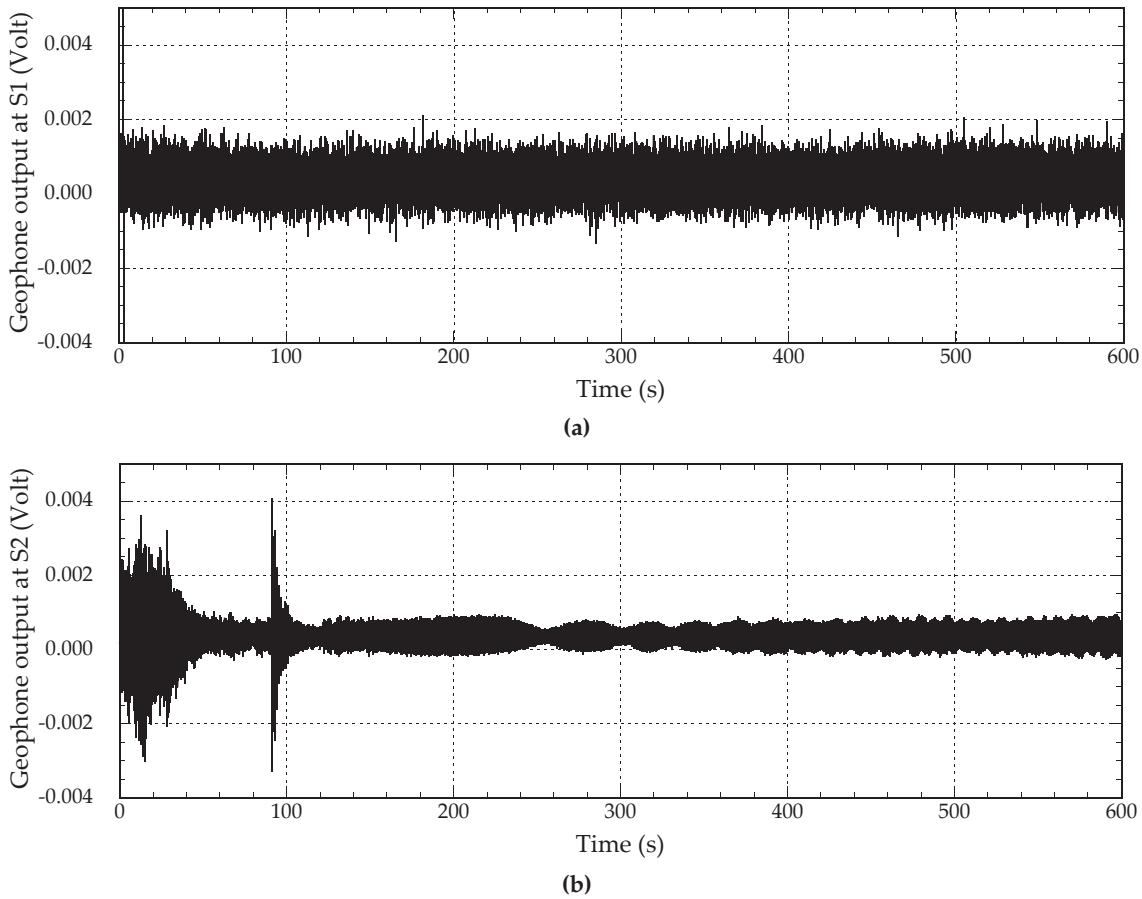

Figure 8.10: Output records of the in-situ measurements acquired from the steel-lined pressure shaft of the Grimsel II power plant during the **shut-down of turbines**, (a) geophone output at section S1, and (b) geophone output at section S2.

analysis presented in Section 8.2.

During turbine shut-down, a small increase of pressure at S1 of about 0.3 bar is detected at the beginning of the manoeuvre. It is followed by pressure fluctuations having a maximum amplitude of 0.5 bar and then by more important perturbations of around 0.8 bar in amplitude near the end of the manoeuvre. The latter perturbations are detected by the pressure and the geophone sensors at section S2. Therefore, they are selected inside a time window of 130 000 samples and analyzed in detail in Section 8.2. The mass oscillation phenomenon is also observed after the end of the turbine shut-down manoeuvre.

8.2 Monitoring of pressure shafts and tunnels by using pressure transients under normal operation conditions

The transient data acquired from the in-situ monitoring system are generated by service loads induced by the normal start-up and shut-down of the pumps and turbines. The relatively small water pressure fluctuations combined with the homogeneous quality of the rock mass surrounding the pressure shaft over its total length make the application of the entire localization procedure very difficult. No important local weak reaches have been identified from the as-built drawing of the Grimsel II shaft (Fig. F.7). Nevertheless, the monitoring of the shaft based on normal operation transient loads was possible by monitoring the time histories of the two general indicators: the water-hammer wave speed and the wave attenuation factor.

The validation of the entire localization procedure can be achieved only from in-situ data acquired from shafts surrounded by more heterogeneous rock masses. The processing of the water-hammer measurements generated by transient sources with higher energy and/or different frequencies can enhance the efficiency of the procedure.

8.2.1 Assessment of water-hammer wave speed based on pressure data

The discussion held in Section 8.1.2 has defined the parts of the acquired in-situ data from the pressure shaft of the Grimsel II plant which will be considered in monitoring. These parts which have been given in the complete pressure records in Figs 8.3, 8.5, 8.7, and 8.9, are shown in Figs. 8.11 and 8.12 for both the pumping and generating modes.

8.2.1.1 Using $\mathcal{F}$ approach of the pressure records P1

A first estimation of the water-hammer wave speed inside the pressure shaft is obtained by the Fast Fourier Transform ($\mathcal{F}$) applied to the pressure records P1 acquired at station S1. The $\mathcal{F}$ with Hanning windowing has been used and the normalized RMS $\mathcal{F}$ density spectrums of the 396 acquired files during pumping

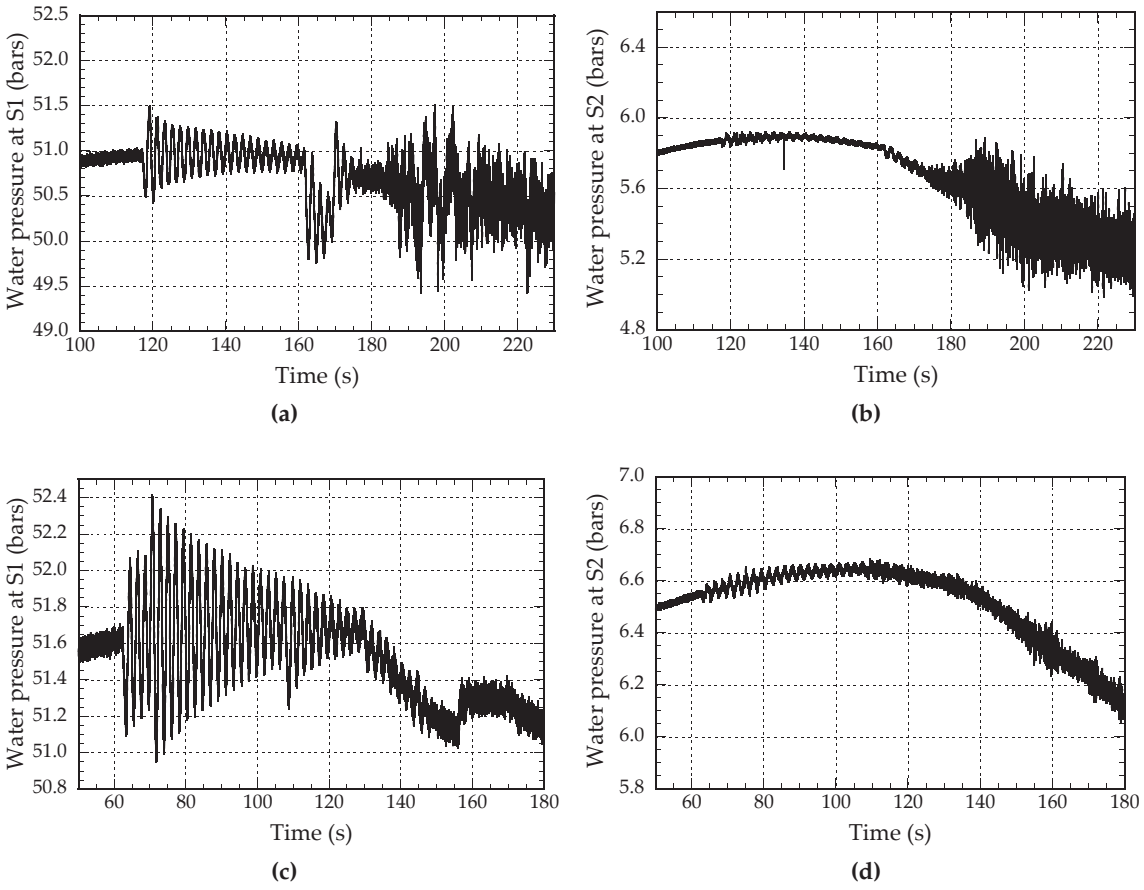

Figure 8.11: Parts of the in-situ output pressure records used for monitoring of the pressure shaft of the Grimsel II power plant, (a) P1 and (b) P2 during **start-up of pumps**, and (c) P1 and (d) P2 during **start-up of turbines**.

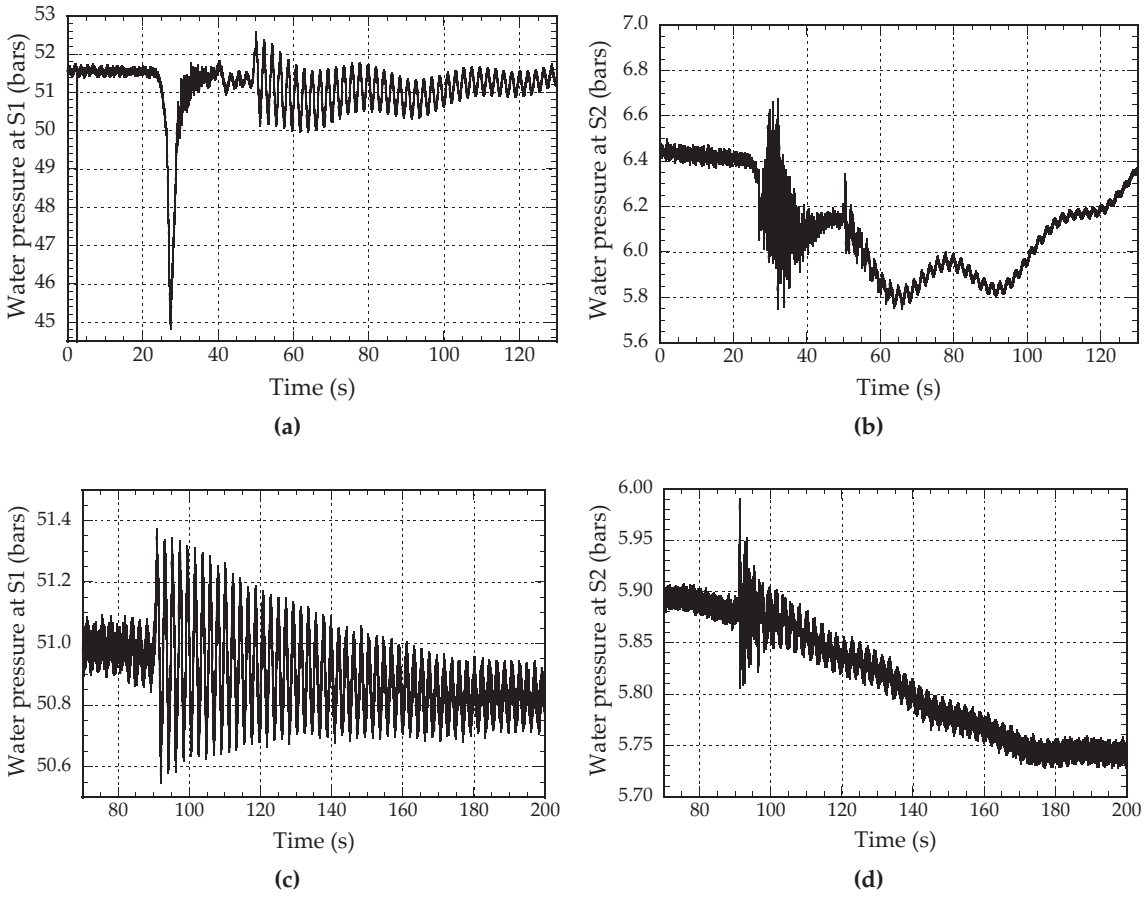

Figure 8.12: Parts of the in-situ output pressure records used for monitoring of the pressure shaft of the Grimsel II power plant, (a) P1 and (b) P2 during **shut-down of pumps**, and (c) P1 and (d) P2 during **shut-down of turbines**.

and generating modes have been computed. The normalization is obtained by dividing all the $\mathcal{F}$ magnitudes by their maximum valued computed inside the frequency interval of interest $[f_{\min}, f_{\max}]$. These frequencies are determined according to the following equations

$$f_{\min} = a_{\min}/(4\,L_{\max}) = 0.21\,\text{Hz}\,,\; f_{\max} = a_{\max}/(4\,\text{L}_{\min}) = 35\,\text{Hz} \tag{8.3}$$

in which $a_{\min}$ and $a_{\max}$ are the two logical wave speed values of 800 m/s and 1 400 m/s, respectively, $L_{\max} \approx 975$ m is the path length between points 1 and 4 of Fig. 8.2, and $L_{\min} \approx 10$ m is the path length 1-a shown on the same figure. The $\mathcal{F}$ density spectrums of the pressure signals P1 depicted in Figs. 8.11 and 8.12 are shown in Figs. 8.13 and 8.14. For each pumping and generating mode, the corresponding $\mathcal{F}$ of all the P1 pressures show the same pattern as in Figs 8.13 and 8.14.

All the $\mathcal{F}$ spectrums show clearly a strong peak near frequency 0.46 Hz with weaker peaks at higher frequencies. The 0.46 Hz is the fundamental frequency, f_{fund}, of the shaft. It corresponds to the water-hammer propagation between the downstream end of the distributor and the main reflexion border located at the junction between the pressure and the surge shafts (points 1 and 2 on Fig. 8.2, respectively). Thus, the wave speed can be estimated from the following formula:

$$a = 4\,L_{1-2}\,f_{\text{fund}} \tag{8.4}$$

where, L_{1-2} is the shaft length between points 1 and 2. For L_{1-2} equal to 762.34 m, the estimated wave speed is $1\,402.7 \pm 23.5$ m/s for a minimum $\mathcal{F}$ resolution of ± 0.0077 Hz. The peak at the fundamental frequency appears also in the $\mathcal{F}$ of the pressure records P2 measured at section S2.

The wave speed values estimated by the $\mathcal{F}$ approach are depicted in Fig. 8.15 for the 396 files acquired between February 17 and June 10, 2011. The mean and standard deviation of these values are 1 433.3 m/s and 35.7 m/s, respectively. The mean of the estimated wave speed is 5.3 % higher than the theoretical value of 1 361.5 m/s. The latter is calculated using Eq. (4.38) and the parameters values given in Table (F.1).

The discrepancy between the values of the estimated and theoretical wave speed can be explained by the uncertainties in the length of the pressure shaft and the frequency or the wave travel time between points 1 and 2 shown in Fig. 8.2. The application of the error propagation approach, presented in Section 3.3, to the Eq. (8.4) with $B_{f_{\text{fund}}} = 0.0077$ Hz yields to the uncertainties in the wave speed shown in Fig. 8.16. These uncertainties are presented versus the bias error in the length of the pressure shaft, $B_{L_{1-2}}$. For an error of 10 % in the pressure shaft length ($B_{L_{1-2}} \approx 75$ m), the uncertainty in the wave speed reaches the value of ± 140 m/s.

A more detail analysis of the $\mathcal{F}$ spectrums reveals that some peaks are nothing else than the odd harmonics of the fundamental frequency while others can be related to certain known features of the shaft. For example, Fig. 8.13a reveals an

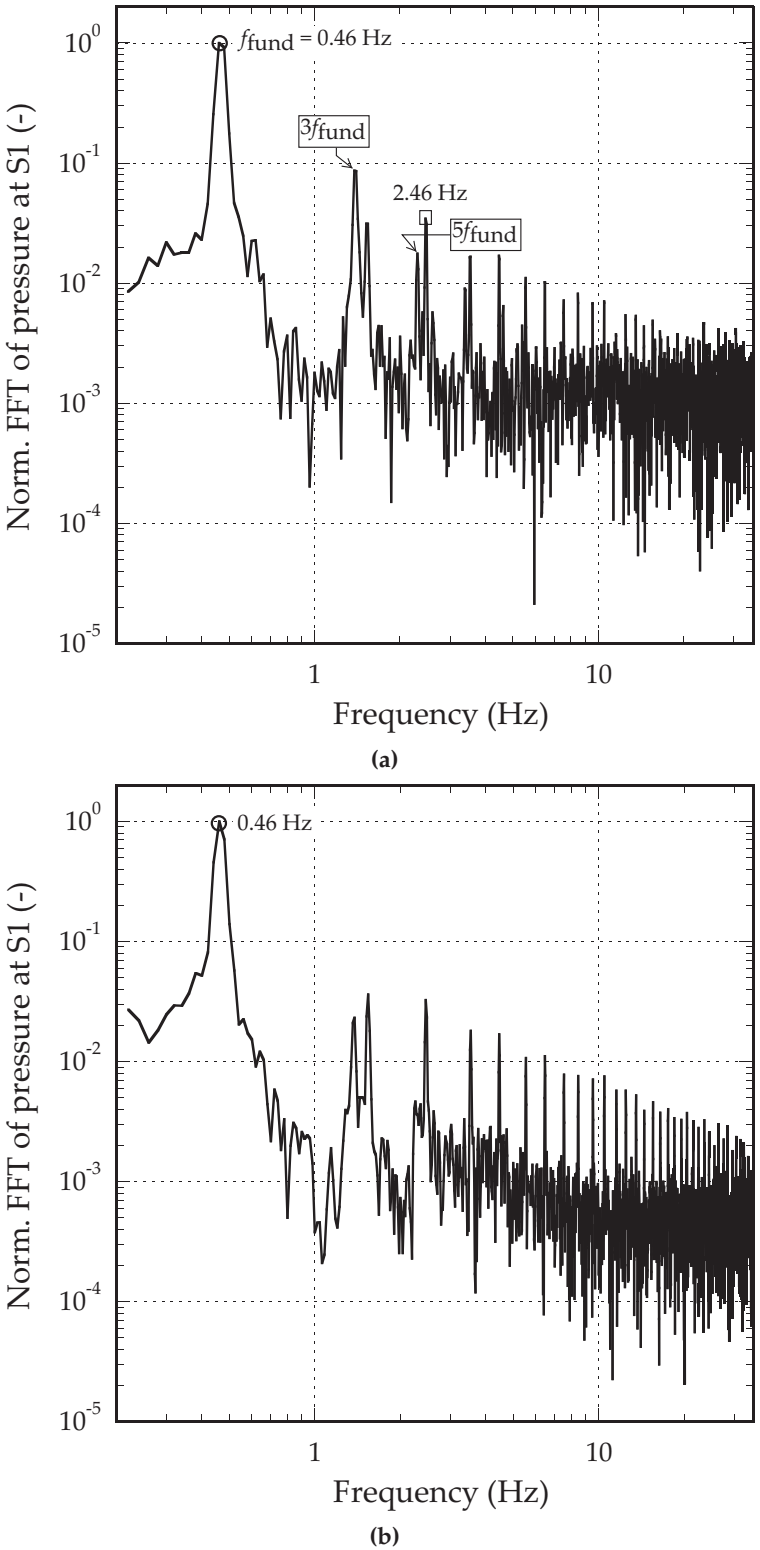

Figure 8.13: Normalized Fast Fourier Transform of pressures P1 shown in Figs 8.11, (a) during **start-up of pumps**, and (b) during **start-up of turbines**.

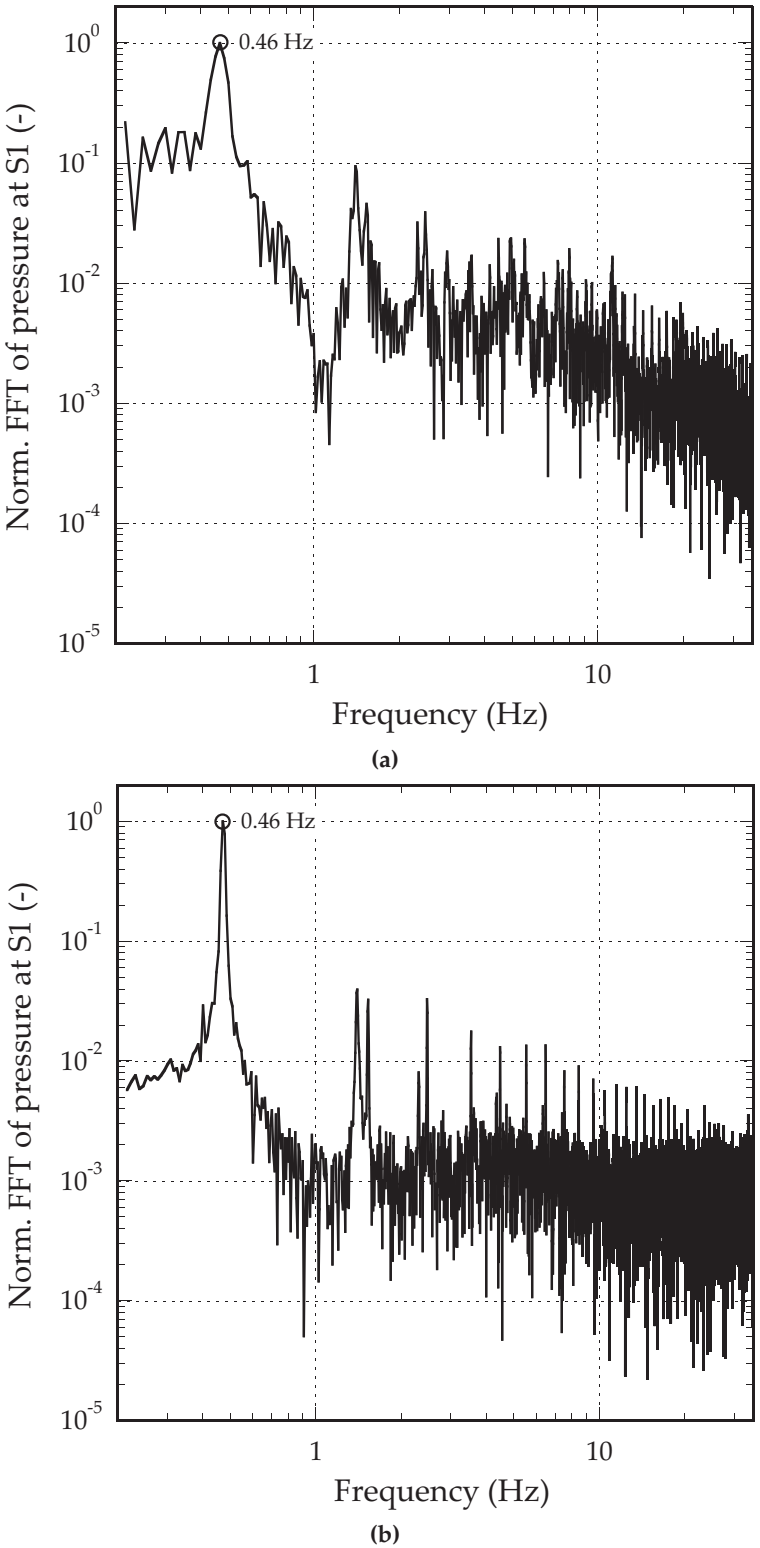

Figure 8.14: Normalized Fast Fourier Transform of pressures P1 shown in Figs 8.12, (a) during **shut-down of pumps**, and (b) during **shut-down of turbines**.

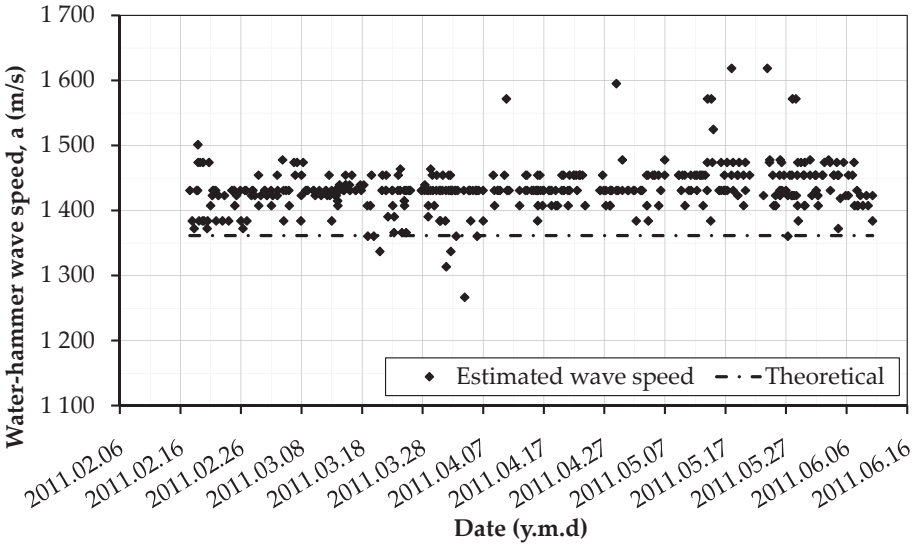

Figure 8.15: Water-hammer wave speed inside the shaft of the Grimsel II plant estimated by the $\mathcal{F}$ of the pressure records P1 for the 396 acquired data files. The theoretical value determined from Eq. (4.38) is also shown.

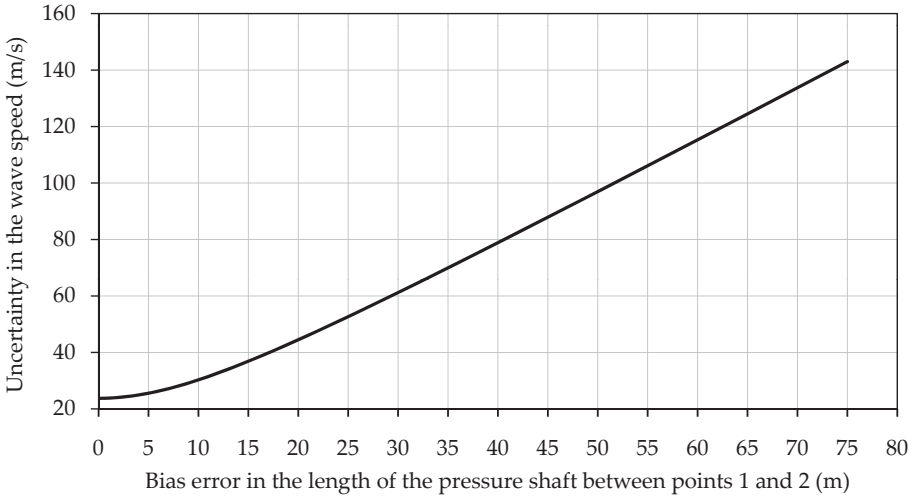

Figure 8.16: Uncertainty in the estimated wave speed values inside the pressure shaft of the Grimsel II plant versus the bias error in the length of the pressure shaft.

interesting peak at 2.46 Hz. The shaft length associated to this frequency obtained from Eq. (8.4), is equal to 142.6 m. This value is close to the pressure shaft length between points 1 and 8 (Fig. 8.2). At point 8, a significant increase of the stiffness of the shaft wall is present. The thick backfill concrete layer and the elbow of the shaft at this point create wave reflection boundaries for the pressure waves.

Finally, it is important to note that the $\mathcal{F}$ approach used to analyze the in-situ data has been tested during analysis of the experimental data of the physical facility. This approach has failed to detect the $\mathcal{F}$ peaks at the fundamental frequency of the test pipe. This is due to the relatively low $\mathcal{F}$ resolution (around 5.7 Hz) of the acquired pressure data and to the short length of the test pipe. In the physical tests, the resolution was governed by the limited number of samples acquired during each test (the part of the signal located inside windows W1 and W2, see Chapter 6) and by the maximum sampling frequency of 20 kHz of the acquisition card. The length of the test pipe has been imposed by the site constraints presented in Section 5.1.

8.2.1.2 Using signals of the two pressure sensors P1 and P2

In time domain

The synchronization method of the two acquisition systems at S1 and S2 was presented in Section 7.2.2.3. It is a crucial step for estimating the wave speed based on the measurements acquired at both stations S1 and S2. Fig. 8.17 shows an extract of the variation of the time delay measured between the internal clocks of the two PCs at the time of trigger. The horizontal axis represents the number of files automatically generated after each trigger. This figure shows that the time delay is not constant. It fluctuates around a mean value of 0.0834 s with some values below 0.04 s and above 0.2 s. For each data file, the value of the corresponding time delay must be added to the time that separates the front pressures at S1 and S2. The result is the travel time of the water-hammer wave between the two measurement sections.

Different time-based techniques similar to those given in Section 6.2.2.1 have been used to estimate the travel time between the pressure sensors positions P1 and P2. The results of the most adequate techniques for each pumping and generating modes are briefly presented hereafter. The pressure records were filtered by using *Daubechies* (db10) mother wavelet before the estimation of the travel time. For each record, the summation of the decomposition details from D_8 to D_{12} has been considered. The full decomposition schemes of details for the first half part of pressure records shown in Figs. 8.11a and 8.11b, are given in Figs. F.8 and F.9.

During start-up of pumps and turbines For the pressure data generated by the bypass opening of the spheric valve, the approach based on the time separating the intersection points of two regression lines correlating the steady-state and the first front pressure of each of them is used.

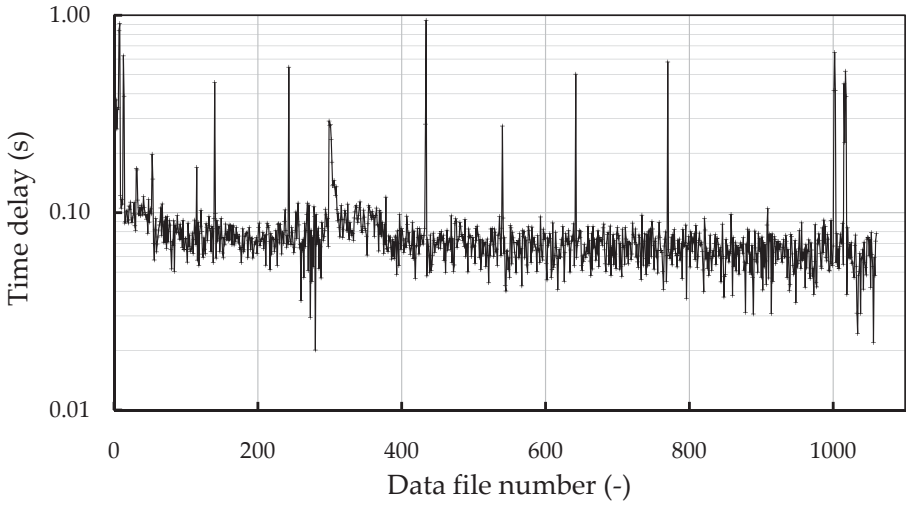

Figure 8.17: Time delay measured between the two PCs of the acquisition systems at stations S1 and S2 of the pressure shaft of the Grimsel II pumped-storage plant

During shut-down of pumps The P1 pressure record was first differentiated relative to time and then cut, with the pressure P2, inside a window time having the lower border at the beginning of the sampling and the upper one at the first maximum peak of P2. The procedure ends by cross-correlating the two signals in order to determine the travel time between them.

During shut-down of turbines In this case, two approaches were used to estimate the water-hammer wave speed inside the pressure shaft. The first approach extracts the time that separates the maximum values of the front pressure measurements while the second uses the same approach as for the pumps and turbines start-up. The mean value of the two estimated travel times is retained.

In frequency domain

The system identification approach presented in Section 3.2.2 which has been applied on the physical experimental data in Section 6.4, is used to assess the pressure measurements P1 and P2 of the pressure shaft of the Grimsel II power plant. Fig. 8.18a shows the frequency response functions $H(f)$ for the pumping and generating modes. Each response curve is obtained by averaging five measurement data histories ($Nb = 5$) acquired in February between 13 and 29, 2011. The phase spectrum of $H(f)$ and the coherence function are presented in Fig. 8.18b and 8.18c, respectively. Unlike the identification results of the experimental data, the magnitude of the response functions do not show peaks at the fundamental frequency (0.46 Hz) of the pressure shaft. The slope of the phase of $H(f)$ is neither constant nor proportional to the slope of the time delay between the two pressure sensors (according to Eq. (6.13)). Therefore, no pertinent results can be

concluded from these graphs. The failure of this method is due probably to the reflection of the major part of the wave by the junction located between the pressure and surge shafts (point 2 in Fig. 8.2). Nevertheless, the coherence function given in Fig. 8.18c shows interesting linearity of the system (coherence is close to 1) near frequencies 0.46 Hz, 1.38 Hz, and 2.30 Hz. The two latter frequencies are the third and fifth harmonics which have been also detected by the $\mathcal{F}$ approach presented in Section 8.2.1.1.

8.2.1.3 Comparison between the $\mathcal{F}$ approach and the one which uses signals P1 and P2 for the estimation of the wave speed

During pumps and turbines start-up, the estimated wave speeds based on the $\mathcal{F}$ approach and on the time domain calculation procedures using the two sensors P1 and P2 are presented in Fig. 8.19a. The horizontal axis of this figure shows the date at which the data file has been acquired. Figs. 8.19b and 8.19c show the estimated wave speed during pumps and turbines shut-down, respectively. A horizontal line representing the theoretical wave speed value of 1 361.5 m/s is also shown.

The wave speed values estimated from the time lag between the first wave front of pressures P1 and P2 show scattered patterns relative to the values obtained from the $\mathcal{F}$ approach. This is specially observed during pumps and turbines start-up and turbines shut-down modes. The estimation method based on the two pressure data is probably affected by the following important sources of error: (i) the unknown synchronization time delay of the internal clocks of the PCs of the two acquisition systems, (ii) the alteration and dispersion of the pressure signals, and (iii) the accuracy of the assessment methods.

Regarding the first point, the synchronization of the pressure transducers was not an issue in the laboratory tests because of their proximity to each other and the ability to directly connect them to a single data acquisition card. In the field, the distance between the measurement sections of the pressure shaft imposes the use of an individual acquisition system at each location. In spite of the fact that important effort has been invested to built the synchronization scheme, the results show that the method adopted was not reliable. In fact, the server used to synchronize the internal clock of the PCs is located inside the powerhouse. Therefore, the time needed by the two acquisition systems to access the server is not exactly the same. For example, an accuracy in the order of 100 ms induces an error of around 20 % on the wave speed between sensors. Another method of synchronization which do not use the internal clock of the PCs, consists in sending an electrical current pulse at the moment of trigger from the powerhouse towards the upstream measurement station. This method is more accurate than the one that has been used. Unfortunately, its application to the Grimsel II plant was not possible because of the absence of an electrical cable connecting the two stations. A radio synchronization system, similar to the one that has been used by Stephens (2008) is an interesting solution for open air pipelines. In this system,

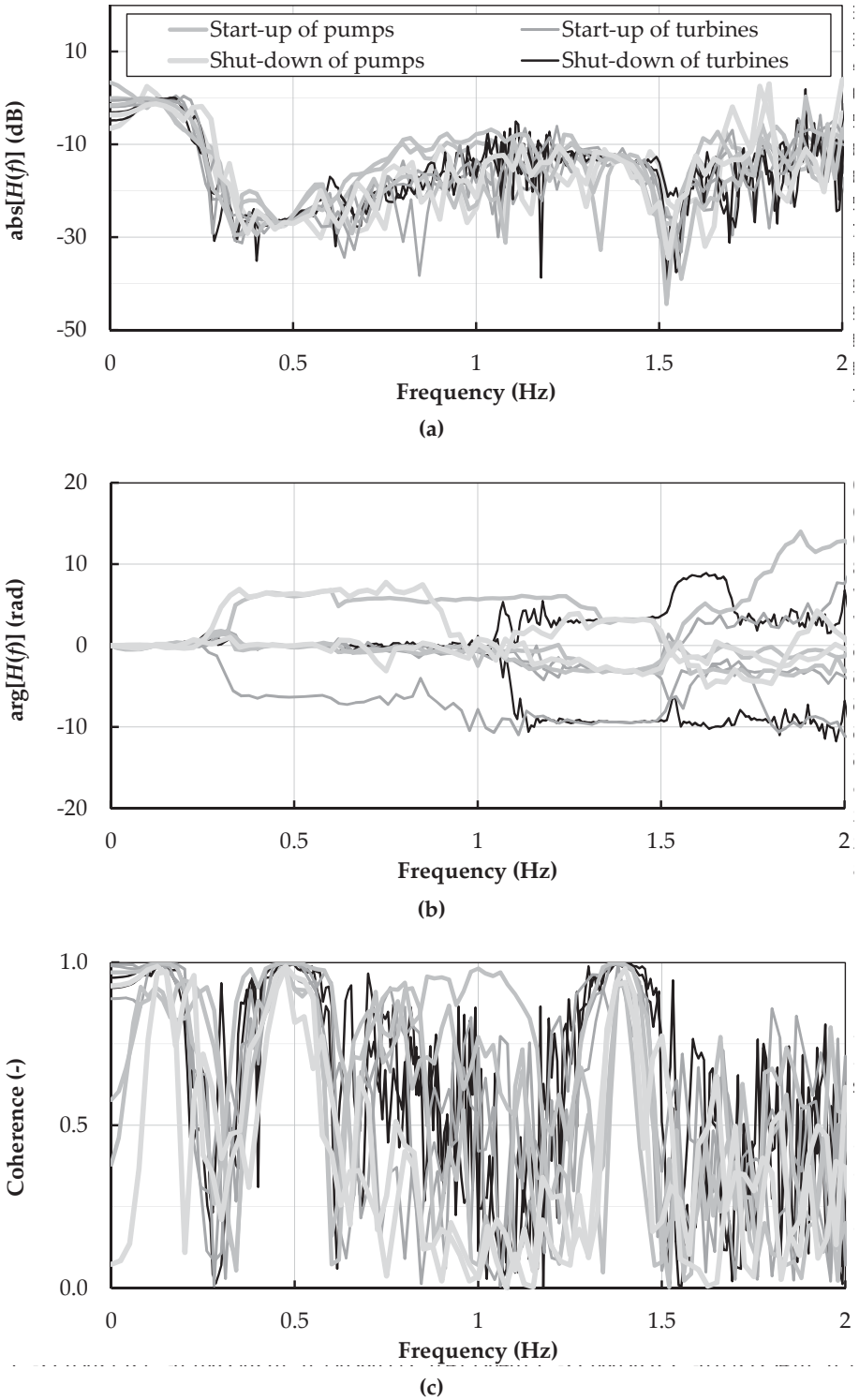

Figure 8.18: Results of the identification approach applied on pressure data P1 and P2 of the pressure shaft of the Grimsel II power plant, (a) magnitude spectrum of the frequency response function $H(f)$ estimated from Eq. (3.12), (b) phase spectrum of $H(f)$, and (c) coherence function estimated from Eq. (3.15).

the synchronization cable was replaced by radio emitter and receiver in which an audio signal of particular frequency was converted to voltage trigger pulse. Its application to the underground Grimsel II site was uncertain, complicated and relatively expensive.

The second source of error is related to the alteration, dissipation and dispersion of the water-hammer wave when it crosses the junction between the headrace pressure tunnel and the inclined surge shaft (point 2 on Fig. 8.2). At this junction, the major part of the wave energy (above 75 %) is reflected back to the powerhouse (Section 8.2.3). The special waterway layout of the Grimsel II plant with an inclined surge shaft located between the two measurement stations has significantly reduced the efficiency of the applied methods used to estimate the wave speed values.

Finally, the accuracy of the assessment methods is closely related to noise level which affects the measurement records. The mean signal to noise ratio at station S1 was around 1 241. The reflection of the water-hammer wave at the surge shaft junction has reduced this ratio to 169 for the measurements at station S2. The decrease of the signal to noise ratio induces higher error in the computed travel time of the wave between the pressure sensors and reduces the accuracy of the determination of the wave speed.

8.2.1.4 Conclusion regarding the wave speed approaches

It may be concluded that the estimation of the wave speed according to the $\mathcal{F}$ approach applied to the pressure records P1 of the Grimsel II plant is more accurate than the methods based on processing the two pressure sensors P1 and P2 in time and frequency domains. Therefore, the $\mathcal{F}$ approach will be used in Section 8.3 to establish the monitoring charts for the water-hammer wave speed.

8.2.2 Estimation of the water-hammer wave speed with geophone data

The basic idea was to try to analyze the output data from the two geophones at sections S1 and S2 in order to determine the travel time of the water-hammer wave inside the pressure shaft. This type of analysis has been done on the measurements acquired from the experimental facility (Section 6.2.2.2). Unfortunately, the signal processing procedure presented in Section 6.2.2.2, was not applicable to the measurements obtained from the Grimsel II plant. The main reasons for that are: (i) the steepness and energy of the pressure wave front and (ii) the synchronization problems of the two measurement stations.

Regarding the first point, the wave fronts generated by the normal operation loads were not steep enough to produce an instantaneous shock on the liner that can be detected by the geophones. The small energy content of the wave fronts made it so difficult to distinguish the measurements induced by the arrival of the wave front from those generated by noise. The small output voltages of the

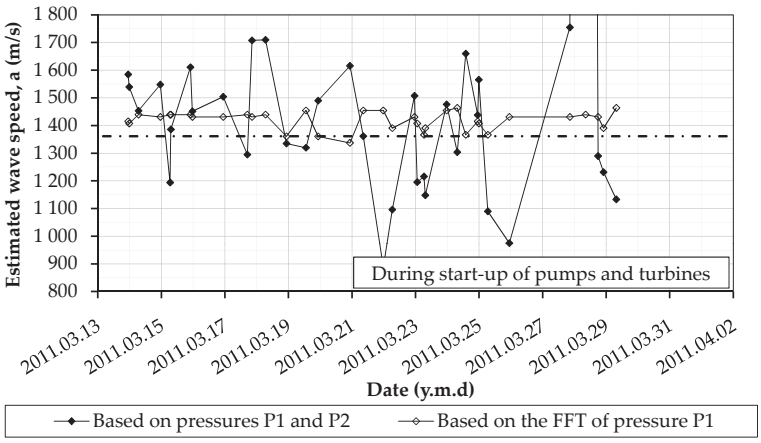

(a)

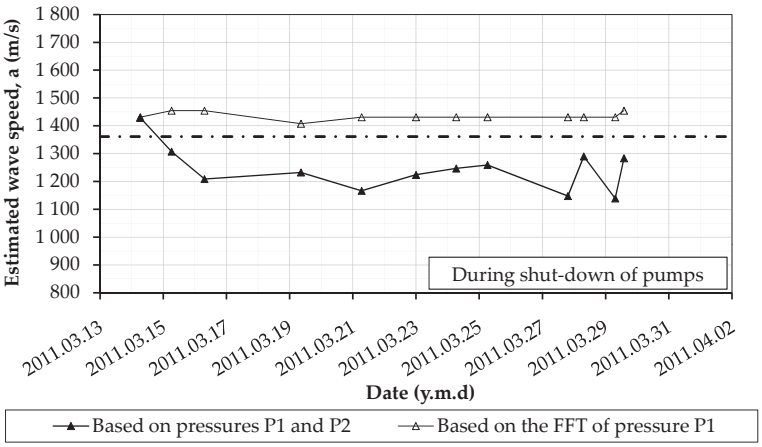

(b)

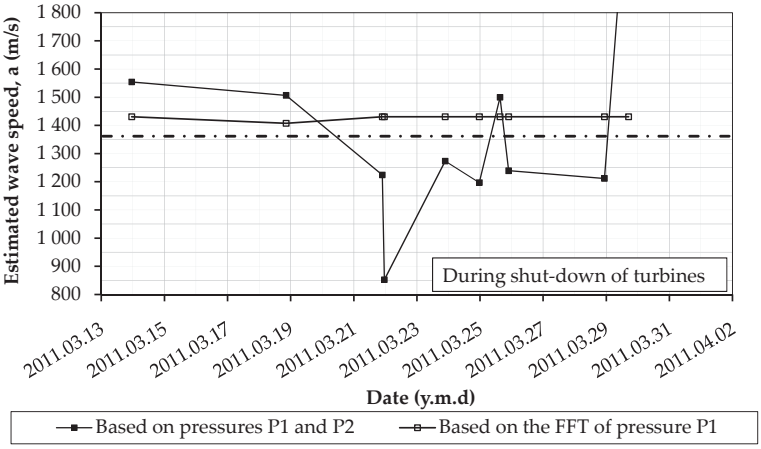

(c)

Figure 8.19: Water-hammer wave speed inside the shaft of the Grimsel II plant estimated by the $\mathcal{F}$ of the pressure records P1 and by the time lag between the first wave front of pressures P1 and P2. The theoretical value determined from Eq. (4.38) is also shown, (a) during **start-up of pumps and turbines**, (b) during **shut-down of pumps**, and (c) during **shut-down of turbines**.

geophones acquired at time 120 s in Figs. 8.4a and 8.4b give an idea on the difficult and rather impossible task to extract the interesting part of the signal from noise.

The second point mentioned above concerns the synchronization difficulties which has been presented and discussed in details in Section 8.2.1.3.

8.2.3 Estimation of the wave dissipation from pressure data

The dissipation of the water-hammer wave inside the pressure shaft of the Grimsel II power plant has been estimated from the dynamic pressure records acquired from transients generated by the service loads. The first part of the pressure records of 50 000 samples in length which follows directly the steady-state flow during start-up of the pumps and turbines is used to evaluate and quantify the wave dissipation (Figs. 8.11). For the pump shut-down mode, the signal considered is also 50 000 samples long and starts after about 10 s from the minimum peak of the pressure P1 records (Fig. 8.12a). For the turbine shut-down mode, the part of the signal starting at the end of the closure manoeuvre and having a length of 130 000 samples is considered.

The wave dissipation has been quantified by using two parameters: (i) the exponential dissipation coefficient obtained from the pressure P1 and (ii) the relative dissipation ratio of the front wave between sensors P1 and P2.

8.2.3.1 Exponential dissipation coefficient from the pressure records P1

The dissipation coefficient, b_2, is defined as the exponential coefficient of the following law inspired from Eq. (4.51):

$$\frac{\mathrm{RMS(P1)}}{\max[\mathrm{RMS(P1)}]} = b_1 \, \mathrm{e}^{b_2 (t/T_{\mathrm{fund}})} \tag{8.5}$$

where, RMS(P1) and max[RMS(P1)] are the Root Mean Square (Eq. (6.11)) of the pressure P1 and its maximum value, respectively, (t/T_{fund}) is a dimensionless variable in which t is the time and T_{fund} is the fundamental period of the pressure shaft, and b_1 is the normalized RMS value at $t = 0$.

The parameters b_1 and b_2 of Eq. (8.5) have been estimated by fitting an exponential regression curve on the normalized RMS values of the filtered pressure signal P1. The pressure records are filtered by using *Daubechies* (db10) mother wavelet where only details from D_8 to D_{12} have been retained. The resolution of the RMS is taken equal to 1 000 Hz/0.46 Hz $\approx$ 2 175.

Figs. 8.20 and 8.21 show the normalized RMS points and the exponential regression equations of the pressure records P1 given in Figs. 8.11 and 8.12. A very good agreement was found between the RMS values determined from measurements and those obtained from the semi-empirical exponential regression. Therefore, a preliminary conclusion can be addressed stating that the dissipation coefficient, b_2 can be considered as an interesting monitoring parameter and a global indicator quantifying the wave dissipation inside the pressure shaft.

To follow up the behaviour of b_2 in time, its value was computed from the 396 data files acquired between February 13 and June 10, 2011. The results of the b_2 parameter and the R-squared (R^2) values of the regressions are plotted on Figs. 8.22 and 8.23, respectively, for the pumping and generating modes.

For the pump and turbine start-up modes, Fig. 8.22a shows scattered pattern of b_2 with values ranging between -0.14 and -0.05. The R^2 values of the exponential regression for these modes are depicted in Fig. 8.23a. It can be shown that the exponential law given in Eq. (8.5) is a good estimator of b_2 with R^2 values higher than 0.8.

In turbine shut-down mode, the b_2 values are plotted in a very compacted pattern. They show a positive shift of about 0.01 from May 05, 2011 onward (Fig. 8.22c). Additional measurements are needed in order to understand and explain this increase of the dissipation coefficient. The corresponding R^2 values are excellent (higher than 0.976) (Fig. 8.23c).

During the pump shut-down manoeuvres, the b_2 histories show similar behaviour as in the turbine shut-down mode. More scattering is observed with some unusual values that are relatively low (Fig. 8.22b). The R^2 values of this mode presented in Fig. 8.23b, are close to the pump and turbine start-up case.

The results reveal the existence of two different families of b_2 with a mean of -0.078 and a standard deviation of 0.015 for the pump and turbine start-up modes and a mean and standard deviation of -0.035 and 0.015, respectively, for the shut-down modes. The relative difference between the b_2 means is about 55 %. The higher wave dissipation detected in the pump and turbine start-up modes can be explained by the fact that additional wave dissipation is encountered by the opened bypass of the spheric valve inside the powerhouse. This boundary condition of the pressure shaft can also explain the scattering of the dissipation coefficient values shown on Fig. 8.22a.

8.2.3.2 Relative dissipation ratio estimated from the pressure signals P1 and P2

The relative dissipation ratio is determined from the amplitude of the dynamic pressures induced by the arrival of the first wave at each of the sensor position. This ratio has been used to estimate the global wave dissipation inside the test pipe of the experimental set-up (Section 6.2.4 and Fig. 6.22).

Fig. 8.24 shows the values of this ratio obtained by processing 57 files measured during the start-up and shut-down modes. As mentioned in Section 8.2.1.2, the high values of the relative dissipation ratio are caused by the reflection, at the junction 2, of the major part of the wave energy towards the powerhouse.

The values of the dissipation ratio during the turbine shut-down mode are more scattered and smaller than those obtained from the three other modes. The mean and standard deviation of the dissipation ratio in the turbine shut-down mode are 82.5 % and 3.1 %, respectively, while in the other modes they are equal to 94.5 % and 0.9 %, respectively. The scattering pattern and the low mean value of the dissipation factor in the turbine shut-down mode are probably caused by

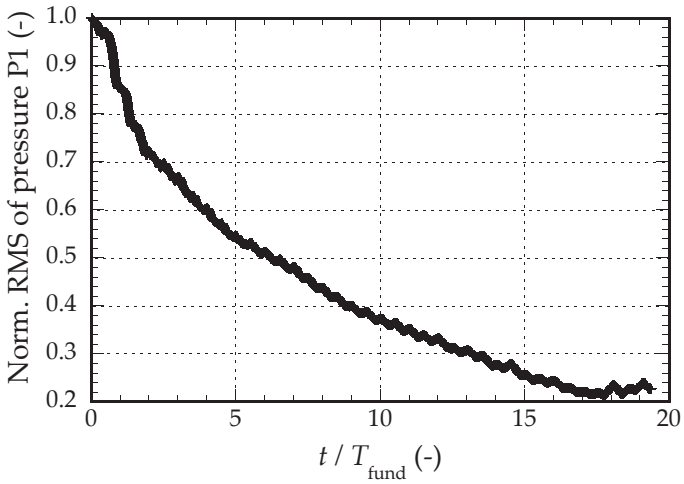

$y = 0.9189\,e^{(-0.0860\,x)}$; $R^2 = 0.993$

(a)

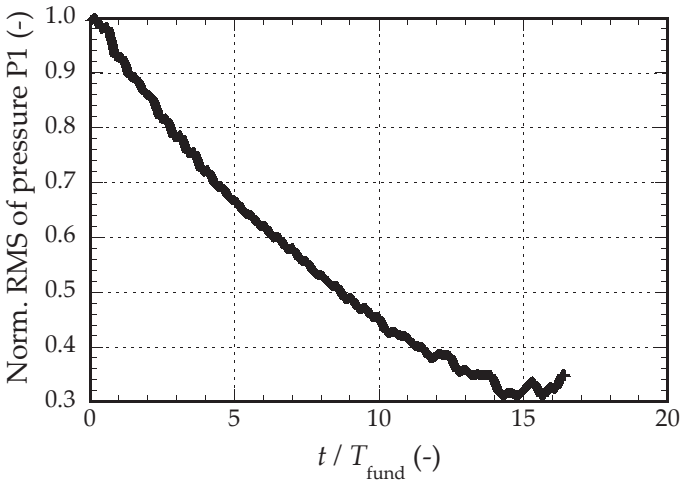

$y = 0.9675\,e^{(-0.0764\,x)}$; $R^2 = 0.984$

(b)

Figure 8.20: Normalized RMS data and the exponential regression equations with their R-squared for the pressure records P1 given in Figs. 8.11, (a) during **start-up of pumps** and (b) during **start-up of turbines**.

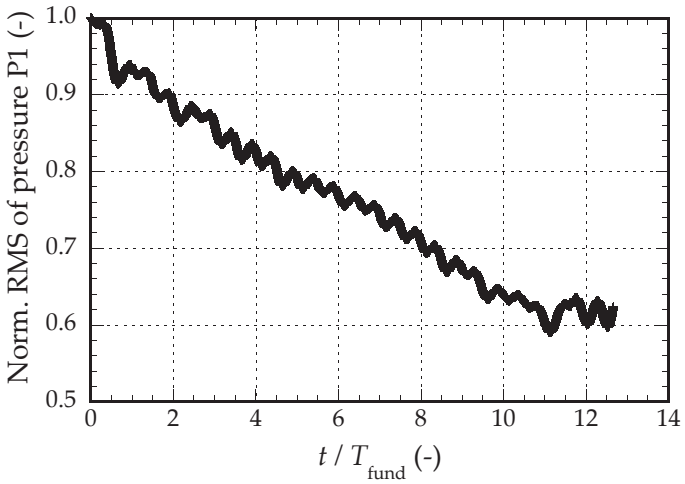

$y = 0.9815\,\mathrm{e}^{(-0.0409\,x)}$; $R^2 = 0.999$

(a)

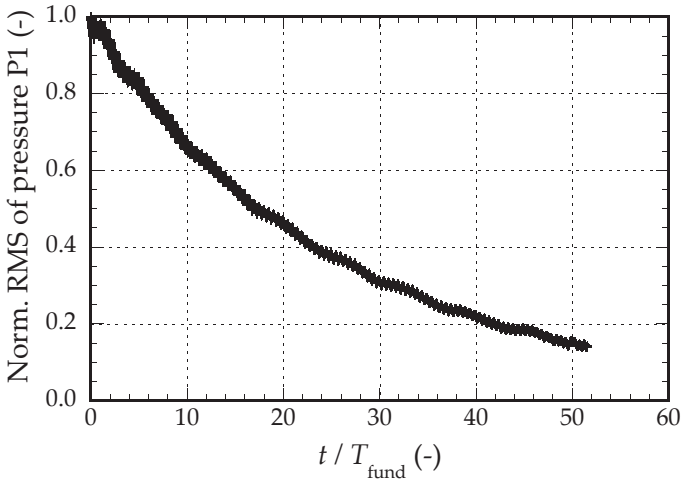

$y = 0.9852\,\mathrm{e}^{(-0.0380\,x)}$; $R^2 = 0.994$

(b)

Figure 8.21: Normalized RMS data and the exponential regression equations with their R-squared for the pressure records P1 given in Figs. 8.12, (a) during **shut-down of pumps** and (b) during **shut-down of turbines**.

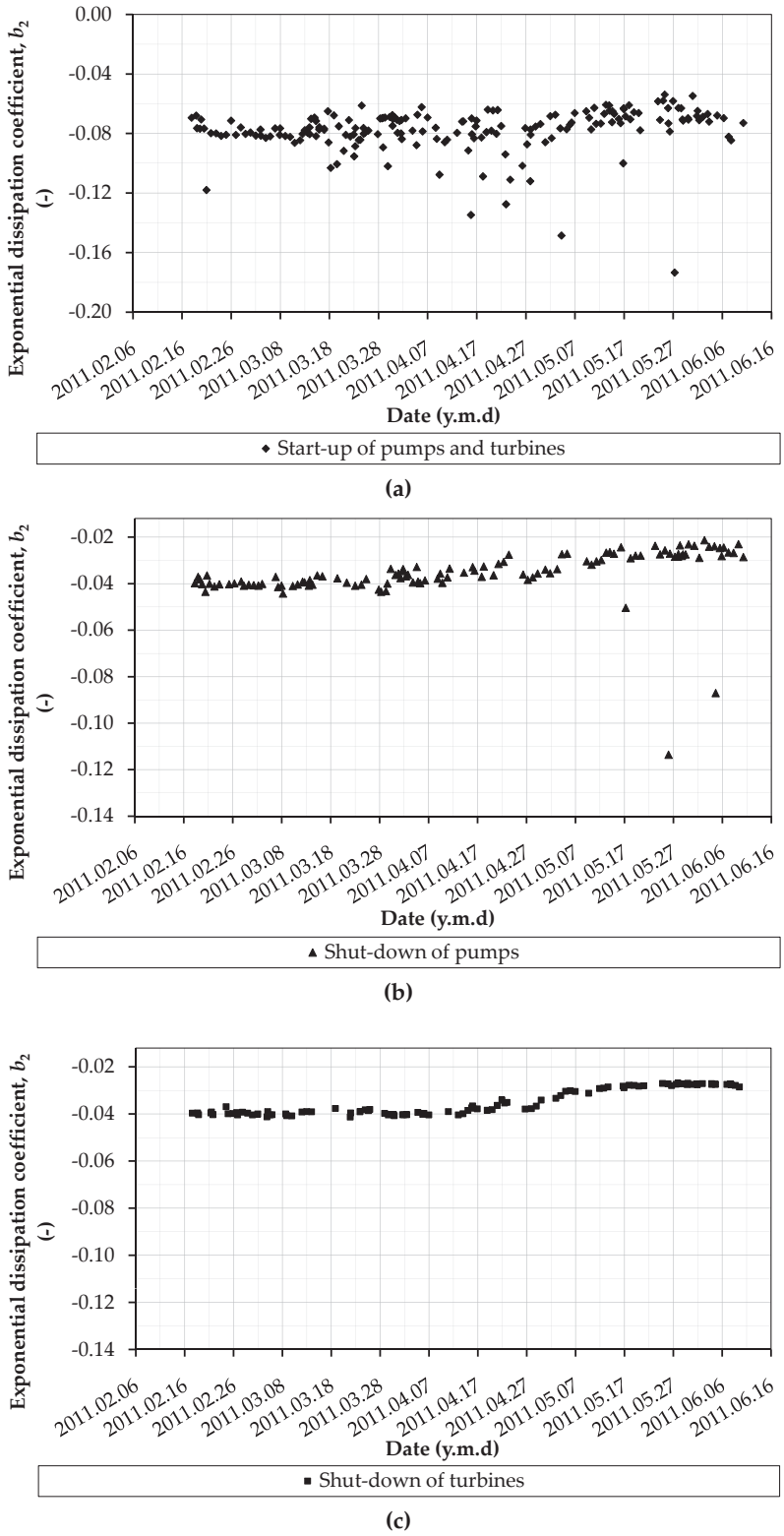

Figure 8.22: Dissipation coefficients values of the exponential regression curves obtained from the processing of the pressure P1 records inside the shaft of the Grimsel II power plant.

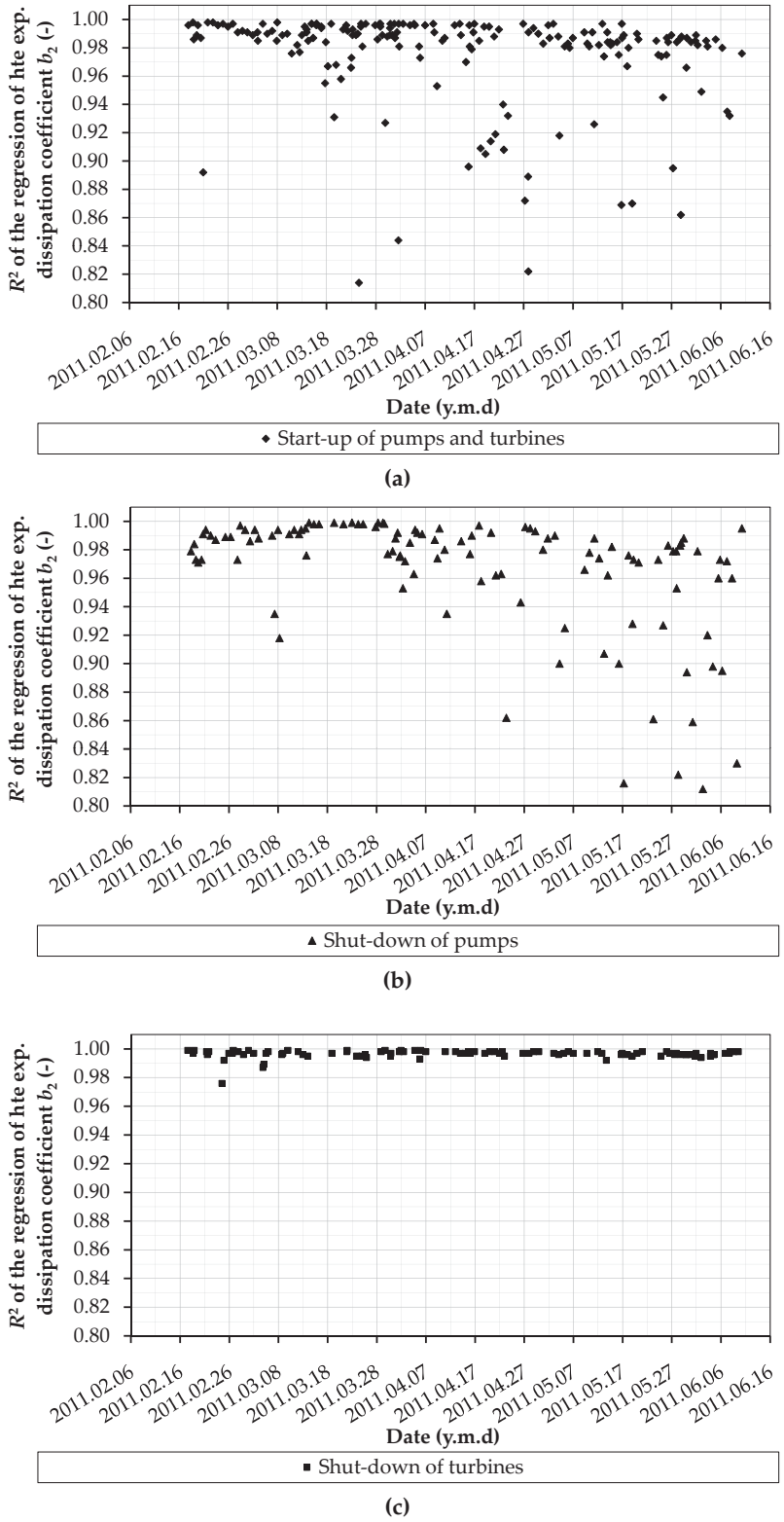

Figure 8.23: R-squared (R^2) values of the exponential regression curves obtained from the processing of the pressure P1 records inside the shaft of the Grimsel II power plant.

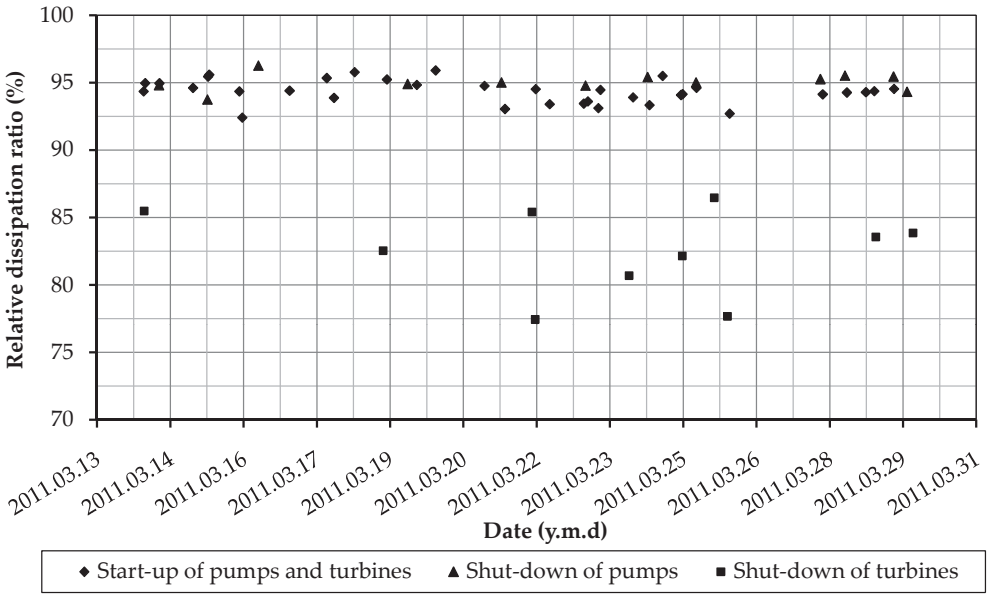

Figure 8.24: Relative dissipation ratio of the water-hammer wave estimated between the two pressure sensors P1 and P2 at the Grimsel II plant.

the pressure fluctuations which proceed the part of the pressure signal considered in the analysis.

It should be mentioned that the wave transmission ratio at the intersection of the pressure and the surge shafts is three times lower than the 2/3 ratio obtained from Eq. (3.5) in case of a junction of three identical pipe branches.

8.2.3.3 Conclusion regarding the estimation of the wave dissipation

The estimation of the water-hammer dissipation inside the pressure shaft of the Grimsel II plant was done by estimating the exponential dissipation coefficient and the relative dissipation ratio. The former was computed from the pressure records P1 while the latter was obtained from the amplitude of the front wave between pressure sensors P1 and P2.

The special scheme of the monitored pressure shaft in which a surge inclined shaft is located between the two measurement stations, induces important dissipation of the water-hammer wave between sensors P1 and P2. This high dissipation combined with low signal-to-noise ratio at pressure sensor P2 can hide small increase of the wave dissipation indicator caused by the formation of weak reaches along the pressure shaft. Therefore, the exponential dissipation coefficient is more accurate for establishing monitoring charts as presented in Section 8.3.

8.3 Development of monitoring charts for steel-lined pressure shafts and tunnels

8.3.1 Theoretical background of the used statistical method

The development of monitoring charts for the wave speed and the exponential dissipation coefficient have been inspired from procedures used in statistical quality control (Montgomery, 2005). Statistical quality or process control is a procedure that sets control limits on the normal operating condition of the system based on initial assessments of the mean and standard deviation of features or characteristics derived from the system data. The control or monitoring chart is a graphical display of the feature that has been measured or computed from a data sample versus the sample number or time. It contains a center line (CL) that represents the average value of the feature corresponding to the in-control state and two other horizontal lines, called the upper control limit (UCL) and the lower control limit (LCL). These control limits are chosen in a way that the process will be considered in control if nearly all the sample points fall between them.

For variables such as the wave speed and the dissipation coefficient, both the mean of the estimated values and their variability are used. The control of the process average or mean quality level is done with the so-called $\bar{x}$ chart while the process variability is monitored with a control chart for the range, called R chart. The former monitors between-sample variability (variability in the process over time) while the latter measures within-sample variability (the process variability between each sample at a given time). The CL, LCL and UCL of the general control model, known as Shewhart model, are given as follows:

$$\begin{aligned} \text{UCL} &= \text{Mean} + \text{Lim} \cdot \text{Std} \\ \text{CL} &= \text{Mean} \\ \text{LCL} &= \text{Mean} - \text{Lim} \cdot \text{Std} \end{aligned} \tag{8.6}$$

where, Mean and Std are the mean and standard deviation of the sample statistic and Lim is the distance of the control limits from the CL, expressed in standard deviation units. For m samples available, each containing n observations x_i on the quality characteristic (m subgroups of n samples), the best estimator of the Mean is given by

$$\widehat{Mean} = \overline{\overline{x}} = \frac{\sum_{j=1}^{m} \overline{x}_j}{m} \tag{8.7}$$

where, $\overline{x}_j$ is the mean value of x_i in each n observations. The estimation of Std is done by the range method. The range R_j of each sample of n values is

$$R_j = \max(x_i) - \min(x_i) = x_{\max} - x_{\min} \tag{8.8}$$

and the unbiased estimator of Std is

$$\widehat{\text{Std}} = \frac{1}{f_{\text{Mean}}(n)} \overline{R} = \frac{1}{f_{\text{Mean}}(n)} \frac{\sum_{j=1}^{m} R_j}{m} \tag{8.9}$$

where, $f_{\text{Mean}}(n)$ is the mean of the relative range variable $RR = R/\text{Std}_{\text{pop}}$ which depends on the size n of the sample and $\text{Std}_{\text{pop}}$is the standard deviation of the population x. Thus, the parameter of the $\bar{x}$ and R charts can be written according to Eq. (8.6) as follows:

$$\text{for } \bar{x}\text{chart} \begin{cases} \text{UCL} & = \widehat{\text{Mean}} + \text{Lim} \cdot \dfrac{\widehat{\text{Std}}}{\sqrt{n}} \\ \text{CL} & = \widehat{\text{Mean}} \\ \text{LCL} & = \widehat{\text{Mean}} - \text{Lim} \cdot \dfrac{\widehat{\text{Std}}}{\sqrt{n}} \end{cases} \tag{8.10}$$

$$\text{for } R\text{chart} \begin{cases} \text{UCL} & = \overline{R} + \text{Lim} \cdot \dfrac{f_{\text{Std}}}{f_{\text{Mean}}} \overline{R} \\ \text{CL} & = \overline{R} \\ \text{LCL} & = \overline{R} - \text{Lim} \cdot \dfrac{f_{\text{Std}}}{f_{\text{Mean}}} \overline{R} \end{cases} \tag{8.11}$$

where, $f_{\text{Std}}(n)$ is the standard deviation of the relative range variable RR. It should be noted here that the above development considers that the variable x is normally distributed. Burr (1967) has noted that the control limits are very robust to the normality assumption and can be employed unless the population is extremely non-normal. The works of Schilling and Nelson (1976), Chan et al. (1988), and Yourstone and Zimmer (1992) show that, in most cases, samples of size higher than $n = 4$ are sufficient to ensure reasonable robustness to the normality assumption. This value of n is also suitable to detect moderate to large process shifts. For $n = 4$, the mean and the standard deviation of the relative range variable RR are 2.059 and 0.88, respectively. For $n = 6$, these values are 2.534 and 0.848, respectively (Montgomery, 2005).

The implementation and use of the monitoring charts follow two phases. In phase I, the control limits are set based on a number of subgroups m, generally higher than 20. The observations inside these subgroups represent the present or basic state of the monitored variable. The control limits established in this phase are used in phase II for future on-line monitoring of the variable values.

The run tolerance chart for each monitored variable can also be set-up. It is a box plot chart that shows if a particular value of $\overline{x}$ or R was generated by one or more unusual observations in the sample.

8.3.2 Monitoring charts for water-hammer wave speed

Fig. 8.25a show the $\overline{x}$ monitoring chart of the wave speed inside the pressure shaft of the Grimsel II plant. The R chart is presented in Fig. 8.25b. The control limits have been defined by classifying 396 subsequent records in 66 subgroups ($m = 66$) of 6 samples each ($n = 6$) (the filled squares in Figs. 8.25a and 8.25b). The Lim value is taken equal to 3 according to the "Three-sigma" criterion.

All the points fall inside or near the control limits of $\overline{x}$ chart and no systematic pattern behaviour is detected. Also, the points plotted on the R chart do not show a specific pattern behaviour but they have four points, between April 27 and May 22, that fall relatively far above the UCL limit. These points are generated by the unusually high values of the wave speed shown on Fig. 8.15 during the same period of time. All these high values are computed from pressures acquired during the pumps and turbines start-up modes. It is clear that the control limits of the monitoring charts can be revised by discarding the points that are out-of-control and by using only the remaining in-process points. Such adjustment will be more relevant if it is done after acquiring a longer series of in-situ measurements.

Dealing with the available data, the observations indicate that the process is in control in the present time and the control limits defined in phase I are suitable and reliable for controlling current and future wave speed values.

The general patterns of points on the $\overline{x}$ and R charts reveal that the data assessment method proposed in this section for estimating the wave speed is stable since no change of the stiffness of the steel-lined shaft is suspected to happen in the short time duration of this monitoring. Any decrease of future wave speed values induced by a drop of the wall stiffness of the pressure shaft should be detected on the $\overline{x}$ chart by a permanent decrease of mean values with more or less the same global behaviour of R. For example, if the $\overline{x}$ of the future monitoring points shifts to 1 320 m/s and if the empirical law presented in Eq. (6.3) is considered, the value of the importance of the stiffness weakness X will be around 0.9. For a $L_{WR}/L_{1-2} = 1.5\,\%$ ($L_{WR} \approx 11.5\,\text{m}$), the relative drop of the wall stiffness of the weak reach will be equal to 88.5 %. The failure of the acquisition system and/or the assessment methods should appear on the R chart by a high scattered pattern of points falling far outside the established control limits.

8.3.3 Monitoring charts for exponential dissipation coefficient

For each family of the exponential dissipation coefficient b_2, an $\overline{x}$ and R chart have been prepared. Figs. 8.26a and 8.26b show the monitoring charts for the pump and turbine start-up modes while Figs. 8.27a and 8.27b depict those relative to the pump and turbine shut-down modes. The control limits were defined by classifying the subsequent records in 45 subgroups of 4 samples each and the Lim value was set to 3.

The patterns of the plotted points in Figs. 8.26a and 8.26b do not exhibit non-random or a particular systematic behaviour. Some points fall close or slightly outside the UCL and LCL limits. The control limits defined in this case can be used in phase II for on-line monitoring of future values of the exponential dissipation coefficient.

In Fig. 8.27a, the establishment of one set of control limits is not possible due to the shift encountered by the b_2 values. Additional measurements need to be collected to understand this global behaviour. The R chart given in Fig. 8.27b do not show any unusual events.

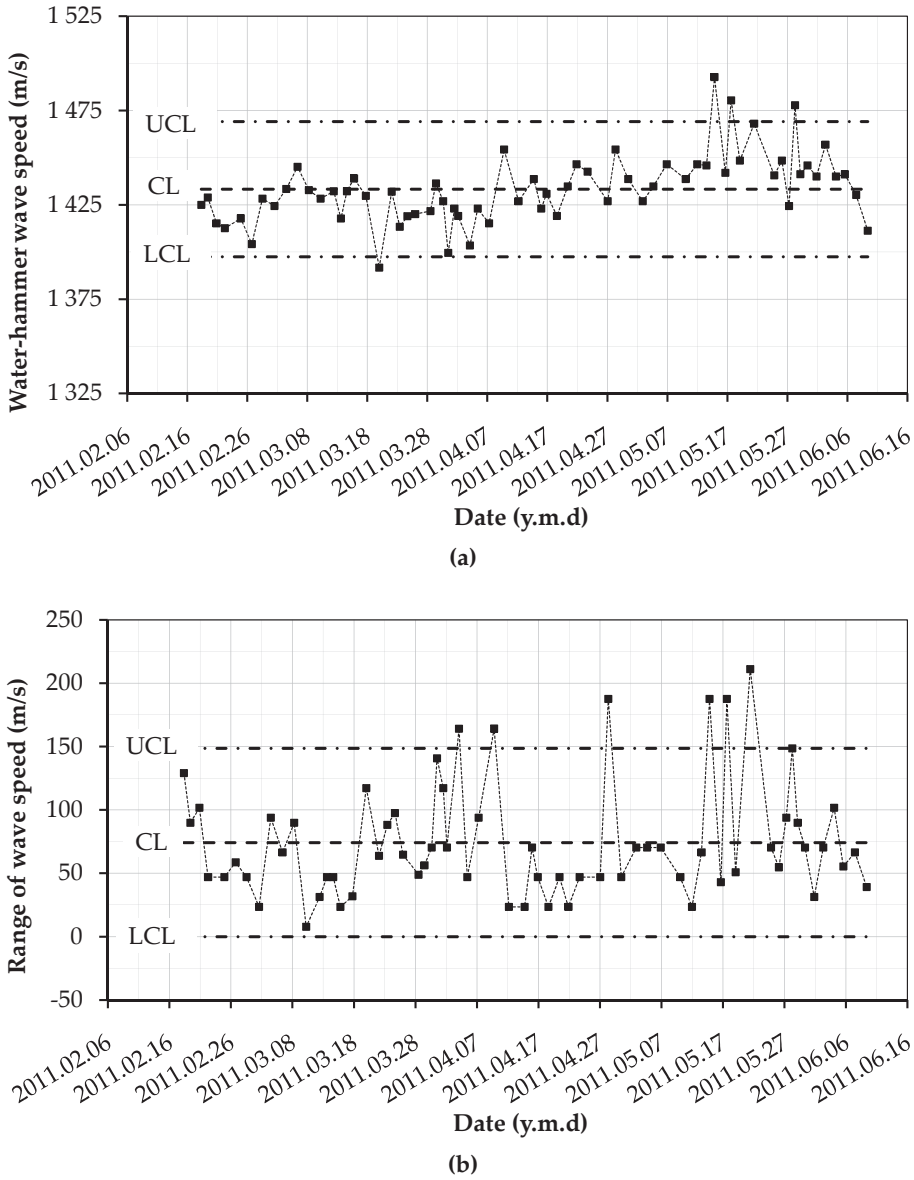

Figure 8.25: The transient based monitoring charts for the wave speed of the pressure shaft of the Grimsel II pumped-storage power plant, (a) $\overline{x}$ and (b) R charts.

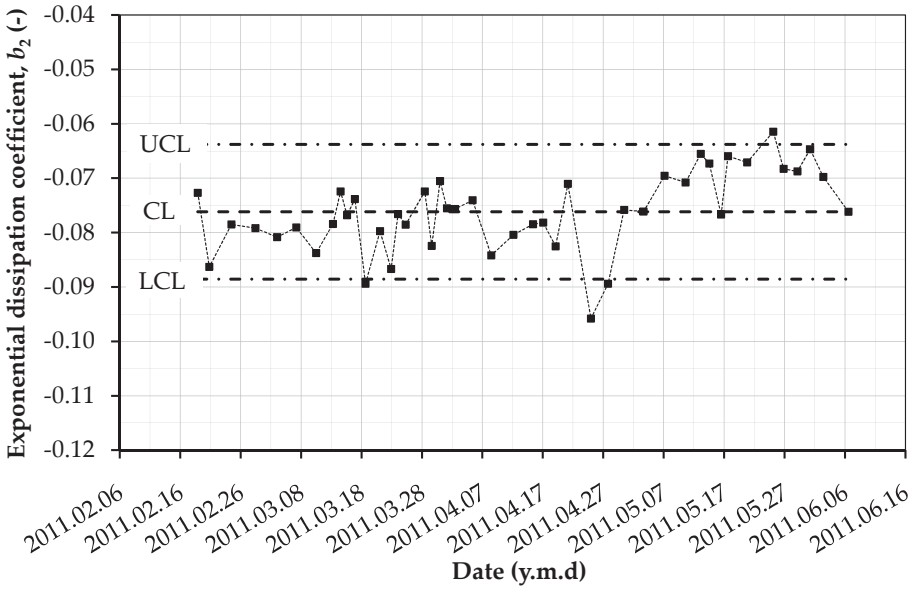

(a)

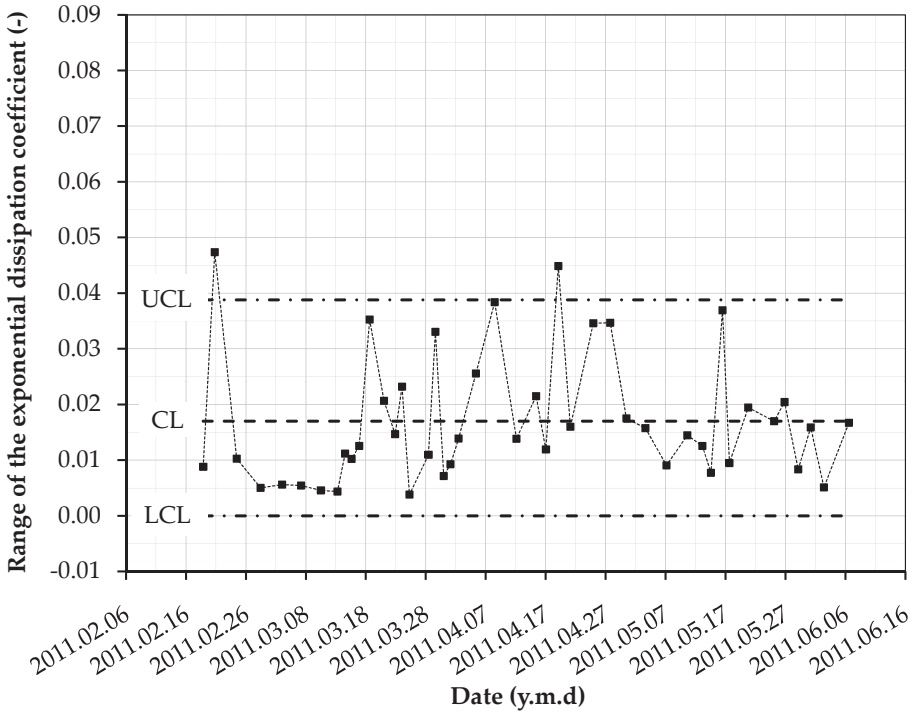

(b)

Figure 8.26: The monitoring charts for the exponential dissipation coefficient of the pressure shaft of the Grimsel II pumped-storage power plant during **start-up modes**, (a) $\overline{x}$ chart and (b) R chart.

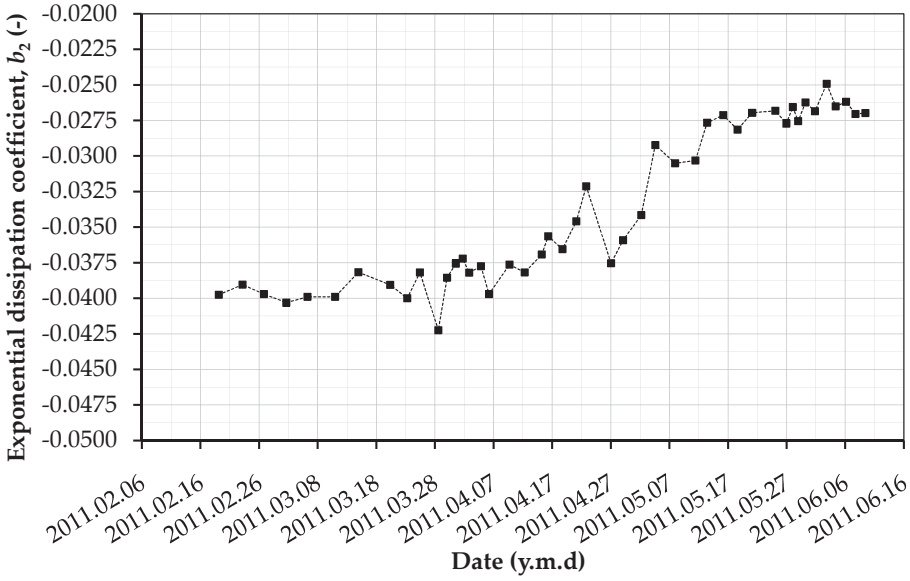

(a)

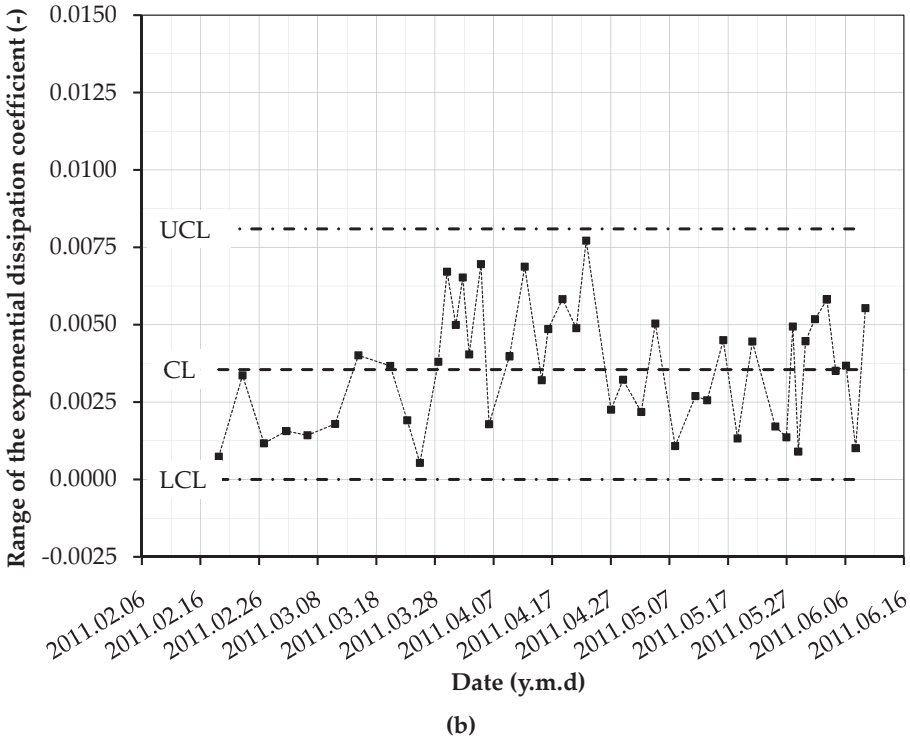

(b)

Figure 8.27: The monitoring charts for the exponential dissipation coefficient of the pressure shaft of the Grimsel II pumped-storage power plant during **shut-down modes**, (a) $\overline{x}$ chart and (b) R chart.

8.4 Conclusion

The headrace waterway system of the Grimsel II pumped-storage plant was described in detail with its most important features which influence the propagation of the water-hammer waves. The sequence of the manoeuvres of the valves and machines during pumping and generating modes were outlined and the in-situ measurements generated by the water transients were presented and discussed. The most relevant parts of the pressure and geophone signals were identified and analyzed in detail to assess the water-hammer wave speed and to quantify the wave dissipation.

The special layout of the high-pressure side of the Grimsel II waterway with the inclined surge shaft situated between the measurement stations, the homogeneous quality of the rock mass surrounding the liner, and the low accuracy of the synchronization scheme between the two acquisition systems made it difficult to validate the new monitoring method. Nevertheless, it was possible to monitor the shaft by using the pressure measurements acquired at station S1 located inside the powerhouse. These records have been processed to estimate the water-hammer wave speed and the exponential dissipation coefficient of the wave. The wave speed was assessed from the $\mathcal{F}$ density spectrums while the dissipation coefficient was determined by computing the RMS of the signal followed by an exponential regression fitting.

The monitoring charts of the mean, $\overline{x}$, and range, R, for the wave speed and dissipation coefficient were established based on the statistical quality control procedure. The control limits of these charts were set by using 396 data files acquired from the Grimsel II site between February 17 and June 10, 2011.

The control limits of the two monitoring charts for the water-hammer wave speed should be revised after acquiring a longer series of in-situ measurements. This revision will be done by discarding the out-of-control points from the data series.

A couple of monitoring $\overline{x}$ and R charts was established for each of the two families of the exponential dissipation coefficient. For the first family which corresponds to the pump and turbine start-up modes, the control limits can be used in phase II for on-line monitoring. During the pump and turbine shut-down modes, the second family of points has encountered a shift of about 55 %. Additional measurements are needed to understand its global pattern behaviour.

Chapter 9

General conclusions, recommendations and future research

9.1 General conclusions

The literature review has showed the existence of some gaps in knowledge for design and monitoring of high head steel-lined pressure shafts and tunnels. The main objectives of this research work are: (i) the enhancement of the existing theoretical design model and (ii) the development of new and non-intrusive monitoring methods to assess the structural state of the wall of steel-lined pressure shafts.

9.1.1 Enhancement of design model

Generally applicable approaches for estimating the "quasi-static", which means without fluid-structure interaction and frequency-dependent water-hammer wave speed in steel-lined pressure tunnels have been analyzed. The reformulated formulas have been compared to commonly used expressions including special cases such of wave speed calculation for unlined pressure tunnels and open-air penstocks. The quasi-static wave speed is significantly influenced by the state of the backfill concrete and the near-field rock zone (cracked or uncracked). In the case when these two layers are cracked, the quasi-static wave speed is overestimated in between 1 % and 8 % compared to uncracked concrete and near-field rock layers. Depending on the stiffness of steel liner and penstock, the fluid-structure interaction leads to significant difference in wave speeds values. Compared to the quasi-static case, the fluid-structure interaction approach, applied to steel-lined tunnels, results up to 13 % higher wave speed values in the high-frequency range (higher than 600 Hz) and up to 150 % lower values for frequencies between 150 and 300 Hz in some cases.

An enhanced theoretical model for the steel-liner has been proposed. The effect of the backfill concrete and the surrounding rock mass has been mechanically modeled by a Kelvin model which includes a spring, a dashpot, and a lumped additional mass. The enhanced model was described by the six-equation (3-mode) model of the FSI problem which was established first by Atabeck (1968) and generalized by Kuiken (1984). This new model can detect the compressional water mode and the radial and axial propagation modes in the steel liner and in the far field rock zone. The importance of such model consists in the resulting time-dependent stress diagrams for steel liner which can be used as input for the deterministic and probabilistic Fracture Mechanics models. Therefore, this model can be considered as the basis of future development to assess the response of high-strength steel which is used as lining in new hydropower projects.

9.1.2 New on-line monitoring approach

A new monitoring approach for detecting, locating and quantifying structurally weak reaches of steel-lined pressure tunnels and shafts has been developed. It is based on the generation of transient pressure and the analysis of the reflected pressure signals using, amongst others, the Fast Fourier Transform and wavelet decomposition methods.

The weak reaches arise from local deterioration of the backfill concrete and the rock mass surrounding the liner. The change of wave speed generated by the weakening of the radial liner supports creates reflection boundaries for the incident pressure waves. The reflections coming from other irregularities such as galleries and caverns near the tunnel and from partially closed valves can easily be discarded due to their known locations. The air pocket sources have a different pressure print out than the gradual drop of wall stiffness. They are characterized by a drastic and scattered drop of the wave speed. The roughness increase due to corrosion of the liner is expected to have minor effect. A local significant change of the cross-section area of the tunnel can be caused by the yielding of the steel liner after the loosening its support.

9.1.2.1 Validation by experimental tests

Laboratory experiments have been carried out to validate the monitoring technique. The multilayer system (steel–concrete–rock) of the pressurized shafts and tunnels was modeled by a one layer system of the test pipe. The latter was divided into several reaches having different wall stiffnesses. Different longitudinal placements of a steel, aluminum, and PVC pipe reach were tested to validate the identification method of the weak reach. A total number of 144 tests have been carried out on the twelve test pipe configurations.

During the experiments, the aluminum reach boundaries have generated reflected waves with small magnitude. Therefore, it was difficult to detect and capture the reflection induced by such reaches. Thus, the monitoring method

was only able to estimate the position of the weak reach when PVC material was used. In this case, the ratio between the elasticity modulus of the weak reach and the other parts of the test pipe is around 1.4 %.

Two types of transient sources have been used to generate water transients inside the test pipe. The first type is induced by the sudden impact of the injected air inside the air jack of the shut-off valve. The second source is generated by the progressive stoppage of the water flow inside the test pipe by the shut-off valve.

By using steep wave front, it was possible to:

- assess the front wave speed of an excitation traveling the test pipe between the measurement sections located at its both ends. The water-hammer wave speed have been computed by using pressure and geophone sensors. The results obtained from the two sensors were in very good agreement. It could be shown that the wave speed could be considered as first global indicator of large changes in stiffness (stiffness decreases down to 98 %) of the pipe wall.

- evaluate the wave dissipation factor by using the steep front of the pressure waves. Significant and proportional dissipation differences of +44 % in "Steel+PVC1,2,3" and +77 % in "Steel+PVC4" relative to the "Steel" configuration have been observed. The wave dissipation factor during transients can be considered as second global indicator of local and large changes in stiffness of the pipe wall.

- estimate the weak reach length and the severity of the local stiffness change of the pipe wall. The maximum relative mean errors were equal to 20.6 % for the tested configurations with one PVC reach.

During transients generated by the progressive stoppage of the flow, it was possible to:

- estimate the water-hammer wave speed from pressure records only. The mean and standard deviation of the wave speeds estimated from steep pressures and from those obtained from the progressive stoppage of the flow have showed a very good agreement with a maximum relative difference of mean of around 5 %.

- localize one PVC weak reach by using the $\mathcal{F}$ analysis for the pressure signals. The error in estimating the position of such reach relative to the real position of its center has varied from 3.3 % to 18.1 %.

It may be concluded that, the proposed monitoring method estimates the values of the two global indicators: the water-hammer wave speed and the wave dissipation factor. If a significant and persistent drop of the former and increase of the latter are detected, a drop of the wall stiffness is suspected to be occurred somewhere along the shaft. At the same time, the pressure $\mathcal{F}$s should reveal a

new peak at a frequency that corresponds to wave reflections from a weak reach. The wavelets approach will be then used to locate the weakness and to estimate its severity. The actual state of the pipe (i.e. penstock, pressure shaft or tunnel) with weak reach will be then considered as the basic configuration for the future monitoring records. Fig. 9.1 is the flow chart represented by the step-by-step procedure of the monitoring method.

9.1.2.2 Application of the monitoring method at prototype

The monitored prototype is Grimsel II pumped-storage power plant located in the Canton of Bern, in the central part of Switzerland. It has an underground powerhouse, equipped with four separated pump-turbine units with a total installed capacity of 350 MW. Two sections of the high pressure side of the steel-lined pressure shaft has been equipped with pressure sensors and geophones. The first measurement station was placed at the accessible steel-liner reach located just upstream of the bifurcation which distributes the water to the four machines inside the powerhouse. The second station was placed near the security valve located on the headrace tunnel between the inclined surge shaft and the vertical surge tank. The two acquisition systems have been synchronized through a fiber optic connection. They can be accessed and controlled on-line by using the internet connection.

The sequence of the manoeuvres of the valves and machines during pumping and generating modes were outlined and the in-situ measurements generated by the water transients were presented and discussed. Some relevant parts of the pressure and geophone signals were identified and processed in detail to assess the water-hammer wave speed and to quantify the wave dissipation inside the pressure shaft.

The inclined surge shaft situated between the two measurement stations has reflected back a major part of the wave energy (above 75 %) to the powerhouse. This has reduced the efficiency of the method which uses the two measurement stations to estimate the global monitoring indicators: the water-hammer wave speed and the wave dissipation ratio. More, the low accuracy of the synchronization results between the two acquisition systems have made difficult the validation task of the new monitoring method. This is a crucial step for estimating the wave speed based on the measurements acquired at both measurement stations. The time delay between the internal clocks of the two stations PCs was not constant. It fluctuated around a mean value of 0.0834 s with some values below 0.04 s and above 0.2 s.

In spite of the problems presented above, it was possible to establish preliminary monitoring charts for the pressure shaft of the prototype. These charts concern the water-hammer wave speed and the exponential dissipation coefficient of the wave and are based on the statistical quality control procedure. Their control limits were set by using 396 data files acquired from the Grimsel II site between February 17 and June 10, 2011. Only the pressure measurements from station S1

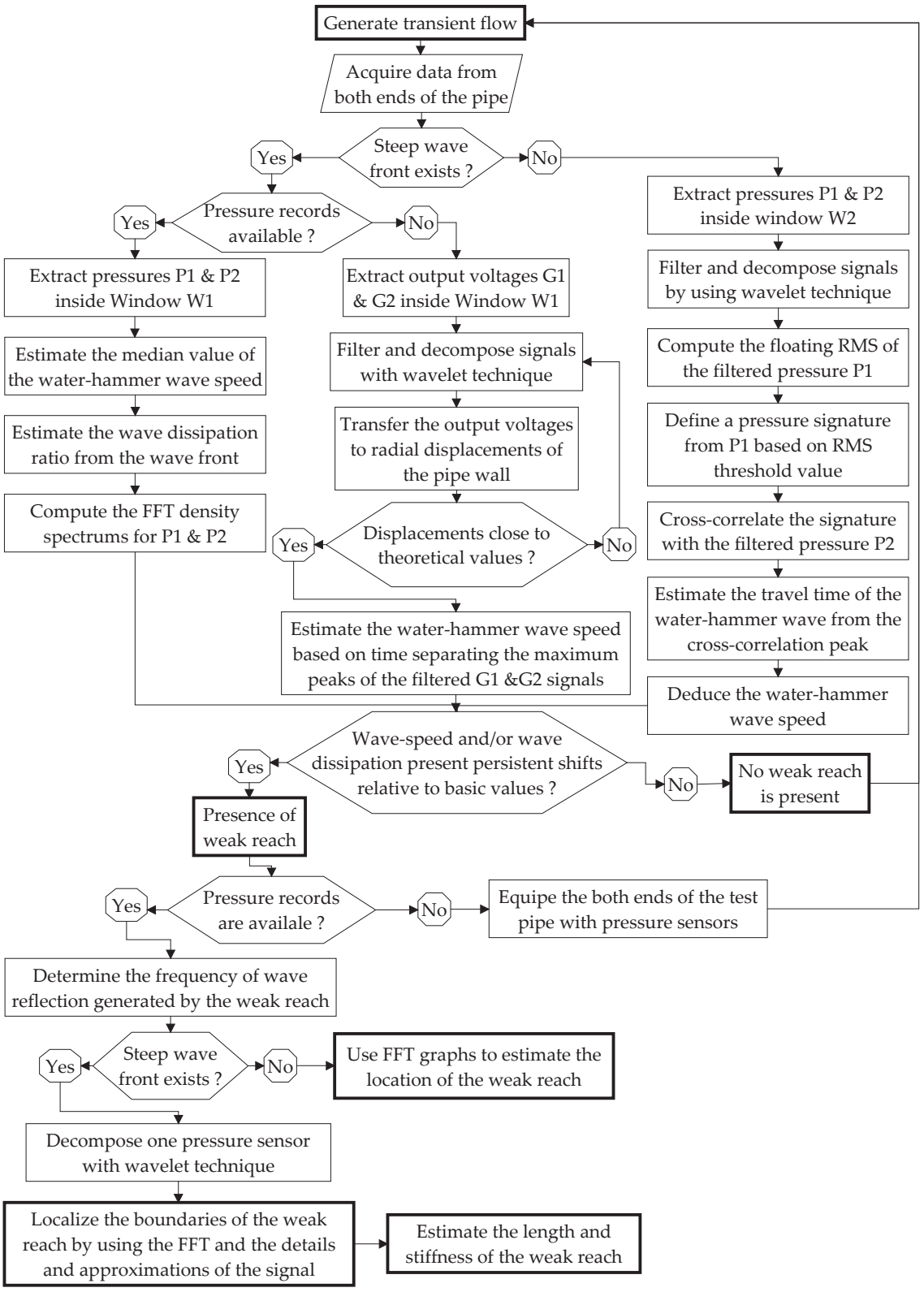

Figure 9.1: Flow chart of the monitoring procedure applied to the experimental facility.

located inside the powerhouse, have been processed to estimate the values of the monitored parameters and set the control limits of the monitoring charts. The wave speed was assessed from the $\mathcal{F}$ density spectrums while the dissipation coefficient was determined by computing the RMS of the filtered signal followed by an exponential regression fitting.

9.2 Recommendations

9.2.1 Design recommendations

- The actual design model based of the compatibility of radial deformation at the interfaces of the steel liner, the cracked backfill concrete and near-field rock mass, and the uncracked far-field rock mass is still the most realistic case to follow. Nevertheless, the actual used model neglects the fluid-structure interaction phenomenon and the failure mode by Fracture Mechanics of the steel liner and the rock mass.
- For practical applications, the differences detected between the values of the "quasi-static" wave speed obtained from the commonly used expressions can be tolerated. This is due to the uncertainty in the estimation of the rock mass characteristics and/or the presence of air in the water. The dynamic pressures obtained from classical water-hammer theory are not overly affected by such differences in wave speed.
- Depending on the system stiffness and constraints, the FSI may lead to different wave speed values and to higher extreme dynamic pressures with higher frequencies. The enhanced design model still need to be solved in frequency domain and results compared to the time domain solutions.

It may be concluded that the actual design rules for pressure steel-lined tunnels and shafts do not consider the true behaviour of combined steel-concrete-rock linings. The response of these structures to dynamic loads is not yet fully understood, especially the influence of severe transient flow phenomena, such as water-hammer effects, on the short and long term structural behaviour, fatigue, and safety of the lining. The existing design methods have been based on the idea of keeping the allowable stress in steel liner below yielding point and respecting some construction details and tolerances to minimize high local concentrated stresses. These design methods and safety assessment need to be revised since the beginning of use of very high strength steel liners which have a significant risk of brittle failure and fatigue.

9.2.2 Monitoring recommendations

- The synchronization of the two measurement stations of the Grimsel II plant used in the prototype study was not sufficiently accurate. The use of shared

variables through Ethernet connection was the only available solution to connect the two stations. This method needs the internal clock of the PCs to be exactly the same. This was not easy to achieve due to the difference in distances which separate the measurement stations and the server used for the time synchronization. For future prototype measurements, electrical current pulse should be sent at the moment of trigger from the powerhouse towards the upstream measurement station. This method needs an electric cable to connect the two stations. Radio synchronization system is uncertain and very complicated to achieve inside the underground caverns and tunnels.

- If the synchronization of the two measurement stations is not possible, the shaft can be monitored by using the dynamic pressures of one measurement station. The assessment results are considered to be enough accurate to monitor a significant and persistent change of the water-hammer wave speed and the exponential dissipation coefficient.

- The monitoring process can be further improved by equipping the bypass conduit of one spherical control valve with a rapid shut-off valve or an active energy transmitter device. The processing of the pressure signals generated by such transient sources during no-flow state may significantly enhance the efficiency of the procedure. The shut-off valve on the bypass conduit can be activated during the pressure balance of the control valve in the pump and turbine start-up modes. Active transient sources with low energy and with frequency near the resonance frequency of the pressure shaft can be used to generate high amplitude water-hammer waves.

- Another artificial type of water pressure excitation could be produced by an explosive shock wave generated in water near the reservoir's intake structure or near the tunnel–shaft junction inside the inclined surge shaft or the vertical surge tank. This type of excitation is more risky and complicated to produce than the water-hammer phenomenon resulting from normal operations. Furthermore, the monitoring of shafts and tunnels would have only a limited number of in-situ data measurements. The main advantage of such artificial excitation, in comparison to normal operation water-hammers, is the possibility of generating an incident wave with a steep front and high energy content, allowing more accurate localization of the weak zones.

9.3 Future research

9.3.1 Future research regarding design of pressure shafts and tunnels

- Further investigations of results of the enhanced model proposed in this work are required with laboratory experiments and in-situ measurements.

They will allow the validation of some cases presented herein and the comparison of a calculated transient event in the time and frequency domains, respectively.

- The comparison of the results of the enhanced model with those obtained from a 3D finite element model can be an interesting topic to investigate. The final results may be used to adapt some existing design procedures using the high-strength steel in aeronautical field, nuclear power plants and long span steel bridges to steel liners design.

9.3.2 Future research regarding monitoring of prototype pressure shafts and tunnels

- A longer series of the in-situ measurement have to be acquired to revise the control limits of the two monitoring charts $\overline{x}$ and R for the water-hammer wave speed. This revision will be done by discarding the out-of-control points from the data series.

- Also, additional measurements are needed to understand the pattern behaviour of the wave dissipation coefficient during the pump and turbine shut-down modes. A persistent shift in the mean values of this coefficient of about 55 % has been observed.

- Equipping the bypass conduit of one spherical control valve in the powerhouse of the Grimsel II plant with a rapid shut-off valve. The controlled rapid manoeuvres of this valve can generate transients with steep wave front and, therefore, decrease the scattering of the monitored indicators values.

- Automation of the on-line monitoring scheme from the data acquisition to the plot of the monitored parameters points on the $\overline{x}$ and R charts. These charts can be shown on the control display of the command center of the power plant.

- Conducting, if possible, in-situ measurements on a pressure shaft surrounded by more heterogeneous rock masses. The validation of the entire localization procedure can be only achieved from such in-situ data.

9.3.3 Future fundamental research

- Solving the enhanced design model in frequency domain and comparing results to the classical time domain solutions.

- Extensive Fluid-Structure Interaction numerical simulations on 3D finite element models to validate the new design model.

- Adaptation and enhancement of the deterministic and probabilistic Fracture Mechanics models for the design of steel liners made of high-strength steel.
- Physical experiments carried out on the test pipe to localize the weak reach by using other type of transient excitations. The shut-off valve can be replaced by an active energy transmitter device having an adjustable energy and frequency values.
- Exploring the capabilities of the standing wave difference method for weak reach detection. This method consists in the generation of steady-oscillatory flow in a pipe system and the analysis of the system pressure response.
- Proposing a pattern recognition model by using, for example, the Neural Network Model to capture the characteristics of the time series of pressure sensors. When structures are damaged changes occur to their dynamic response. Such system identification methods are able to determine the structural properties such as the stiffness and natural periods and frequencies.

Bibliography

Al-Shidhani, L., Beck, S., and Staszewski, W. (2003). Leak monitoring in pipeline networks using wavelet analysis. *Key Engineering Materials*, 245-246:51–58.

Allievi, L. (1913). *Teoria del colpo d'ariete, (English translation by Halmos E.E. 1925) The Theory of Waterhammer*. Ricardo Garoni, Rome.

ANSI (1998). *Test uncertainty*. American Society of Mechanical Engineers, PTC 19.1, New York.

ANSYS (2008). ANSYS Mechanical, Release 12.0, ANSYS Inc, www.ansys.com.

ASME (2007). *Section VIII, Division 1 - Design and Fabrication of Pressure Vessels*. American Society of Mechanical Engineers.

Atabeck, H. (1968). Wave propagation through a viscous fluid contained in a tethered initially stressed, orthotropic elastic tube. *Biophysics Journal*, 8:626–649.

AWWA (2004). *External corrosion - Introduction to chemistry and control, Manual of water supply practices (M27, 2004)*. American Water Works Association, Denver.

Barsom, J. and Rolfe, S. (1999). *Fracture and fatigue control in structures: Applications of fracture mechanics*. ASTM, Butterworth Heinemann, West Conshohocken, third edition.

Beck, S., Curren, M., Sims, N., and Stanway, R. (2005). Pipeline network features and leak detection by cross-correlation analysis of reflected waves. *Journal of Hydraulic Engineering*, 131(8):715–723.

Benson, R. (1986). Design of steel lined penstocks and high pressure power tunnels. In *Fifth Canadian Tunneling Conference*, Niagara Falls.

Bergant, A., Simpson, A., and Vitkovsky, J. (2001). Developments in unsteady pipe low friction modeling. *Journal of Hydraulic Research*, 39(3):249–257.

Besuner, P. and Tetelman, A. (1977). Probabilistic fracture mechanics. *Nuclear Engineering and Design*, 43(1):99–114.

Bieniawski, Z. (1973). Engineering classification of jointed rock masses. *Journal of the South African Institution of Civil Engineering*, 15(12):335–343.

Blevins, R. (1979). *Formulas for natural frequency and mode shape*. Krieger publishing company, Florida.

Brekke, T. and Ripley, B. (1987). Design strategies for pressure tunnels and shafts. Technical report, University of California, Berkeley.

Broch, E. (1984). Unlined high pressure in areas of complex topography. *International Water Power and Dam Construction*, 36(11):21–23.

Brunone, B., Golia, U., and Greco, M. (1991). Some remarks on the momentum equation for fast transients. In *Proc. International Conference on Hydraulic Transients with water column separation, IAHR*, pages 201–209, Valencia, Spain.

Buchs, M. (2010). Recherche tuyaux pour prévenir les ruptures de conduites. *energeia*, (3):12–13.

Budny, D., Wiggert, D., and Hatfield, F. (1991). Influence of strutural damping on internal pressure during a transient pipe flow. *ASME Journal of Fluids Engineering*, 113(3):424–429.

Burr, I. (1967). The effect of nonnormality on constants for $\bar{x}$ and R charts. *Industrial Quality Control*, 23(11):563–569.

Bustamante, S. (2009). Influence of local change of stiffness in liquid filled pipe on water-hammer signal propagation. Master's thesis, School of Engineering, Mechanical Engineering, Ecole Polytechnique Fédérale de Lausanne.

C.E.C.T. (1980). *Recommendations for the design, manufacture and erection of steel penstocks of welded construction for hydroelectric installations*. European Committee of Boiler, Vessel and Pipe work Manufacturers.

Chan, L., Haquarachchi, K., and Macpherson, B. (1988). Robustness of $\bar{x}$ and R charts. *IEEE Transactions on the Reability*, 37(3):117–123.

Chaudhry, H. (1987). *Applied hydraulics transients*. Van Nostrand Reinhold Company, New York, second edition.

Coleman, H. and Steele, W. (1999). *Experimentation and uncertainty analysis for engineers*. Wiley-Interscience, New York, second edition.

Cordelle, F. and Doucerain, T. (1985). Essais de conduite forcée à super-bissorte. *Tunnels et ouvrages souterrains*, (71):201–215.

Covas, D., Ramos, H., and Betâmio de Almeida, A. (2005a). Standing wave difference method for leak detection in pipeline systems. *Journal of Hydraulic Engineering*, 131(12):1106–1116.

Covas, D., Stoianov, I., Mano, J., Ramos, H., Graham, N., and Maksimovic, C. (2004). The dynamic effect of pipe-wall viscoelasticity in hydraulic transients. part I - Experimental analysis and creep characterization. *Journal of Hydraulic Research*, 42(5):516–530.

Covas, D., Stoianov, I., Mano, J., Ramos, H., Graham, N., and Maksimovic, C. (2005b). The dynamic effect of pipe-wall viscoelasticity in hydraulic transients. part II - Model development, calibration and verification. *Journal of Hydraulic Research*, 43(1):56–70.

Daily, J., Hankey, W., Olive, R., and Jordaan, J. (1956). Resistance coefficients for accelerated and decelerated flows through smooth tubes and orifices. In *Trans. ASME*, volume 78, pages 1071–1077.

Eristov, V. (1967). Experimental studies of pressure tunnel linings in anisotropic formations. *Gidrotekhnicheskoe Stroitel'stvo*, 12:19–21.

Eristov, V. (1968). Computation of pressure tunnel linings in anisotropic rocks. *Hydrotechnical Construction*, 1(5):436–442.

Fanelli, M. (1973). Hydraulic resonance in rock-bored penstocks. *Water Power*, September:342–346.

Ferrante, M. and Brunone, B. (2003). Pipe system diagnosis and leak detection by unsteady-state tests. 2. Wavelet analysis. *Advances in Water Resources*, 26:107–116.

Flügge, W. (1973). *Stresses in Shells*. Springer-Verlag, Berlin.

Fuentes, D., Galvis, L., and Valderrama, J. (2006). Hydraulic transients with genetic algorithms used for leakage detection in real water distribution networks. In *Proceedings of the 2006 Pipeline Division Specialty Conference-Pipelines 2006: Service to the Owner Fuentes*, volume 211 40854, page 15.

Ghidaoui, M., Zhao, M., Mclnnis, D., and Axworthy, D. (2005). A review of water hammer theory and practice. *Applied Mechanics Reviews*, 58:49–76.

Grant, F. and West, G. (1965). *Interpretation theory in applied geophysics*. McGraw-Hill, New York.

Gurocak, Z., Solanki, P., and Zaman, M. (2007). Empirical and numerical analyses of support requirements for a diversion tunnel at the Boztepe dam site, eastern Turkey. *Engineering Geology*, 91(2-4):194–208.

Hachem, F. (2009a). Monitoring system for Grimsel II power plant - Objectives, final product and materials cost. Technical report.

Hachem, F. (2009b). Sensing requirements for Grimsel II power plant - Pressurized shafts and tunnels. Technical report.

Hachem, F. (2009c). Sensing requirements for Grimsel II power plant - Pressurized shafts and tunnels, Technical and commercial proposition. Technical report.

Hachem, F. and Schleiss, A. (2009). The design of steel-lined pressure tunnels and shafts. *International Journal on Hydropower and Dams*, 16(3):142–151.

Hachem, F. and Schleiss, A. (2010). Influence of local stiffness of conduits on water hammer propagation signal. In *Proceedings of the First European IAHR Congress, www.iahr.net*, Edinburgh.

Hachem, F. and Schleiss, A. (2011a). Detection of local wall stiffness drop in steel-lined pressure tunnels and shafts of hydroelectric power plants using steep pressure wave excitation and wavelet decomposition. *Journal of Hydraulic Engineering*, DOI: 10.1061/(ASCE)HY.1943-7900.0000478.

Hachem, F. and Schleiss, A. (2011b). The influence of drop in pipe wall stiffness on water-hammer speed and attenuation. *Journal of Hydraulic Research*, Accepted for publication.

Hachem, F. and Schleiss, A. (2011c). Monitoring of steel-lined pressure shafts and tunnels. *International Journal on Hydropower and Dams*, 18(3):74–77.

Hachem, F. and Schleiss, A. (2011d). Monitoring of steel-lined pressure shafts using water-hammer records and wavelet filtering and decomposition. In *Proceedings of the 34th IAHR Biennial Congress*, Brisbane, Australia.

Hachem, F. and Schleiss, A. (2011e). On-line monitoring of steel-lined pressure shafts and tunnels by using pressure transients under normal operation conditions. *Journal of Hydraulic Engineering*, Submitted for publication.

Hachem, F. and Schleiss, A. (2011f). Physical tests for estimating the water-hammer wave speed in pipes and tunnels with local weak wall stiffness. In *Proceedings of 2011 World Environmental and Water Resources Congress (EWRI)*, Palm Springs, California.

Hachem, F. and Schleiss, A. (2011g). A review of wave celerity in frictionless and axisymmetrical steel-lined pressure tunnels. *Journal of Fluids and Structures*, 27:311–328.

Haimson, B. and Cornet, F. (2003). "ISRM" suggested methods for rock stress estimation-part 3: Hydraulic fracturing ("HF") and/or hydraulic testing of pre-existing fractures ("HTPF"). *International Journal of Rock Mechanics and Mining Sciences*, 40(7-8):1011–1020.

Halliwell, A. (1963). Velocity of a waterhammer wave in an elastic pipe. *ASCE Journal of the Hydraulics Division*, 89:1–21.

Hoek, E. (2006). Practical Rock Engineering, Course notes in rock engineering at the University of Toronto. www.rocsience.com/hoek/.

Hunaidi, O. (2006a). Condition assessment of water pipes. Technical report, National Research Council Canada, Institute for Research in Construction, NRCC-50306.

Hunaidi, O. (2006b). New acoustic technology for non-destructive assessment of pipe wall thickness. In *Workshop on Performance and Cost Targets for Water Pipeline Inspection Technologies*, Atlanta, GA.

HYTRAN (2004). Hytran Solutions, Release v3.2.3, www.hytran.net.

Indian-Standards (1996). *Indian Standard, Code of practice for design of tunnels conveying water, Division 14*. Bureau of Indian Standards.

Jaeger, C. (1933). *Théorie générale du coup de bélier: application au calcul des conduites à caractéristiques multiples et des chambres d'équilibre*. Dunod, Paris.

Jaeger, C. (1972). *Rock mechanics and engineering*. Cambridge University Press.

Jaeger, C. (1977). *Fluid Transients in Hydro-Electric Engineering Practice*. Blackie and Son Limited, Glasgow and London.

Kuiken, G. (1984). Wave propagation in fluid lines. *Applied Scientific Research*, 41:69–91.

Kuiken, G. (1988). Amplification of pressure fluctuations due to fluid-structure interaction. *Journal of Fluids and Structures*, 2:425–435.

Kumar, N., Varughese, A., Kapoor, V., and Dhawan, A. (2004). In situ stress measurement and its application for hydro-electric projects-An Indian experience in the Himalayas. *International Journal of Rock Mechanics and Mining Sciences*, 41(Suppl. 1).

KWO (2011). Kraftwerke Oberhasli AG, www.grimselstrom.ch.

LabVIEW (2008). Release 8.6, National Instruments, www.ni.com/labview/.

Lang, F. (1987). *Correlation Techniques*. Van Nostrand Reinhold Company, New York.

Langenberg, P., Niessen, T., and Dahl, W. (2000). Bruch- und Verformungsverhalten von hochfesten Stählen mit Streckgrenzen von 690 bis 890 MPa. *Stahlbau*, (69):283–291.

Lavooij, C. and Tijsseling, A. (1991). Fluid-structure interaction in liquid-filled piping systems. *Journal of Fluids and Structures*, 5:573–595.

Li, Q., Yang, K., and Zhang, L. (2003). Analytical solution for fluid-structure interaction in liquid-filled pipes subjected to impact-induced water hammer. *ASCE Journal of Engineering Mechanics*, 129:1408–1417.

Liggett, J. and Pudar, R. (1992). Leaks in pipe networks. *Journal of Hydraulic Engineering*, 118(7):1031–1046.

Lister, M. (1960). *The numerical solution of Hyperbolic Partial Differential Equations by the Method of Characteristics, A Ralston and HS Wilf (eds), Numerical Methods for Digital Computers*. Wiley, New York.

Lüthi, T. (2010). Non-destructive evaluation methods, Course notes in the Doctoral School at the Ecole Polytechnique Fédérale de Lausanne.

Lyons, R. (1997). *Understanding digital signal processing*. Addison-Wesley, USA.

Maddox, S. (1991). *Fatigue strength of welded structures*. Abington publishing, second edition.

Mallat, S. (1990). *A Wavelet Tour of Signal Processing*. Academic Press, San Diego, CA.

Mallat, S. (1992). Singularity detection and processing with wavelets. *IEEE transactions on Information Theory*, 38(2 pt II):617–643.

Mathworks (2008). MATLAB, Natick, Mass, www.mathworks.com.

Mays, L. (2000). *Water distribution systems handbook*. McGraw-Hill.

McStraw, B. (1996). Inspection of steel penstocks and pressure conduits. Technical report, Denver, Colorado.

Misiunas, D., Vitkovsky, J., Olsson, G., Simpson, A., and Lambert, M. (2005). Pipeline break detection using pressure transient monitoring. *Journal of Water Resources Planning and Management*, 131(4):316–325.

Montgomery, D. (2005). *Introduction to statistical quality control*. John Wiley and Sons, Inc., USA, fifth edition.

Moore, E. (1989). Design of steel tunnel liners. In *Proceedings of the international conference on Hydropower*, pages 384–394, New York.

Müller, W. (1968). *Druckrohrleitungen neuzeitlicher Wasserkraftwerke*. Springer-Verlag Berlin Heidelberg, New York.

Nicholson, D. and Ni, P. (1997). Extreme value probabilistic theory for mixed-mode brittle fracture. *Engineering Fracture Mechanics*, 58(1-2):121–130.

Nicolet, C. (2007). *Hydroacoustic modelling and numerical simulation of unsteady operation of hydroelectric systems*. PhD thesis, Ecole Polytechnique Fédérale de Lausanne.

Nicolopoulos, A. (1983). Current design procedures for steel-lined pressure tunnels. *Canadian Journal of Civil Engineering*, 10(1):150–161.

Nishida, T., Matsumura, Y., Miyanaga, Y., and Hori, M. (1982). Rock mechanical viewpoint on excavation of pressure tunnel by Tunnel Boring Machine. In *International Symposium on Rock Mechanics*, pages 150–161, Aachen.

Pahl, A., Heusermann, S., Bräuer, V., and Glöggler, W. (1989). Grimsel test site - Rock stress investigations. Technical report.

Parmakian, J. (1963). *Waterhammer analysis*. Dover Publications, Inc., New York.

Provan, J. (1987). *Probabilistic fracture mechanics and reliability*. Martinus nijhoff publishers, Quebec, Canada.

Rieutord, E. (1982). Transient response of fluid viscoelastic lines. *ASME Journal of Fluids Engineering*, 104:335–341.

Rubinov, S.I., K. J. (1971). Wave propagation in a fluid-filled tube. *Journal of the Acoustical Society of America*, 50:198–223.

Rubinov, S.I., K. J. (1978). Wave propagation in viscoelastic tube containing a viscous fluid. *Journal of Fluid Mechanics*, 88:181–203.

Salah, B., Massouh, F., Kettab, A., and Mbangangoye, B. (2001). Célérité de l'onde de coup de bélier dans les conduites enterrées. *La Houille Blanche*, 3/4:3–17.

Samuelsson, A. and Schröter, F. (2005). High-performance steels in Europe. Technical report.

Schilling, E. and Nelson, P. (1976). The effect of nonnormality on the control limits of $\bar{x}$ charts. *Journal of Quality Technology*, 8(4):183–188.

Schleiss, A. (1985). Bemessung von Druckstollen - Teil I: Literatur, Grundlagen, Felshydraulik, insbesondere Sickerströmungen durch Auskleidung und Fels. Mitteilung VAW 78.

Schleiss, A. (1986). Bemessung von Druckstollen - Teil II: Einfluss der Sickerströmung in Betonauskleidung und Fels, mechanisch-hydraulische Wechselwirkungen, Bemessungskriterien. Mitteilung VAW 86.

Schleiss, A. (1988). Design criteria applied for the Lower Pressure Tunnel of the North Fork Stanislaus River Hydroelectric Project in California. *Rock Mechanics and Rock Engineering*, 21(3):161–181.

Schleiss, A. (1992). Erforderliche Felsüberdeckung bei Druckstollen und Druckschächten. *Wasser, Energie, Luft*, (11/12):321–324.

Schleiss, A. (2002). Berücksichtigung des Restrisikos bei der Konzeption und Bemessung von hochbeanspruchten Druckschächten. In *Int. Symposium Moderne Methoden und Konzepte im Wasserbau, Versuchsanstalt für Wasserbau, Hydrologie und Glaziologie (VAW-Mitteilung)*, volume 175, pages 385–394.

Schleiss, A. (2007). Pressurized waterway structures - Module C2, Design of pressure tunnels and shafts, Course notes in the Master of Advanced Studies in Water Resources Management and Engineering at the Ecole Polytechnique Fédérale de Lausanne.

Seeber, G. (1975). Neue Entwicklungen für Druckstollen und Druckschächte. *Österreichische Ingenieur-Zeitschrift*, 18(5):140–149.

Seeber, G. (1985a). Power conduits for high-head plants (Part one). *Water Power and Dam Construction*, June:50–54.

Seeber, G. (1985b). Power conduits for high-head plants (Part two). *Water Power and Dam Construction*, July:95–98.

Seeber, G. and Danzl, K. (1988). Zur Bemessung von Druckschachtpanzerungen auf Innendruckbelastung. *Österreichische Ingenieur-Zeitschrift*, 133(4):259–266.

Shamloo, H. and Haghighi, A. (2009). Leak detection in pipelines by inverse backward transient analysis. *Journal of Hydraulic Research*, 47(3):311–318.

Sheory, P. (1994). A theory for in situ stresses in isotropic and transversely isotropic rock. *International Journal of Rock Mechanics and Mining Science and Geomechanics*, 1:23–34.

Shin, K. and Hammond, J. (2008). *Fundamentals of signal processing for sound and vibration engineers*. John Wiley and Sons, Ltd, New York.

Shuy, E. (1996). Wall shear stress in accelerating and decelerating turbulent pipe flows. *Journal of Hydraulic Research*, 34(2):173–183.

Skalak, R. (1956). An extension of the theory of waterhammer. In *Transactions of the ASME*, volume 78, pages 116–195.

Smith, S. (1997). *The scientist and engineer's guide to digital signal processing*. California Technical Publishing, San Diego, CA.

Starnberger, R. and Chène, O. (2011). Rehabilitation of the Cleuson-Dixence pressure shaft. *International Journal on Hydropower and Dams*, 18(3):78–80.

Stephens, M. (2008). *Transient response analysis for fault detection and pipeline wall condition assessment in field water transmission and distribution pipelines and networks*. PhD thesis, School of Civil and Environmental Engineering, University of Adelaide, South Australia.

Stephens, M., Simpson, A., and Lambert, M. (2008). Internal wall condition assessment for water pipelines using inverse transient analysis. In *Proceedings of the 10th Annual Symposium on Water Distribution Systems Analysis, ASCE*, Kruger National Park, South Africa.

Streeter, V. (1963). Discussion of Halliwell A.R. 1963 velocity of a water-hammer wave in an elastic pipe. *ASCE Journal of the Hydraulics Division*, (89):295–296.

Stuckenbruck, S., Wiggert, D., and Otwell, R. (1985). The influence of pipe motion on acoustic wave propagation. *ASME Journal of Fluids Engineering*, (107):518–522.

Suo, L. and Wylie, E. (1990a). Complex wavespeed and hydraulic transients in viscoelastic pipes. *ASME Journal of Fluids Engineering*, 112:496–500.

Suo, L. and Wylie, E. (1990b). Hydraulic transients in rock-bored tunnels. *Journal of Hydraulic Engineering*, 116(2):196–210.

Surber, A. (1958). Etude expérimentale du comportement d'un blindage de puits forcé d'une importante centrale hydro-électrique. *Bulletin Escher Wyss*, pages 3–11.

Tâche, J. (1949). Contribution à la théorie et au calcul du blindage d'une galerie circulaire. *Bulletin Technique Vevey*, (1):19–27.

Taghvaei, M., Beck, S., and Boxall, J. (2010). Leak detection in pipes using induced water hammer pulses and cepstrum analysis. *International Journal of COMADEM*, 13(1):19–25.

Taghvaei, M., Beck, S., Boxall, J., Seth, A., and Staszewski, W. (2008). Leak detection in water distribution network. In *Proceedings of the 10th International conference on Pressure surges*, pages 125–135, Edinburgh.

Tagwerker, J. (1980). The frequency of surge tank oscillations and their effect on the fatigue resistance of tunnel liners. *Oesterr. Wasserwirtsch.*, 32(5-6):105–113.

Talobre, J. (1967). *La méchanique des roches et ses applications*. Dunod, Paris.

Tijsseling, A. (1996). Fluid-structure interaction in liquid-filled pipe systems: a review. *Journal of Fluids and Structures*, 10:109–146.

Tijsseling, A. (2003). Exact solution of linear hyperbolic four-equation system in axial liquid-pipe vibration. *Journal of Fluids and Structures*, 18:179–196.

Tijsseling, A. (2007). Water hammer with fluid-structure interaction in thick-walled pipes. *Computers and Structures*, 85:844–851.

Tijsseling, A., Lambert, M., Simpson, A., Stephens, M., Vitkovsky, J., and Bergant, A. (2008). Skalak's extended theory of water hammer. *Journal of Sound and Vibration*, 310:718–728.

Timoshenko, S. and Gere, J. (2009). *Theory of elasticity*. Dover Publications, Inc., New York.

Trefethen, L. (1997). *Numerical linear algebra*. Society for Industrial and Applied Mathematics, Philadelphia.

USACE (1995). *Planning and design of hydroelectric power plant structures (EM 1110-2-3001)*. US Army Corps of Engineers.

USACE (1997). *Tunnels and shafts in rock (EM 1110-2-2901)*. US Army Corps of Engineers.

Vardy, A. and Brown, J. (1995). Transient turbulent smooth pipe friction. *Journal of Hydraulic Research*, 33:435–456.

Vardy, A. and Brown, J. (1997). Discussion on wall shear stress in accelerating and decelerating turbulent pipe flows. *Journal of Hydraulic Research*, 35(1):137–139.

Vardy, A., Hwang, K., and Brown, J. (1993). A weighting model of transient turbulent pipe friction. *Journal of Hydraulic Research*, 31:533–548.

Vaughan, E. (1956). Steel linings for pressure shafts in solid rock. In *Proceedings of the Society of civil Engineers*, pages 9491–9493.

Welch, P. (1967). The use of fast Fourier transform for the estimation of power spectra: a method based on time averaging over short, modified periodograms. In *IEEE Transactions on Audio and Electroacoustics*, volume AU-15, pages 70–73.

Wood, D., Dorsch, R., and Lightnor, C. (1966). Wave-plan analysis of unsteady flow in closed conduits. *ASCE Journal of the Hydraulics Division*, 92(HY12):83–110.

Wylie, E., Suo, L., and Streeter, V. (1993). *Fluid Transients in Systems*. Prentice Hall, Fascimile Edition.

Yang, W., Barry Hull, J., and Seymour, M. (2006). Detecting the singularities in engineering signals. *Journal of Materials Processing Technology*, 175:435–445.

Yourstone, S. and Zimmer, W. (1992). Non-normality and the design of control charts for averages. *Decision Sciences*, 23(5):1099–1113.

Zerjeski, B. (2006). Pressurized waterway structures - Module C2, Penstocks, Course notes in the Master of Advanced Studies in Water Resources Management and Engineering at the Ecole Polytechnique Fédérale de Lausanne.

Zielke, W. (1968). Frequency-dependent friction in transient pipe flow. *ASME Journal of Basic Engineering*, 90(1):109–115.

Nomenclature

Roman Symbols

A internal cross-sectional area of the steel liner, (m^2)

a quasi-static wave speed of water-hammer, (m/s)

a_{WR} front wave speed in water inside the weak reach of pipes, penstocks or steel-lined pressure tunnels, (m/s)

a_c depth of the critical crack in the steel liner, (m)

A_h cross-sectional area of the headrace tunnel, (m^2)

A_i i^{th}-level approximation coefficient in wavelet decomposition, (-)

b_1, b_2 real numbers (Eq. (8.5)), (-)

c complex wave speed, (m/s)

c_0 reference wave speed used in FSI model, (m/s)

C_1,C_2 complex constants of solution used in FSI model, (-)

c_{0eq} complex wave speed defined in (Eq. (4.52)), (m/s)

c_c half-length of the critical crack in the steel liner, (m)

c_{gi} group velocity of the i^{th} mode defined in (Eq. (4.52)), (m/s)

C_G damping coeffcient of the geophone, (N.s/m)

c_i phase or group velocities of the i^{th} mode, (m/s)

c_{pi} phase velocity of the i^{th} mode defined in (Eq. (4.52)), (m/s)

$C_{r,l}$ radial (resp. longitudinal) damping coefficient per unit area of the Kelvin model, ((N s/m)/m^2)

c_T speed of sound in unconfined water, (m/s)

D complex integration constant used in FSI model, (-)

$D^{'}$ mode-dependent factor used in FSI model and defined in (Eq. (4.33)), (-)

$d_{f\,\max}$ width of the biggest crack in backfill concrete, (m)

D_i ith-level detail coefficient in wavelet decomposition, (-)

d_i internal diameter of the pipe or the steel liner, (m)

E elasticity modulus, (MPa)

e steel liner, penstock or pipe wall thickness, (m)

E_{app} apparent elasticity modulus of rock mass defined in (Eq. (4.45)), (MPa)

E_{crm} elasticity modulus of the near-field loosened rock zone, (MPa)

E_{rm} elasticity modulus of the far-field rock zone, (MPa)

E_c elasticity modulus of backfill concrete, (MPa)

E_r in-situ rock modulus, (MPa)

E_s elasticity modulus of steel, (MPa)

F cross-sectional area of the vertical surge tank, (m^2)

f excitation frequency, (Hz)

$f_c^{'}$ compression strength of backfill concrete, (MPa)

f_0 natural frequency of the geophone, (Hz)

f_{cent} central frequency of the db10 wavelet, (Hz)

f_{fund} estimated fundamental frequency od the test pipe defined in (Eq. (6.6)), (Hz)

f_{samp} sampling rate or frequency, (Hz)

f_a pseudo-frequency of the db10 wavelet, (Hz)

f_c tensile strength of backfill concrete, (MPa)

f_{D-W} Darcy-Weisbach steady-state friction factor, (-)

f_f steel brittle fracture strength, (MPa)

f_m steel maximum strength, (MPa)

F_r resultant of radial forces applied on the liner per unit area used in FSI model, (MN/m^2)

f_s allowable stress in steel, (MPa)

f_u steel tensile strength, (MPa)

F_x resultant of axial forces applied on the liner per unit area used in FSI model, (MN/m^2)

f_y steel yield strength, (MPa)

G geophone sensitivity, (V.s/m)

g gravitational acceleration, (m/s^2)

G_{rm} shear modulus of rock, (MPa)

h piezometric head, (m)

$H(f)$ transfer function

h_0 steady-state piezometric head, (m)

h_i piezometric head of the incident pressure wave, (m)

$h_{t\mathrm{n}}$ piezometric head of the transmitted pressure wave crossing the n$^{\mathrm{th}}$ boundary, (m)

h_t piezometric head of the transmitted pressure wave, (m)

i the complex number (-1)$^{0.5}$, (-)

j scale index in wavelet decomposition, (-)

k ratio of the reference wave speed c_0 to the complex wave speed c used in FSI model, (-)

k_0 ratio of the minimum horizontal to vertical in-situ stresses, (-)

k_θ radial reaction coefficient of rock at θ coordinate (Eristov method), (MPa)

K_G spring constant of the geophone, (N/m)

K_{IC} steel fracture toughness, (MPa.m$^{0.5}$ or ksi.in$^{0.5}$)

K_I stress intensity factor, (MPa.m$^{0.5}$ or ksi.in$^{0.5}$)

k_p ratio of plastic to elastic deformation of rock, (-)

$k_{t\theta}$ tangential reaction coefficient of rock at θ coordinate (Eristov method), (MPa)

k_t time index in wavelet decomposition, (-)

K_w bulk modulus of water, (MPa)

k_x reaction coefficient of rock mass in x direction (Eristov method), (MPa)

k_y reaction coefficient of rock mass in y direction (Eristov method), (MPa)

$Ks_{r,l}$ radial (resp. longitudinal) spring stiffness coefficient per unit area of the Kelvin model, $((\mathrm{N/m})/\mathrm{m}^2)$

L length of tunnel or shaft between surge tank and control valves, (m)

L_1 incident-reflection distance between the weak reach and the downstream reservoir, (m)

L_2 incident-reflection distance between the weak reach and the upstream reservoir, (m)

$L_{\mathrm{P1,P2}}$ length of the test pipe between the two pressure sensors P1 and P2, (m)

L_{WR} estimated length of the weak reach, (m)

L_{WR} estimated length of the weak reach, (m)

L_h length of the headrace tunnel measured from the surge tank to the upper reservoir, (m)

L_p length of the test pipe between the vertical axis of the shut-off valve and the air vessel, (m)

L_T total length of the test pipe between the supply reservoir and the air vessel, (m)

M Mach number, (-)

m positive integer (Eq. (3.16)), (-)

m_1 positive integer (Eq. (3.19)), (-)

m_2 positive integer (Eq. (3.19)), (-)

M_G oscillating mass of the geophone, (kg)

$M_{r,l}$ radial (resp. longitudinal) additional mass per unit area of the Kelvin model, $(\mathrm{kg/m}^2)$

N number of samples of the digitized signals in time domain, (-)

n positive integer (Eq. (3.16)), (-)

N_{RMS} real parameter defining the RMS resolution, (-)

n_b number of beam elements of the steel liner in Eristov method, (-)

n_p pump rotation speed of the experimental set-up, (rpm)

p internal water pressure in excess of p_0 used in FSI model, (MPa)

p_0 internal water pressure in the steady-state conditions used in FSI model, (MPa)

p_θ elastic reaction forces of rock mass in θ direction (Eristov method), (MN)

p_a uniform pressure transmitted to the rock zone at radius r_a, (MPa)

p_c uniform pressure transmitted to backfill concrete at radius r_c, (MPa)

p_f uniform pressure transmitted to the rock zone at radius r_f, (MPa)

p_i internal quasi-static water pressure, (MPa)

p_r pressure taken by the concrete-rock system, (MPa)

p_s pressure taken by the steel liner, (MPa)

q flow discharge, (m^3/s)

r radius measured from tunnel or pipe axis, (m)

r_a internal radius of the near-filed rock zone, (m)

r_c internal radius of the backfill concrete, (m)

r_f internal radius of the far-filed rock zone, (m)

r_i internal radius of the pipe or the steel liner, (m)

s wavelet dilation, (s)

$S_{\max}$ maximum surge height measured from the steady-state level, (m)

t time, (s)

t_{int} time separating the intersection point of the regression line for the steady-state pressure and the regression line for the first pressure front, (s)

T_{osc} surge oscillation period, (s)

$t_{\text{P1,P2}}$ travel time of water-hammer wave between sensors P1 and P2, (s)

T_d radial diffusion time scale, (s)

u wavelet translation, (s)

u_r radial deformation of the rock mass, (m)

u_l^s longitudinal deformation of the steel liner, (m)

u_r^{crm} radial deformation of the near-field rock zone, (m)

u_r^{rm} radial deformation of the far-field rock zone, (m)

u_r^c radial deformation of the backfill concrete, (m)

u_r^s radial deformation of the steel liner or the test pipe wall, (m)

V volume of air or sediment inside the flow, (m^3)

v_0 steady-state flow velocity in the axial direction, (m/s)

v_l flow velocity in the axial direction, (m/s)

v_r flow velocity in the radial direction, (m/s)

V_T total reference volume of the multiphase or multicomponent flow mixture, (m^3)

Wf continuous wavelet transform coefficients, (-)

x spatial coordinate along the longitudinal axis, (m)

z depth of the tunnel below surface, (m)

Greek Symbols

α arc defining the beam element (Eristov method), (rad)

α_1 thermal coefficient of expansion of steel, ($^\circ C^{-1}$)

Δh piezometric head increase at the wave front, (m)

Δp pressure increase at the wave front, (Pa)

Δ_i logarithmic decrement of the i^{th} propagating mode defined in (Eq. (4.52)), (-)

$\Delta r(\theta)$ radial deformation of the steel liner at θ angle (Eristov method), (m)

Δr_0 initial gap between steel liner and concrete, (m)

Δr_x rock mass deformation in the x direction (Eristov method), (m)

Δr_y rock mass deformation in the y direction (Eristov method), (m)

ΔS beam element length of the steel liner (Eristov method), (m)

ΔT temperature variation of the steel liner, ($^\circ C$)

η pump efficiency, (%)

Γ dimensionless parameter (Eq. (3.7)), (-)

κ bulk viscosity of water used in FSI model, (Pa.s)

λ_i wave length of the ith propagating mode (=c_i/f) defined in (Eq. (4.52)), (m)

μ dynamic viscosity of water, (Pa.s)

μ_{sc} friction between steel and concrete, (-)

ν_c Poisson's ratio of backfill concrete, (-)

ν_r Poisson's ratio of the near- and far-fields of the rock mass, (-)

ν_s Poisson's ratio of steel, (-)

ω angular frequency of transient excitations (=$2\pi f$), (rad/s)

ω_0 natural angular frequency of the geophone, (-)

$\Psi f_{u,s}$ mother wavelet of translation u and dilation s, (-)

ρ unit mass of water in excess of ρ_0 used in FSI model, (kg/m^3)

ρ_0 unit mass of water in the steady-state conditions used in FSI model, (kg/m^3)

ρ_r unit mass of rock, (kg/m^3)

ρ_s unit mass of steel, (kg/m^3)

ρ_w unit mass of water, (kg/m^3)

σ_{eq} equivalent stress in steel liner (Hencky-Von Mises stress), (MPa)

σ_l longitudinal stress in the theory of thick-walled cylinder, (MPa)

σ_l^+ perturbation of longitudinal stress in the liner per unit length, (MN/m)

σ_l^0 initial longitudinal stress in the liner per unit length, (MN/m)

σ_r radial stress in the theory of thick-walled cylinder, (MPa)

σ_r^+ perturbation of circumferential stress in the liner per unit length, (MN/m)

σ_r^0 initial circumferential stress in the liner per unit length, (MN/m)

σ_{s1} tangential steel stress in liner, (MPa)

σ_{s2} radial steel stress in liner, (MPa)

σ_{s3} longitudinal steel stress in liner, (MPa)

σ_t tensile stress in the theory of thick-walled cylinder, (MPa)

τ_w shear stress at the water-wall interface, (N/m^2)

θ polar angle coordinate (Eristov method), (°)

ε_l longitudinal strain in the theory of thick-walled cylinder, (-)

ε_m steel deformation at f_m, (-)

ξ positive real number (Eq. (3.7)), (-)

ζ damping ratio for the Kelvin model used in FSI model, (-)

ζ_G damping ratio of the geophone, (-)

Sub- and Superscripts

c superscript for backfill concrete

l subscript for longitudinal direction

r subscript for radial direction

s superscript for steel

Alu subscript for aluminum reach

crm superscript for near-field rock mass

fund subscript for fundamental period or frequency

max subscript for maximum value

min subscript for minimum value

P1 subscript for pressure records P1

P2 subscript for pressure records P2

PVC subscript for PVC reach

rm superscript for far-field rock mass

Steel or s subscript for steel reach

WR subscript for Weak Reach

List of Acronyms

CCEM Swiss Competence Center Energy and Mobility

CCTV Closed Circuit Television

DFT Discrete Fourier Transform

EPFL Ecole Polytechnique Fédérale de Lausanne

FSI Fluid-Structure Interaction

FZ Fusion Zone in weldings

HAZ Heat Affected Zone in weldings

KWO Kraftwerke Oberhasli AG

LCH Laboratoire de Constructions Hydrauliques

LMH Laboratoire de Machines Hydrauliques

MOC Method of Characteristics

NDT Non-Destructive Testing

PDF Probabilistic Distribution Function

PFM Probabilistic Fracture Mechanics

PF4 The name of the experimental test rig

PVC Polyvinyl Chloride Pipe

Q Rock Quality index

QT Quenching and Tempering process

RMR Rock Mass Rating

RMS Root Mean Square

TBM Tunnel Boring Machines

Acknowledgement

The present research work is the outcome of an amazing four-years of my career at the Laboratory of Hydraulic Constructions (LCH) of the Swiss Federal Institute of Technology in Lausanne (EPFL).

This work would not have been possible without the support of many people. First and foremost, I wish to express my gratitude to Prof. Dr. Anton Schleiss who was abundantly helpful and offered invaluable assistance, support and guidance from the preliminary to the concluding level. I owe my deepest thanks to him for having confidence in my abilities and for the freedom granted to achieve my own ideas and goals. I would like to thank him also for offering me an excellent working conditions and the opportunity to attend several national and international scientific conferences. It was a great honor for me to work under his supervision.

Deepest gratitude are also due to Prof. Dr. François Avellan for his courtesy and kindness of giving me the opportunity to carry out the physical experiments in the Laboratory of Hydraulic Machines (LMH) of the EPFL.

I am indebt to Ass. Prof. Dr. Didia Isabel Cameira Covas who has shared with me her remarkable knowledge in transient flows. I greatly appreciated her valuable comments, encouragement and advice during her stay at LCH as invited professor.

The author would like to convey thanks for the financial support to the Swiss Competence Center Energy and Mobility, CCEM-CH, to the Swisselectric research and to the Swiss Office for Energy. He wishes also to acknowledge Lombardi Foundation for providing a part of the financial means for the experimental facility and Kraftwerke Oberhasli AG (KWO) for supporting the installation and the operation of prototype measurements. Without their help the author could not have gotten such relevant experiment and in-situ data.

I also would like to make a special reference to Dr. Jean-Louis Boillat who I appreciated a lot. It has always been a great pleasure to work with him.

Gratitude is dedicated to Prof. Dr. Alain Nussbaumer for accepting to be the president of my PhD jury and to Prof. Dr. François Avellan, Ass. Prof. Dr. Didia Isabel Cameira Covas, and Dr. Christophe Nicolet who have attend my PhD committee, their valuable review and comments.

Special thanks to all my friends and colleagues at LCH for their help, support and wonderful friendships. Appreciations are specially addressed to Michael Müller for his great assistance in the in-situ measurements and for the "Zusam-

menfassung", and to Sebastien Bustamente for his help during physical tests.

It is a pleasure to thank also Michel Teuscher, Cédric Bron, Louis Bezencon, and Fritz Büchi. They made this thesis possible through their technical support.

I wish to express my deepest thanks and gratitude to my beloved family; my parents, Elia and Soumaya and my sisters, Mirna and Lena for making possible my education and for their continuous support and encouragement.

And last but not least, my warmest recognition to my lovely wife, Karima, and to my little princess, Catherina, for their understanding, patience, and endless love.

Lausanne, September 2011

FADI HACHEM

Appendix A

Description and analysis of an in-situ test carried out on a steel-lined tunnel reach at the "Super-Bissorte" power plant

The layout drawing and the main characteristics of the in-situ test described in this appendix, have been taken from Cordelle and Doucerain (1985). Some details of the test scheme are shown in Fig. A.1. The load testing diagram is given in Fig. A.2. The following measurements have been acquired from the sensors shown in cross-sections 1-1 and 2-2 of Fig. A.1.

- Radial displacements of rock at four points located at the top, bottom and at the both lateral sides of the liner. The displacements at the rock-concrete interface have been also measured
- Pressures transmitted to the backfill concrete near the liner-concrete and the concrete-rock interfaces
- Three internal diametrical deformations of the steel liner

At the end of the test, three steel and concrete samples have been taken from three different places: two samples from zones where the steel liner was localy highly deformed and one sample from normal behaviour zones. These samples have been tested in laboratory and results have showed that no significant modifications of the mechanical properties of steel have been occurred. Many cracks have been found in the concrete sample which has been taken from the normal behaviour zone. The other concrete samples were completely crushed.

The analysis of the test results are based on the curves shown in Figs. A.3 and A.4. These figures give the variations of the radial deformation of the three components (steel-concrete-rock) of the tunnel wall as a function of the internal water pressure. The following observations can be formulated:

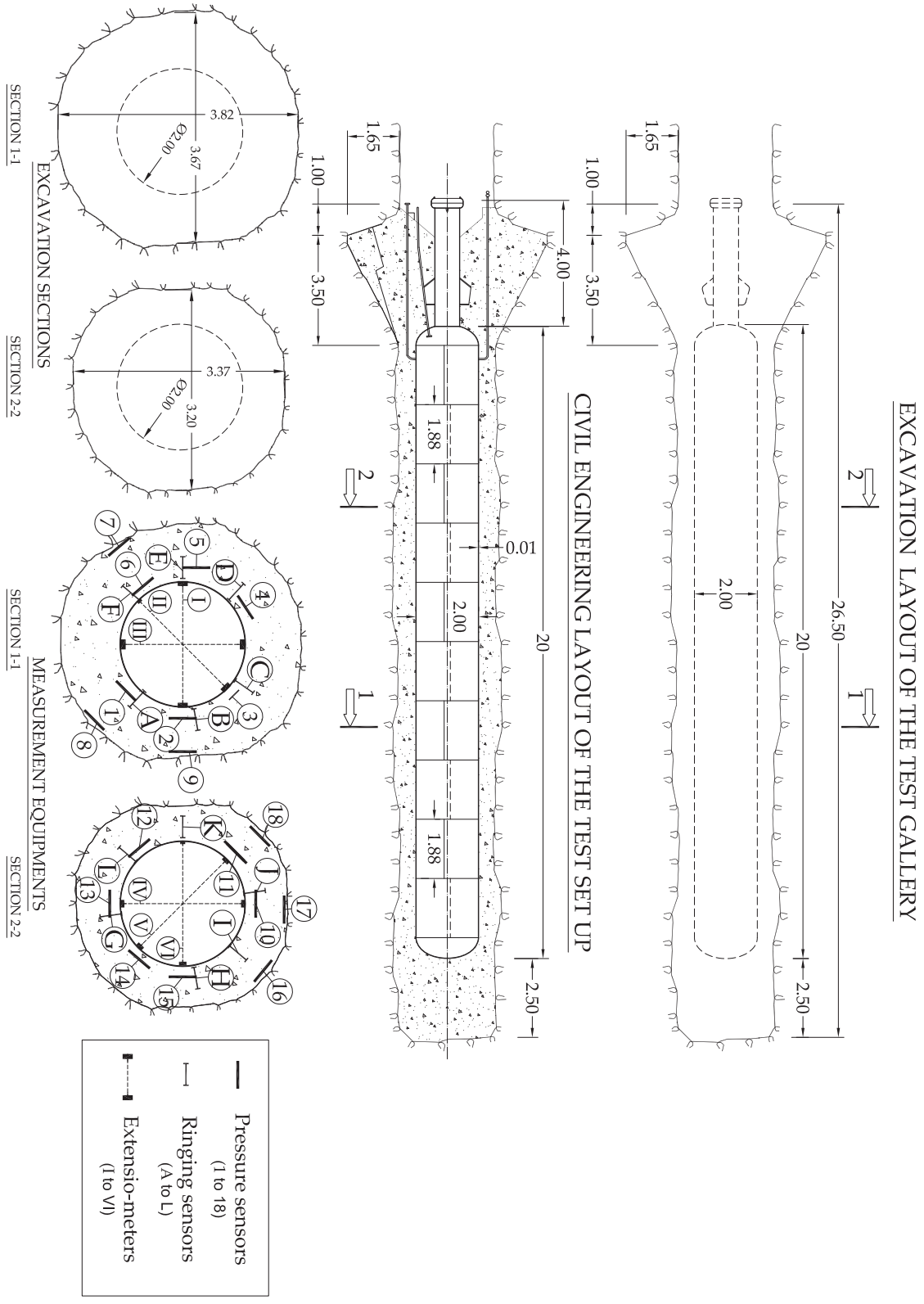

Figure A.1: Layout and sections of the test reach of the steel-lined pressure tunnel constructed at the "Super-Bissorte" power plant.

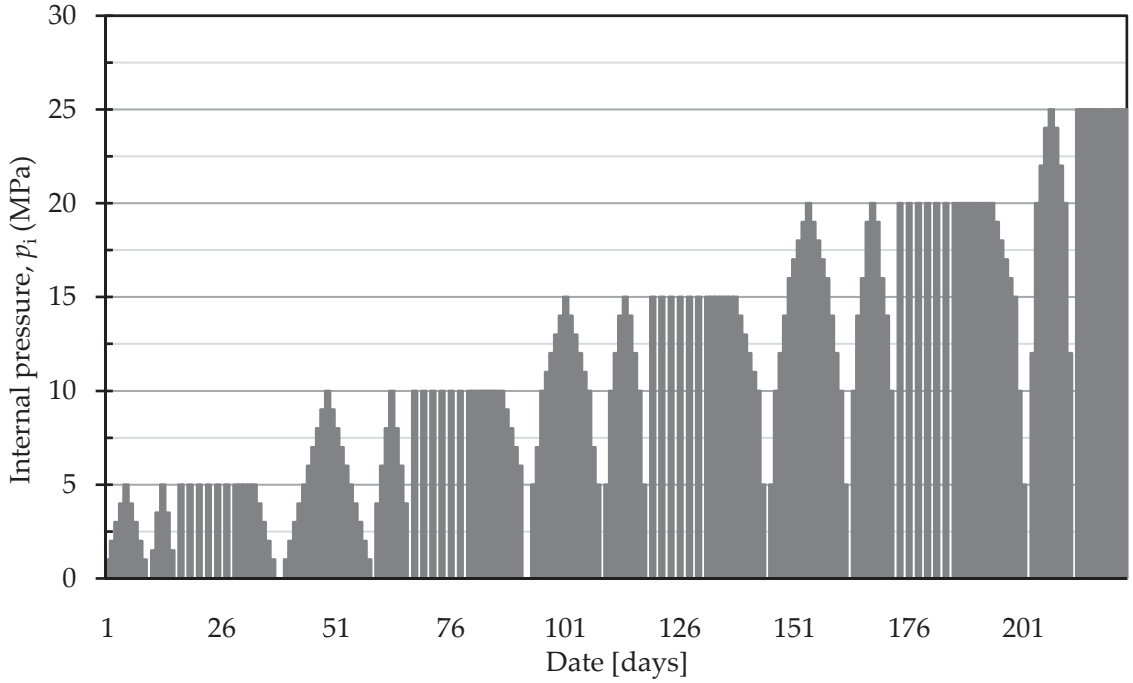

Figure A.2: Pressure test diagram.

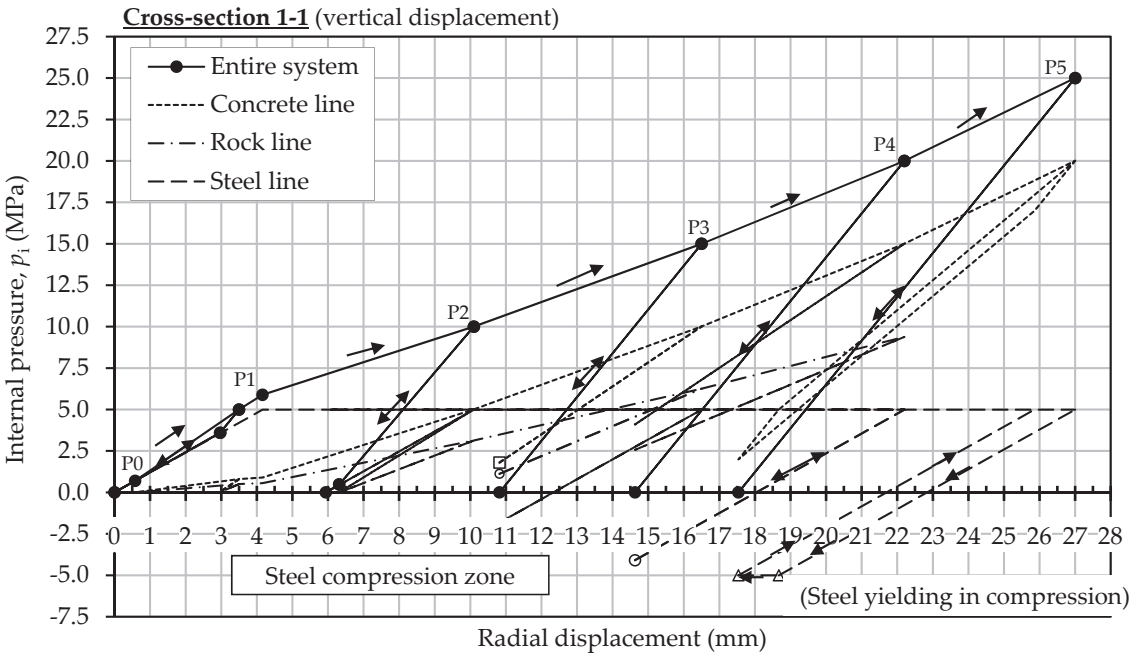

Figure A.3: Radial deformation at cross-section 1-1 of the test tunnel wall of the "Super-Bissorte" power plant as a function of the internal water pressure.

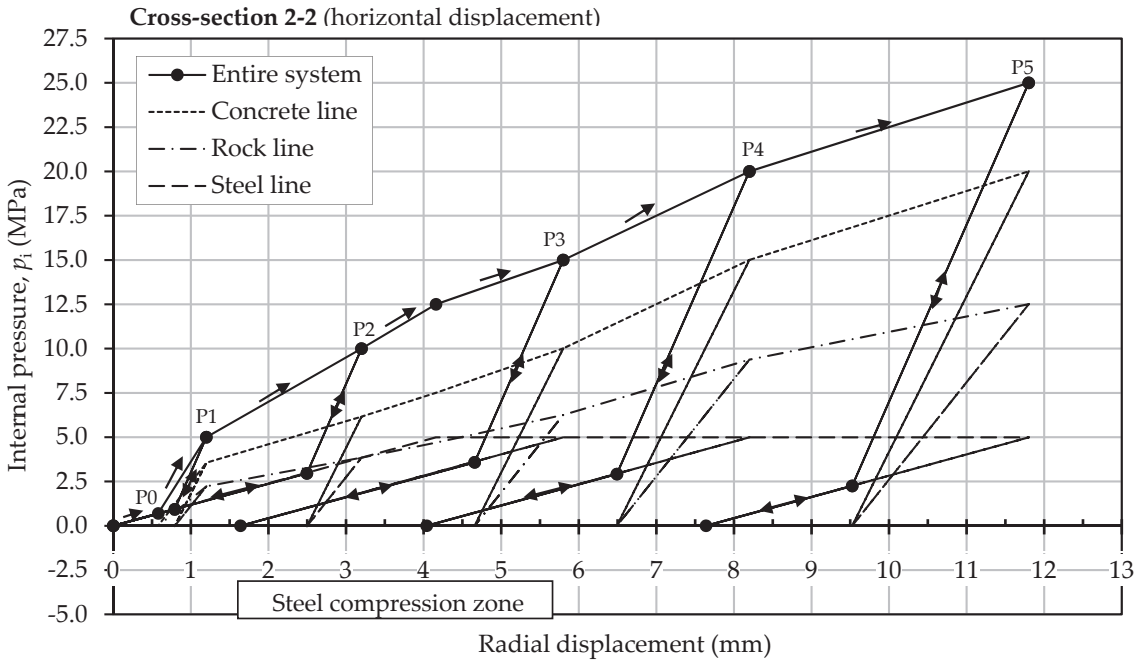

Figure A.4: Radial deformation at cross-section 2-2 of the test tunnel wall of the "Super-Bissorte" power plant as a function of the internal water pressure.

- From zero pressure to $P_0 \approx 0.7\,\text{MPa}$, the steel liner is acting alone. This indicates the presence of an initial thermal gap between the liner and the backfill concrete
- From P_0 to $P_1 = 5\,\text{MPa}$, the internal pressure is transmitted to the concrete and rock layers. The liner is still working in its elastic range. After the unloading phase from P_1 to zero pressure, a residual gap between the liner and the backfill concrete was observed in cross-section 2-2. This gap is probably caused by the creep of the surrounding rock mass. No such gap was detected in cross-section 1-1.
- For the second loading phase from zero pressure to $P_2 = 10\,\text{MPa}$, the structure behaves in a same way as before until the pressure reaches P_1. From this point, the participation of the concrete and rock layers is much higher. In cross-section 2-2, the steel liner is still working elastically, while in section 1-1, steel yielding was observed when the internal pressure goes above P_1. In this case, the increase of the internal pressure was totally transmitted to rock
- Unloading the tunnel from P_2 to zero pressure creates in cross-section 2-2 an important residual gap between the liner and the backfill concrete (around 2.5 mm). In cross-section 1-1, the gap is much smaller (around 0.5 mm). This important difference is caused by the yielding of the steel liner in section 1-1.

- Repeating the same loading-unloading procedure between pressures P_2 and $P_3 = 15\,\text{MPa}$ generates yielding of the steel liner in cross-section 2-2. In cross-section 1-1, the unloading phase from P_3 to zero pressure creates compression in the liner (up to 1.8 MPa). This is probably caused by the high deformability of rock surrounding the liner at this. The same behaviour was observed during the unloading phases from $P_4 = 20\,\text{MPa}$ and $P_5 = 25\,\text{MPa}$. During the last unloading phase, the steel reaches its yielding stress in compression at section 1-1.

The behaviour of the tunnel wall and its components during this test shows clearly the complex interaction phenomenon between the liner, the backfill concrete and the rock layer. The heterogeneity of the rock mass and the ductility of the steel liner have an important influence on the structure deformation and load transfer between the tunnel wall components. It is obvious that with high-strength steel and with more rapid load-unload sequences, the structure behaviour will be completely different.

Appendix B

Description of the experimental set-up

B.1 Photos of the initial configuration of the test rig at LMH

(a)

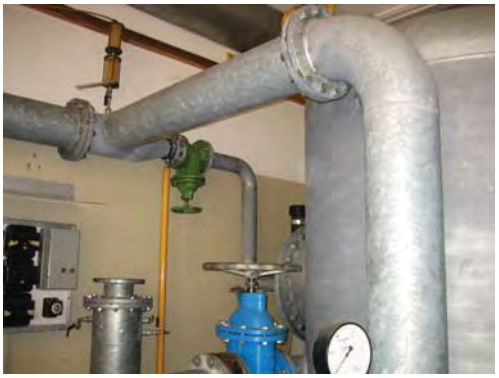

(b)

(c)

(d)

(e) (f)

Figure B.1: Photos of the main components of the old experimental test rig, (a) variable speed pump (to preserve), (b) part of the supply conduit (to preserve), (c) Francis turbine and its generator (to dismantle), (d) downstream connection of the turbine to the supply reservoir (to adapt), (e) water supply reservoir (to preserve), and (f) air-vessel (to preserve).

B.2 Height-capacity curves and some detail drawings of the supply reservoir

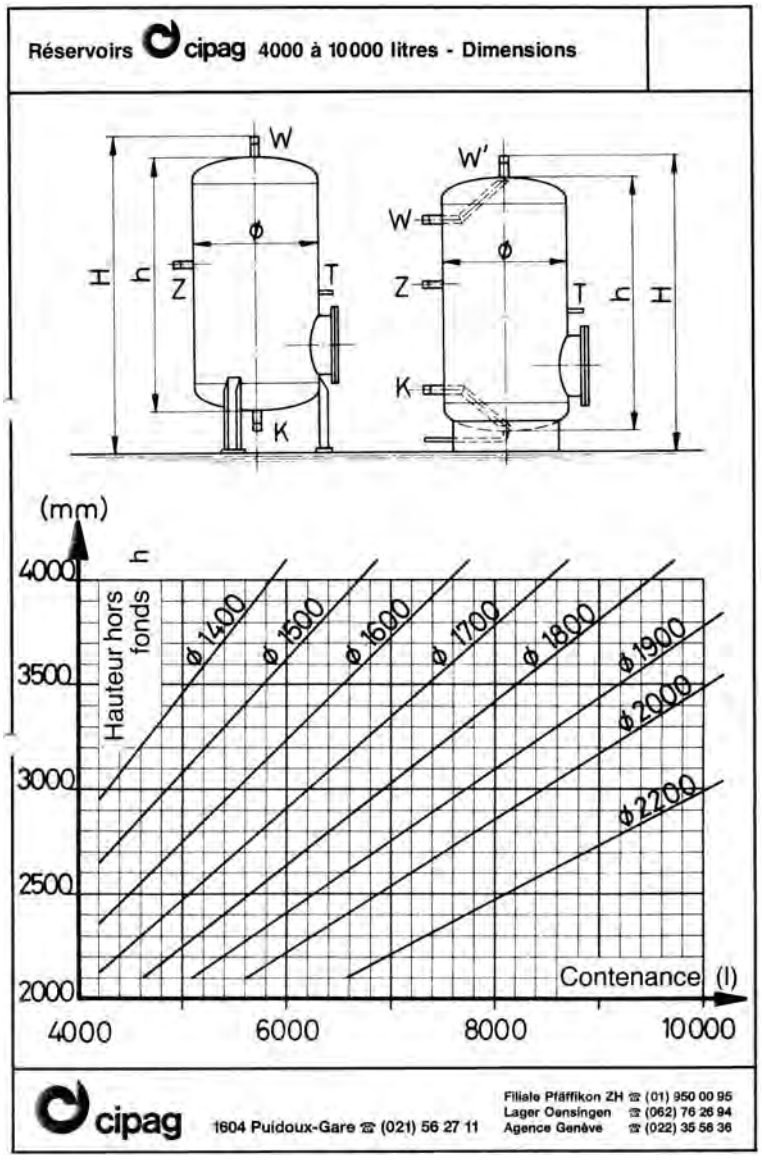

Figure B.2: Height-capacity curves of the supply reservoir type "cipag W" (source: LMH archives).

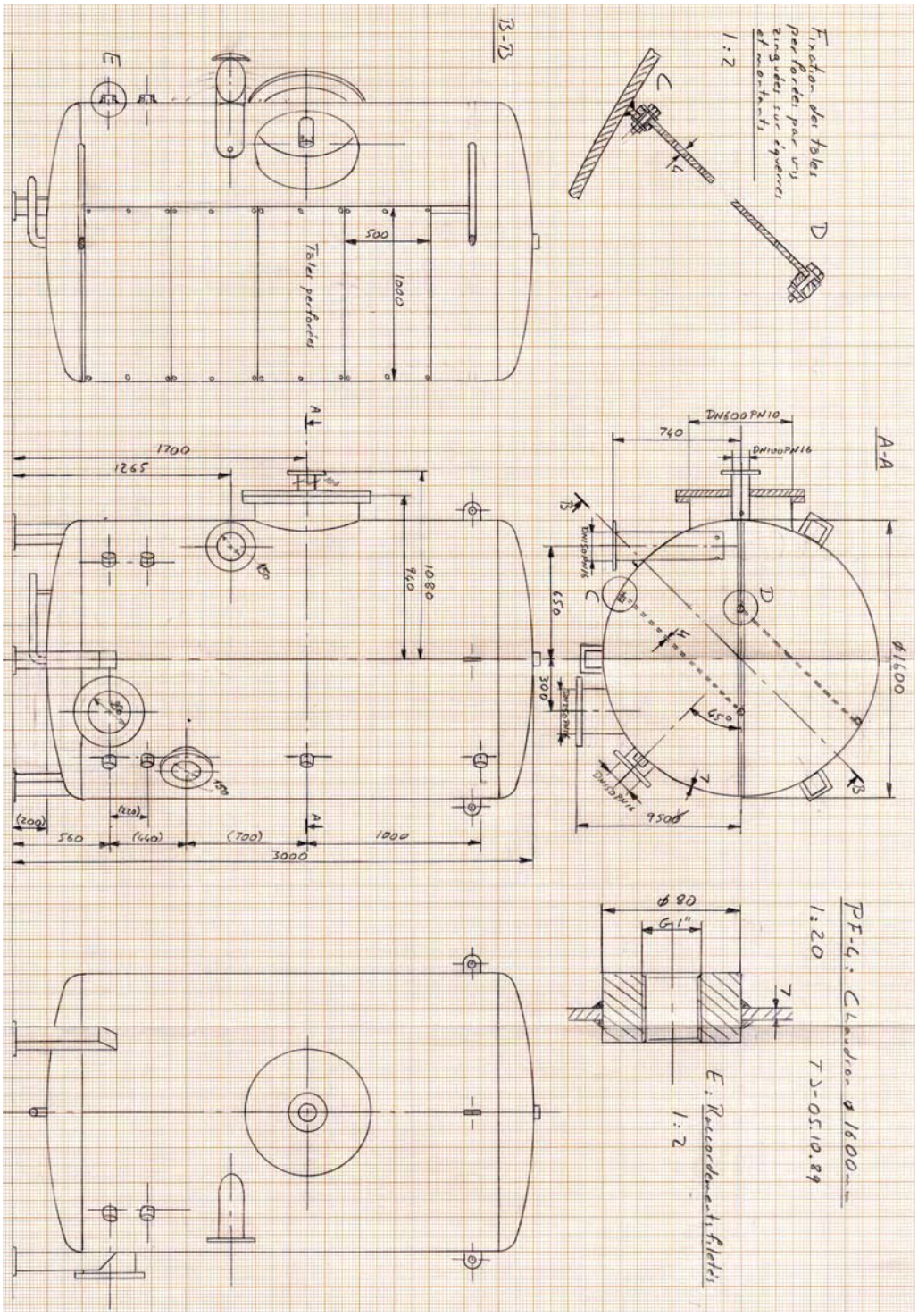

Figure B.3: Detail drawings of the supply reservoir of the test rig "PF4" (source: LMH archives).

B.3 Detailed drawings of the air vessel

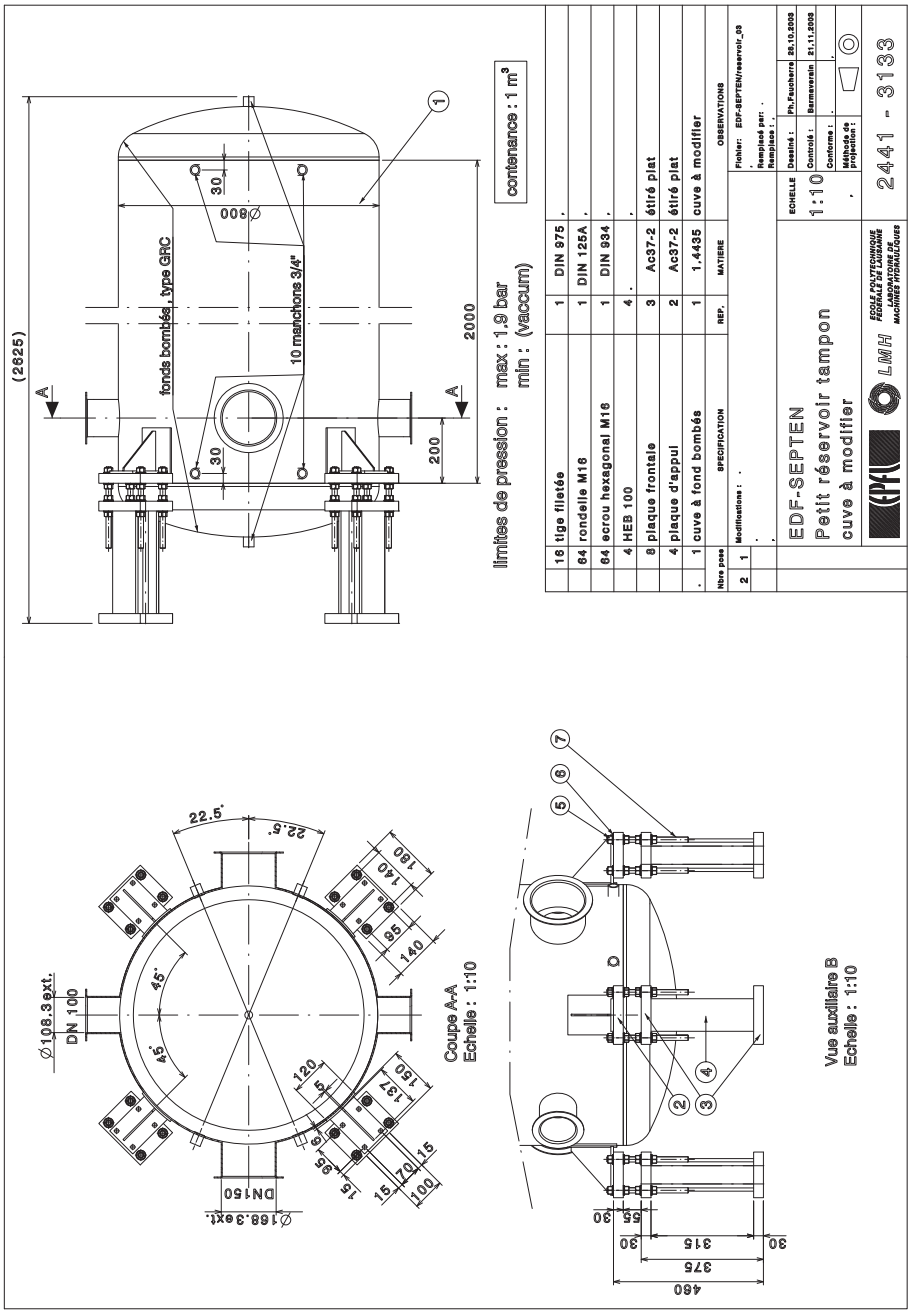

Figure B.4: Detail drawings of the air vessel (source: LMH archives).

B.4 Photos of the new supply conduit

(a) (b)

Figure B.5: Photos of the new PVC supply conduit of the experimental facility, (a) supply conduit supported against the Laboratory wall and the electromagnetic flowmeter, (b) downstream part of the supply conduit with the control valve and the elastic TUBOFLEX joint.

B.5 Photos of the shut-off valve

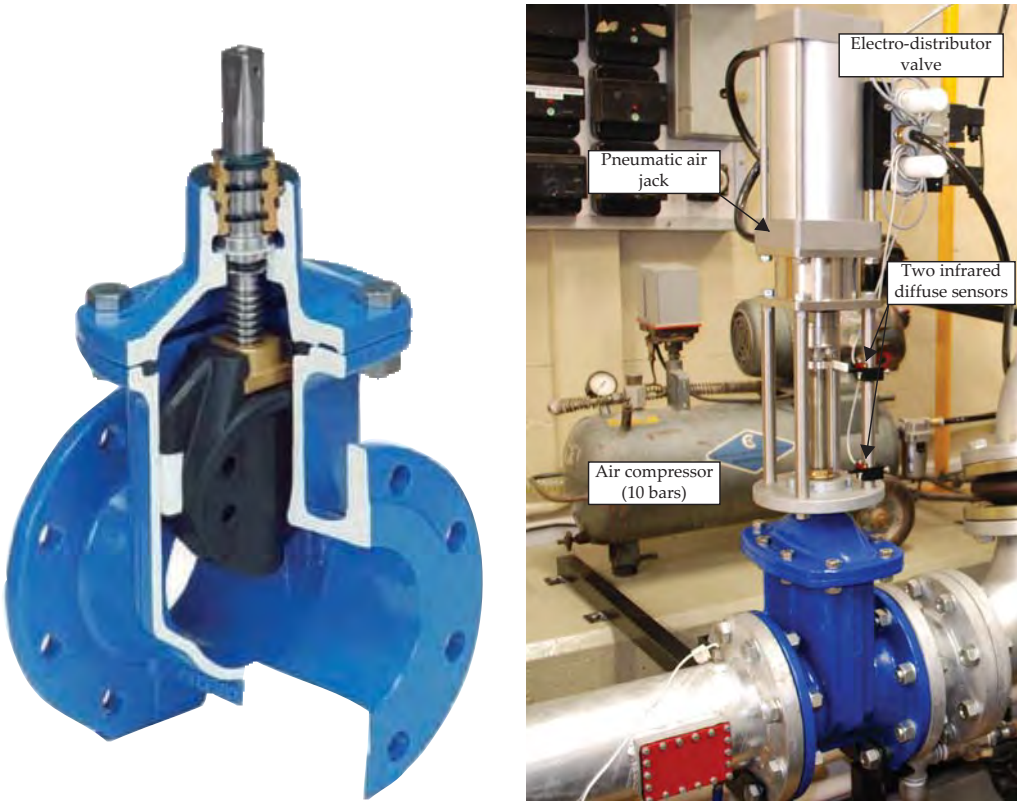

(a) (b)

Figure B.6: Photos of the shut-off valve of the experimental facility, (a) 3D section of the "vonRoll*hydrotec* 5000plus PN10 EN-GJS-500-7" slide gate valve (source: vonRoll catalogues), (b) the valve with its adapted upper part, the pneumatic air jack, and the air compressor.

B.6 Photos of the steel test pipe

(a) (b)

Figure B.7: Photos of the steel test pipe of the experimental facility, (a) a global view of the test pipe including the pipe supports, (b) downstream part with the two elbows, the elastic joint, the control "hawle" valve, and the shut-off "VonRoll" valve.

(a) (b)

Figure B.8: Photos of the aluminum and PVC pipe reaches, (a) three 1 m long and three 0.5 m long aluminum pipes, two 0.5 m long PVC reaches and one steel pipe of 0.5 m length, (b) from left to right, a PVC, an aluminum, and a steel pipe reach 0.5 m long and 150 mm of internal diameter.

Appendix C

Calibration of the pressure sensors

This appendix describes the procedure and presents the results of the calibration process of the eight "kulite" pressure sensors. The objective is to determine the coefficients of the linear transformation of the output voltage to pressure in bars.

The pressure sensors were screwed in the radial direction to a special thick wall steel cylinder (Fig. C.1a). This cylinder has an input and output holes along its axial direction. The former is used to inject pressurized air inside the cylinder while the latter is connected to the "Huber" pressure transducer of the laboratory (Fig. C.1b). The eight "kulite" sensors are excited by the "GWinstek, GPD-3303S" AC/DC power supply and the data output voltage are digitized by using a "NI-USB-6259 M series" acquisition card controlled by a LabView program code (LabVIEW, 2008).

The calibration procedure consisted on injecting air at a predefined pressure inside the cylinder. The air pressure has been manually controlled in order to reduce it from 16 bars (available in the laboratory) to five different pressure plateau between 0 and 7 bars. For each plateau and after 2 to 3 minutes of stabilization time, the pressure value was read in bars on the "Huber" sensor and the output voltages of the eight pressure sensors were acquired during 20 s at a sample frequency of 15 kHz. The software uses the data of the five pressure plateau to generate the coefficients of the linear regression between the "Huber" pressures (in bar) and the mean voltage values of the "kulite" sensors (in Volt). This procedure has been repeated several times for both upward and downward pressure variations. The mean coefficients values of the linear regression $p\,(\mathrm{bar}) = b_i\,p(\mathrm{Volt}) + c_i$ for the eight pressure sensors ($i = 1 \ldots 8$) are given in Table C.1.

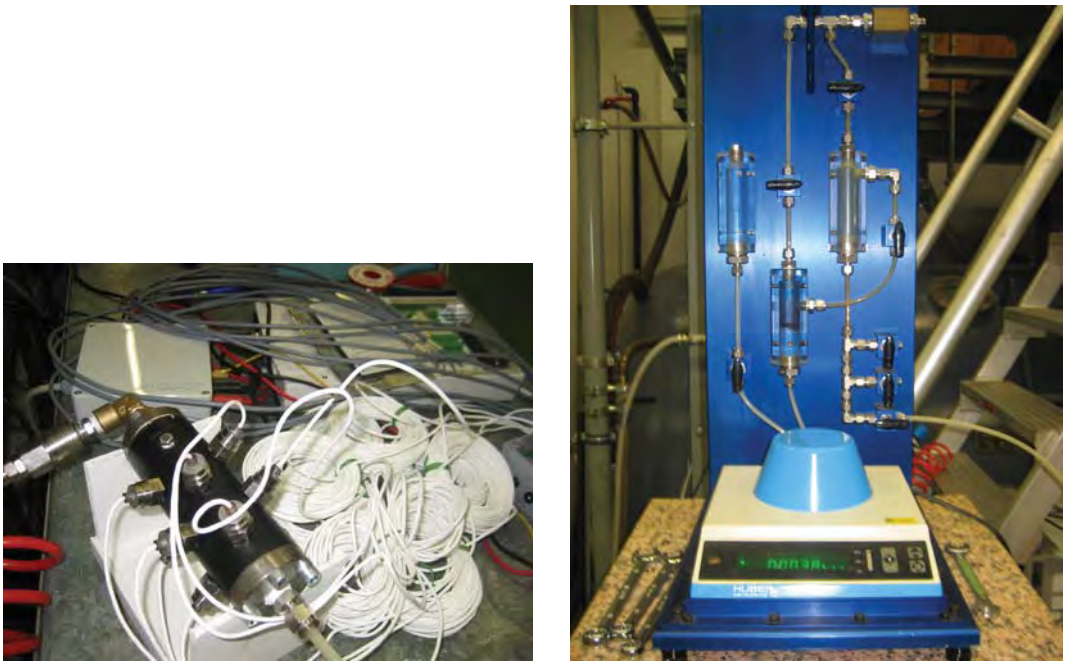

(a) (b)

Figure C.1: Photos of the two main components of the calibration set-up of the "kulite" pressure sensors, (a) thick steel cylinder which supports the pressure sensors, (b) "Huber" pressure transducer of high precision ($\pm 0.1\,\%$).

Table C.1: Mean values of the linear regression transformation for the eight "kulite" pressure sensors obtained from the calibration process.

$p\,(\text{in bar}) = b_i\,p(\text{in Volt}) + c_i$		
Sensor number, i	b_i	c_i
1	58.1399128202451	-1.12092344414648
2	58.3621871978047	-0.92044730322187
3	58.2731379124956	-0.957380019638092
4	58.0359574565066	-0.940375791340463
5	58.4362182461565	-0.919601550975595
6	58.0894023042337	-0.925478768301893
7	58.3805484068414	-0.918089034500612
8	58.5521022645017	-0.917009490434598

Appendix D

Transfer function H of the geophone sensors

The purpose of this appendix is to present in detail, the mathematical development to determine the transfer function of the geophone sensors.

D.1 Definition

The transfer function H is defined as the relationship between the input and output of a system. It is given by

$$H = \frac{B}{A} \tag{D.1}$$

where B is the output and A is the input of the system. In our case, the geophone is the system, the radial displacement of the pipe wall is the input and the measured output voltage is the output.

D.2 Mathematical development

The geophone can be modeled by a mass M_G attached, in the vertical direction, to a spring of constant K_G and to a damper of coefficient C_G (Fig. D.1). The spring force of the vibration system can be expressed as

$$F_G = K_G \left(X_G - u_r^s\right) \tag{D.2}$$

and the equation of motion of the mass M_G can be written as follows:

$$M_G \ddot{X}_G + C_G \left(\dot{X}_G - \dot{u}_r^s\right) + K_G \left(X_G - u_r^s\right) = 0 \tag{D.3}$$

in which the dot and double dots represent single and double time differentiation, respectively.

Eq. (D.3) can be transformed into a linear differential equation with constant coefficients by dividing it by M_G and by defining the following parameter

$$z_G = X_G - u_r^s \quad ; \omega_0 = \sqrt{\frac{K_G}{M_G}} \quad ; \zeta_G = \frac{C_G}{2\sqrt{K_G\, M_G}} \tag{D.4}$$

where z_G is the displacement of the mass M_G relative to the geophone case, ω_0 is the natural angular frequency ($= 2\,\pi\, f_0$) and ζ_G is the damping ratio of the geophone. The linear differential equation is then written as follows

$$\ddot{z}_G + 2\,\zeta_G\,\omega_0 \dot{z}_G + \omega_0^2\, z_G = -\ddot{u}_r^s \tag{D.5}$$

Since an arbitrary signal can be described as a superposition of harmonics (Fourier series), the simplest way to solve Eq. (D.5) is to assume an input of a harmonic $u_r^s(t)$ motion and solve for the solution in the frequency domain. According to Eq. (3.17), for each harmonic $Z_G(\omega)\,\mathrm{e}^{\mathrm{i}\,\omega\,t}$ or $U_r^s(\omega)\,\mathrm{e}^{\mathrm{i}\,\omega\,t}$, we can write (the same for $U_r^s(\omega)$):

$$\frac{\mathrm{d}}{\mathrm{d}t}\left(Z_G(\omega)\,\mathrm{e}^{\mathrm{i}\,\omega\,t}\right) = \mathrm{i}\,\omega\, Z_G(\omega)\,\mathrm{e}^{\mathrm{i}\,\omega\,t} \quad \text{and} \quad \frac{\mathrm{d}^2}{\mathrm{d}t^2}\left(Z_G(\omega)\,\mathrm{e}^{\mathrm{i}\,\omega\,t}\right) = -\omega^2\, Z_G(\omega) \tag{D.6}$$

By inserting Eqs. (D.6) and their similar for $U_r^s(\omega)$ in Eq. (D.5) and by dividing it with the common non zero factor $\mathrm{e}^{\mathrm{i}\,\omega\,t}$, we obtain the following equation

$$-\omega^2\, Z_G(\omega) + 2\,\mathrm{i}\,\zeta_G\,\omega_0\,\omega\, Z_G(\omega) + \omega_0^2\, Z_G(\omega) = \omega^2\, U_r^s(\omega) \tag{D.7}$$

from which it is easy to define the relationship between the case displacement and the relative movement of the coil. This relationship is as follows

$$H^{'}(\omega) = \frac{Z_G(\omega)}{U_r^s(\omega)} = \frac{\omega^2}{\omega_0^2 - \omega^2 + 2\,\mathrm{i}\,\zeta_G\,\omega_0\,\omega} \tag{D.8}$$

For velocity transducers like geophones, the output voltage signal $v(t)$ is proportional to the relative mass velocity $\dot{z}_G$ and to the sensitivity G ($v(t) = -G\,\dot{z}_G$). Therefore, the transfer function, H, is the ratio between the harmonic of output voltage $V_G(\omega)$ ($= -G\,\mathrm{i}\,\omega\, Z_G(\omega)$) and the displacement $U_r^s(\omega)$. Thus, H can be defined as

$$H(\omega) = \frac{V_G(\omega)}{U_r^s(\omega)} = \frac{-\mathrm{i}\,\omega^3\, G}{\omega_0^2 - \omega^2 + 2\,\mathrm{i}\,\zeta_G\,\omega_0\,\omega} \tag{D.9}$$

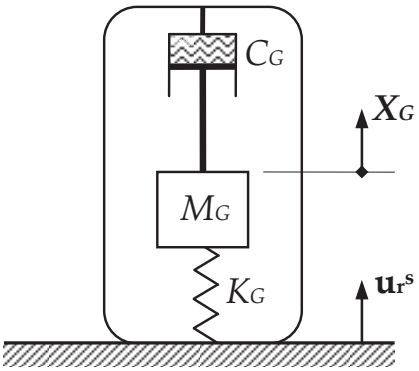

Figure D.1: Linear vibration model which simulate the relative displacement of the coil and the magnet of a geophone sensor.

Appendix E

Results of wavelet decomposition for the experimental pressure and geophone records

This appendix presents the wavelet decomposition graphs of the Approximations A_i and Details D_i of pressures (P1 and P2) and vibrations (G1 and G2) shown in Figs. 6.2a and 6.2b. These records have been acquired at the both ends of the experimental test pipe. The wavelet decomposition was done by using MATLAB (Wavelet 1-D) software package (Mathworks, 2008). In these graphs, the vertical axis represents pressures in bars or geophone outputs in Volts while the horizontal axis gives the number of the sampled points.

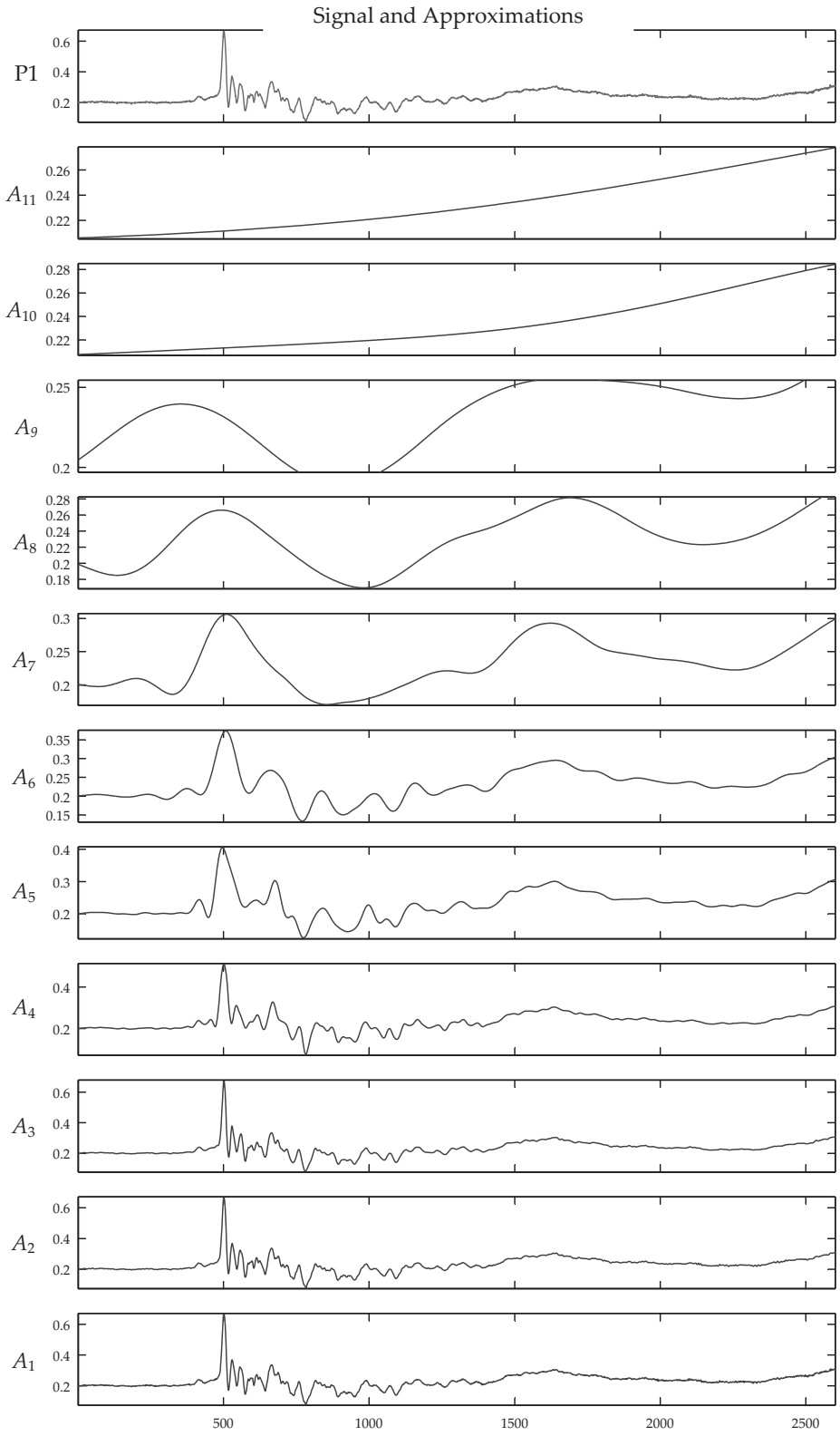

Figure E.1: Approximations of the wavelet decomposition results for pressure record P1 inside window W1 of Fig. 6.2a.

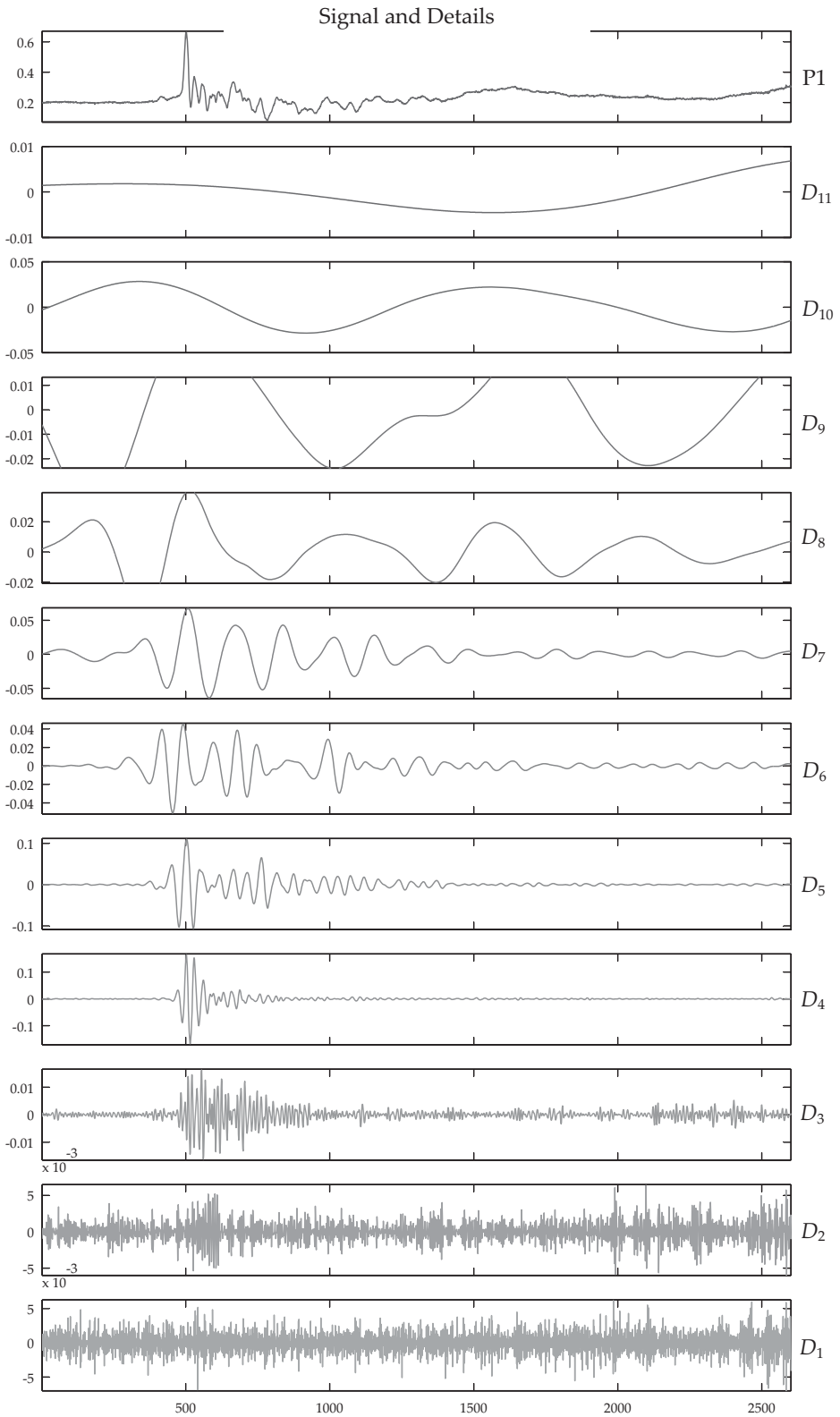

Figure E.2: Details of the wavelet decomposition results for pressure record P1 inside window W1 of Fig. 6.2a.

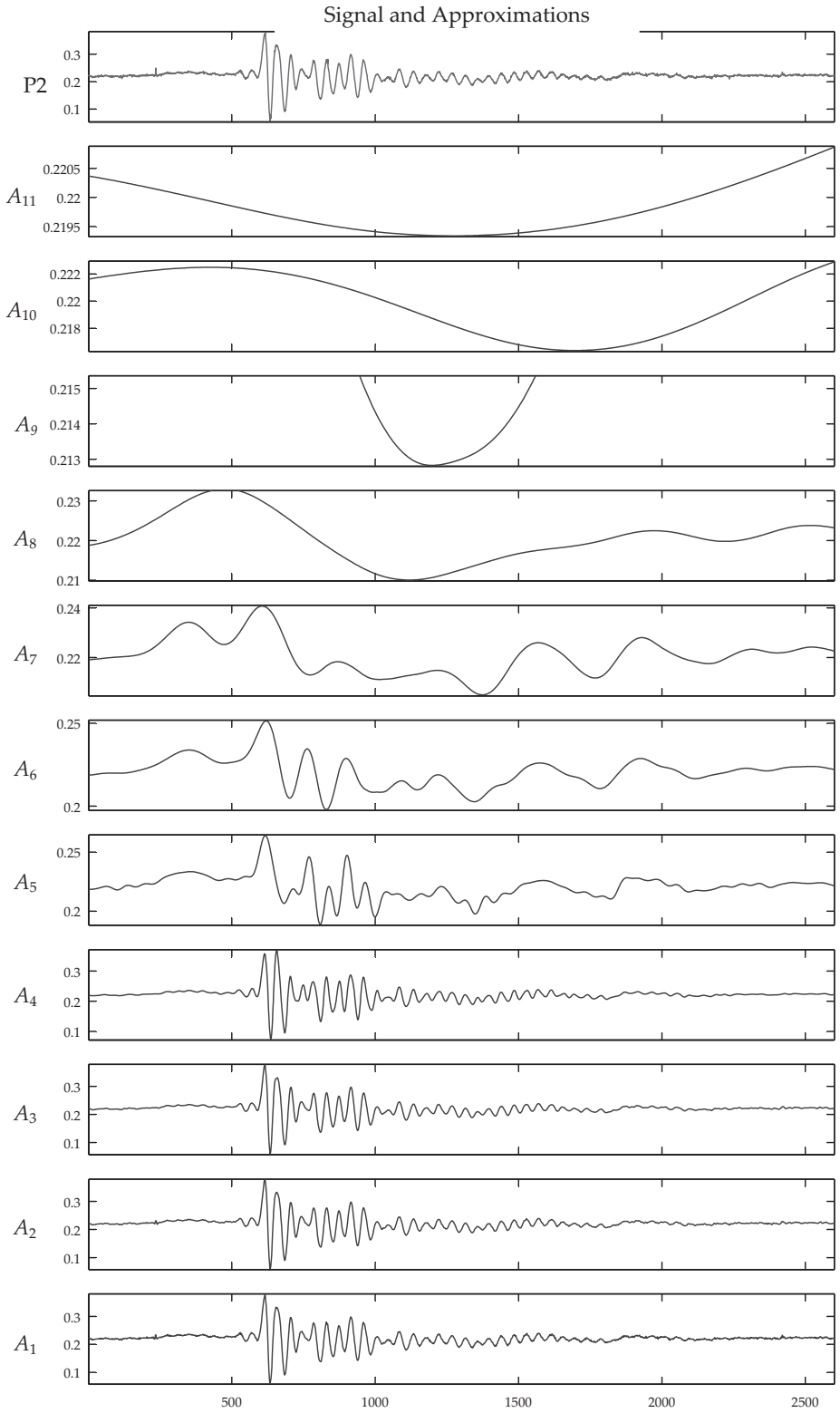

Figure E.3: Approximations of the wavelet decomposition results for pressure record P2 inside window W1 of Fig. 6.2a.

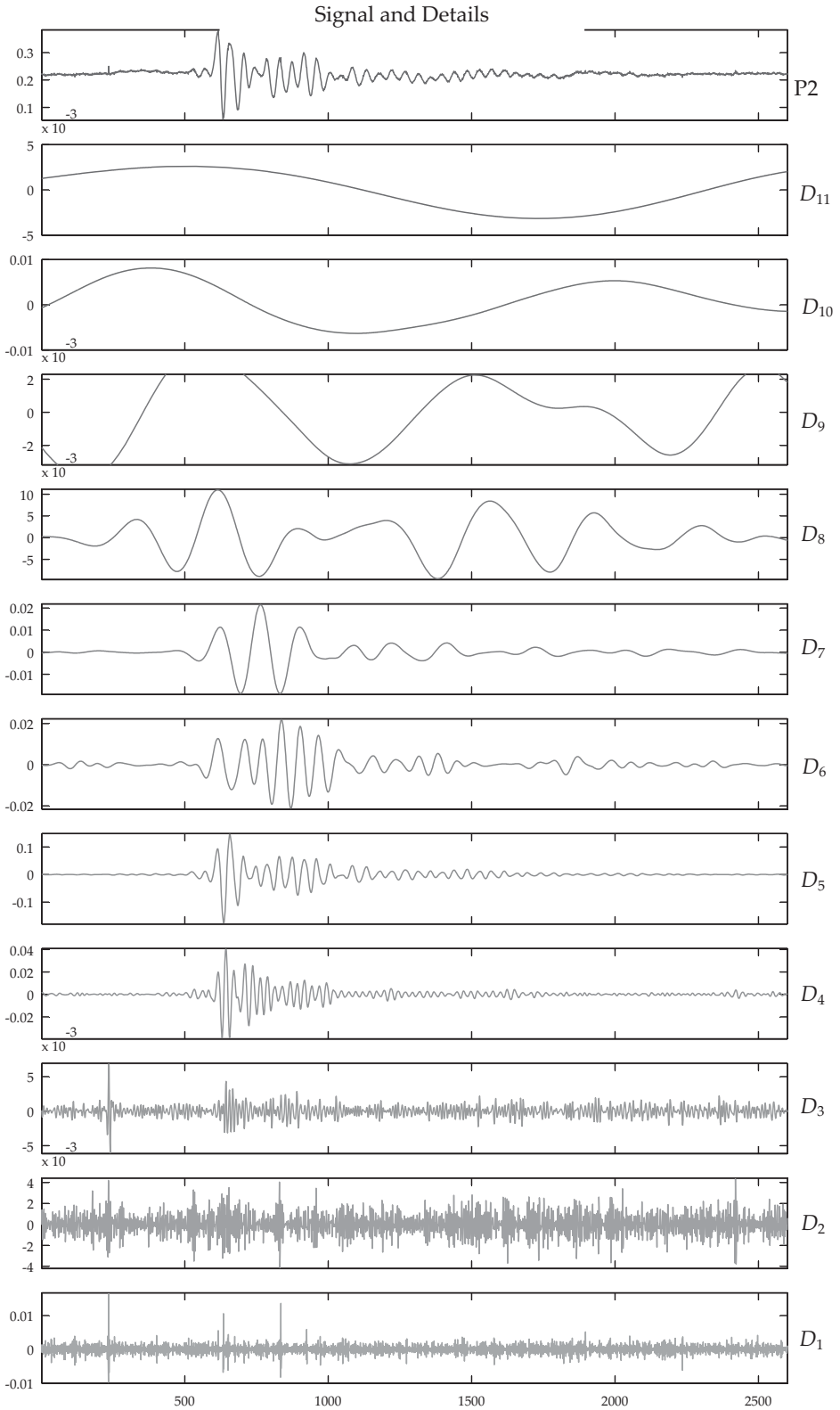

Figure E.4: Details of the wavelet decomposition results for pressure record P2 inside window W1 of Fig. 6.2a.

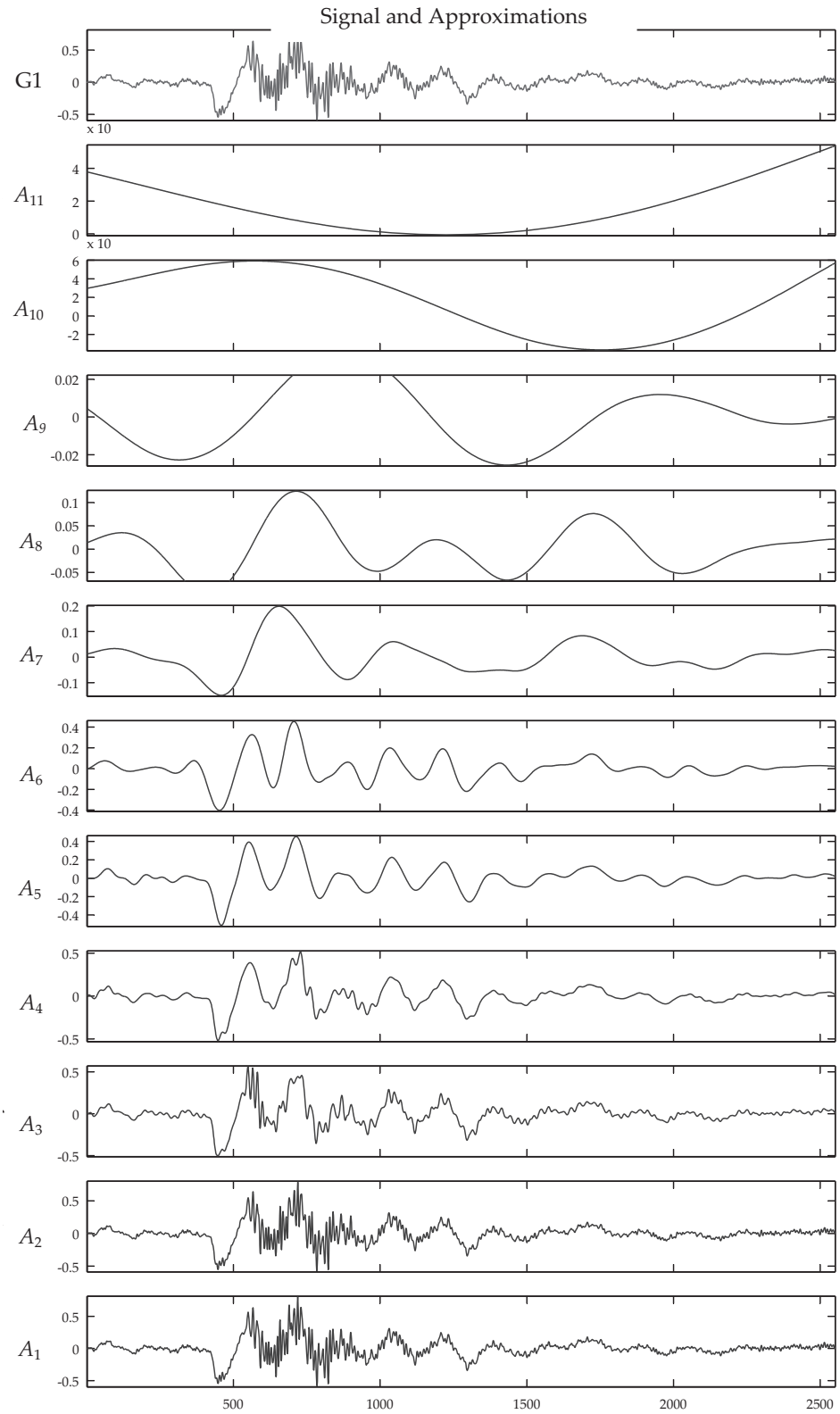

Figure E.5: Approximations of the wavelet decomposition results for geophone output G1 inside window W1 of Fig. 6.2b.

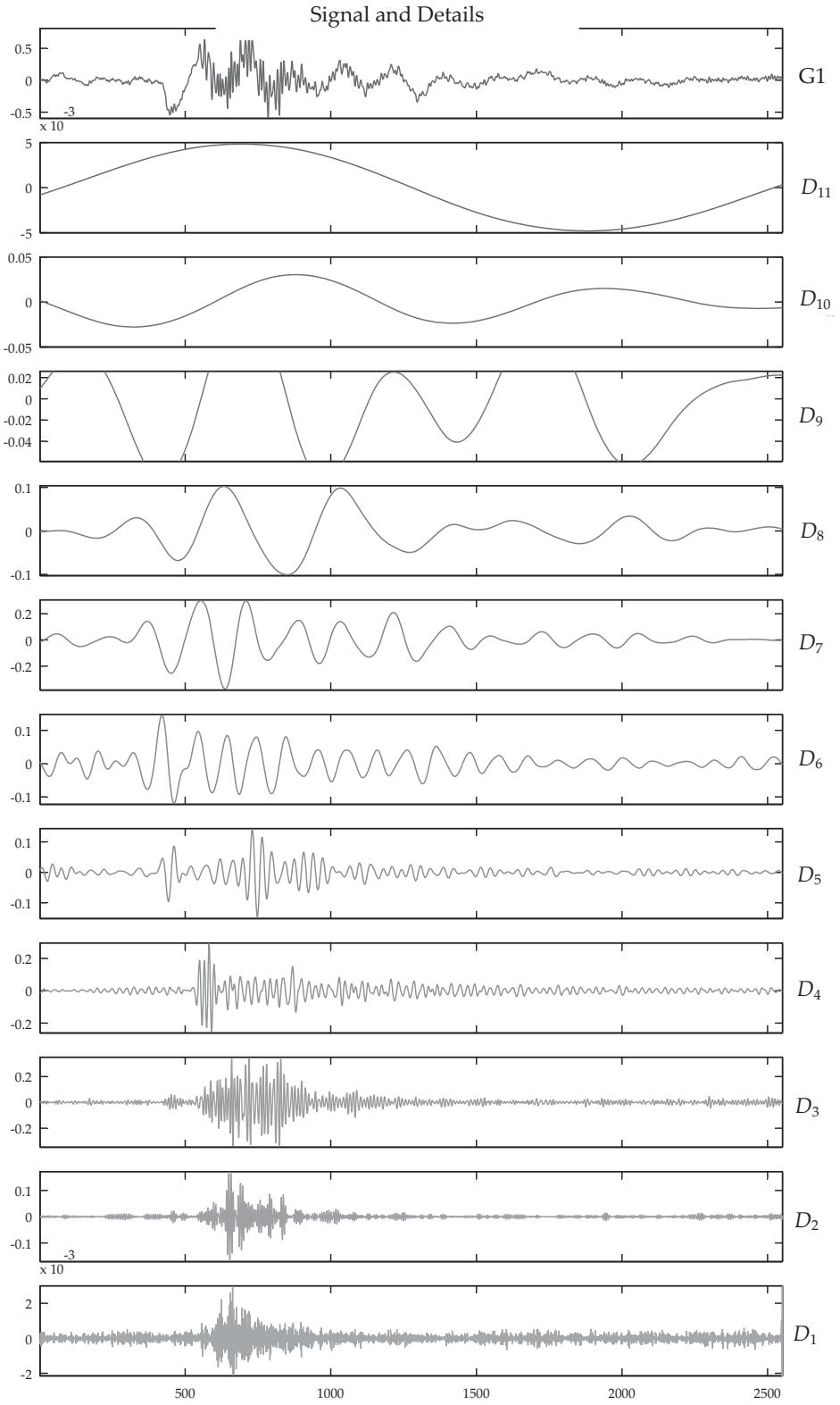

Figure E.6: Details of the wavelet decomposition results for geophone output G1 inside window W1 of Fig. 6.2b.

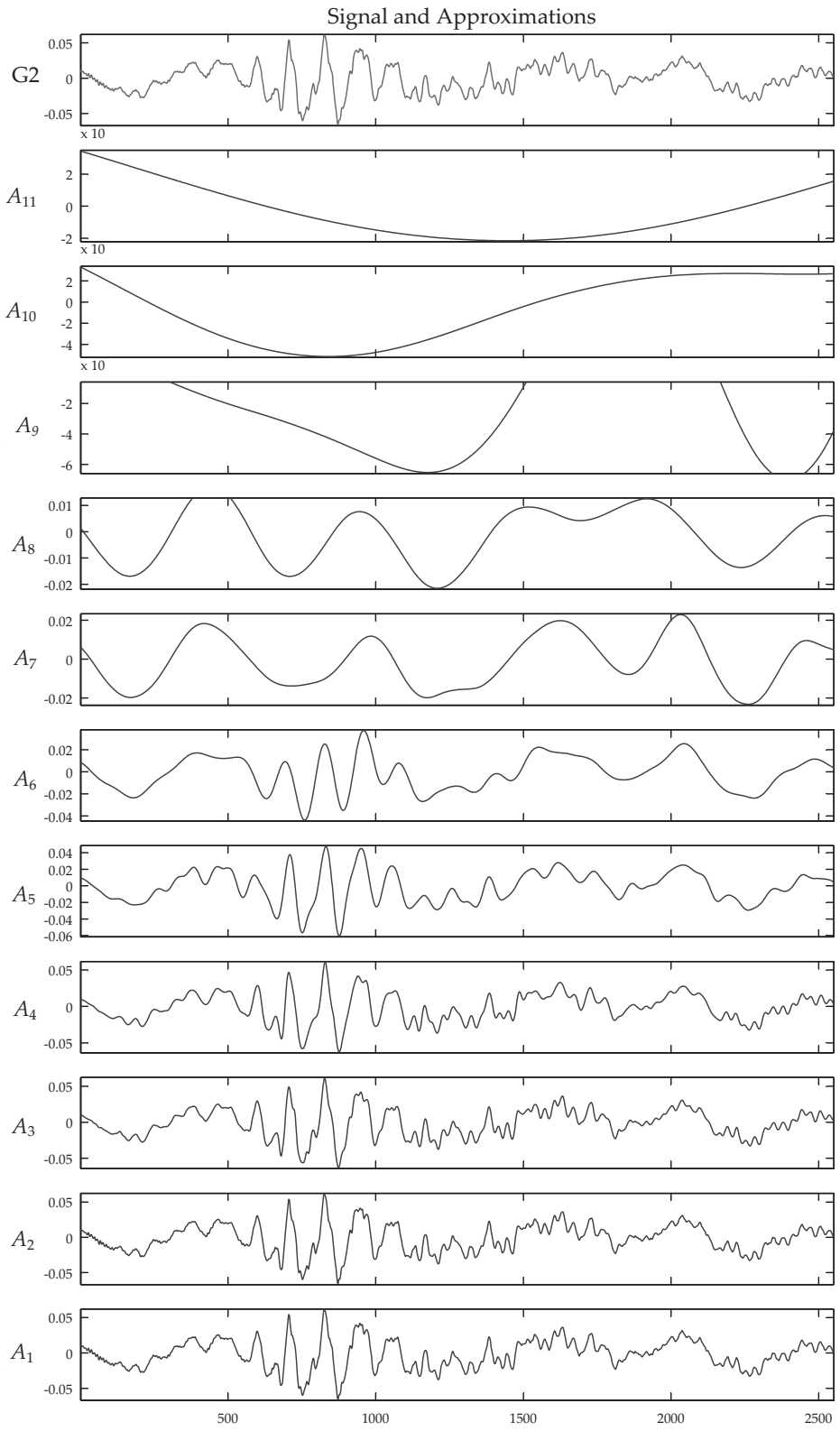

Figure E.7: Approximations of the wavelet decomposition results for geophone output G2 inside window W1 of Fig. 6.2b.

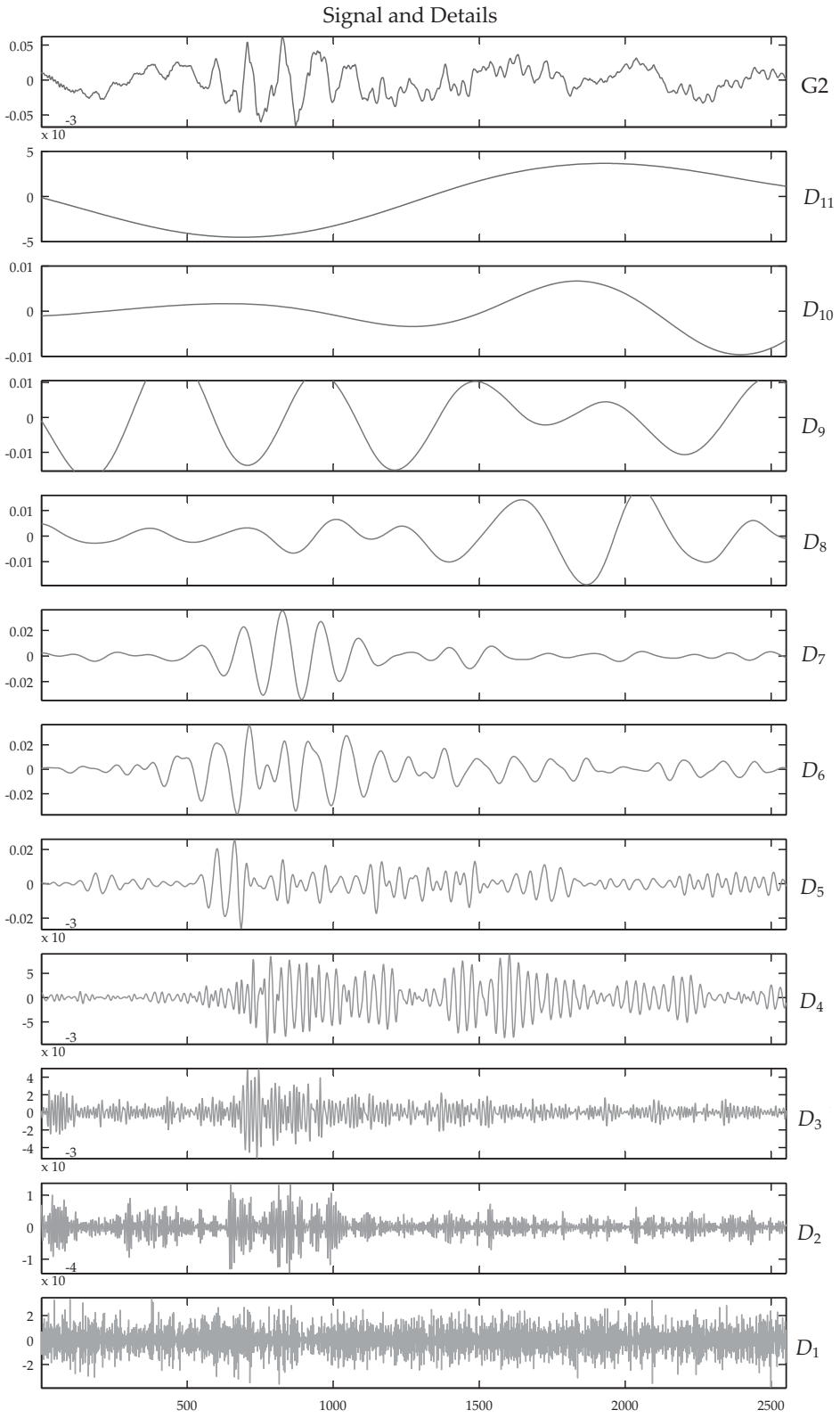

Figure E.8: Details of the wavelet decomposition results for geophone output G2 inside window W1 of Fig. 6.2b.

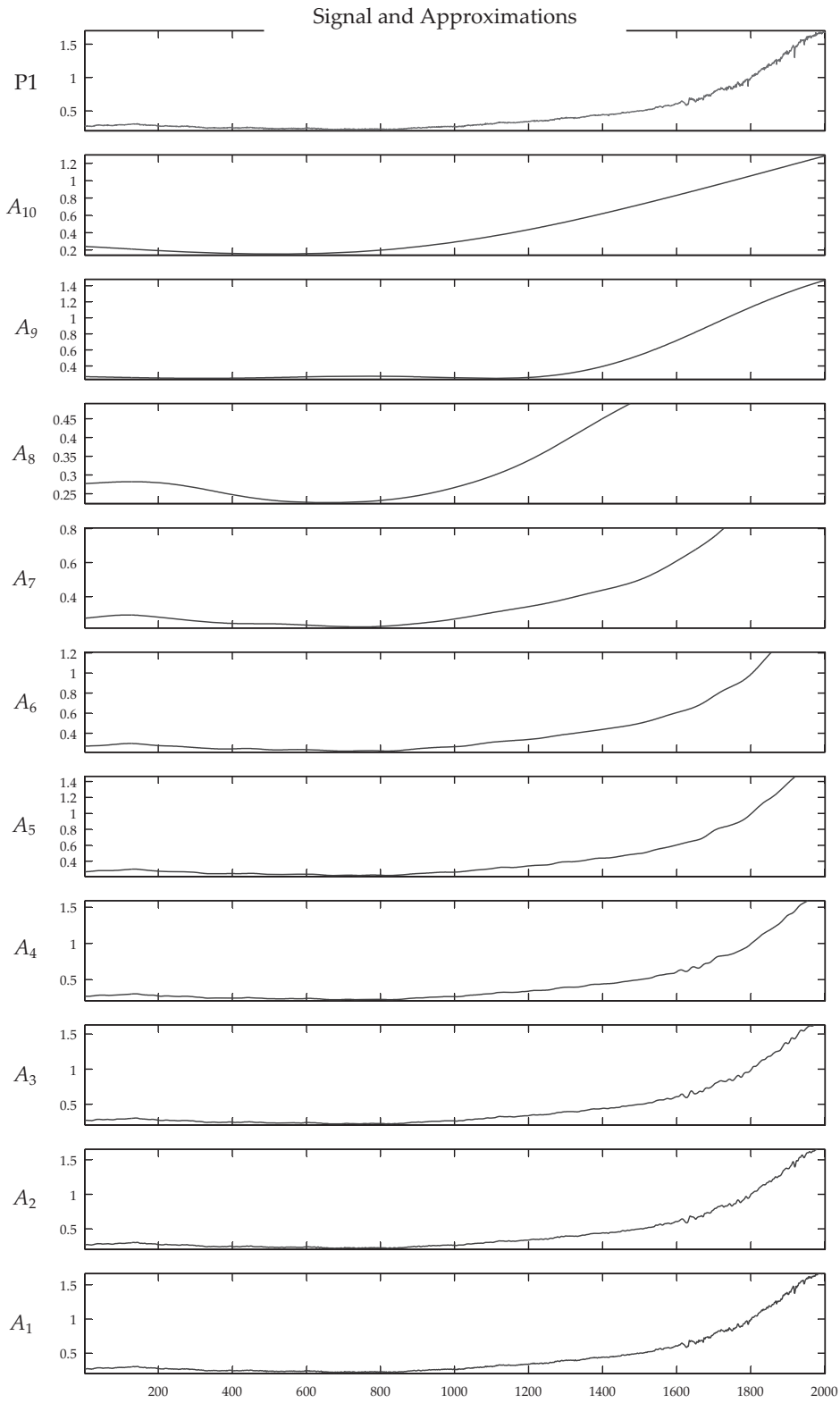

Figure E.9: Approximations of the wavelet decomposition results for pressure record P1 inside window W2 of Fig. 6.2a.

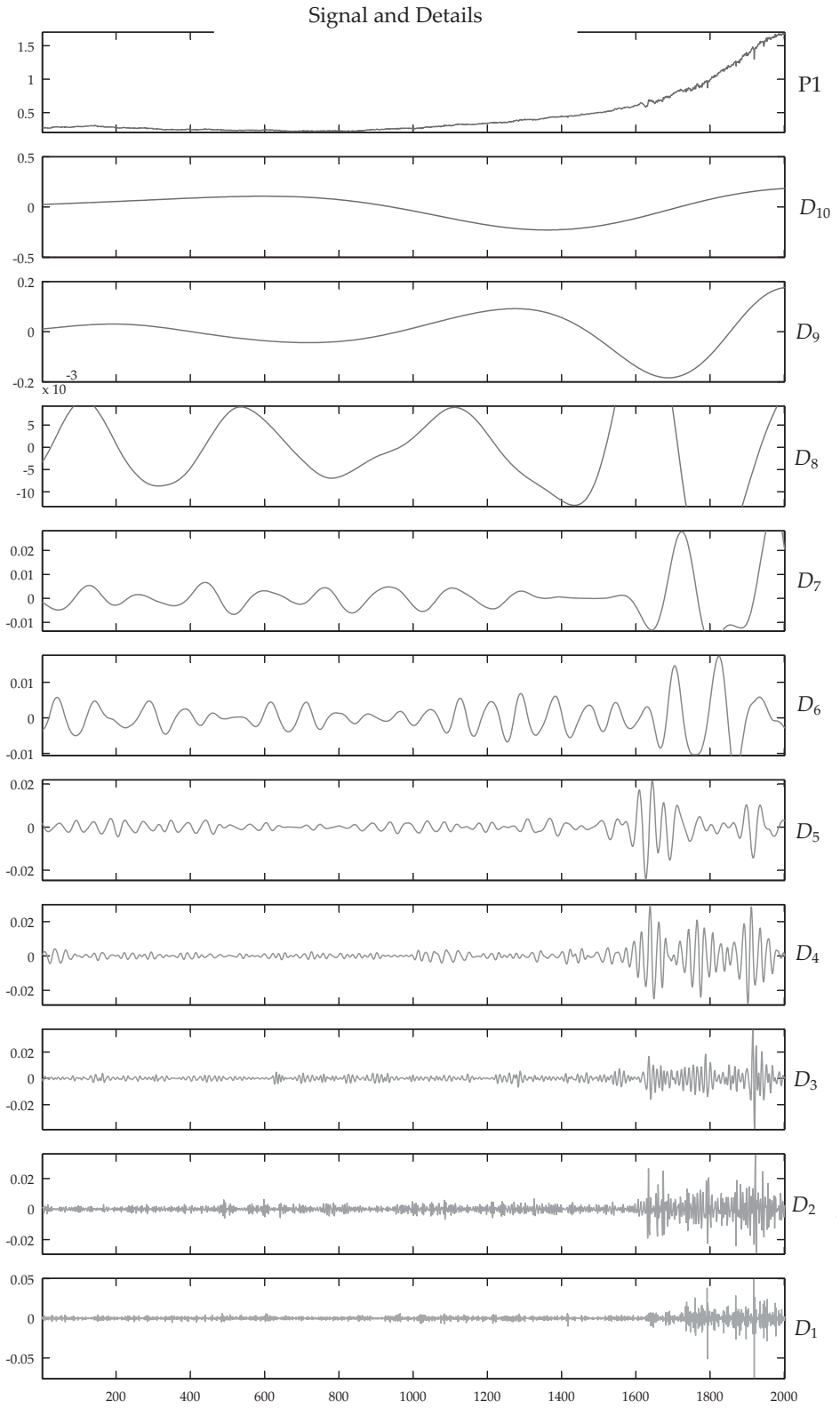

Figure E.10: Details of the wavelet decomposition results for pressure record P1 inside window W2 of Fig. 6.2a.

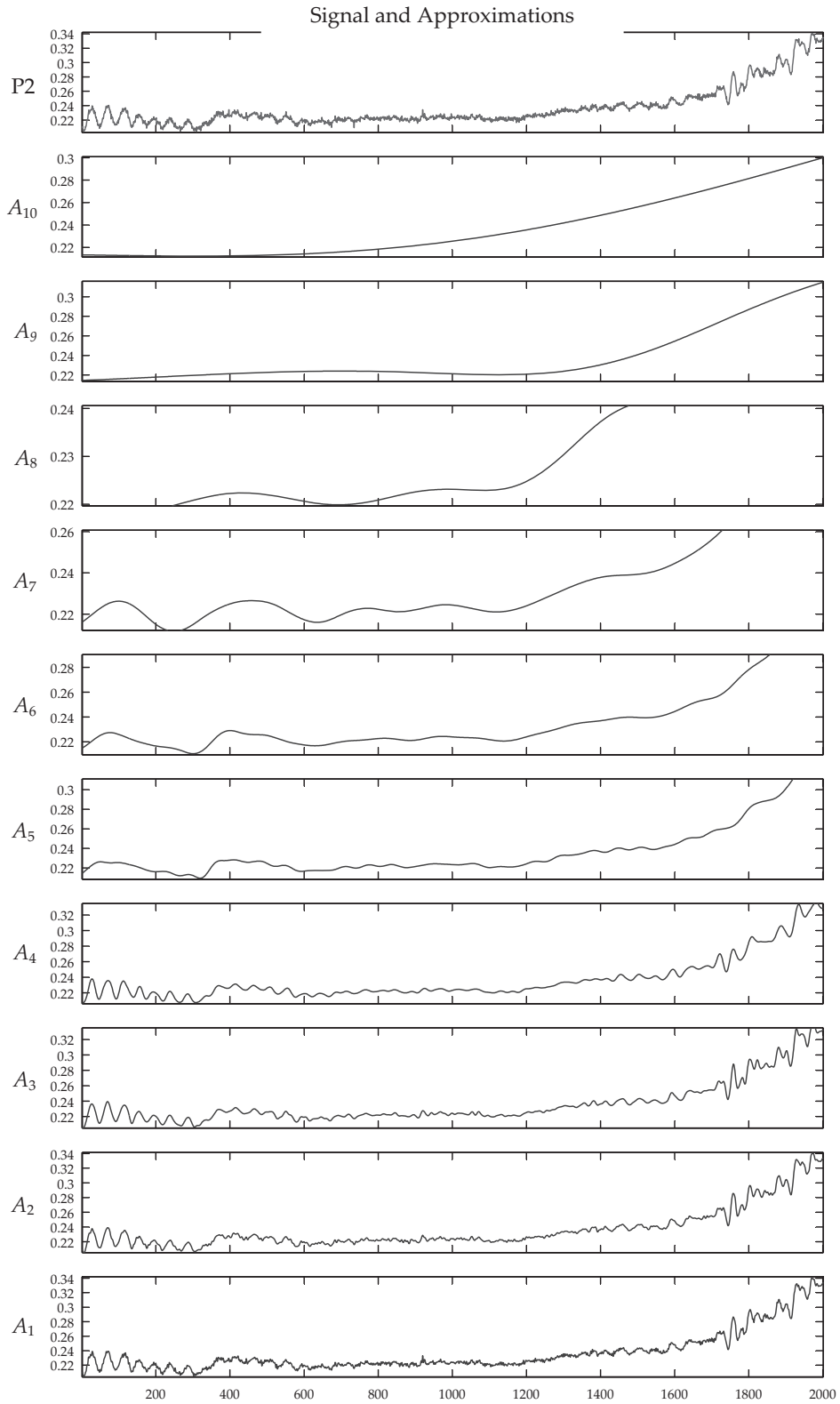

Figure E.11: Approximations of the wavelet decomposition results for pressure record P2 inside window W2 of Fig. 6.2a.

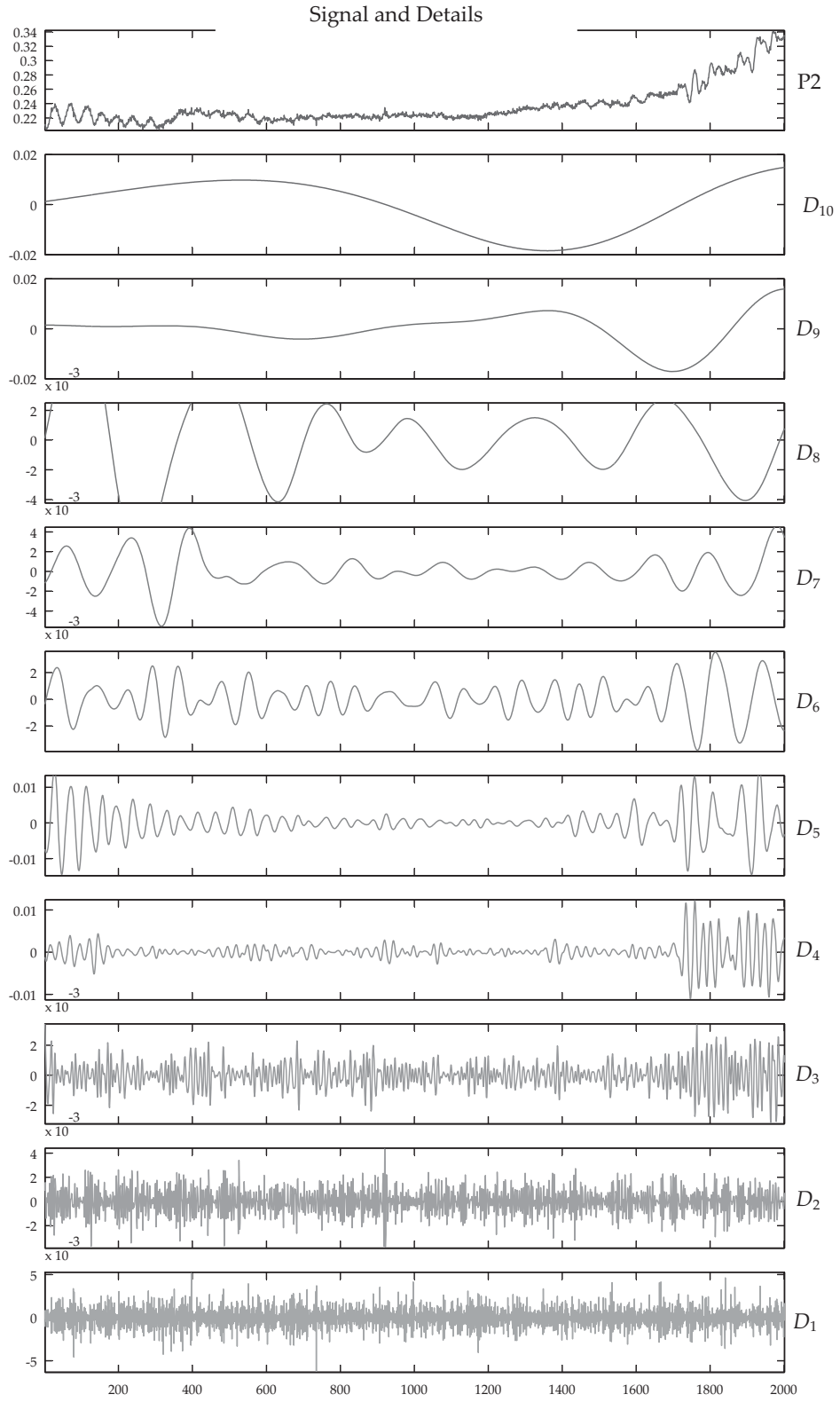

Figure E.12: Details of the wavelet decomposition results for pressure record P2 inside window W2 of Fig. 6.2a.

Appendix F

Description of the Grimsel II prototype site

F.1 Photos of the powerhouse, the control valves, and the by-passe conduits at the two measurement sections S1 and S2 of the pressure shaft

(a) (b)

Figure F.1: Photos of the Grimsel II plant, (a) two of the four pump-turbine units (units 1 and 2), and (b) spherical and butterfly valves between the water distributors and the pump-turbine machines (photos: F. Hachem).

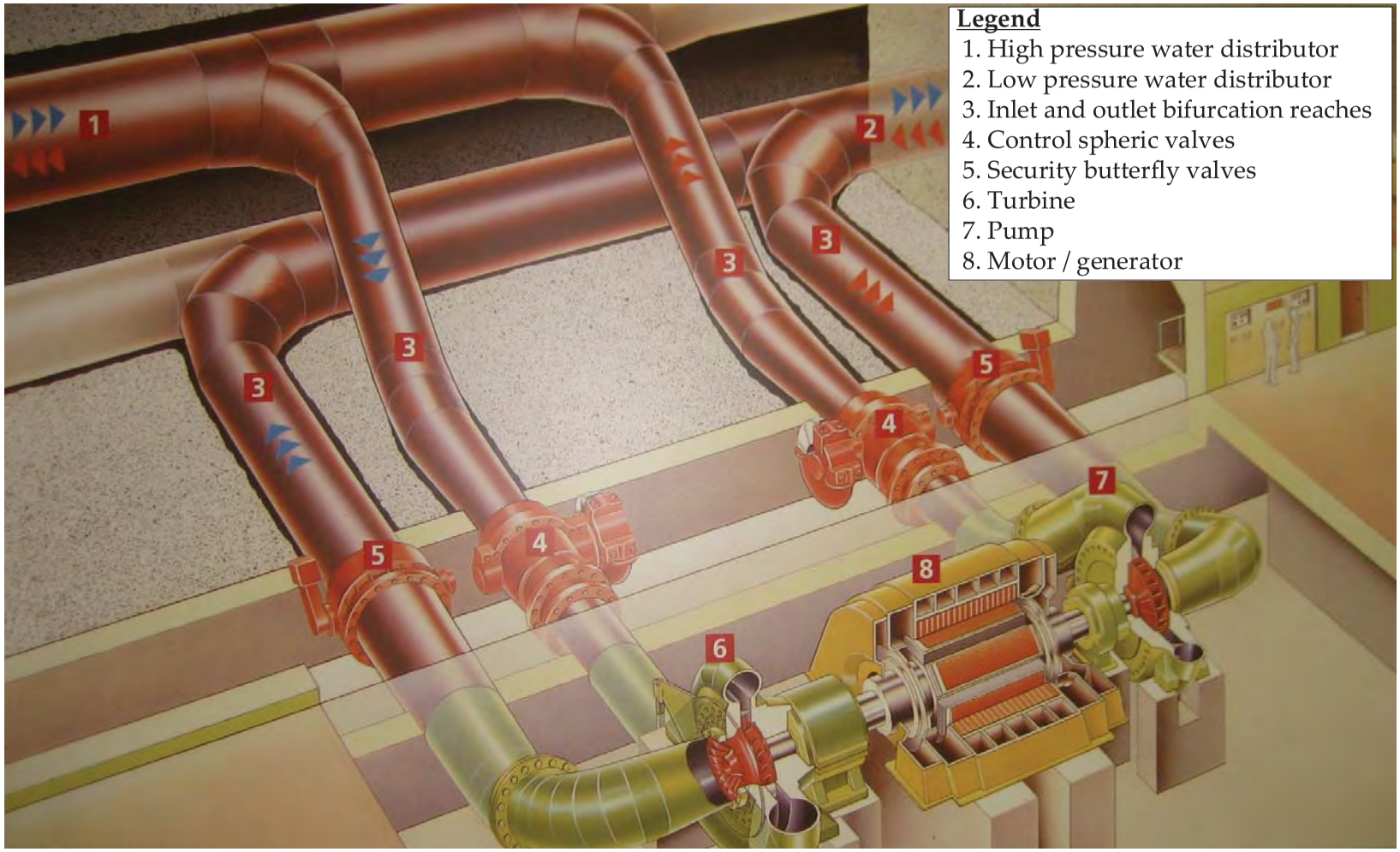

Figure F.2: 3D schematic view of one Francis pump-turbine unit of the Grimsel II plant with its control and security valves and the high and low pressure water distributors (source of the drawing: KWO archives).

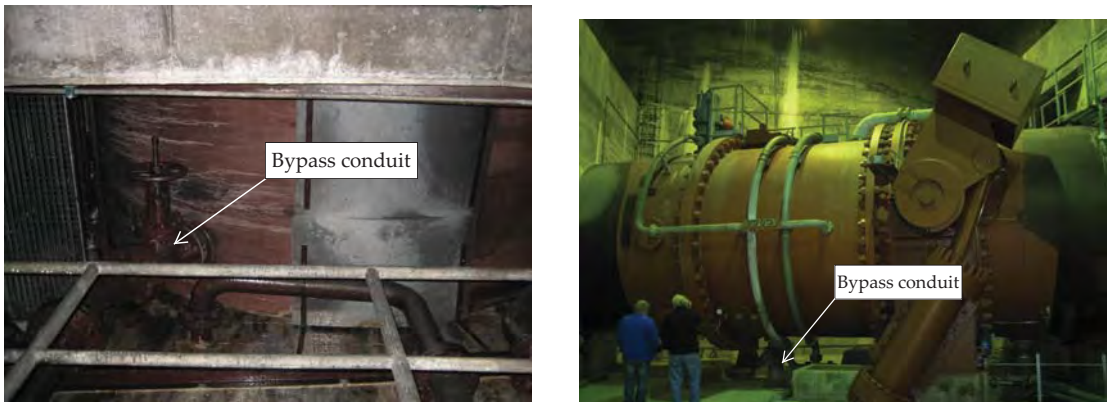

(a) (b)

Figure F.3: Photos of the two measurement sections of the Grimsel II plant, (a) accessible reach of the steel-liner at the entrance of the powerhouse (measurement station S1), and (b) security valve at the upstream side of the shaft between the surge tank and the inclined surge shaft (measurement station S2) (photos: F. Hachem).

F.2 Parameters values used to estimate the theoretical water-hammer wave speed inside the Grimsel II pressure shaft

Table F.1: The values of the parameters used to calculate the theoretical water-hammer wave speed inside the pressure shaft of the Grimsel II plant.

Parameter	Value		
	Min	Mean	Max
K_w (GPa)		2.2	
ρ_w (kg/m^3)		1 000	
E_s (GPa)		210	
E_c (GPa)		21	
E_{rm} (GPa)*	35.0	40.0	45.0
$E_{crm} = 0.5\,E_{rm}$ (GPa)	17.5	20.0	22.5
ν_s (-)		0.30	
ν_c (-)		0.20	
ν_r (-)		0.25	
r_i (m)		1.9	
e_{mean} (mm)		19.25	
r_a (m)		2.15	
$r_f = 1.25\,r_a$ (m)		2.6875	
a (m/s)	1 349.6	1 361.5	1 371.3

* Values extracted from (Pahl et al., 1989)

F.3 Plan views of the powerhouse and the connection of the headrace tunnel with the steel-lined shaft

F.4 Detail drawing of the existing flow discharge measurement system

F.5 The as-built geological longitudinal profile of the high pressure steel-lined shaft of the Grimsel II plant

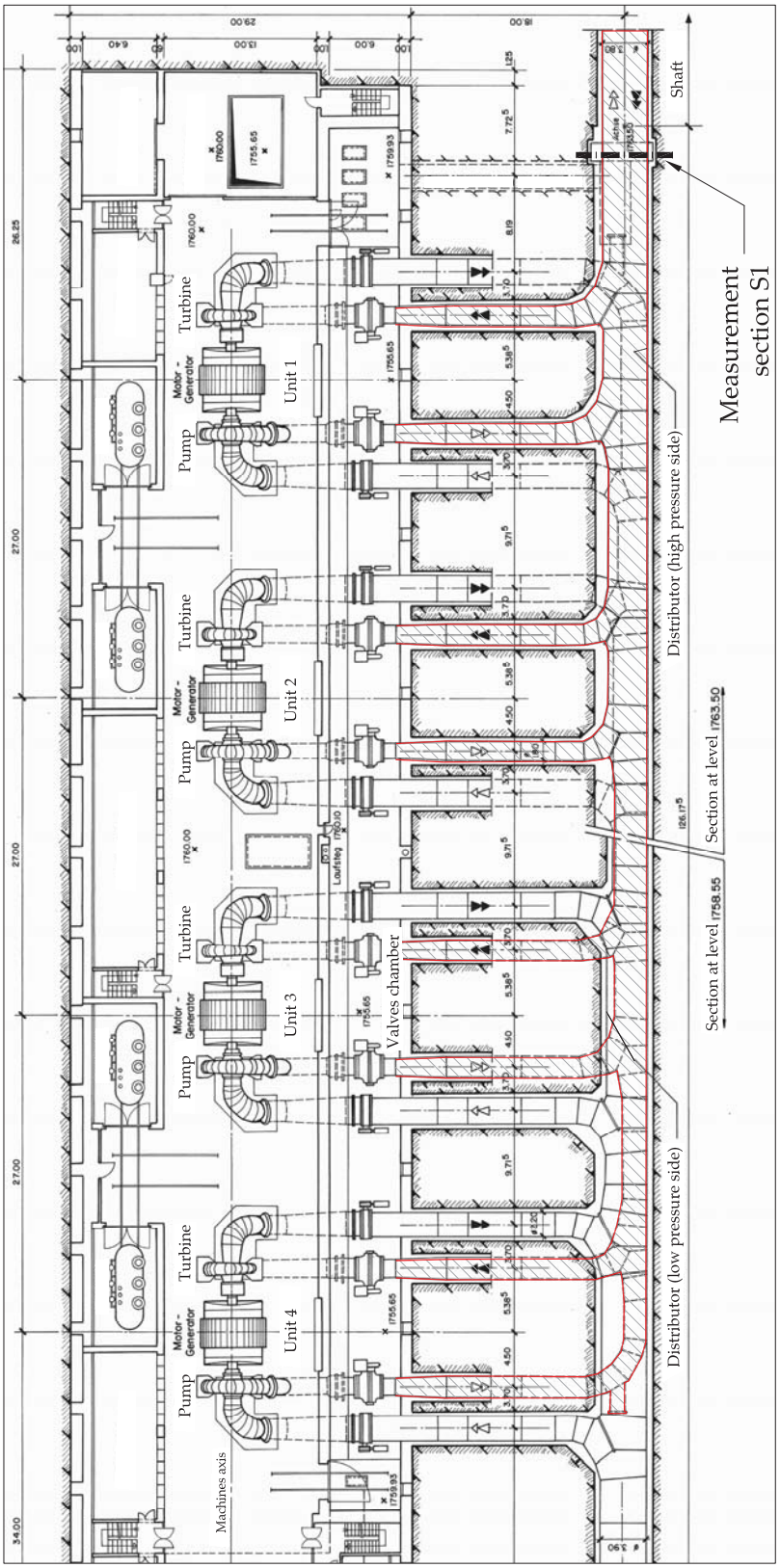

Figure F.4: Plan view of the Grimsel II powerhouse. The measurement section S1 is also shown (source of the drawing: KWO archives).

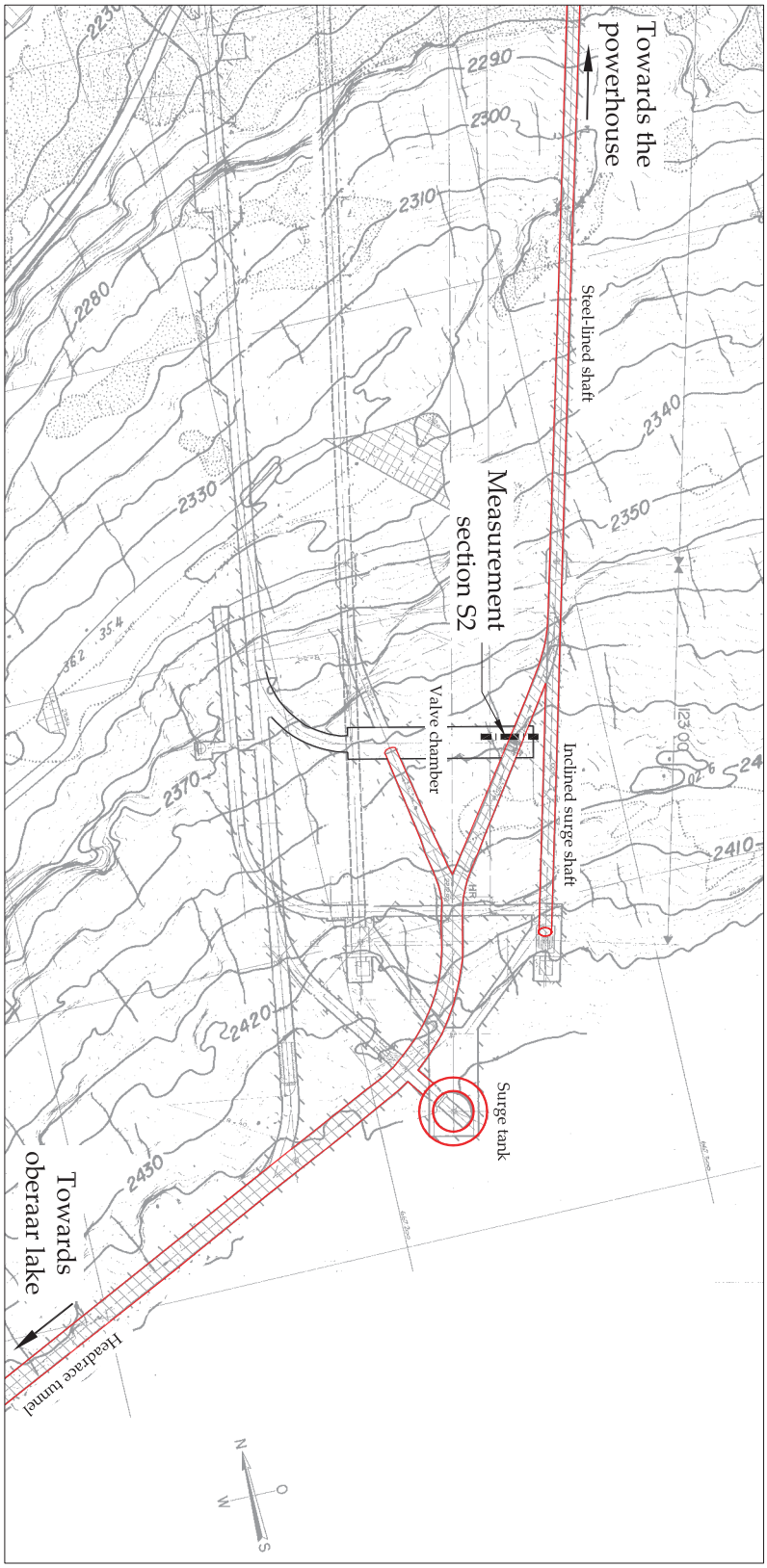

Figure F.5: Layout of the connection between the headrace tunnel and the steel-lined shaft of the Grimsel II plant. The vertical surge tank, the inclined surge shaft and the measurement section S2 are also shown (source of the drawing: KWO archives).

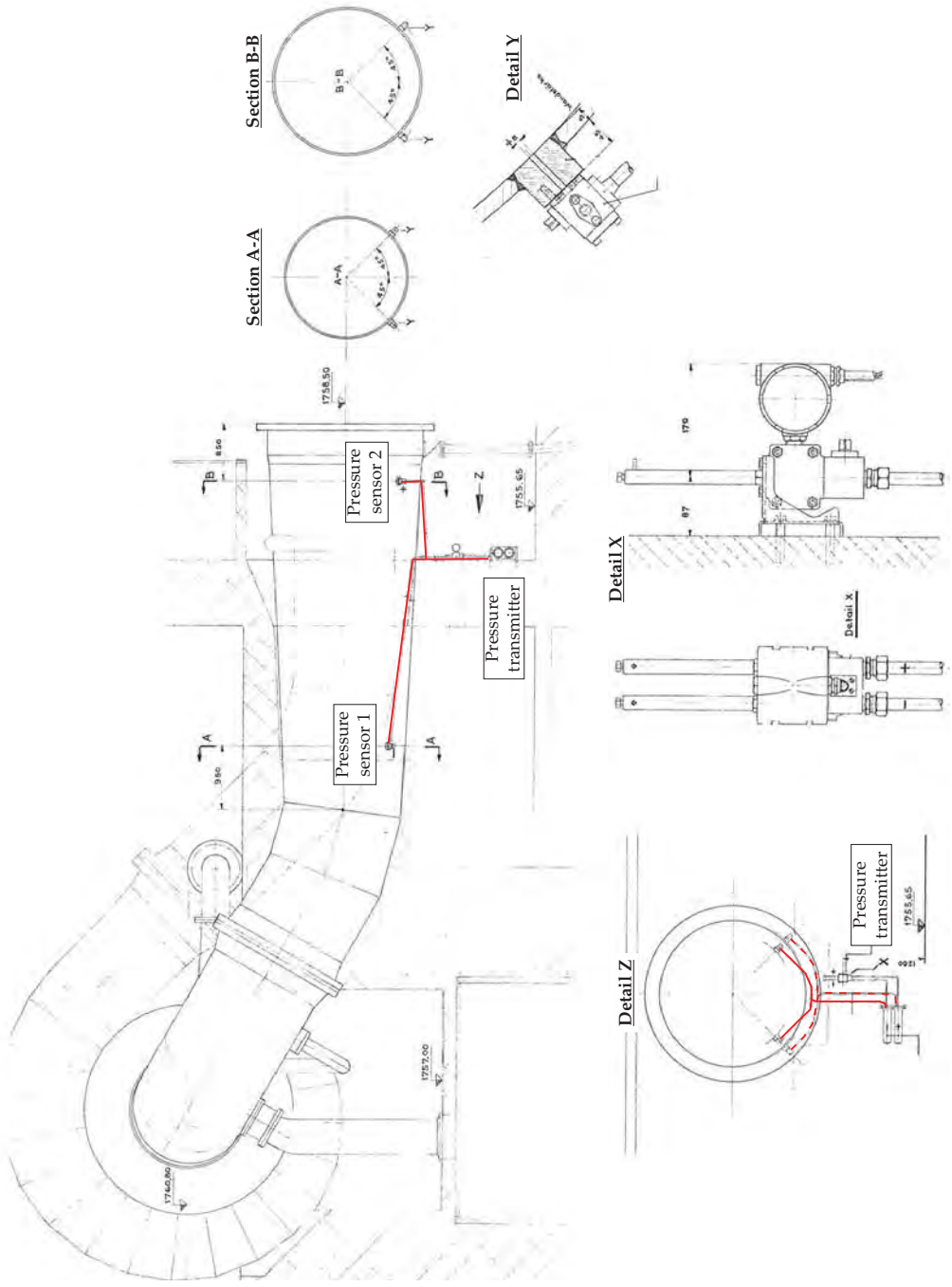

Figure F.6: Detail drawing of the existing Venturi measurement system for each pump and turbine in Grimsel II plant (source of the drawing: KWO archives).

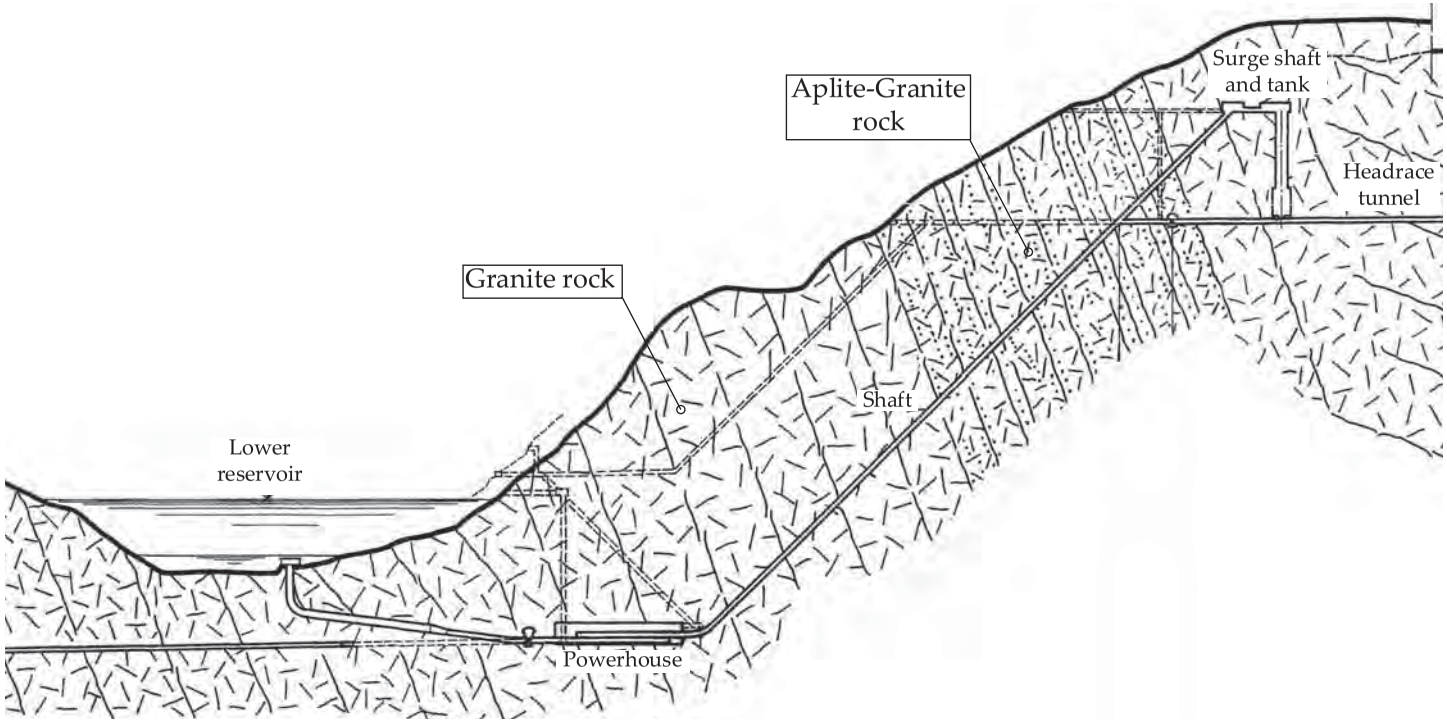

Figure F.7: The geological longitudinal profile of the high pressure steel-lined shaft of the Grimsel II pumped-storage plant (source of the drawing: KWO archives).

F.6 An example of the wavelet decomposition results for the in-situ measurement pressures at sections S1 and S2 of the pressure shaft of the Grimsel II plant

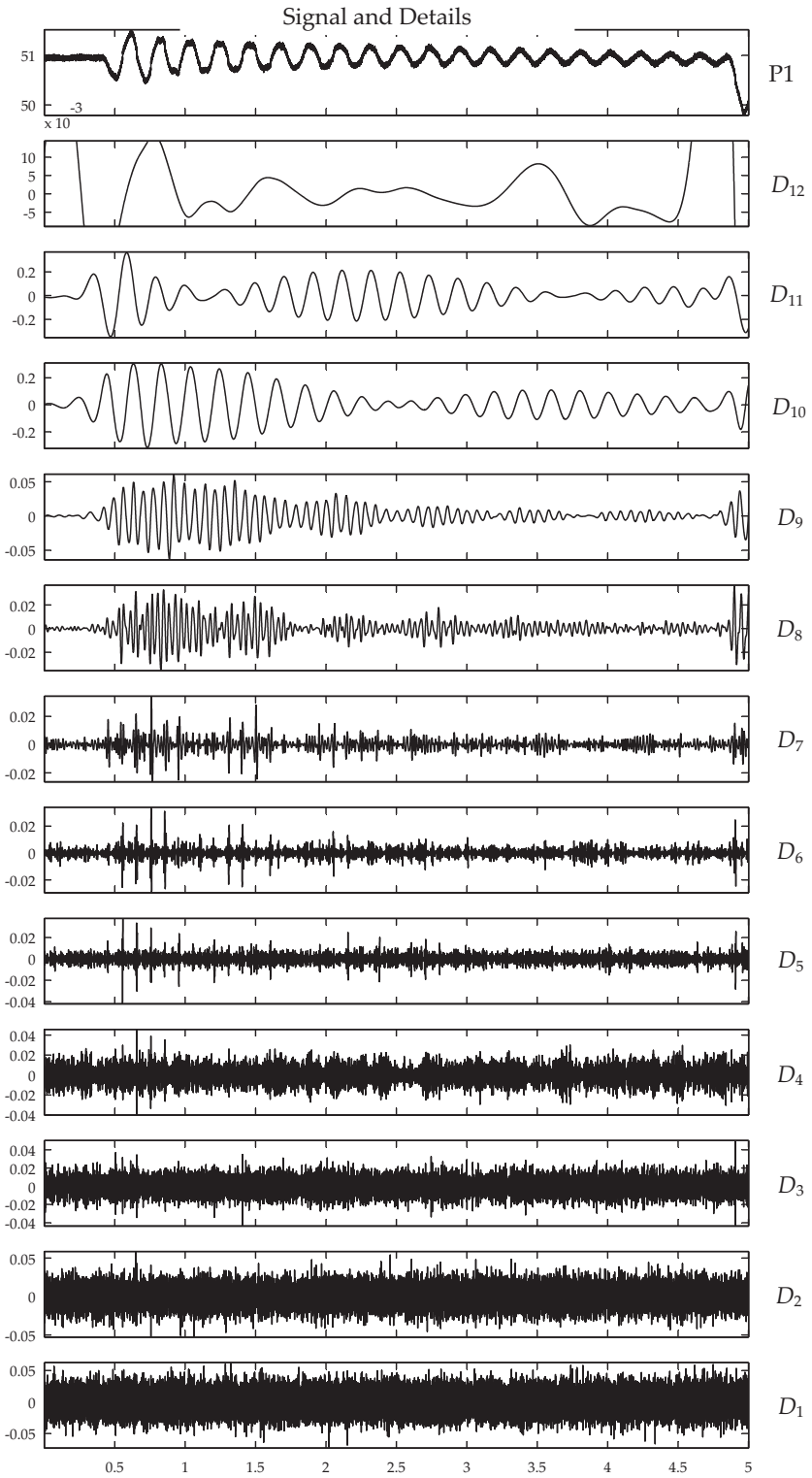

Figure F.8: Wavelet decomposition results of details for pressure records P1 shown in Fig. 8.11a.

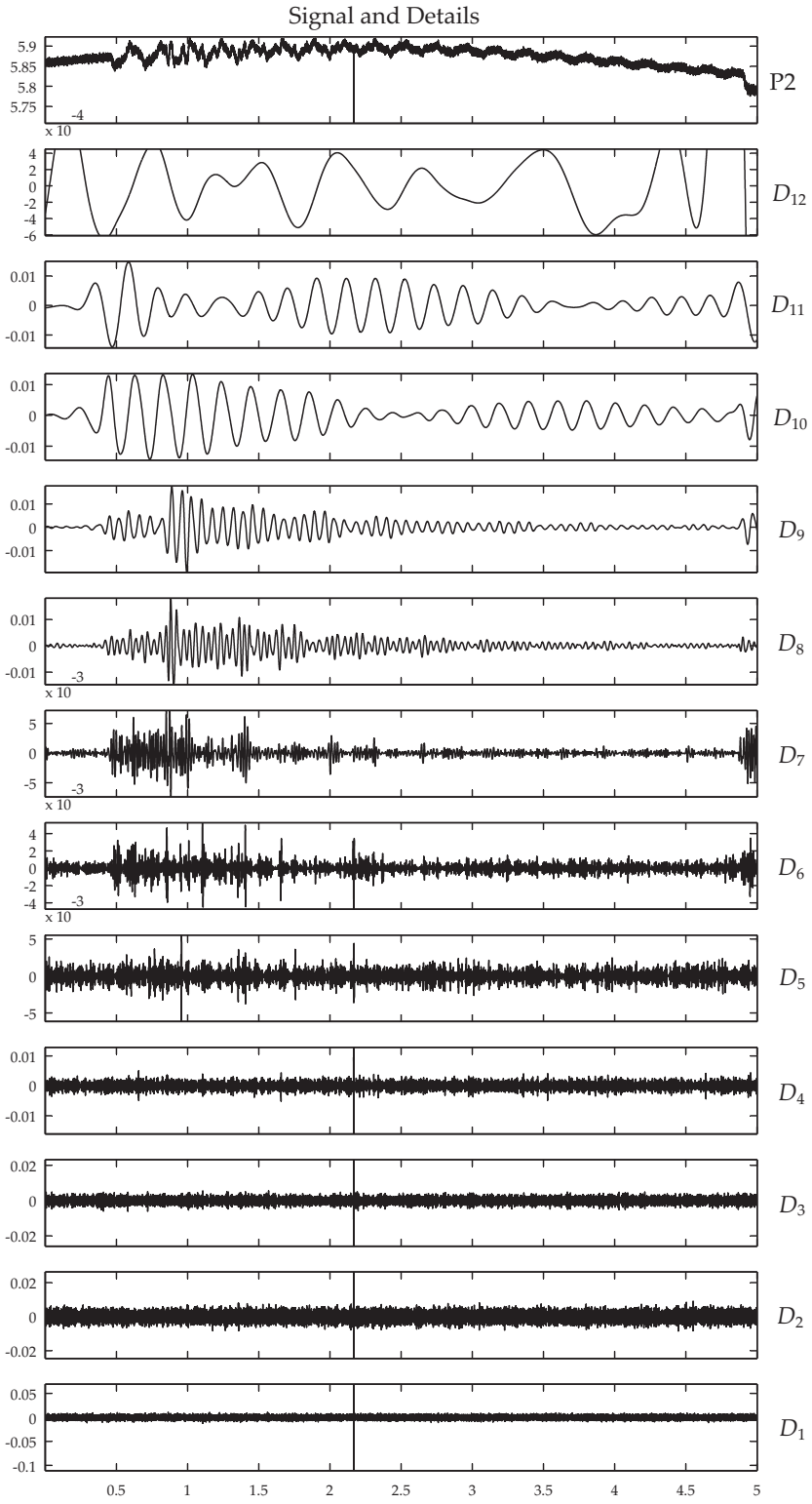

Figure F.9: Wavelet decomposition results of details for pressure records P2 shown in Fig. 8.11b.

Communications du Laboratoire de Constructions Hydrauliques ISSN 1661-1179
Ecole Polytechnique Fédérale de Lausanne
Editeur: Prof. Dr A. Schleiss

N° 36 2008 T. Meile
Influence of macro-roughness of walls on steady and unsteady flow in a channel

N° 37 2008 S. A. Kantoush
Experimental study on the influence of the geometry of shallow reservoirs on flow patterns and sedimentation by suspended sediments

N° 38 2008 F. Jordan, J. García Hernández, J. Dubois, J.-L. Boillat
Minerve - Modélisation des intempéries de nature extrême du Rhône valaisan et de leurs effets

N° 39 2009 A. Duarte
An experimental study on main flow, secondary flow and turbulence in open-channel bends with emphasis on their interaction with the outer-bank geometry

N° 40 2009 11. JUWI
Treffen junger Wissenschafterinnen und Wissenschafter an Wasserbauinstituten

N° 41 2010 Master of Advanced Studies (MAS) in Water Resources Management and Engineering, édition 2005-2007 - Collection des articles des travaux de diplôme

N° 42 2010 M. Studer
Analyse von Fliessgeschwindigkeiten und Wassertiefen auf verschiedenen Typen von Blockrampen

N° 43 2010 Master of Advanced Studies (MAS) in Hydraulic Engineering, édition 2007-2009 - Collection des articles des travaux de diplôme

N° 44 2010 J.-L. Boillat, M. Bieri, P. Sirvent, J. Dubois
TURBEAU – Turbinage des eaux potables

N° 45 2011 J. Jenzer Althaus
Sediment evacuation from reservoirs through intakes by jet induced flow

N° 46 2011 M. Leite Ribeiro
Influence of tributary widening on confluence morphodynamics

N° 47 2011 M. Federspiel
Response of an embedded block impacted by high-velocity jets

N° 48 2011 J. García Hernández
Flood management in a complex river basin with a real-time decision support system based on hydrological forecasts

N° 49 2011 F. Hachem
Monitoring of steel-lined pressure shafts considering water-hammer wave signals and fluid-structure interaction

ISSN 1661-1179

Prof. Dr A. Schleiss
Laboratoire de constructions hydrauliques - LCH
EPFL, Bât. GC, Station 18, CH-1015 Lausanne
http://lch.epfl.ch
e-mail: secretariat.lch@epfl.ch